Summer 7-15-2020

INTERACTION OF OPTOMECHANICAL CAVITIES WITH ACOUSTIC WAVES AND OSCILLATORS

Ke Huang

Recommended Citation

Huang, Ke. "INTERACTION OF OPTOMECHANICAL CAVITIES WITH ACOUSTIC WAVES AND OSCILLATORS." (2020). https://digitalrepository.unm.edu/ose_etds/78

Ke Huang

Candidate

Physics & Astronomy

Department

This dissertation is approved, and it is acceptable in quality and form for publication:

Approved by the Dissertation Committee:

Prof. Mani Hossein-Zadeh, Chairperson

Prof. Francesco Sorrentino

Prof. Arash Mafi

Prof. Daniel Feezell

INTERACTION OF OPTOMECHANICAL CAVITIES WITH ACOUSTIC WAVES AND OSCILLATORS

by

KE HUANG

B. S., Optical Information Science and Technology, Beijing Jiaotong University, 2008
M. S., Optical Engineering, Chinese Academy of Sciences, 2011

DISSERTATION

Submitted in Partial Fulfillment of the
Requirements for the Degree of

Doctor of Philosophy
Optical Science & Engineering

The University of New Mexico
Albuquerque, New Mexico

July 2020

Dedication

-*To my wife, who always gives me the most support on whatever I decide to do!*

-*To my parents for always putting my education in the first place!*

ACKNOWLEDGEMENTS

First and foremost, I would like to thank my Supervisor Dr. Mani Hossein-Zadeh for offering me the opportunity to work with him, for patiently leading me onto the right track of research about how to do, to think and to solve the problems. I would like to thank him for giving me the freedom, encouragement and confidence to explore and to succeed. I would like to thank him for all the kind help he gave me whenever I need a hand no matter whether in research or my life. Without his help and guidance, I can't imagine obtaining the achievement during my PhD course!

Secondly, I would like to thank Dr. Francesco Sorrentino, who guided me kindly on part of my research about the nonlinear dynamics of coupled oscillators. He taught me a lot from the initial state in this region. I have always appreciated his insight to research and valuable suggestions.

Thirdly, I would like to thank my great friends for their help on my life and research. I had a great time in the lab with Dr. Behsan Behzadi, Miss. Lala Rukh and Dr. Karen Blaha, to whom I can always talk about all kinds of interesting, exciting or even funny things. I also want to thank Dr. Chengyong Feng, Dr. Zhixiang Ren, Douglas Eury and Lynn Eury…… for making the graduate school life colorful experience.

Finally, I would like to thank my wife, my son, my parents and my brother, for all the great family time they have been giving me!

Interaction of optomechanical cavities with acoustic waves and oscillators

By

Ke Huang

B.S., Optical Information Science and Technology, Beijing Jiaotong University, 2008

M.S., Optical Engineering, Chinese Academy of Sciences, 2011

Ph.D., Optical Science & Engineering, University of New Mexico, 2020

ABSTRACT

Resonators and oscillators are key elements in a wide variety of natural and manmade systems. As such understanding and exploiting their dynamics both as isolated devices and members of coupled systems has been the subject of intensive investigation for more than a century. The advent of optomechanical resonators (OMRs) that support strong coupling between optical and mechanical modes resulting in self-sustained optomechanical oscillations, has created new opportunities for device development and implementation of coupled oscillatory systems. One aspect of this thesis is focused on exploring some of the unique features of OMRs and optomechanical oscillators (OMOs) that can be exploited for efficient acousto-optical transduction and signal processing in the context of underwater communication and sensing. Another aspect is related to interaction of OMOs with other types of oscillators and the behavior of the resulting oscillatory systems as well as closely related heterogenous oscillatory systems.

Notable achievements and results discussed in this dissertation include: 1) Demonstrating a new and practical method for stabilizing an OMO; 2) First demonstration of injection locking of an OMO via acoustic waves; 3) Studying the performance of optomechanical resonator as an acousto-optical receiver with optomechanical gain; 4) First demonstration of OMO functioning as a local oscillator and mixer in an acousto-optical underwater communication link; 5) Theoretical and experimental study of cluster synchronization in a multilayer network of Colpitts oscillators; 6) Theoretical study of the dynamics of a heterogeneous coupled oscillatory system comprising an optoelectronic oscillator and an OMO; 7) Experimental observations of synchronization between an optoelectronic and a Colpitts oscillator both in periodical oscillatory and chaotic regimes; 8) Application of homogeneous and heterogeneous oscillatory systems in sensing and detection.

TABLE OF CONTENTS

Chapter 1 Introduction

Chapter 2 Microtoroidal optomechanical cavities and Optoelectronic oscillators

Chapter 3 Direct stabilization of optomechanical oscillators

Chapter 4 Injection locking of optomechanical oscillators via acoustic waves

Chapter 5 Acousto-optical transducer with optomechanical gain

Chapter 6 Underwater acoustic signal detection and down conversion using optomechanical resonance and oscillation

Chapter 7 Dynamics of coupled oscillators and their applications in sensing

Chapter 8 Future directions

LIST OF FIGURES

LIST OF TABLES

LIST OF ABBREVIATIONS

FEM	Finite element modeling
FWHM	Full width at half maximum
OMO	Optomechanical oscillator
OMR	Optomechanical resonator
OEO	Optoelectronic oscillator
PZT	Piezoelectricity transducer
RBW	Resolution bandwidth
RF	Radio frequency
LO	Local oscillator
IF	Intermediate frequency
WGM	Whispering-gallery mode
LoD	Limit of Detection
TE	Transverse Electric
TM	Transverse Magnetic
SM	Single mode
MEH-PPV	Poly[2-methoxy-5-(2-ethylhexyloxy)-1,4-phenylenevinylene]
SAWs	Surface acoustic waves
IDT	Interdigital transducer
CMOS	Complementary metal–oxide–semiconductor

SNR	Signal to Noise Ratio
LE	Lyapunov exponent
PD	Photo detector
MZM	Mach-Zehnder Modulator
Osc	Oscilloscope
ESA	Electrical spectrum analyzer
OTF	Optical transmission function
FBG	Fiber Bragg gratings
FP	Fabry–Pérot
PC	Photonic crystal
SWaP	Size, Weight, and Power
UAVs	Underwater autonomous vehicles
CMT	Coupled mode theory
PS	Power spectrum
PID	Proportional–Integral–Derivative
DAQ	Data Acquisition device
CW	Continuous wave

Chapter 1

Introduction

1.1 Motivations

Coupling between optical and mechanical degrees of freedom is a fascinating phenomenon that has been intensively studied using different platforms and configurations [1-6] and furtherly extended to high-Q optical microcavities [7-9]. Optomechanical coupling in microscale and on-chip cavities [10] enables new functionalities that may be exploited in various applications, such as optical signal processing [11, 12], quantum information processing [13, 14], sensing [15, 16] and the like. Recent developments of microscale fabrication technologies have facilitated the fabrication of optomechancial devices and reduced the cost and complexity of investigating physics and application of cavity optomechanics. Combining cavity optomechanics with other transduction mechanisms may enable exploring the full potential of micromechanical devices and exploit them in new applications. One objective of this thesis is exploring and exploiting the dynamics of optomechanical resonators and oscillators in the presence of external perturbation or when they are coupled to other types of oscillators.

Study of the dynamics of coupled oscillatory systems has been an active area of research for a long time. Beyond its importance in many practical applications, the models and outcomes of these studies have played a crucial role in understanding the behavior of many complex systems. In particular, the study of coupled physically dissimilar oscillators may help with understanding the behavior of intercoupled natural and artificial systems.

For example, human body contains several coupled complex oscillators which are almost impossible to explore *in vivo*, as it is hard to isolate cells and control coupling among them *in vitro*. Experiments with non-biological systems may enable to provide a proxy for much more complex experiments using actual biological systems. Previous studies have revealed the similarity between the biological oscillators and various types of man-made oscillators. For example, Adhikari and collaborators observed a phase-flip bifurcation, or a transition from in-phase synchrony to out-of-phase synchrony in neuron models involving a large number of interacting neurons [17]. The same behavior was previously observed in certain electrical oscillators [18].

For the same reason, the theoretical and experimental study of coupled homogeneous and heterogeneous oscillators presented in this dissertation may provide insights and help with understanding the behavior of certain biological systems. Note that most of the previous experimental studies were based on coupling between oscillators of the same type. Here we study coupling between OMOs, Colpitts oscillators (a type of electrical oscillator) and optoelectronic oscillators (OEOs) as three different types of oscillators each having a different dynamic, some of which are analogous to those of biological oscillators. For example, optomechanical oscillator can exhibit multiple spatial modes of oscillation like the heart [19, 20]; while same as the lungs and individual neurons, the OEOs cannot exhibit special modes.

Understanding the dynamical behavior of the coupled oscillatory systems can also pave the way for exploring the unique properties of such systems. One example, reported in this dissertation, is exploring the enhanced sensitivity of both homogeneous and heterogeneous oscillatory systems to external perturbations for detection. We propose and demonstrate that the changes made into one of the oscillators in a pair of coupled oscillators can be measured with a sensitivity much higher than the sensitivity of the same oscillator to the same change as an individual oscillator. An additional advantage of sensors designed based on coupled heterogeneous oscillatory systems, is the ability of simultaneously detecting and measuring multiple physically dissimilar perturbations (detected by different types of oscillators in the coupled oscillatory system).

1.2 Chapter overview and collaborative work

The studies and ideas presented in this thesis were supervised and guided by Prof. Mani Hossein-Zadeh. Some of the theoretical analysis and experimental activities presented in chapter 7 was co-guided by Prof. Francesco Sorrentino and was performed collaboratively with two members of Prof. Francesco Sorrentino's group.

In what follows the content of the individual chapters are briefly descried:

Chapter 2 is an introduction to the main devices used in the experimental and theoretical studies covered in this dissertation. The topics covered in this chapter include a brief introduction to: Whispering Gallery (WGM) optical modes and optical microcavities, toroidal optical microcavity, optomechanical interaction, optomechanical resonators (OMRs), optomechanical oscillators (OMOs), and Optoelectronic oscillators (OEOs). Given that OMOs and OMRs have been used in nearly all of our studies, different aspects of their performance are discussed with more details including important parameters and the terminology used to describe and analyze the behavior of these devices (e.g., optomechanical coupling via radiation pressure, optomechanically induced gain and loss, optomechanical effective mass, and the like). Theoretical frame works used to describe the behavior of OMOs and OMRs and the resulting modes of operation (i.e., self-sustained optomechanical oscillation and optomechanical cooling) and impact of various noise mechanism are also covered in this chapter.

Chapter 3 describes a new and relatively simple technique for stabilizing the amplitude and frequency of optomechanical oscillators. The effectiveness of this method has been examined using microtoroidal optomechanical oscillators. We have experimentally demonstrated that this method can suppress the oscillation frequency and amplitude variations caused by changes of the surrounding temperature, optical pump power, and optical coupling gap.

Chapter 4 introduces acoustic waves as a mean for coupling one or more optomechanical oscillators with other oscillators of the same or different type (in particular, electronic and electromechanical oscillators). In particular we experimentally demonstrate that a microtoroidal OMO can be injection locked to another oscillator that generates acoustic waves that are coupled and propagate on the chip which carries the OMO. Various aspects of the injection locking via acoustic waves are experimentally characterized and also analyzed using both general injection locking theory and time domain differential equations of optomechanical oscillator combined with the finite element modeling.

Chapter 5 describes a new type of resonant acousto-optical transducer that exploits optomechanical gain in an OMR to provide enhanced sensitivity. It has been shown that the radiation pressure gain in an OMR may significantly enhance the sensitivity of acousto-optical transduction in an optomechanical cavity. As proof of concept, a microtoroidal OMR was used to experimentally demonstrate and characterize such enhancement.

Chapter 6 describes the performance of OMRs as hydrophones with optomechanical gain and OMOs as hydrophones that are also capable of down converting the baseband signals from ultrasonic carriers. The performance of the aforementioned hydrophones is characterized using an ultrasonic underwater link based on a modulated ultrasonic carrier. Both systems are theoretically analyzed, the challenges and limitations associated with frequency response and packaging of such devices are also discussed.

Chapter 7 presents the experimental and theoretical study of the dynamics of certain coupled oscillatory systems. First, the experimental results and theoretical analysis of cluster synchronization in a multilayer network of four coupled Colpitts oscillators is reported. While the theoretical framework for modeling the behavior of such system was well-known, to our knowledge this work is the first experimental demonstration of cluster synchronization in a multilayer network comprising four oscillators coupled via two different types of coupling mechanisms. Dr. Karen Blaha was involved with the related experimental activities and the theoretical analysis was done collaboratively by Prof. Francesco Sorrentino, Dr. Louis Pecora, and Dr. Fabio Della Rossa.

Next, we report the outcomes of the theoretically study of two mutually coupled oscillators: 1) an OMO coupled with an OEO, 2) an OMO coupled with a Colpitts oscillator.

We also report the first experimental observation of phase synchronization and chaos synchronization between an OEO and a Colpitts oscillator, mutually coupled via two different coupling mechanisms (i.e., optical and electrical). Finally, using two examples we demonstrate that coupling between two homogeneous (e.g., two Colpitts oscillators) or two heterogeneous oscillators (a Colpitts and an OEO), may be exploited to design oscillatory sensors for detecting and measuring small variations in certain parameters associated with one of the oscillators.

Chapter 8 briefly discusses an incomplete effort on using the acousto-optical transduction in OMR (assisted by radiation pressure induced optomechanical gain) for acousto-optical imaging as well as some future directions including: injection locking of OMO via surface acoustic waves, addressing challenges associated with using OMR and OMO based hydrophones for underwater sensing and communication, developing a phase model for coupled heterogeneous oscillators and theoretical modeling of the behavior of coupled OEO and Colpitts oscillator.

1.3 References

[1] C. K. Law, “Interaction between a moving mirror and radiation pressure: A Hamiltonian formulation,” Phys. Rev. Lett., **51**(3), 2537-2541 (1995).

[2] A. Heidmann, Y. Hadjar, and M. Pinard, “Quantum nondemolition measurement by optomechanical coupling,” Appl. Phys. B., **64**, 173-180 (1997).

[3] A. B. Klimov, V. Altuzar, “Spectrum of photons generated in a one-dimensional cavity with oscillating boundary,” Phys. Lett. A., **226**(1-2), 41-45 (1997).

[4] S. Mancini, D. Vitali, and P. Tombesi, “Optomechanical Cooling of a Macroscopic Oscillator by Homodyne Feedback,” Phys. Rev. Lett., **80**(4), 688-691 (1998).

[5] D. Vitali, S. Mancini, L. Ribichini, and P. Tombesi, “Macroscopic mechanical oscillators at the quantum limit through optomechanical cooling,” J. Opt. Soc. Am. B., **20**(5), 1054-1065 (2003).

[6] D. Vitali, S. Gigan, A. Ferreira, H. R. Böhm, P. Tombesi, A. Guerreiro, V. Vedral, A. Zeilinger, and M. Aspelmeyer, “Optomechanical Entanglement between a Movable Mirror and a Cavity Field,” Phys. Rev. Lett., **98**(3), Art. no. 030405 (2007).

[7] H. Rokhsari, T. J. Kippenberg, T. Carmon, and K. J. Vahala, “Radiation-pressure-driven micro-mechanical oscillator,” Opt. Express., **13**(14), 5293-5301 (2005).

[8] H. Rokhsari, T. J. Kippenberg, T. Carmon, and K. J. Vahala, “Theoretical and Experimental Study of Radiation Pressure-Induced Mechanical Oscillations (Parametric Instability) in Optical Microcavities,” *IEEE* J. Sel. Top. Quantum Electron., **12**(1), 96-107 (2006).

[9] T. J. Kippenberg and K. J. Vahala, “Cavity Opto-Mechanics,” Opt. Express., **15**(25), 17172-17205 (2007).

[10] M. Metcalfe, "Applications of cavity optomechanics," Appl. Phys. Rev., **1**(3), Art. no. 031105 (2014).

[11] H. Li, Y. Chen, J. Noh, S. Tadesse, and M. Li, "Multichannel cavity optomechanics for all-optical amplification of radio frequency signals," Nat. Commun.,**3**, Art. no. 1091 (2012).

[12] Wei C. Jiang, and Q. Lin, “Chip-scale cavity optomechanics in lithium niobite,” Sci. Rep., **6**, Art. no. 36920 (2016).

[13] S. Blien, P. Steger, N. Hüttner, Ri. Graaf, and A. K. Hüttel, “Quantum capacitance mediated carbon nanotube optomechanics,” Nat. Commun., **11**, Art. no. 1636 (2020).

[14] K. Stannigel, P. Rabl, A. S. Sørensen, M. D. Lukin, and P. Zoller, “Optomechanical transducers for quantum-information processing,” Phys. Rev. A., **84**(4), Art. no. 042341 (2011).

[15] F. F. Liu, S. Alaie, Z. C. Leseman, and M. Hossein-Zadeh, “Sub-pg mass sensing and measurement with an optomechanical oscillator,” Opt. Express., **21**(17), 19555-19567 (2013).

[16] A. G. Krause, M. Winger, T. D. Blasius, Q. Lin, and O. Painter, “A high-resolution microchip optomechanical accelerometer,” Nat. Photonics., **6**, 768–772 (2012).

[17] B. M. Adhikari, A. Prasad, and M. Dhamala, “Time-delay-induced phase-transition to synchrony in coupled bursting neurons,” Chaos, **21**(2), Art. no. 023116 (2011).

[18] A. Prasad, S. K. Dana, R. Karnatak, J. Kurths, B. Blasius, and R. Ramaswamy, “Universal occurrence of the phase-flip bifurcation in time-delay coupled systems,” Chaos, **18**(2), Art. no. 023111 (2008).

[19] A. Schliesser, G. Anetsberger, R. Rivière, O. Arcizet, and T. J. Kippenberg “High-sensitivity monitoring of micromechanical vibration using optical whispering gallery mode resonators,” New J. Phys., **10**(9), Art. no. 095015, (2008).

[20] R. H. Clayton, O. Bernus, E. M. Cherry, H. Dierckx, F. H. Fenton, L. Mirabella, A. V. Panfilov, F. B. Sachse, G. Seemann, and H. Zhang, “Models of cardiac tissue electrophysiology: Progress, challenges and open questions,” *Progress in Biophysics and Molecular Biology*, 1–27, Jun (2010).

Chapter 2

Microtoroidal optomechanical cavities and Optoelectronic oscillators

Optomechanical resonators/oscillators (OMRs and OMOs) and optoelectronic oscillators (OEOs) are the main devices used in the work presented in this dissertation. As such, understanding their working mechanism and theoretical frameworks used to study various aspects of their behavior, is critical for understanding the corresponding systems and applications that have been studied and explored during the course of this project. Moreover, familiarity with the terminology used to describe and characterize these devices and systems, may facilitate understanding their role in systems that exploit their unique characteristics.

In this chapter, first we review the relevant aspects of the of cavity optomechanics starting from the characteristics of the optical and mechanical modes of microcavities that support radiation pressure based coupling between these modes (hereafter referred to as "optomechanical resonators" or "OMRs"). In particular, we focus on a specific class of optomechanical resonators that their optical cavities can sustain Whispering-Gallery modes (WGMs). Then, we review the dynamics of radiation pressure based interaction between the resonant optical power of a WGM and the motion of a mechanical mode of the OMR (referred to as "optomechanical interaction"), covering concepts such as, optomechanical coupling, effective mass, optomechanical damping, optomechanical gain, optomechanical oscillation and optical spring effect. Next, we review the basic principles of optoelectronic oscillation in the context of a basic single-loop optoelectronic oscillator (OEO). Finally, we briefly review the theoretical framework that we used to investigate the dynamics of an OEO in particular in the context of coupled oscillatory systems.

2.1 Microtoroidal optical cavities and WGMs

The main optical device used in this work is a silica microtoroid that is a toroidal optical microcavity formed from silica and supported by a slight silicon pillar. This type of optical microresonator is well known for supporting high quality optical and mechanical modes within a single structure. Silica microtoroids can support optical modes with quality factors in excess of 10^8 [1] and mechanical modes with quality factors in excess of 2000 (at atmospheric pressure) [2]. More importantly, many mechanical modes of a microtoroidal structure can strongly couple to the optical modes (WGMs residing in the toroidal section) with a relatively small effective mass resulting in low threshold optical power for optomechanical oscillation [1-3]. Additionally, due to strong confinement in azimuthal direction, the modal spectrum of a microtoroid is relatively simple compared to other microresonators such as microspheres. Finally, yet importantly, the fabrication process of silica microtoroid is relatively easy and with low cost compared to most optical microresonators.

2.1.1 High-Q WGMs in microtoroidal optical cavities

Toroidal microcavities sustain a type of resonant optical modes called “Whispering Gallery Modes” or “WGMs”. WGMs are traveling electromagnetic modes that are confined in a circular trajectory just within the surface of the toroidal structure by means of total internal reflection (TIR). WGMs have a relatively small cross-sectional modal area (compared to the radius of the microcavity) and feature small mode volume and may support long photon lifetime (or equivalently high-quality factors or high-Q) if the level of loss inside the corresponding microcavity is low. As such, the strength of light-matter interactions inside microcavities that support high-Q WGMs is enhanced by orders of magnitude. In the context of optomechanical interaction, the above mentioned properties result in large level of radiation pressure and therefore strong bidirectional coupling between a WGM and one or more mechanical modes of the toroidal microcavity. The history of WGMs goes back to almost a century ago when Lord Rayleigh explained the unusual propagation of sound around the curved surface of the so-called Whispering-Gallery of St Paul's cathedral in London [4-6]. The first observation of optical WGM was reported back in 1961, when stimulated emission was coupled to the WGMs of a crystalline spherical resonator [7]. As opposed to conventional optical resonators (e.g., Fabry–Perot or FP cavities) that recirculate optical waves using two or more mirrors, in WGM cavities optical waves are trapped in a circular dielectric boundary by means of total internal reflection (TIR). WGM cavities, such as the microtoroid, microring, microsphere and microdisk cavities, support very small mode volumes and optical quality factors that are usually very high. The quality factor, as one of the main characteristics that distinguishes WGM cavities from other cavities, is defined as the ratio of the energy stored inside a cavity and the round-trip loss. As such, quality factor essentially quantifies the loss in a cavity. In practice, the quality factor can be measured using $Q \sim \nu/\Delta\nu = \lambda/\Delta\lambda$ where ν and λ are the resonance frequency and wavelength of the corresponding mode (WGM in this case), and $\Delta\nu$ and $\Delta\lambda$ are the FWHM of the same mode (in frequency or wavelength domain). The measured value of quality factor that includes all optical losses experienced by the mode is referred to as total-Q (Q_{tot}) or loaded Q_{L}. Q_{tot} can be expanded in terms of intrinsic quality factor Q_{int} (quantifying all losses except coupling loss), and external quality factor Q_{ext} (quantifying coupling loss):

$$\frac{1}{Q_{tot}} = \frac{1}{Q_{int}} + \frac{1}{Q_{ext}}. \tag{2.1}$$

with

$$Q_{int} = \frac{\lambda_{res}}{\delta\lambda_0} = \frac{\omega_{res}}{\delta\omega_0} = \omega_{res}\tau_0 = \omega_{res}\kappa_0^{-1}. \tag{2.2}$$

$$Q_{tot} = \frac{\lambda_{res}}{\delta\lambda} = \frac{\omega_{res}}{\delta\omega} = \omega_{res}\tau_{tot} = \omega_{res}\kappa_{tot}^{-1}. \tag{2.3}$$

here λ_{res} and ω_{res} are the optical resonant wavelength and frequency ($\omega_{\mathrm{res}} = 2\pi c/\lambda_{\mathrm{res}}$, c is the speed of light) of the cavity, respectively. $\delta\lambda_0$ and $\delta\omega_0$ are the intrinsic FWHM of the cavity resonance in wavelength and frequency, respectively. $\delta\lambda$ and $\delta\omega$ are the loaded FWHM. τ_0 and τ_{tot} are the intrinsic and loaded cavity photon (energy) decay time. κ_0 and κ_{tot} are the intrinsic and loaded photon (energy) decay rate.

Figure 2.1 shows a schematic view of a toroidal WGM resonator and its associated access line that represents the optical coupling [8]. The input signal field A_{in} is coupled to the resonator mode (whose amplitude is noted as A_0) with a characteristic lifetime τ_{e} that is determined by the coupling gap. The light trapped inside the resonator can escape from the cavity 1) through radiative or absorptive processes with a characteristic duration τ_0 and 2) through back coupling to the output field A_{out} in the access line, still with a characteristic duration τ_{e}.

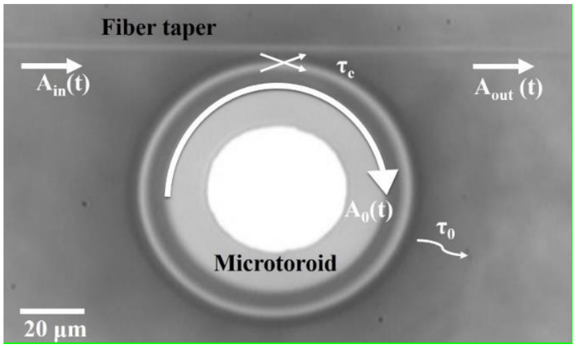

Fig. 2.1. Micrograph of a toroidal microresonator coupled to a fiber-taper.

The intrinsic optical loss in a WGM cavity or resonator includes: the surface roughness induced scattering loss, the optical absorption in the structural material of the cavity and the bending loss (radiation loss) associated with curved optical path inside the cavity. The external loss associated with the power exchange between the cavity and the waveguide(s) used to couple light into and out of the cavity. The most common microsphere WGM microresonators are spherical WGM cavities made of fused silica, which can sustain WGMs with *Q*-factors of as large as 9×10^9 [9]. Silica microtoroids, the microcavities used in this work, are the on-chip version of silica microspheres and can sustain WGMs with *Q*-factors in excess of 10^8. The large quality factor of the WGM in silica microspheres and microtoroids is a result of extremely low optical absorption of silica in the visible and near infrared range, as well as extremely low scattering loss due to small surface roughness. For toroidal and spherical cavities, the smooth surface is a result of melting and solidification process, typically used to fabricate these types of cavities, as well as unique physical properties of silica. The shape and smoothness of these cavities is naturally controlled by heat transfer and surface-tension during the melting-solidification process. The fabrication of silica microtoroid is relatively simple and it was first proposed and demonstrated in Ref [10], and which only involves photolithography, wet etching, dry etching and laser melting.

Figure 2.2 shows the fabrication process of a silica microtoroid on a silicon chip. First a silica microdisk is formed on silicon substrate having a thin (~ 2 micron) layer of silica (SiO_2) using photolithography and wet etching with Hydro fluoric acid (HF). Next, XeF_2 etching is used to remove the Si under the silica microdisk and creates a tapered silicon pillar as shown in Fig. 2.2(c). Finally, the microtoroid is formed by shining a collimated beam of CO_2 laser to melt the silica disk. The melting process is self-quenching and for a given laser power stops when the diameter of toroidal section and its distance from the silicon pillar is such that the heat generated by CO_2 laser absorption is balanced with the heat transfer from the silica microtoroid to the silicon pillar.

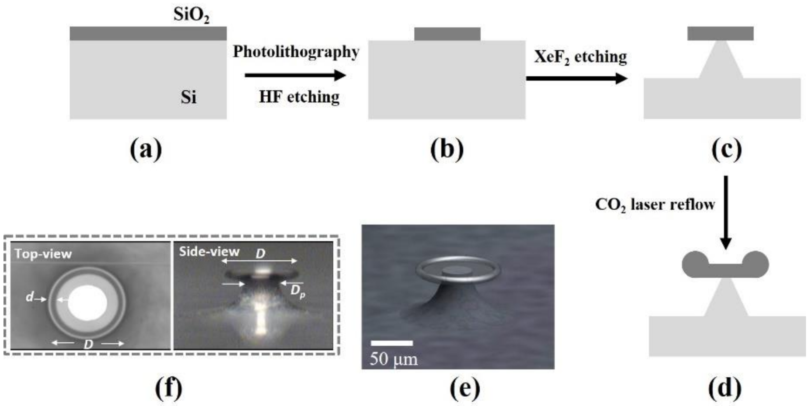

Fig. 2.2. (a)-(d) Show the fabrication process of microtoroid, and (e) shows the 3D picture of the microtoroid. (f) shows the top and side view of the microtoroid, here D is the major diameter of the toroid, d is the minor diameter of the donut shape cavity and D_p is the diameter of the pillar at the contact point.

Whispering gallery modes (WGMs) in circular dielectric cavities resonators has been subject of intensive study and is well understood [11-13]. WGMs are typically characterized by two polarizations (modes with transversal electrical field or TE modes, modes with transversal magnetic field or TM modes) and three mode numbers *s*, *l* and *m* which are the radial, angular and azimuthal mode numbers respectively. The value of *l* is close to the number of wavelengths that fit into the optical length of equator. The value $l-m+1$ is equal to the number of the field maxima in the polar direction, and $2l$ is the number of maxima in the azimuthal direction around the equator. The resonant wavelength is determined by the value of *s* and *l*. Figure 2.3 shows a 3D view of three typical WGMs of a spherical dielectrical potential wall calculated using resonance theory [14, 15].

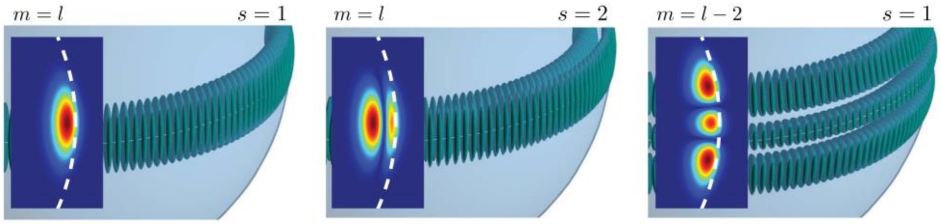

Fig. 2.3. Iso-intensity surfaces and intensity cross sections (inset) for the fundamental TE mode $l = m$ and $s = 1$ (left), second radial mode $l = m$ and $s = 2$ (middle), third polar mode $m = l - 2$ and $s = 1$ (right) in a spherical resonator [15].

Generally, the field distribution associated with WGMs of a spherical dielectric resonator can be calculated by solving Helmholtz equation in spherical coordinates [11,16]. If the sphere is composed of a homogeneous dielectric material, light that circulates near the dielectric-air boundary inside the cavity, maintains a constant polarization along its trajectory and the solutions can be divided into two categories of modes, transverse magnetic (TM) or transverse electric (TE). The field components can be expressed in terms of a single field component (E_φ for TM mode and H_φ for TE mode) and the solutions can be found by solving the scalar wave equation for either the E_φ or H_φ alone by the separation of variables, i.e., E_φ or $H_\varphi = \psi(\varphi,\theta,r) = \psi_\varphi(\varphi)\psi_\theta(\theta)\psi_r(r)$. The mode numbers ($s$, l, m) correspond to the eigen values of the resulting eigen functions. The azimuthal eigen function can be written as:

$$\psi_\varphi = \frac{1}{\sqrt{2\pi}}\exp\left(\pm im\varphi\right). \tag{2.4}$$

The polar angle dependent function (ψ_θ) should satisfy:

$$\frac{1}{\cos(\theta)}\frac{d}{d\theta}\left(\cos(\theta)\frac{d}{d\theta}\psi_\theta\right) - \frac{m^2}{\cos(\theta)^2}\psi_\theta + l(l+1)\psi_\theta = 0. \tag{2.5}$$

and the radius dependent function(ψ_r) has to obey:

$$\frac{d^2}{dr^2}\psi_r + \frac{2}{r}\frac{d}{dr}\psi_r + \left(k^2 n(r)^2 - \frac{l(l+1)}{r^2}\right)\psi_r = 0. \tag{2.6}$$

The last two equations have the analytical solutions that can be expanded as a function of generalized Legendre Polynomials $P_m^l(cos\theta)$ and the Bessel function $j_l(kr)$ [16]. For each polar mode number l, the allowed azimuthal mode numbers are limited to $-l < m < l$, resulting in $2l + 1$ degenerate azimuthal modes, the non-zero value of $\psi_r(r)$ when r is larger than the resonator radial indicates that an evanescent field exists in the surrounding. In spite of the simplicity of analytical solution for the WGMs in spherical cavities, finding such analytical solutions for WGMs of toroidal microcavities is much more challenging. The complexity of obtaining approximate solutions for toroidal geometry arises from the inseparability of a scalar wave equation in the local toroidal coordinates and the absence of a standard technique for finding the solutions of the corresponding two-dimensional problems. In order to circumvent these difficulties, B. Min *et al.*, applied a perturbation method using a proper expansion parameter for a "fiber-like" (small inverse aspect ratio: d/D) toroidal geometry to calculate the cavity mode field inside and near the periphery of a toroidal microcavity [12]. Using this method, the modal volume, resonant wavelength, mode index, and radiative quality factor of WGMs of toroidal geometry can be derived. Numerical modelling is another efficient way to simulate optical WGMs in toroidal microcavities, commercial Finite Element Method (FEM) software, like COMSOL Multiphysics and Lumerical, have been successfully used for calculating the WGMs in these microcavities.

2.1.2 Coupling light to the WGMs of toroidal microcavities

Evanescent wave coupling between a waveguide and the microcavity is the most efficient way to couple optical power into and out of the WGMs without degrading their quality factor [8, 17, 18]. The strength of evanescent coupling depends on two critical factors: 1) The overlap between the evanescent field of the wave propagating in the coupler and the evanescent field of the WGM. 2) Phase matching (velocity matching) between the light traveling in the coupler and the WGM circulating inside the microcavity. Figure 2.4 shows three different evanescent wave coupling methods: prism coupling, angle-polished fiber coupling and fiber taper/waveguide coupling.

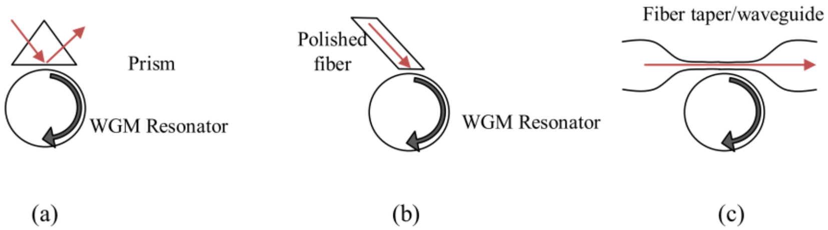

Fig. 2.4. (a) Optical power is coupled to the WGM resonator through (a) prism, (b) angle-polished fiber, and (c) fiber taper or optical waveguide.

Prism coupling was the first method proposed for coupling light into WGM cavities

[19]. This method may enable a coupling efficiency up to 75% [20], however, it is not practical for coupling light into the micron scale toroidal cavities. Angle-polished fiber coupling can reach up to 60% coupling efficiency [21], however the fabrication of angle-polished fibers with accurate angle is difficult and the optical coupling factor cannot be optimized easily. Fiber taper coupling is the most popular technique used in the laboratory, the fabrication of fiber taper is easy and cheap, the coupling efficiency can reach 99.97% [22], fiber taper coupling was used for all the experiments presented in this thesis.

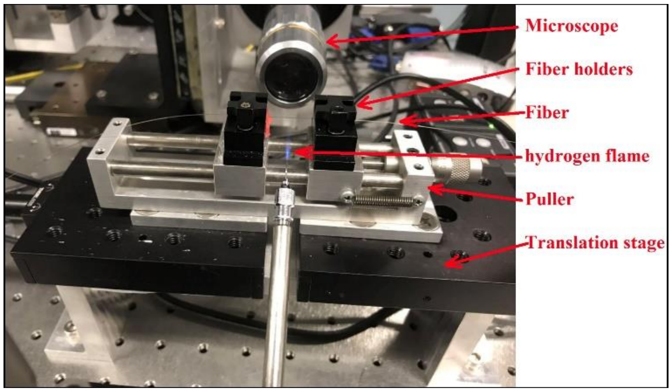

Fig. 2.5. Fiber pulling setup, the fiber is held by two V-grooves using magnetic clamps. The fiber holders are pulled away from each other by two computer controlled motors. The relative distance between the flame and the exposed section of the fiber is controlled using an XYZ translation stage on which the torch (that generates the hydrogen flame) is mounted.

The silica fiber taper used here can be fabricated by heating and pulling a regular SMF28+ single mode fiber. Figure 2.5 shows the fiber taper pulling setup that is used in this work. First the plastic coating is removed from a small section (1-2 cm long) of an optical fiber that supports only one mode at a wavelength of 1550 nm (SEM28+ in this case). Next, the exposed section is cleaned with acetone, methanol and isopropyl alcohol and the fiber is held by two magnetically clamped V-grooves holders such that the exposed section is placed between the holders. A hydrogen flame is brought close to the fiber using a 3D translation stage that hold the torch, in order to heat the exposed section of the fiber and meanwhile the holders are pulled away from each other by two pullers (on which they are mounted) using two computer controlled DC motors.

During the pulling process, the thickness of the fiber taper and the optical power transmitted through the fiber are monitored (in real time) using a microscope and a photodetector. The resulting fiber taper has a symmetrical shape around a narrow waist starting from a minimum diameter of between 0.8 -1.2 microns and gradually growing to a maximum diameter of 125 microns (the diameter of a single mode fiber). As such, given that the core diameter of the single mode SM fiber is 8-9 microns, a section of the fiber taper will be air cladded. The section near the taper waist only support one transverse mode with relatively large evanescent tail (residing in air) suitable for coupling to WMGs of toroidal or spherical microcavities.

2.2 Optomechanical coupling in microtoroidal cavities

The structure of the microtoroid cavity described above, not only supports high-Q WGMs but also relatively low loss mechanical modes. The motion of these mechanical modes can alter the resonant frequencies (wavelengths) of WGMs, by changing their optical path lengths. In the meantime, the magnitude of the circulating optical power in WGMs can become so large that the resulting radiation pressure will affect the mechanical motion of the mechanical mode. In this section we explore the dynamics of this mutual “optomechanical” coupling. Note that the optical mode may also affect the motion of the mechanical mode through thermal effects (e.g., thermomechanical deformation caused by the heat generated through optical absorption), however such effects are absent or negligible in a silica microtoroid.

2.2.1 Optical radiation pressure force and optomechanical coupling

The most basic optomechanical resonator that supports radiation pressure based optomechanical coupling is a Fabry–Pérot optical cavity with a movable mirror shown in Fig. 2.6(a). Here we use Fabry–Pérot optical cavity to explain the optical radiation pressure and optomechanical coupling. The optical input (pump) power can be coupled to the optical cavity if its wavelength is within the bandwidth and close to the resonant frequency (wavelength) of a cavity mode. The magnitude of the coupled power and therefore the resulting circulating optical power depends on the difference between the pump wavelength and the resonant wavelength. The circulating power inside the cavity can be much larger than the CW input power if the reflectivity of the mirrors is high enough to support large resonant power build up. Each photon circulating inside the cavity is reflected twice during each round trip. Upon each reflection the momentum transferred to the mirror by the photon is $|\Delta p| = 2h/\lambda$ (where λ is the photon wavelength) resulting in a pressure (called “radiation pressure”) equal to $2I_{circ}/c$ inserted on each mirror (here I_{circ} is the intensity of the circulating optical power in the cavity).

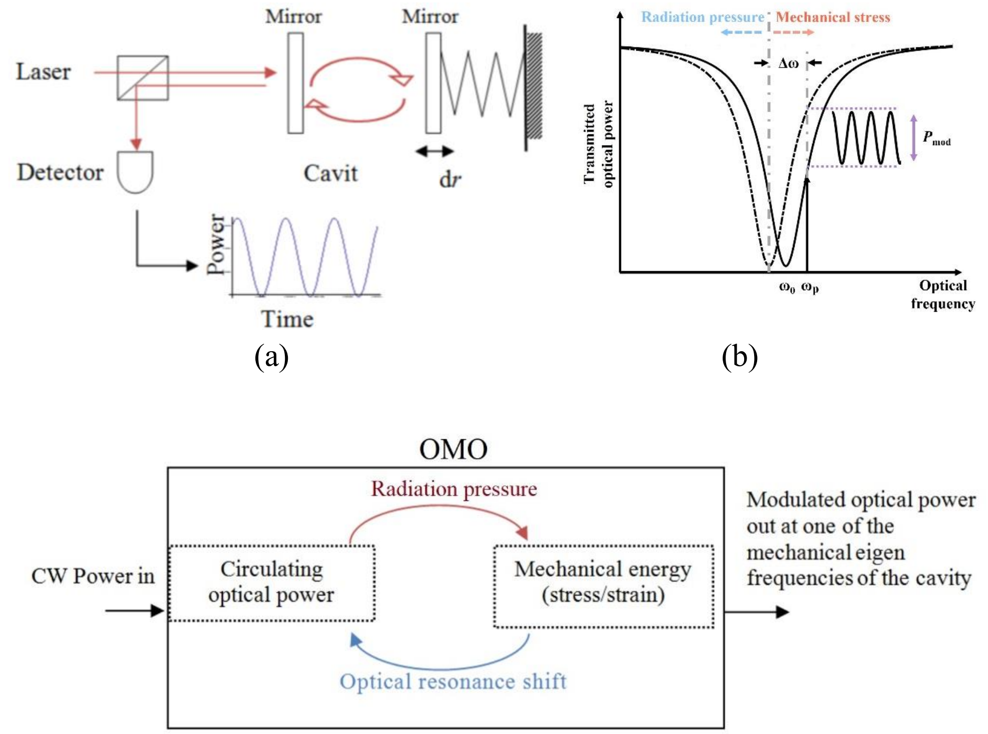

(a) (b)

(c)

Fig. 2.6. (a) Optomechanical interaction between optical field in a Fabry–Pérot cavity with a movable mirror. (b) The reflection transfer function of the FP cavity near a resonant mode with a resonance frequency of ω_0. The interplay between radiation pressure and the mechanical stress results in harmonic oscillation of the optical path length and therefore ω_0; at a fixed pump frequency ω_p, oscillation of ω_0 results in modulation of the reflected optical power. (c) Optomechanical oscillation mechanism [23].

If the mirror is movable, it is pushed forward by the radiation pressure increasing the resonant optical path and therefore the resonant wavelength of the corresponding mode. Depending on the original detuning between the pump wavelength (which is fixed) and the resonant wavelength of the optical mode, this shift may increase or decrease the magnitude of the circulating power in the mode and therefore the resulting radiation pressure. As such, in a high-Q FP optical cavity with a movable mirror, the motion of the movable mirror and the magnitude of the circulating optical power are mutually coupled. This is what is known as radiation pressure based optomechanical coupling [24]. If originally the pump wavelength is smaller (blue shifted) than the resonant wavelength of the cavity mode, optomechanical coupling amplifies the motion of the mirror through a feedback mechanism. In this case when the mirror is pushed by the radiation pressure, the circulating optical power drops (since the difference between the pump wavelength and resonant wavelength is increased). As a result, the radiation pressure decreases, and the mirror moves back by restoring mechanical force (similar to a spring). Figure 2.6(b) shows the transmission spectra of the Fabry-Perot cavity shown in part-a, at maximum and minimum displacement of the movable mirror. At a fixed pump power, the transmitted optical power from the cavity is proportional to the resonant wavelength (frequency) of the mode and therefore follows the dynamic of the movable mirror. As shown in Fig. 2.6(c), optomechanical oscillation is essentially the interplay between the energy stored in two reservoirs: a mechanical resonator (spring loaded movable mirror)) and an optical resonator (cavity). When the pump power is large enough this energy exchange results in self-sustained oscillation of the mirror and the circulating optical power with a frequency equal to the natural mechanical resonant frequency of the mirror [24-26]. Consequently, the optical transmitted (or reflected) optical power will be modulated at the same frequency. Such a system that converts CW optical input power to modulated optical power, using the intrinsic optomechanical coupling, is called optomechanical oscillator [27]. Self-sustained optomechanical oscillation in an FP cavity with a movable mirror was first predicted by Braginsky *et al* in the context of Laser Interferometric Gravitational-Wave Observatory (LIGO) [28].

2.2.2 Mechanical modes of the microtoroidal cavity

The vibration modes of any objects can be calculated by solving the equations of the linear theory of elasticity under the appropriate boundary conditions that are determined by the geometry [29]. The eigen value problem yields a set of normal modes and each mode has its own eigenfrequency Ω_m (m stands for "mechanical"), the loss of the mechanical energy is described by the (energy) damping rate Γ_m, which is related to the mechanical quality factor by $Q_m = \Omega_m/\Gamma_m$. The temporal evolution of the radial displacement $r(t)$ of the motion can be described by the simple canonical equation of motion for a harmonic oscillation of an effective mass m_{eff}:

$$m_{eff}\frac{dr^2(t)}{dt^2} + m_{eff}\Gamma_m\frac{dr(t)}{dt} + m_{eff}\Omega_m^2 r(t) = F_{ex}(t). \tag{2.7}$$

here, the $F_{ex}(t)$ denotes the sum of all forces acting on the mechanical resonator. In the absence of any external forces, $F_{ex}(t)$ is the thermal Langevin force.

The vibration modes of the object can be easily simulated using any FEM software. Here we used COMSOL to simulate the mechanical modes of the toroid microcavities used in various experiments. Figure 2.7 shows the simulated deformation associated with the first three mechanical modes of a silica microtoroid (with major diameter of D = 110 µm, pillar diameter of D_p = 60 µm and minor diameter of d = 8 µm).

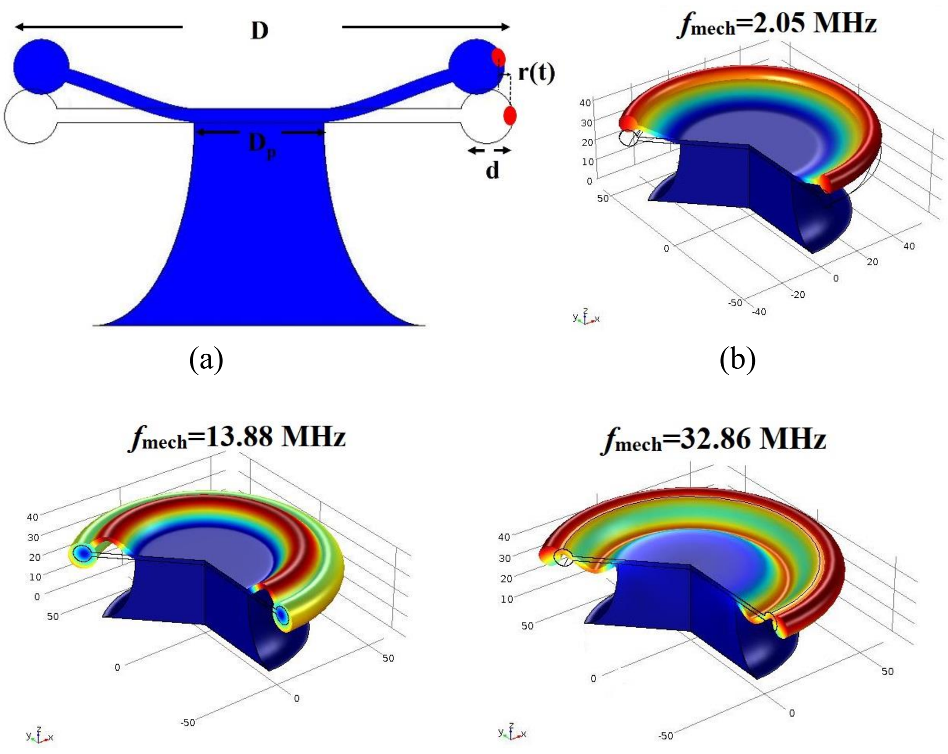

(a) (b)

(c) (d)

Fig. 2.7. (a) 2D cross-sectional illustration of the deformation associated with the first mechanical mode of a silica microtoroid. The red dot is the location of the WGM and r(t) is the radial displacement of the WGM resulted from the mechanical deformation. (b)-(d) show the 3D cross-sectional illustration of the first three mechanical modes of a silica microtoroid. The simulated microtoroid has a major diameter of D = 110 μm, pillar diameter of D_p = 60 μm and a minor diameter d = 8 μm. Simulation are performed using COMSOL FEM software. Color drawing indicates the relative magnitude of displacement. Here $f_{\mathrm{mech}} = \Omega_{\mathrm{mech}}/2\pi$.

2.2.3 Dynamic of optomechanical cavities.

In this section, first the relevant parameters of an optomechanical oscillator (or resonator) are defined and then the dynamics of the radiation pressure coupled optical and mechanical modes is discussed.

1) *Relevant parameters in an optomechanical resonator*

1.1) *Mechanical quality factor* Q_{m}

The loss of mechanical excitations, i.e., phonons, is quantified by the energy dissipation rate Γ_m, and the mechanical quality factor is defined as $Q_m = \frac{\Omega_m}{\Gamma_m}$, Q_m may include various dissipation processes where $\frac{1}{Q_m} = \sum \frac{1}{Q_i}$, here i labels different loss mechanisms, these loss mechanisms may be associated with energy loss to the molecules of the surrounding medium, thermoelastic damping, phonon-phonon interactions and material induced losses (e.g., by the relaxation of intrinsic or extrinsic defects state in the bulk or surface of the resonators).

1.2) *Optomechanical coupling coefficient* g_OM

The coupling between optical and mechanical modes of an optomechanical cavity is a parametric process. The change of optical resonant frequency due to optomechanical interaction can be expressed as $\omega_\mathrm{res}(r) = \omega_0 + r(\partial\omega_\mathrm{res}/\partial r) + \cdots$, where r is the mechanical displacement or the amplitude of the mechanical deformation of the cavity. Accordingly, the optomechanical coupling coefficient, which quantifies the strength of coupling between the optical and mechanical modes of the cavity, is defined as $g_\mathrm{OM} = \partial\omega_\mathrm{res}/\partial r$.

1.3) *Optical detuning*

Optical detuning is defined as $\Delta\omega_0 = \omega_\mathrm{L} - \omega_0$ where ω_L is the frequency of the pump laser, ω_0 is the cold cavity resonance (where optical pump power is so small that radiation pressure has no impact on the optical boundary). Optical detuning can be also defined based on wavelength ($\Delta\lambda_0 = \lambda_\mathrm{L} - \lambda_0$). In the presence of optomechancial interaction (when optical pump power is large enough to move the optical cavity boundary, $\Delta\omega = \omega_\mathrm{L} - \omega_\mathrm{res}(r) = \Delta\omega_0 + g_\mathrm{OM}r$. A normalized detuning ($\Delta\omega_\mathrm{N}$) is defined as the frequency (or wavelength) detuning divided by the loaded linewidth ($\delta\omega$) of the optical mode, so $\Delta\omega_\mathrm{N} = \Delta\omega/\delta\omega$. When $\Delta\omega < 0$, the laser is *red detuned (with respect to the cavity)* and the radiation pressure damps the mechanical motion; when $\Delta\omega > 0$, the laser is *blue detuned,* and the radiation pressure amplifies the mechanical motion [27]. As explained with more details in the following sections, the sign of the detuning controls the direction of energy transfer (from optical to mechanical modes or from mechanical to optical modes), and results in oscillation or cooling.

1.4) *Effective mass*

Optomechanical effective mass is defined as the mass involved in the motion at the direction that can change the optical path length of the cavity, it is written as $m_{eff} = 2E^2/(r_{max}\Omega)^2$. Here, E is the total energy stored in the mechanical mode, and $r_{\max}$ is the maximum displacement in the direction that changes the optical path length. Effective mass can be calculated through COMSOL FEM.

2) *Dynamics of radiation pressure coupled optical and mechanical modes*

In the absence of optomechanical coupling, the susceptibility of the mechanical resonator (or a mechanical mode of the optomechanical cavity) can be written as: $\chi_m^{-1}(\Omega) = m_{eff}[(\Omega_m^2 - \Omega^2) - i\Gamma_m\Omega]$. It can be shown [27] that when the mechanical mode is coupled to an optical mode (within the same optical cavity) via radiation pressure, the susceptibility is *optomechanically* modified and may be expressed as:

$$\chi_{m,eff}^{-1}(\Omega) = \chi_m^{-1}(\Omega) + 2m_{eff}\Omega_m g^2\left(\frac{1}{(\Delta\omega+\Omega)+\frac{i\kappa}{2}} + \frac{1}{(\Delta\omega-\Omega)-\frac{i\kappa}{2}}\right). \tag{2.8}$$

where $g = \hbar g_{OM}^2|\bar{a}|^2/(2m_{eff}\Omega_m)$, and $|\bar{a}|^2$ is proportional to the circulating photon number or optical intensity, Ω is the instant mechanical oscillation frequency, $\Delta\omega$

is the optical detuning. The effective susceptibility of Eq. (2.8) may be rewritten as:

$$\chi_{m,eff}^{-1}(\Omega) = m_{eff}[\left(\left(\Omega_m + \delta\Omega_m(\Omega)\right)^2 - \Omega^2\right) - i(\Gamma_m + \Gamma_{opt}(\Omega))\Omega]. \qquad (2.9)$$

with

$$\delta\Omega_m(\Omega) = g^2 \frac{\Omega_m}{\Omega}\left(\frac{\Delta\omega+\Omega}{(\Delta\omega+\Omega)^2+\frac{\kappa^2}{4}} + \frac{\Delta\omega-\Omega}{(\Delta\omega-\Omega)^2+\frac{\kappa^2}{4}}\right). \qquad (2.10)$$

and

$$\Gamma_{opt}(\Omega) = g^2 \frac{\Omega_m}{\Omega}\left(\frac{\kappa}{(\Delta\omega+\Omega)^2+\frac{\kappa^2}{4}} - \frac{\kappa}{(\Delta\omega-\Omega)^2+\frac{\kappa^2}{4}}\right). \qquad (2.11)$$

Equation (2.8) – (2.11) show that the impact of optomechanical coupling on the dynamics of the mechanical mode can be explained with a modified dissipation rate and modified resonant frequency.

2.1) *Optical spring effect*

The modification of resonant frequency is referred to as optical spring effect. When $\Omega = \Omega_m$, Eq. (2.10) shows the frequency shift of the oscillator induced by the light field:

$$\delta\Omega_m = g^2\left(\frac{\Delta\omega+\Omega_m}{(\Delta\omega+\Omega_m)^2+\frac{\kappa^2}{4}} + \frac{\Delta\omega-\Omega_m}{(\Delta\omega-\Omega_m)^2+\frac{\kappa^2}{4}}\right). \qquad (2.12)$$

In the limit of large cavity decay rate (i.e., $\kappa >> \Omega_m$), this equation yields

$$\delta\Omega_m = g^2 \frac{2\Delta\omega}{(\Delta\omega)^2+\frac{\kappa^2}{4}}. \qquad (2.13)$$

Equation (2.13) shows the spring constant of the mechanical resonator is softened when the pump laser is red-detuned ($\Delta\omega < 0$) and is hardened when the pump laser is blue detuned ($\Delta\omega > 0$).

2.2) *Optomechanical gain*

Optomechanically modified dissipation rate interaction may be referred to as *optomechanical gain* or *optomechanical loss* depending on the sign of the optomechanically induced change. Considering the last term of Eq. (2.9), we have:

$$\Gamma_{eff} = \Gamma_m + \Gamma_{opt}. \tag{2.14}$$

Where Γ_{eff} is the effective damping rate, Γ_m is the intrinsic mechanical damping rate (in the absence of optical power or optomechanical coupling) and Γ_{opt} is the optomechanically induced damping rate given by Eq. (2.11).

The Γ_{opt} can be positive or negative, in other words it can increase or decrease the mechanical damping rate. If $\Gamma_{\mathrm{opt}} > 0$, it increases the damping (what can be interpreted as cooling the cavity), if $\Gamma_{\mathrm{opt}} < 0$, it amplifies the amplitude of the mechanical motion above its natural thermal fluctuation. When Γ_{opt} is negative and large enough to completely cancel the intrinsic mechanical damping, self-sustained optomechanical oscillation will emerge. The optical pump power at which Γ_{eff} becomes zero and self-sustained optomechanical oscillation begins is called the threshold optical pump power (P_{th}) for the regenerative optomechanical oscillation. P_{th} can be calculated by equating the expression for the optomechanical damping (Eq. 2.11) to its intrinsic damping ($\Gamma_{\mathrm{m}} = \Omega_{\mathrm{m}}/\mathrm{Q}_{\mathrm{m}}$), the following expression for the threshold optical pump power results [30].

$$P_{th} = \frac{\Omega_m^2}{\mathrm{Q}_m}\frac{m_{eff}c^2}{\omega_0\mathcal{F}^2 8n^2 C}\left(\frac{1}{4(\Delta\omega-\Omega_m)^2\tau_{tot}^2+1}-\frac{1}{4(\Delta\omega+\Omega_m)^2\tau_{tot}^2+1}\right)^{-1}. \tag{2.15}$$

where the $\mathcal{F}$ is finesse of the cavity, and $C = (\tau/\tau_{ext})/(4(\Delta\omega\tau_{tot})^2 + 1)$. When the optical power is above threshold, the optomechanical resonator (OMR) becomes and optomechanical oscillator (OMO). Note that above threshold, Eq. (2.11) is not valid and cannot be used to estimate the linewidth of the mechanical resonance. Above threshold the optomechanical oscillation is limited by the Brownian noise in the mode [31].

Optomechanical cooling and amplification can be also explained in frequency domain [3]. Effectively the variation of the optical boundary of an optomechanical cavity caused by mechanical vibration leads to generation of Stokes and anti-Stokes sidebands (at frequencies, $\omega_0 \pm \omega_m$ where ω_0 is the optical and ω_m the mechanical frequency). Here we limit the analysis to the case where Stokes and anti-Stokes sidebands fall within the same cavity resonance (i.e., $\omega_m < \omega_0/Q_{tot}$). The energy exchanges between optical and mechanical modes may be explained based on the population of the Stokes and anti-Stokes photons circulating in the cavity. Figure 2.8 shows the spectrum of the mechanical vibration and the optical waves circulating inside an optomechanical cavity assuming the period of mechanical vibration is comparable or longer than the cavity lifetime. The mechanical vibration modulates the pump laser frequency (ω_L) and generates anti-Stokes and Stokes sidebands at $\omega_L + \Omega_m$ and $\omega_L - \Omega_m$ where Ω_m is the frequency of the mechanical mode that is coupled to the optical mode.

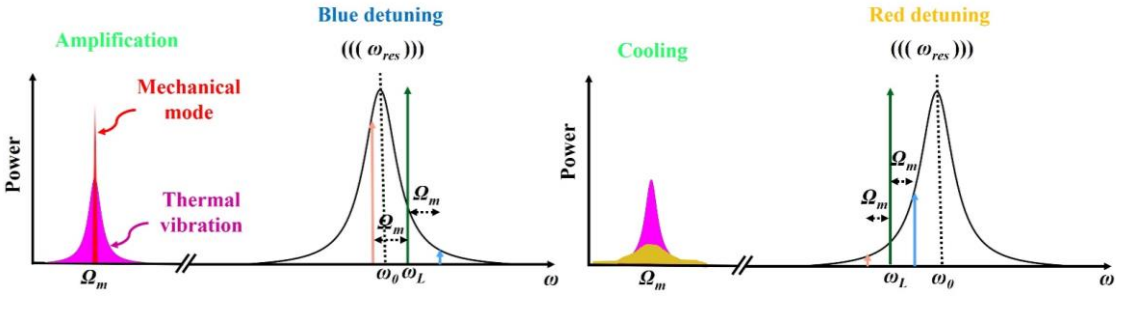

(a) (b)

Fig. 2.8. Diagrams showing spectrum of the mechanical vibration and the optical waves circulating inside an optomechanical cavity. (a) Optomechancial amplification where the pump is blue detuned, and the strength of anti-Stokes scattering is reduced compared to Stokes scattering. (b) Optomechanical cooling where the pump is red detuned, and the strength of Stokes scattering is reduced compared to anti-Stokes scattering [27].

At a non-zero detuning the resonant enhancement inside the optical cavity is different for the Stokes and anti-Stokes fields resulting in an asymmetric distribution of Stokes and anti-Stokes. Since the anti-Stokes photons have more energy than the low Stokes photons (because $E = h\nu$), the asymmetry between sidebands results in power loss or gain for the optical mode. As evident from Fig. 2.8(a), when the laser is blue detuned, the amplitude of anti-Stokes ($\omega_L + \Omega_m$) field is smaller than the amplitude of the Stokes field ($\omega_L - \Omega_m$) and energy is transferred from the optical mode to the mechanical mode (optomechanical amplification). As such, the linewidth of the mechanical vibrations becomes narrower and its amplitude grows above the natural thermal vibrations. With sufficient optical pump power ($>P_{th}$), the energy transferred to the mechanical mode will overcome the mechanical loss resulting in self-sustained optomechanical oscillation that manifests itself as extremely narrow linewidth that is only limited by the thermal noise [31]. Note that since mechanical oscillation can be observed only if the Stokes and anti-Stokes sidebands fall within the same cavity resonance (i.e., $\Omega_m < \omega_0/Q_{tot}$) the oscillation frequency is limited by the loaded linewidth of the optical mode. For a Q_{tot} in the 10^6 - 10^8 range the mechanical modes with frequencies within 1 - 100 MHz can be optomechanically excited and, if the optical pump power is above a threshold power (P_{th}), oscillate.

Figure 2.8(b) shows the opposite case where the laser is red detuned, and the amplitude of the anti-Stokes field is larger than the amplitude of the Stokes field resulting in power transfer from the mechanical mode to the optical mode or optomechanical cooling (damping). In this case the linewidth of the mechanical vibrations becomes wider and its amplitude is suppressed below the natural thermal vibrations. Both optomechanical oscillation (amplification) and cooling have been observed experimentally [1, 30].

2.2.4 Thermal and back action noise in optomechanical resonators (OMR)

When $P < P_{\mathrm{th}}$, OMR can be considered as a harmonic oscillator with the damping and mechanical frequency modified by the optical power:

$$m_{eff}\frac{d^2r(t)}{dt^2}+m_{eff}\Gamma_{eff}\frac{dr}{dt}+m_{eff}\Omega_m^2 r(t)=F_{appl}. \tag{2.16}$$

$$\Gamma_{eff}=\Gamma_m(1-\frac{P_{in}}{P_{th}}). \tag{2.17}$$

$$\Omega_m=\Omega_0(1+\zeta_P P_{in}). \tag{2.18}$$

where F_{appl} is any external forces that may be applied on the OMR, ζ_{P} is a coefficient combining the thermal drift due to optical absorption in the structure and the optical spring effect [2]. Equation (2.16) can be transformed to frequency domain as:

$$-\Omega^2 r+i\Omega\Gamma_{eff}r+\Omega_m^2 r(t)=\frac{F_{appl}(\Omega)}{m_{eff}}. \tag{2.19}$$

As such, the motion of the OMR cavity can be written as:

$$r(\Omega)=\chi_{m,eff}(\Omega)\frac{F_{appl}(\Omega)}{m_{eff}}=\frac{1}{\Omega_m^2-\Omega^2+i\Omega\Gamma_{eff}}\frac{F_{appl}(\Omega)}{m_{eff}}. \tag{2.20}$$

Equation (2.20) can be used to evaluate the response of the OMR to external excitations in applications where OMR is used as an acousto-optical transducer (an example is discussed in Chapter 5). In such applications, the presence of two noise mechanism may limit the performance of such transducer namely thermal noise and backaction noise. In what follows these two noise mechanisms are briefly discussed.

The motion of a single harmonic OMR in thermal equilibrium r(t) follows a trajectory oscillating at frequency Ω_{m}. However, this oscillation has randomly time-varying amplitude and phase, both the amplitude and phase change in time scale given by $\Gamma_{\mathrm{eff}}^{-1}$ [32].

Figure 2.9 shows the typical noise spectrum of the OMR in thermal equilibrium. For weak damping ($\Gamma_{\mathrm{eff}} < \Omega_{\mathrm{m}}$), the spectrum is a Lorentzian peak of width Γ_{eff}, located at ± Ω_{m}.

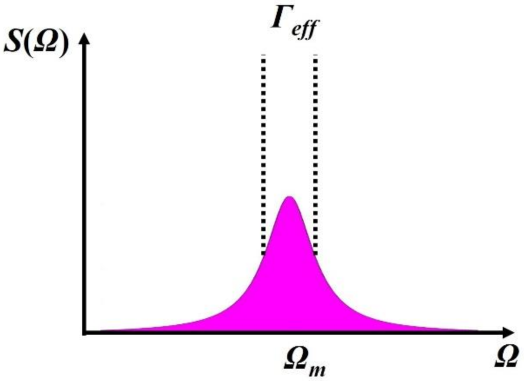

Fig. 2.9. Noise spectrum of an OMR in thermal equilibrium.

Using equipartition theory, the thermal force inducing thermal fluctuations can be written as [33]:

$$F_{thermal} = \sqrt{4K_B BTm_{eff}\Gamma_m}. \tag{2.21}$$

using Eq. (2.20) and (2.21), it can be shown that the resulting fluctuations of the radial mechanical displacement is:

$$r_{thermal} = \frac{\sqrt{4K_B BTm_{eff}\Gamma_m}}{m_{eff}\sqrt{\Omega_m^2 - \Omega^2 + i\Omega\Gamma_{eff}}}. \tag{2.22}$$

and the power spectral associated with thermal Brownian noise can be expressed as:

$$S_{thermal}(\Omega) = \frac{4K_B BT\Gamma_m}{m_{eff}} \frac{1}{(\Omega_m^2 - \Omega^2)^2 + (\Omega\Gamma_{eff})^2}. \tag{2.23}$$

Backaction noise is the optical noise arising from the classical amplitude noise induced by the shot noise of the photons circulating inside the optomechanical cavity. The optical shot noise exerts a random force on the mechanical mode via radiation pressure. The resulting fluctuations in the mechanical displacement is called back action noise and can be written as:

$$r_{ba} = \frac{2\hbar g_{OM}}{m_{eff}}\sqrt{\frac{2n_{cav}}{\kappa_{tot}}}\frac{1}{\sqrt{\Omega_m^2-\Omega^2+i\Omega\Gamma_{eff}}}. \quad (2.24)$$

the spectrum of the backaction noise can be expressed as:

$$S_{ba}(\Omega) = 2(\frac{2\hbar g_{OM}}{m_{eff}})^2\frac{n_{cav}}{\kappa_{tot}}\frac{1}{(\Omega_m^2-\Omega^2)^2+(\Omega\Gamma_{eff})^2}. \quad (2.25)$$

where n_{cav} is the intracavity photon number.

2.2.5 Microtoroidal optomechanical oscillation (OMO)

Silica toroid microcavity is an excellent optomechanical resonator for supporting optomechanical oscillation, its high optical Q, small dimensions, unique geometry, relatively large mechanical quality factor and reasonable large effective mass enable very low threshold powers and low oscillation phase noise. For a typical silica microtoroid with $Q_0 \sim 10^8$, 1 mW input power can result in circulating power of about 100 W, which is much larger than the threshold power to induce the self-sustained optomechanical oscillation in the micro scale structures. The first optomechanical oscillation in air and room temperature was observed and reported in the silica microtoroid in 2005 [1], and the characteristics of the microtoroidal OMO was comprehensively studied in 2006 [2, 34].

The dynamics of an OMO have been investigated by many researchers using a variety of theoretical frame works for representing the corresponding coupled differential equations in different equivalent forms, for example, classical Newtonian theory [35], Lagrangian mechanics [36], in frequency domain based on Stokes and anti-Stokes fields [3] and quantum mechanical Hamiltonian [37]. In this thesis, the classical Newtonian approach is used to analyze the behavior of OMO in different configurations.

The dynamics of optomechanical oscillation can be expressed by two coupled differential equations that govern the dynamics of the optical field and the mechanical motion:

$$m_{eff}\frac{d^2r(t)}{dt^2}+m_{eff}\Gamma_m\frac{dr}{dt}+m_{eff}\Omega_0^2r(t)=F_{rp}=\frac{2\pi n_{eff}}{cm_{eff}}\frac{cn_{eff}\varepsilon_0}{2}s|E(t)|^2. \quad (2.26)$$

$$\frac{dE(t)}{dt}+E(t)\left[\frac{\omega}{2Q_{tot}}+i\Delta\omega_0+i\frac{\omega_0}{r_0}r(t)\right]=i\sqrt{\frac{(2lcn_{eff}\varepsilon_0 s')P_{in}\omega}{\tau_0 Q_{ext}}}. \quad (2.27)$$

where F_{rp} is the radiation pressure force, n_{eff} is the effective refractive index of the resonant cavity that the optical power is experiencing, s and s' are the cross-sectional areas of the optical modes in the cavity and waveguide, respectively, E(t) is the intracavity optical field, $\tau_0 = 2\pi R_0 n/c$ is the photon round trip time in the optical resonator. The first equation describes the motion of the harmonic oscillator in the presence of radiation pressure, and the second equation describes the variation of circulating optical field in the resonant cavity. the detuning here becomes $\Delta\omega = \omega_{laser} - \omega_{cav}(r) = \Delta\omega_0 + \omega_0 r(t)/R_0$, and $r(t)/R_0$ is the approximation of the optomechanical coupling coefficient. In the above threshold regime, the behavior of the oscillation frequency can still be explained by Eq. (2.18).

While these equations can be used to estimate the oscillation amplitude of an OMO, as mentioned earlier, they cannot describe the oscillation linewidth that is limited by the thermal noise. The oscillation linewidth can be explained using the general theory of linewidth narrowing in self-sustained oscillators that also governs optical oscillators (laser) and electronic oscillators [38-40]. Prior theoretical studies of regenerative oscillator performance, when embedded in a thermal bath at temperature T, predict that the fundamental oscillation linewidth that is limited by thermal equipartition of energy becomes increasingly narrowed as the oscillation power is boosted in the system. The oscillation linewidth of OMO can be written as [2]:

$$\Delta\Omega = \frac{K_B T}{2P_d}(\Delta\Omega_0)^2. \tag{2.28}$$

where $\Delta\Omega_0$ is the intrinsic linewidth of the mechanical mode, P_d is the output power of the oscillator, in mechanical resonator the output power can be related to the stored mechanical energy as $P_d = \Omega_0 E_{stored}/Q_m = \Delta\Omega_0 E_{stored}$, K_B is the Boltzman constant, T is the temperature. the Brownian noise limited linewidth of microtoroid OMO has been verified experimentally [31], and the linewidth matches the Eq. (2.28). Eq. (2.28) can be also expressed as [2]:

$$\Delta\Omega = \left(\frac{4K_B T Q_{tot}^2}{m_{eff}\Omega_0^2 R_0^2}\right)\frac{\Gamma_\Omega{}^2 \Delta\Omega_0}{M^2}. \tag{2.29}$$

where $M = P_{mod}/P_{max}$ is the optical modulation depth induced by resonator motion, P_{mod} and P_{max} are the modulated and maximum power of the output, Γ_Ω is the optical modulation transfer function that can be estimated by solving Eqs. (2.26) and (2.27).

The oscillation stability of a free running OMO is maintained by the self-thermal locking mechanism [41]. Basically, In the thermal equilibrium state when the cavity Lorentzian is on the right side of the pump line (pump frequency is blue detuned relative to the resonance frequency of the cavity), there is a self-stable equilibrium since a small pump power decrease will reduce the cavity temperature and consequently the cavity wavelength will drift to the left; this will increase the absorbed power and hence will compensate for the pump reduction (an increase in pump power will cause a small compensation to the other direction). Self-thermal locking strength is proportional to the pump power strength and is a weak stabilization mechanism that can only maintain the OMO's oscillation for up to several minutes. In chapter 3, we will discuss our new technique to stabilize the OMO by using a novel feedback locking method.

2.3 A brief review of existing optomechanical cavities

The simplicity and superior properties of silica microtoroidal optomechanical resonator/cavity have made it a suitable platform for investigating the applications of OMR/OMO particularly in communication and sensing. Relatively low threshold optical power (less than 1 mW), operation at room temperature and atmospheric pressure, supporting multiple mechanical modes that can be selectively excited and low phase noise oscillation (sub-Hz oscillation linewidth) are the most important characteristics of a silica microtoroidal OMO. However, relying on silica fiber-tapers for optical coupling, challenges associated with monolithic integration with other optical components, and limitation on the g_{OM} imposed by geometry and dimensions, have fueled the search for alternative optomechanical resonators. During the past ten years many high quality optomechanical resonators have been developed and served as platforms for a large number of experiments. These devices appear as different architectures and based on variety of material systems, but they all are designed to support efficient coupling between the mechanical modes and the optical modes in a small integrated configuration. Figure 2.10 shows some of these optomechancial resonators.

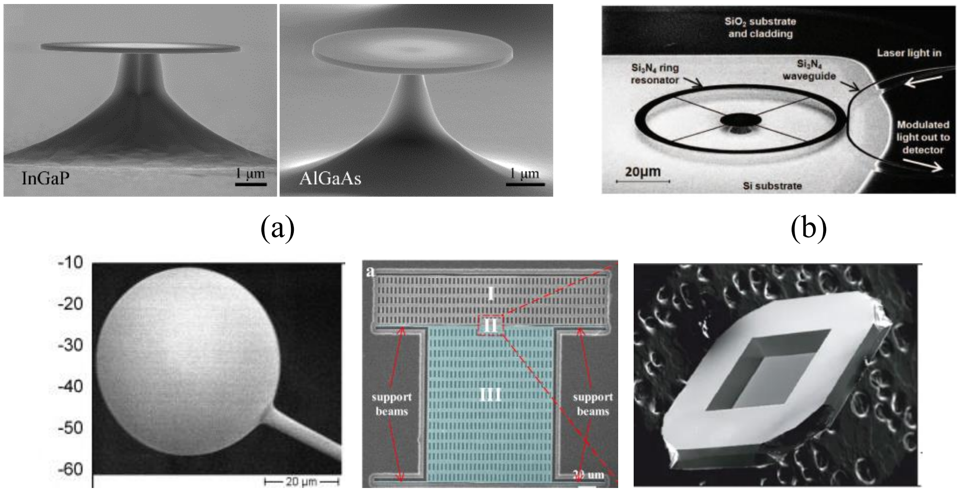

(a) (b)

(c) (d) (e)

Fig. 2.10. Examples of optomechanical resonators: (a) Microdisk OMRs [42], f_m = 480 MHz and 757 MHz, Q_m = 1500 and 350, $Q_{tot} = 1\times10^5$ and 5×10^4 for InGaP and AlGaAs, respectively. (b) Micro-ring OMR [43], f_m = 41.97 MHz, Q_m = 2000, $Q_{tot} = 3\times10^5$. (c) Microsphere OMR [44], f_m = 63 MHz, Q_m = 10000, $Q_{tot} \sim 10^8$. (d) Zipper photonics crystal OMR [45], f_m = 77.7 kHz, Q_m = 16, Q_{tot} = 5400. (e) Suspended membrane in Fabry-Perot cavity-based OMR [50], f_m = 134 kHz, $Q_m = 1.1\times10^6$, Q_{tot} = 16100.

Microdisk resonator [42], shown in Fig. 2.10(a), is another example of WGM based optomechanical resonators (OMRs) with a structure similar to microtoroid. The fabrication process of these OMRs is similar to the hat of the silica microtoroid, however the reflow process (with CO_2 laser) is eliminated. As a result, the optical quality factor of microdisk OMRs is smaller than that of the silica microtoroid but they can be made of a variety of materials. As such, microdisk OMRs can be made of materials with interesting nonlinear optical properties and optical gain material. These OMRs can support radiation pressure based optomechanical oscillation in room temperature and atmosphere [42]. InGaP and AlGaAs microdisk OMRs are two examples both fabricated on top of GaAs pillar. Their WGMs are excited in the wavelength range of 1500 ~ 1600 nm, with a measured Q_{tot} of 1×10^5 and 1×10^4 for the InGaP and AlGaAs microdisk OMRs, respectively. The self-sustained oscillation has observed in both microdisks. The InGaP microdisk reported in Ref. 42 oscillates at 480 MHz with threshold power of 1.1 mW and the AlGaAs microdisk oscillates at 757 MHz with a threshold power of 4.2 mW.

Microring OMR is another type of optomechanical resonator [43], the SEM micrograph of an example microring OMR is shown in Fig. 2.10(b). In the OMR shown in Fig. 2.10(b), the structure is composed of a pair of vertically stacked silicon nitride rings connected to a pillar via very thin spokes. Using the spokes, instead of a membrane, reduces the mechanical loss to the pillar and reduces the mechanical stiffness of each ring resonator (enhancing the sensitivity to the optical forces between the rings). At the same time the optical scattering of the light circulating near the outside edge of the rings is negligible. In Ref. 43, the oscillation threshold power of 17.4 mW at WGM wavelength of ~1.55 µm has been reported.

Silica microsphere, as the most well-known WGM microcavity, can also support optomechanical oscillation. Silica microsphere can be simply fabricated by melting the tip of a single mode fiber using CO_2 laser. WGMs of silica microsphere can have optical quality factors as large as 10^8. Figure 2.10(c) shows an example of a silica microsphere OMO with two mechanical modes, with frequencies of 98 MHz and 63 MHz, that can be excited via radiation pressure with a threshold optical power of about 600 µW [44].

Optomechanical interaction has been also reported in photonic crystal (PC) resonators with small dimensions down to nanometers. The first PC structure that was specifically designed to support strong optomechanical coupling, was the Zipper cavity

[45-47]. Typically, these kinds of OMRs are made of two closely spaced parallel beams that each supports a confined optical mode, the optical modes are coupled to each other and to the mechanical motion of the beams (via radiation pressure force [45, 46] or optical gradient force [47]). The extremely small optical mode volumes and device dimensions result in very strong optomechanical coupling (coupling constant $g_{\mathrm{OM}} > 100$ GHz/nm) and high oscillation frequencies in the gigahertz regime. However, the optical quality factor is very low for these devices. In Ref [45] the optomechanical oscillation was observed with threshold power of 200 μW in vacuum.

Fabry–Pérot cavity with a moving mirror is the oldest platform, in fact the first platform, used to study the optomechanical coupling via radiation pressure [48]. One of the typical reported Fabry–Pérot OMR [49] has mechanical modes with sub-MHz frequencies. Figure 2.10(e) shows the photograph of a SiN membrane on a silicon chip which was inserted in a Fabry–Pérot cavity in Ref. [40]. Due to the large cavity length (~67 mm) of this device, the optomechanical phenomena has been only observed in vacuum. Another example of using movable cavity end mirrors to study radiation pressure induced optomechanical coupling was discussed in Ref [50] and which was working at cryogenic temperature.

One of the important parameters of the optomechanical devices is the frequency of the mechanical modes. Table 2.1 lists several examples of OMR devices sorted based on the frequency of their optomechanically coupled mechanical mode, the main parameters of each device are included.

Table. 2.1. Parameters of several examples of optomechanical resonators.

Cavity	Fabry-Perot cavity [51]	Trampoline resonator [52]	Zipper cavity [53]	Photonic crystal [45]	Waveguide-DBR microcavity [54]	Silica microtoroid [2]
f_{m}	84.8 Hz	9.71 kHz	27.5 kHz	77.7 kHz	100 kHz	0.2~150 MHz
Q_0	775 (Finesse)	29000 (Finesse)	9500	5400	5000	10^8
Q_{m}	44500	940000	1.4×10^6	16	20000	2000
g_{OM}	/	/	5.5 GHz/nm	44 GHz/nm	4.5 GHz/nm	40 GHz/nm
m_{eff}	0.69 g	110 ng	10 ng	5.6 ng	6.8 ng	20~2000 ng
P_{th}	1.6 mW	/	>116 µW	200 µW	32 µW	0.05~1 mW
dimension	12.3 mm	40 µm	150 µm×60 µm×400 nm	470 nm	1mm×1mm×50 nm	40~150 µm
Working conditions	Vacuum, room temperature	Vacuum, room temperature	Vacuum, room temperature	Vacuum, room temperature	Vacuum, room temperature	Air, room temperature

Cavity	Photonic crystal Zipper [55]	Silicon micro-disk [56]	Photonic crystal nanobeam [47]	AlN micro-disk [57]
f_{m}	5~200 MHz	1.3 GHz	0.805~3.7 GHz	10.4 GHz
Q_0	3×10^8	3.5×10^5	4×10^5	81000
Q_{m}	50~150	1.5×10^6	2700	1830
g_{OM}	430 GHz/nm	722 GHz/nm	800 GHz/nm	100 GHz/nm
m_{eff}	40 pg	6 pg	pg~fg	/
P_{th}	<1 mW	3.56 µW	100 µW	/
dimension	1×40 µm	4 µm	1×30 µm	550 nm
Working conditions	Air, room temperature	Air, room temperature	Air, room temperature	Air, room temperature

As evident from the table, the frequency of the mechanical modes range from serveral Hertz to tens of gigahertz, so, in principle, OMR devices could meet the frequency requirement of many applications that may benefit from the unique properties of OMR and OMOs such as those described in this thesis.

2.4 Optoelectronic oscillators (OEO)

In 1994, a novel photonic oscillator, characterized by high spectrum purity, high frequency stability, was developed by X. S. Yao *et al* [58]. This oscillator, called optoelectronic oscillator (OEO), directly converts the continuous emission from a pump laser to radio frequency (RF) or microwave oscillations. OEO can produce spectrally pure RF oscillations with high level of frequency tunability and low phase noise, also it is capable of generating ultra-high frequency oscillations (up to 90 GHz reported [59]) which is limited by the speed of electro-optic modulator and photoreceiver used in the OEO loop. As a hybrid oscillator, OEO's operation involves electromagnetic oscillations both at optical (~200 THz) and microwave/millimeter wave (1-90 GHz) and its output can be collected either as a microwave signal or as an intensity modulated optical carrier. OEO has unique properties that may be exploited in many applications in particular those that involve a combination of optical and electrical elements, devices, or systems. In this thesis, OEO has been used for sensing applications and study of nonlinear dynamics in coupled heterogeneous oscillators.

Figure 2.11 shows the configuration used in a typical OEO [58, 60, 61]. Light generated by a laser is coupled to an electro-optical (E/O) modulator (e.g., Mach-Zehnder Modulator or MZM), the optical output of the modulator transmitted through a long optical fiber (serving as an optical delay line) and is detected by a photodetector. The output of the photodetector is amplified by an RF amplifier and then filtered by a bandpass RF filter. Finally, the filtered signal is applied to the RF drive port of the E/O modulator closing the oscillator feedback loop. The feedback loop supports self-sustained electro-optical oscillations at frequency determined by the total group delay of the loop (dominated by the optical delay in the optical fiber), the bias point of E/O modulator, and the bandpass of the RF filter. The output of the OEO can be extracted as an optical signal using an optical fiber coupler or as an electrical signal using an RF coupler (as shown in Fig. 2.11).

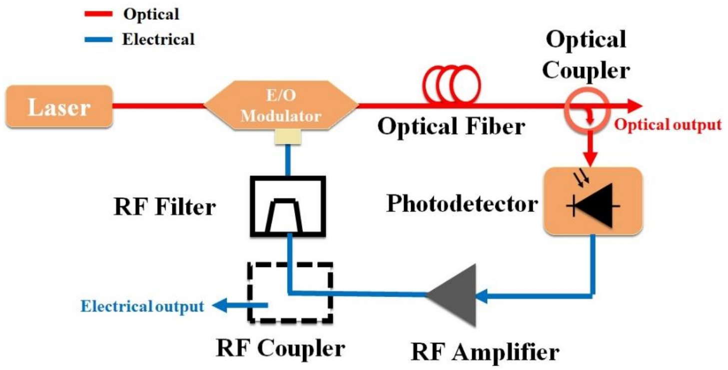

Fig. 2.11. A typical configuration used in a single loop OEO.

Typically, two types of optical delay may be used in the feedback loop of an OEO: 1) A non-resonant optical delay based on a long waveguide (e.g., an optical fiber). 2) A resonant optical delay on an optical cavity (e.g., a WGM optical microcavity). Both optical delays may also provide optical gain in the feedback loop.

It is challenging to use a long optical delay line to maintain a stable oscillation frequency because the oscillation frequency of the OEO is determined by the optical path length inside the delay line that can be affected by temperature change (as the refractive index of the fiber may change via thermos-optic effect and the physical length may change due to thermal expansion). The long length of the optical delay line (that may be more than a kilometer), make the delay sensitive to small temperature changes. Moreover, the large size of the fiber loop may also restrict its use in certain applications.

An elegant solution to overcome the drawback of fiber delay line based OEO is replacing the fiber delay line by a high optical quality factor (Q_{tot}) optical resonator [62~69] that provides a long delay proportional to its long photon life time in a small form factor. The long delay and the intrinsic narrow linewidth filter function provided by a high-Q optical resonator reduces OEO's oscillation linewidth and its phase noise. Various optical resonators may be used in an OEO, for example, fiber based Fabry-Perot resonator [62, 63], microspherical and microdisk resonators [64-67], fiber ring resonator [68, 69] and many others. Advantageously, high-Q optical resonators can also reduce the size of an OEO and enable its integration with other components and devices in one compact package.

OEOs are widely studied and used in the scientific research and application domains. OEOs are very good candidates of either low phase noise RF sources or optical pulse generators. The RF frequency of OEOs can cover the band from HF all the way to V band with the phase noise as low as ~140 dBc/Hz at the frequency offset of 10 kHz [70, 71]. In addition to its application as an RF source, the low phase noise optical pulses generated by OEO may be used in optical networking [72] and optical sampling [73]. OEOs are also useful for processing of optical data signals, for example, frequency multiplexing [74] and down-conversion/up conversion [75].

An important application of OEO is sensing. As mentioned above, the oscillation frequency of an OEO is very sensitive to optical properties of the delay line. The optical path length of a delay line may be affected by parameters such as temperature, strain, vibration, and the like. As such each OEO may be used to monitor and measure small changes in these parameters. OEOs have been used to monitor and measure strain [76, 77], temperature [78-80], load stress [81], and refractive index [82, 83]. In chapter 7 of this thesis, a new sensing mechanism has been proposed and demonstrated based on coupling OEO to an electronic oscillator. It has been shown that these coupled systems may provide much higher sensitivity compared to sensors that use a single OEO.

Another interesting application of OEOs is exploiting its rich dynamics to study nonlinear dynamical systems that may help understanding the oscillation mechanism in certain biological systems.

Delayed feedback enables the OEOs to generate a wide variety of waveforms, with differing degrees of complexity that depend on the values used for parameters that control the behavior of OEO. In particular, the time-delay, feedback strength and filter parameters can be tuned to produce highly stable periodic waveforms [84, 85], as well as complex waveforms that show the characteristics of robust, high dimensional chaos [86-88]. In chapter 7 of this thesis, the nonlinear dynamics of OEO coupled to a physically dissimilar oscillator is studied both experimentally and theoretically.

The basic characteristics of OEO have been studied by several research groups and several theoretical frameworks have been developed to capture the dynamics of the OEO. Here a brief review of two well-known theoretical frameworks used to describe oscillation in an OEO is provided.

2.4.1 Quasi-linear theory of the OEO

Based on the typical configuration of OEO shown in Fig. 2.11, the optical power from the output port of E/O modulator is related to the applied voltage on the modulator $V_{in}(t)$ by [59]:

$$P(t) = \alpha \frac{P_0}{2}\{1 - \eta \sin [\pi(\frac{V_{in}(t)}{V_\pi} + \frac{V_B}{V_\pi})]\}. \tag{2.30}$$

where α is the fractional insertion loss of the modulator, V_π is the half-wave voltage of the modulator, V_B is the bias voltage, P_0 is the input optical power, and η determines the extinction ratio of the modulator by $(1+\eta)/(1-\eta)$.

The optical output of the modulator is fed to the photodetector that generates an electrical signal proportional to the received optical power; this signal is then amplified by the RF amplifier. The output voltage of the RF amplifier can be written as:

$$V_{out}(t) = \rho P(t) R G_A = V_{ph}\{1 - \eta \sin [\pi(\frac{V_{in}(t)}{V_\pi} + \frac{V_B}{V_\pi})]\}. \tag{2.31}$$

where ρ and R are the responsivity and load impedance of the photodetector, G_A is the amplifier's voltage gain, and $V_{ph} = (\alpha P_0 \rho/2) R G_A$ is the photovoltage. The OEO is formed by feeding the voltage signal of Eq. (2.31) back to the RF input port of the E/O modulator. The small signal open loop gain G_s of the OEO can be obtained by solving dV_{out}/dV_{in} at $V_{in} = 0$. If we assume the input signal $V_{in}(t)$ to the modulator is a sinusoidal wave with an angular frequency of ω, an amplitude of V_0, and an initial phase β as $V_{in}(t) = V_0 \sin(\omega t + \beta)$, the linearized output of the RF amplifier can be solved to be:

$$V_{out}(t) = G_s \frac{2V_\pi}{\pi V_0} J_1\left(\frac{\pi V_0}{V_\pi}\right) V_{in}(t) = G(V_0) V_{in}(t). \tag{2.32}$$

J_1 is the Bessel function. It is obviously that the $G(V_0)$ is a nonlinear function of the input amplitude V_0 and its magnitude decreases monotonically with V_0.

Similar to other oscillators, the oscillation of the OEO starts from the noise transient, which is then built up and sustained by the feedback loop. we can suppose that the $V_{\mathrm{in}}(\omega,\mathrm{t})$ is a noise transient which is a collection of sine waves with random phases and amplitudes, once the loop is closed, this noise circulates in the loop and the total field at any instant is the summation of all circulating fields, however only the frequencies satisfying a resonant condition can circulate in the loop. These frequencies may be determined by:

$$\omega_k \tau' + \phi(\omega_k) + \phi_0 = 2k\pi. \tag{2.33}$$

k is the mode number, τ' is the time delay resulting from the physical length of the feedback, ϕ_0 is the initial phase induced by the modulator, its value is determined by the bias voltage V_{B}. With Eq. (2.33) the oscillation frequency of OEO can be written as:

$$f_{osc} = \left(k + \frac{1}{2}\right)\frac{1}{\tau} \qquad \text{for } G(V_{\mathrm{osc}})<0. \tag{2.34a}$$

$$f_{osc} = k\frac{1}{\tau} \qquad \text{for } G(V_{\mathrm{osc}})>0. \tag{2.34b}$$

here, τ is the total group delay of the loop, including the physical length delay τ' and the group delay resulting from dispersion in components used in the OEO circuit. Finally, the one or subset of frequencies that may exist in OEO may be selected by the pass band of the RF filter in the loop.

The quality factor Q of the oscillator is

$$Q = \frac{f_{osc}}{\Delta f_{FWHM}} = 2\pi f_{osc}\frac{\tau^2}{\delta}. \tag{2.35}$$

δ is the input noise to signal ratio [60]. We can see the quality factor is larger for higher order modes and the longer delay line.

2.4.2 Delay differential equations of the OEO

While the Quasi-linear model is a useful tool for understanding the intrinsic working mechanism of OEO and estimating he value of certain OEO parameters, i.e., frequency, linewidth, power and other similar parameters. but this model cannot capture the dynamical processes in the OEO. As such a brief review of a model that may be used to simulate the nonlinear dynamics of OEO is presented [86].

In most OEOs the E/O modulator is a Mach-Zehnder modulator (MZM), so the output optical power of the modulator is related to the input voltage of the modulator as:

$$P(t) = P_0 cos^2(\frac{\pi}{2}\frac{V(t)}{V_\pi} + \varphi_0). \tag{2.36}$$

where P_0 is the continuous-wave optical power entering the modulator, V(t) is the voltage applied to the modulator and φ_0 is the angle describing the bias point of the modulator. This output power incident on the photodetector and then is amplified by the RF amplifier. The output voltage of the amplifier may be expressed as:

$$V_{out}(t) = \rho R G_A P(t). \tag{2.37}$$

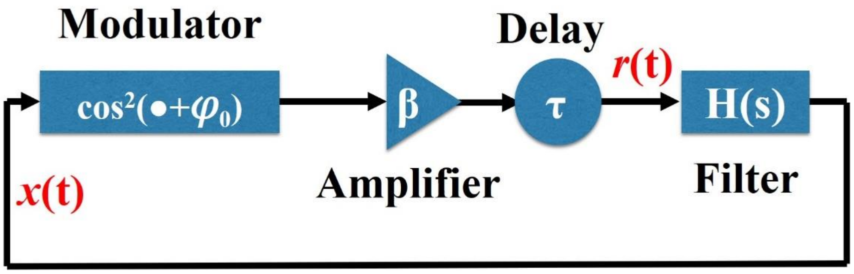

Fig. 2.12. OEO block diagram that illustrates the implementation of delay differential equation model.

A simplified block diagram for the OEO circuit that shown in Fig. 2.12 may help with understanding the nonlinear model discussed here. In order to simplify the analysis, all variables are made dimensionless. The feedback voltage fed to the modulator is normalized to be $x(t) = \frac{\pi}{2}\frac{V(t)}{V_\pi}$, and all the remaining proportionality constants are also normalized to a single dimensionless factor that describes the round trip gain of the loop $\beta = \frac{\pi}{2}\frac{RG_AP_0}{V_\pi}$. Using these normalized parameters, the input to the RF filter can be written as:

$$r(t) = \beta cos^2[x(t-\tau) + \varphi_0]. \tag{2.38}$$

the RF filter here can be regarded as a two-pole band-pass filter with the transformation function written as:

$$H(s) = \frac{s\tau_H}{(1+s\tau_L)(1+s\tau_H)}. \tag{2.39}$$

where τ_L and τ_H are the time constants describing the low-pass and high-pass filters, respectively. In the time domain, a linear filter can be represented by state-space differential equations of the form:

$$\frac{d\boldsymbol{u}}{dt} = \boldsymbol{A}\boldsymbol{u}(t) + \boldsymbol{B}r(t). \tag{2.40}$$

and

$$x(t) = \boldsymbol{C}\boldsymbol{u}(t) + \boldsymbol{D}r(t). \tag{2.41}$$

here r(t) is the input to the filter, and x(t) is the output, $\boldsymbol{u}$(t) is the two-dimensional state vectors for the filter, **A**, **B**, **C**, and **D** are the matrices that describe the band-pass filter:

$$\boldsymbol{A} = \begin{bmatrix} -(\frac{\mathbf{1}}{\boldsymbol{\tau_L}} + \frac{\mathbf{1}}{\boldsymbol{\tau_H}}) & -\frac{\mathbf{1}}{\boldsymbol{\tau_L}} \\ \frac{\mathbf{1}}{\boldsymbol{\tau_H}} & \mathbf{0} \end{bmatrix}, \quad \boldsymbol{B} = \begin{bmatrix} \frac{\mathbf{1}}{\boldsymbol{\tau_L}} \\ 0 \end{bmatrix}, \ \boldsymbol{C} = [1 \quad 0], \quad \text{and } \mathbf{D}\text{=0}. \tag{2.42}$$

now the dynamics of OEO can be described by:

$$\frac{d\boldsymbol{u}}{dt} = \boldsymbol{A}\boldsymbol{u}(t) + \boldsymbol{B}\beta cos^2[Cu(t-\tau) + \varphi_0]. \tag{2.43}$$

that may be written as the function of filter's output:

$$\frac{dx(t)}{dt} = -(\frac{1}{\tau_L} + \frac{1}{\tau_H})x(t) - \frac{1}{\tau_L}u_2(t) + \frac{1}{\tau_L}\beta cos^2[x(t-\tau) + \varphi_0]. \quad (2.44)$$

$$\frac{du_2(t)}{dt} = \frac{1}{\tau_H}x(t). \quad (2.45)$$

u_2 is one of the two components of the state vector of the filter, another one is x.

Equation (2.44) is a delay differential equation (DDE) that in chapter 7, will be used to investigate the dynamics of the OEO particularly in the context of coupled oscillatory systems.

2.5 References

[1] H. Rokhsari, T. J. Kippenberg, T. Carmon, and K. J. Vahala, "Radiation-pressure-driven micro-mechanical oscillator," Opt. Express., **13**(14), 5293-5301 (2005).

[2] M. Hossein-Zadeh, H. Rokhsari, A. Hajimiri, and K. J. Vahala, "Characterization of a radiation pressure driven micromechanical oscillator," Phys. Rev. A., **74**(2), Art. no. 023813 (2006).

[3] T. J. Kippenberg, H. Rokhsari, T. Carmon, A. Scherer, and K. J. Vahala, "Analysis of radiation-pressure induced mechanical oscillation of an optical microcavity,", Phys. Rev. Lett., **95**(3), Art. no. 033901 (2005).

[4] J. W. Strutt, "The Theory of Sound". New York: Dover, 1945. Lord Rayleigh.

[5] L. Rayleigh, "Further applications of Bessel's functions of high order to the whispering gallery and allied problems," Phil. Mag., **27**(157), 100-109 (1914).

[6] L. Rayleigh, "The problem of the whispering gallery," Phil. Mag., **20**(120),1001-1004 (1910).

[7] C. G. B. Garrett, W. Kaiser, and W. L. Bond, "Stimulated emission into optical whispering gallery modes of spheres," Phys. Rev., **124**(6), 1807-1809 (1961).

[8] M. Cai, O. Painter, and K. J. Vahala, "Observation of Critical Coupling in a Fiber Taper to a Silica-Microsphere Whispering-Gallery Mode System," Phys. Rev. Lett., **85**(1), 74-77 (2000).

[9] M. L. Gorodetsky, A. A. Savchenkov, and V. S. Ilchenko, “Ultimate Q of optical microsphere resonators,” Opt. Lett., **21**(7), 453-455 (1996).

[10] D. K. Armani, T. J. Kippenberg, S. M. Spillane, and K. J. Vahala, “Ultrahigh-Q toroid microcavity on a chip,” Nature, **421**(6926), 925-928 (2003).

[11] A. N. Oraevsky, “Whispering-gallery waves,” Quantum Electronics, **32**(5), 377-400 (2002).

[12] B. Min, L. Yang, and K. J. Vahala, “Perturbative analytic theory of an ultrahigh- Q toroidal microcavity,”. Phys. Rev. A., **76**(1), Art. no. 013823 (2007).

[13] G. C. Righini, Y. Dumeige, P. Féron, M. Ferrari, G. Nunzi Conti, D. Ristic and S. Soria, “Whispering Gallery Mode microresonators: Fundamentals and applications,” La Rivista del Nuovo Cimento, **34**(7), 435-488 (2011).

[14] B. R. Johnson, “Theory of morphology-dependent resonances: shape resonances and width formulas,” J. Opt. Soc. Am. A., **10**(2), 343–352 (1993).

[15] M. R. Foreman, J. D. Swaim, and F. Vollmer, “Whispering gallery mode sensors,” Adv. Opt. Photonics., **7**(2), 168-240 (2015).

[16] B. E. Little, J. -P. Laine, and H. A. Haus, “Analytic Theory of Coupling from Tapered Fibers and Half-Blocks into Microsphere Resonators,” J. Light. Technol., **17**(4), 704-715 (1999).

[17] V. B. Braginsky, M. L. Gorodetsky, V. S. Ilchenko, “Quality-factor and nonlinear properties of optical whispering-gallery modes,” Phys. Lett. A., **137**(7-8), 393-397 (1989).

[18] V. S. Ilchenko, X. Steve Yao, and L. Maleki, “Pigtailing the high-Q microsphere cavity: a simple fiber coupler for optical whispering-gallery modes,” Opt. Lett., **24**(11), 723-725 (1999).

[19] S. Schiller, I. I. Yu, M. M. Fejer, and R. L. Byer, "Fused-silica monolithic total-internal-reflection resonator," Opt. Lett., **17**(5), 378-380 (1992).

[20] Y. L. Pan and R. K. Chang, “Highly efficient prism coupling to whispering gallery modes of a square μ cavity,” Appl. Phys. Lett., **82**(4), 487-489 (2003).

[21] V. S. Ilchenko, X. S. Yao, and L. Maleki, "Pigtailing the high-Q microsphere cavity: a simple fiber coupler for optical whispering-gallery modes," Opt. Lett., **24**(11), 723-725 (1999).

[22] S. M. Spillane, T. J. Kippenberg, O. J. Painter, and K. J. Vahala, “Ideality in a Fiber-Taper-Coupled Microresonator System for Application to Cavity Quantum Electrodynamics,” Phys. Rev. Lett., **91**(4) 043902 (2003).

[23] F. F. Liu, "Optical and optomechanical resonators and their applications in communication and sensing," Ph.D. dissertation, Dept. Physics and Astronomy., University of New Mexico, Albuquerque, 2013.

[24] O. Arcizet, P. -F. Cohadon, T. Briant, M. Pinard, and A. Heidmann, "Radiation-pressure cooling and optomechanical instability of a micromirror," Nature, **444**,71–74 (2006).

[25] A. Heidmann, and S.Reynaud, "Photon noise reduction by reflection from a movable mirror," Phys. Rev. A., **50**(5), 4237-4243 (1994).

[26] D. Vitali et al, "Optomechanical Entanglement between a Movable Mirror and a Cavity Field," Phys. Rev. Lett., **98**(3), Art. no. 030405 (2007).

[27] M. Aspelmeyer, T. J. Kippenberg, and F. Marquardt, "Cavity optomechanics," Rev. Mod. Phys., **86**(4), 1391-1452 (2014).

[28] V. B. Braginsky, S. E. Strigin, and S. P. Vyatchanin, “Parametric Oscillatory Instability in Fabry-Perot (FP) Interferometer,”, Phys. Lett. A **287**(5-6), 331-338 (2001).

[29] A. N. Cleland, “Foundations of Nanomechanics,” (Springer, Berlin) 2003.

[30] T. J. Kippenberg, and K. J. Vahala, “Cavity Opto-Mechanics,” Opt. Express., **15**(25), 17172-17205 (2007).

[31] H. Rokhsari, M. Hossein-Zadeh, Ali Hajimiri, and K. J. Vahala, “Brownian noise in radiation-pressure-driven micromechanical oscillators,” Appl. Phys. Lett., **89**(6), Art. no. 261109 (2006).

[32] Y. Hadjar, P. F. Cohadon, C. G. Aminoff, M. Pinard and A. Heidmann, “High-sensitivity optical measurement of mechanical Brownian motion,” Europhys. Lett., **47**(5), 545-551 (1999).

[33] E. Majorana, Y. Ogawa, "Mechanical thermal noise in coupled oscillators," Phys. Lett. A., **233**, 162-168 (1997).

[34] H. Rokhsari, T. J. Kippenberg, T. Carmon, and K. J. Vahala, "Theoretical and Experimental Study of Radiation Pressure-Induced Mechanical Oscillations (Parametric Instability) in Optical Microcavities," *IEEE* J. Sel. Top. Quantum Electron., **12**(1), 96-107 (2006).

[35] T. Carmon, H. Rokhsari, L. Yang, T. J. Kippenberg, and K. J. Vahala, “Temporal Behavior of Radiation-Pressure-Induced Vibrations of an Optical Microcavity Phonon Mode,” Phys. Rev. Lett., **94**(22), Art. no. 223902 (2005).

[36] H. K. Cheung and C. K. Law, “Optomechanical coupling between a moving dielectric sphere and radiation fields: A Lagrangian-Hamiltonian formalism,” Phys. Rev. A., **86**(3), Art. no. 033807 (2012).

[37] C. K. Law, “Interaction between a moving mirror and radiation pressure: A Hamiltonian formulation,” Phys. Rev. A., **51**(3), 2537-2541 (1995).

[38] A. L. Schawlow and C. H. Townes, “Infrared and Optical Masers,” Phys. Rev., **112**(6), 1940-1948 (1958).

[39] W. A. Edson, “Noise in Oscillators,” *Proc. IRE*., **48**(8), 1454-1466 (1960).

[40] F. Herzel, “An analytical model for the power spectral density of a voltage-controlled oscillator and its analogy to the laser linewidth theory,” *IEEE* Trans. Circuits Sys. I, Fundam. Theory Appl, **45**(9), 904-908 (1998).

[41] T. Carmon, L. Yang, and K. J. Vahala, “Dynamical thermal behavior and thermal self-stability of microcavities,” Opt. Express., **12**(20), 4742-4750 (2004).

[42] B. Guha, S. Mariani, A. Lemaître, S. Combrié, G. Leo, and I. Favero, “High frequency optomechanical disk resonators in III–V ternary semiconductors,” Opt. Express., **25**(20), 24639-24649 (2017).

[43] S. Tallur, S. Sridaran, and S. A. Bhave, "A monolithic radiation-pressure driven, low phase noise silicon nitride opto-mechanical oscillator," Opt. Express., **19**(24), 24522-24529 (2011).

[44] R. Ma, A. Schliesser, P. Del'Haye, A. Dabirian, G. Anetsberger, and T. J. Kippenberg, "Radiation-pressure-driven vibrational modes in ultrahigh-Q silica microspheres," Opt. Lett., **32**(15), 2200-2202 (2007).

[45] Y. J. Huang et al., "A low-frequency chip-scale optomechanical oscillator with 58 kHz mechanical stiffening and more than 100th-order stable harmonics," Sci. Rep., **7**, Art. no. 4383 (2017).

[46] T. Tetsumoto, T. Tanabe, "High-Q silica zipper cavity with strong opto-mechanical coupling for optical radiation pressure driven directional switching," *IEEE* Photonics Conference, San Diego, (2014).

[47] M. Eicheneld, "Cavity optomechanics in photonic and phononic crystals: engineering the interaction of light and sound at the nanoscale," Dissertation (Ph.D.), California Institute of Technology (2010).

[48] A. Dorsel, J. D. McCullen, P. Meystre, E. Vignes, and H. Walther, "Optical Bistability and Mirror Confinement Induced by Radiation Pressure," Phys. Rev. Lett., **51**(17) 1550-1553 (1983).

[49] J. D. Thompson, B. M. Zwickl, A. M. Jayich, Florian Marquardt, S. M. Girvin & J. G. E. Harris, "Strong dispersive coupling of a high-finesse cavity to a micromechanical membrane," Nature, **452**, 72-75 (2008).

[50] M. Pinard, A. Dantan, D. Vitali, O. Arcizet, T. Briant, and A. Heidmann, "Entangling movable mirrors in a double-cavity system," Europhys. Lett., **72**(5), 747–753 (2005).

[51] C. M. Mow-Lowry, A. J. Mullavey, S. Goßler, M. B. Gray, and D.E. McClelland, "Cooling of a Gram-Scale Cantilever Flexure to 70 mK with a Servo-Modified Optical Spring," Phys. Rev. Lett., **100**(1), Art. no. 010801 (2008).

[52] D. Kleckner, B. Pepper, E. Jeffrey, P. Sonin, S. M. Thon, and D. Bouwmeester, "Optomechanical trampoline resonators," Opt. Express., **19**(20), 19708-19716 (2011).

[53] A. G. Krause, M. Winger, T. D. Blasius, Q. Lin, and O. Painter, "high-resolution microchip optomechanical accelerometer," Nature Photonics, **6**, 768-772 (2012).

[54] M. W. Pruessner, T. H. Stievater, J. B. Khurgin, and W. S. Rabinovich, "Integrated waveguide-DBR microcavity opto-mechanical system," Opt. Express., **19**(22), 21904-21918 (2011).

[55] J. Chan, M. Eichenfield, R. Camacho, and O. Painter, “Optical and mechanical design of a “zipper” photonic crystal optomechanical cavity,” Opt. Express., **17**(5), 3802-3817 (2009).

[56] W. C. Jiang, X. Y Lu, J. D. Zhang, and Q. Lin “High-frequency silicon optomechanical oscillator with an ultralow threshold,” Opt. Express., **20**(14), 15991-15996 (2012).

[57] Xu Han, King Y. Fong, and Hong X. Tang, “A 10-GHz film-thickness-mode cavity optomechanical resonator,” Appl. Phys. Lett., **106**(16), Art. no. 161108 (2015).

[58] X. S. Yao, and L. Maleki, “High frequency optical subcarrier generator,” Electron. Lett., **30**(18), 1525-1526 (1994).

[59] A. Ly et al., "Highly Spectrally Pure 90-GHz Signal Synthesis Using a Coupled Optoelectronic Oscillator," *IEEE* Photonics Technol. Lett., **30**(14), 1313-1316 (2018).

[60] X. S. Yao, and L. Maleki, “Optoelectronic microwave oscillator,” J. Opt. Soc. Am. B., **13**(8), 1725-1735 (1996).

[61] X. S. Yao, and L. Maleki, “Converting light into spectrally pure microwave oscillation,” Opt. Lett., **21**(7), 483-485 (1996).

[62] M. Bagnell, J. Davila-Rodriguez, and P. J. Delfyett, “Millimeter-Wave Generation in an Optoelectronic Oscillator Using an Ultrahigh Finesse Etalon as a Photonic Filter,” J. Lightwave. Technol., **32**(6), 1063-1067 (2013).

[63] J. Dai, Y. T. Dai, F. F. Yin, Y. Zhou, J. Q. Li, Y. T. Fan, and K. Xu “Compact optoelectronic oscillator based on a Fabry–Perot resonant electro-optic modulator,” Chin. Opt. Lett., **14**(11), Art. no. 110701 (2016).

[64] V. S. Ilchenko, X. Steve Yao. L. Maleki “High-Q microsphere cavity for laser stabilization and optoelectronic microwave oscillator,” *Proc. SPIE.*, **3611**, 190 (1999).

[65] L. Maleki, V. Iltchenko, S. Huang, and A. Savchenkov, “Micro-optical resonators and applications in optoelectronic oscillator,” *Proc. IEEE.*, 37 (2002).

[66] W. F. Zhang, and J. P. Yao, “On-chip silicon photonic integrated frequency-tunable bandpass microwave photonic filter,” Opt. Lett., **43**(15), 3622-3625 (2018).

[67] A. B. Matsko, L. Maleki, A. A. Savchenkov, and V. S. Ilchenko, “Whispering gallery mode based optoelectronic microwave oscillator,” J. Mod. Opt., **50**(15), 2523-2542 (2003).

[68] J. Chen, Y. Q. Zheng, C. Y. Xue, C. F. Zhang, and Y. Chen “Filtering effect of SiO_2 optical waveguide ring resonator applied to optoelectronic oscillator,” Opt. Express., **26**(10), 12641-12647 (2018).

[69] K. Saleh, A. Bouchier, P. H. Merrer, O. Llopis, and G. Cibiel, “Fiber ring resonator based opto-electronic oscillator: phase noise optimisation and thermal stability study,” *Proc. SPIE.*, **7936**, 79360A (2011).

[70] A. B. Ustinov1, A. A. Nikitin1, V. V. Lebedev, A. A. Serebrennikov, A. V. Shamray, A. V. Kondrashov, B. A. Kalinikos, "A Low Phase Noise Tunable Microwave Spin Wave Optoelectronic Oscillator," IOP Conf. Serises: J. Physcis., **1038**, Art. no. 012033 (2018).

[71] Z. H. Zhou, C. Yang, Z. W. Cao, Y. H. Chong, X. H. Li, “An Ultra-Low Phase Noise and Highly Stable Optoelectronic Oscillator Utilizing IL-PLL,” *IEEE* Photon. Technol. Lett., **28**(4), 516-519 (2016).

[72] K. Fukuchi, T. Kasamatsu, M. Morie et al., “10.92-Tb/s (273 × 40-Gb/s) triple-band/ultra-dense WDM optical-repeatered transmission experiment,” in *Proceedings of the Optical Fiber Communication Conference*, pp. PD24, March (2001).

[73] W. Ng, R. Stephens, D. Persechini, and K. V. Reddy, “Ultra-low jitter mode locking of Er-fibre laser at 10 GHz and its application in photonic sampling for analogue-to-digital conversion,” Electron. Lett., **37**(2), 113-115 (2001).

[74] M. Shin and P. Kumar, “Optical microwave frequency up-conversion via a frequency-doubling optoelectronic oscillator,” *IEEE* Photon. Technol. Lett., **19**(21), 1726-1728 (2007).

[75] H. Tsuchida, “Simultaneous prescaled clock recovery and serial-to-parallel conversion of data signals using a polarization modulator-based optoelectronic oscillator,” J. Lightwave Technol., **27**(17), 3777-3782 (2009).

[76] M. Li, W. Li, J. P. Yao, and J. Azana, “Femtometer-resolution wavelength interrogation using an optoelectronic oscillator,” IPC 2012, 23 - 27 September 2012, Burlingame, California, USA.

[77] Z. Q. Fan, J. Su, T. H. Zhang, N. Yang, and Q. Qiu, “High-precision thermal-insensitive strain sensor based on optoelectronic oscillator,” Opt. Express., **25**(22), 27037-27050 (2017).

[78] Y. H. Zhu, X. F. Jin, H. Chi, S. L. Zheng, and X. M. Zhang “High-sensitivity temperature sensor based on an optoelectronic oscillator,” Appl. Opt., **53**(22), 5084-5087 (2014).

[79] D. Q. Feng, L. Kai, T. Zhu, Y. Gao, L. Gao, and J. D. Zhang, “High-precision strain-insensitive temperature sensor based on an optoelectronic oscillator,” Opt. Express., **27**(26), 37532-37540 (2019).

[80] L. Liu, H. Gao, T. G. Ning, L. Pei, J. J. Zheng, J. Li, J. Xua, “High accuracy temperature sensing system exploiting a Sagnac interferometer and an optoelectronic oscillator,” Optics & Laser Technology, **123**, Art. no. 105951 (2020).

[81] F. Q. Kong, W. Z. Li, and J. P. Yao, “Transverse load sensing based on a dual-frequency optoelectronic oscillator,” Opt. Lett., 38(14), 2611-2613 (2013).

[82] L. Du. Nguyen, K. Nakatani, and B. Journet, “Refractive Index Measurement by Using an Optoelectronic Oscillator,” *IEEE* Photon. Technol. Lett., **22**(12), 857-859 (2010).

[83] Y. G. Yang *et al.*, “Refractive Index and Temperature Sensing Based on an Optoelectronic Oscillator Incorporating a Fabry–Perot Fiber Bragg Grating,” *IEEE* Photon. Technol. Lett., **10**(1), Art. no. 6800309 (2018).

[84] Y. K. Chembo, L. Larger, P. Colet, “Nonlinear Dynamics and Spectral Stability of Optoelectronic Microwave Oscillators,” *IEEE* J. Quantum Electron., **44**(9), 858-866 (2008).

[85] O. Okusaga, E. J. Adles, E. C. Levy, W. Zhou, G. M. Carter, C. R. Menyuk, and M. Horowitz, “Spurious mode reduction in dual injection-locked optoelectronic oscillators,” Opt. Express., **19**(7), 5840-5854 (2011).

[86] T. E. Murphy, A. B. Cohen, B. Ravoori, K. R. B. Schmitt, A. V. Setty, F. Sorrentino, C. R. S. Williams, E. Ott, and R. Roy, “Complex dynamics and synchronization of delayed-feedback nonlinear oscillators,” Phil. Trans. R. Soc. A., **368**(1911), 343-366 (2010)

[87] K. E. Callan, L. Illing, Z. Gao, D. J. Gauthier, and E. Schöll, “Broadband Chaos Generated by an Optoelectronic Oscillator,” Phys. Rev. Lett., **104**(11), Art. no. 113901 (2010).

[88] A. Neyer, and E. Voges, "Dynamics of electrooptic bistable devices with delayed feedback," *IEEE* J. Quantum Electron., **18**(12), 2009-2015 (1982).

Chapter 3

Direct stabilization of optomechanical oscillators

3.1 Introduction

Since the observation of radiation-pressure-induced optomechanical RF oscillation in high-Q silica toroidal microresonators [1–3], optomechanical oscillators (OMOs) based on various platforms are fabricated [4–6], and their applications in sensing [7, 8] and RF-over-fiber communication have been demonstrated [9, 10]. In almost all of these demonstrations, the stability of the oscillation has been limited by the intrinsic thermal optical self-stability [11, 12] and, therefore, the stability of pump laser power. As described in chapter 2, thermal optical stability, is simply a result of the interplay between the laser detuning resonant wavelength ($\Delta\lambda_{\mathrm{det}} = \lambda_{\mathrm{res}} - \lambda_{\mathrm{laser}}$) and the heat generated by the absorption of the circulating optical power (through thermo-optical effect). While this relatively weak and short-lived stability is sufficient for proof-of-concept demonstrations, for practical applications, the oscillation has to be stabilized for a long period of time. Note that the intrinsic thermo-optical self-stability is only effective at high optical pump power which also results in the generation of high harmonics in optomechanical oscillation spectrum [13, 14]. For single tone oscillation, the low optical pump power reduces the effectiveness of thermal stabilization resulting in random variation of oscillation amplitude and, eventually, complete suppression of optomechanical gain. Besides, thermal self-stability cannot prevent oscillation amplitude changes due to ambient temperature variations, and cavity-waveguide coupling gap change [11]. Stability of the oscillation amplitude and frequency of an OMO is critical in all applications where OMO serves as an oscillator or sensor. For example, when OMO is employed in RF over fiber communication links [9, 10], underwater acoustic communication links [15, 16], or used to suppress the phase noise of other oscillators (e.g., electrical oscillators) via injection locking as discussed in chapter 7 of this thesis, its stability directly affects the performance of the system.

Well-known techniques developed for locking the laser wavelength to resonant wavelength of optical resonators (i.e., Pound–Drever–Hall [17] and Hansch–Couillaud [18]) have been used for stabilizing microcavity-based devices such as lasers and parametric oscillators and measuring the mechanical quality factor of optomechanical resonators [17, 18]. These methods can only lock the laser detuning from the cavity resonance ($\Delta\lambda_{\mathrm{det}} = \lambda_{\mathrm{res}} - \lambda_{\mathrm{laser}}$), while the optomechanical oscillation amplitude is directly affected also by the pump power and coupling gap (in addition to wavelength detuning). As shown in Fig. 3.1 and discussed in chapter 2, the optomechanical gain (and consequently optomechanical oscillation amplitude), is affected by four parameters [13]: 1) The detuning between the pump laser wavelength and the resonant wavelength of the cavity ($\Delta\lambda_{\mathrm{det}}$), 2) pump laser power ($P_{\mathrm{Laser}}$), 3) the frequency of the excited mechanical mode (f_{mech}) , and 4) the coupling factor (g_{OM}). Temperature variation affects both f_{mech} and $\Delta\lambda$, by changing the geometrical characteristics of the microresonator (e.g., minor and major diameters). f_{mech} can be also affected by $\Delta\lambda_{\mathrm{det}}$ and P_{laser} through optical spring effect. As such, the impact of optical input power, coupling gap or temperature variation on the optomechanical oscillation amplitude cannot be mitigated only by keeping $\Delta\lambda_{\mathrm{det}}$ constant.

Moreover, implementation of the above mentioned techniques adds to cost, complexity, and, more importantly, power consumption of the system because they use extra components (e.g., optical phase modulator, RF mixer, RF power source, etc.). The Hansch–Couillaud method uses perpendicularly polarized beams to generate the error signal which also makes the system more susceptible to polarization fluctuations in fiber-based systems. Apart from these disadvantages, to the best of our knowledge, none of the above mentioned methods has been used for stabilizing OMOs. In this chapter, we demonstrate that the stabilization of the oscillation amplitude (A_{osc}) of silica microtoroid OMOs using A_{osc} itself as the feedback parameter and laser detuning ($\Delta\lambda_{\mathrm{det}}$) as the control parameter, can suppress the slow amplitude and frequency variations resulting from temperature variation, coupling gap variation and laser wavelength shift.

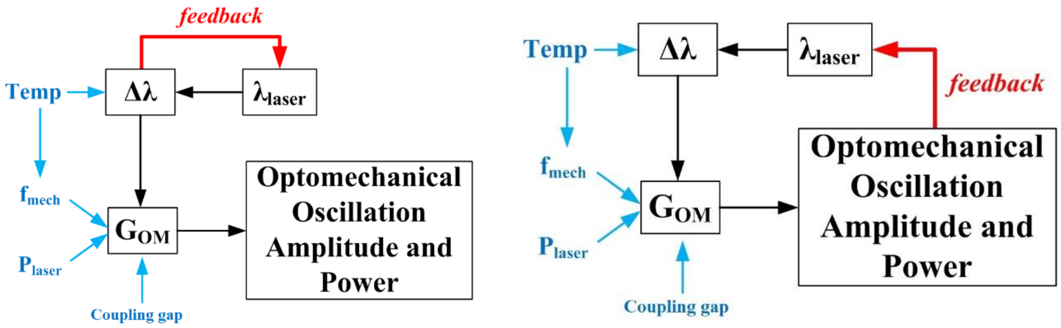

(a) (b)

Fig. 3.1. Relation between oscillation amplitude and feedback system parameters: $\Delta\lambda_{\mathrm{det}} = \lambda_{\mathrm{resonance}} - \lambda_{\mathrm{laser}}$, pump laser detuning from the cavity resonance; G_{OM}, optomechanical gain; P_{laser}, pump laser power; f_{mech}, mechanical oscillation frequency; Temp, ambient temperature. (a) Standard locking method where $\Delta\lambda_{\mathrm{det}}$ is locked and (b) proposed method where the oscillation amplitude or RF power is locked.

Figure 3.1 shows the difference between the feedback in conventional cavity locking techniques (part-a) and the proposed method for OMO (part-b). Clearly the conventional approach (shown in part-a) cannot suppress the variations of the optomechanical gain due to a change in coupling gap, pump laser power or mechanical frequency variation, simply because $\Delta\lambda_{\mathrm{det}}$ can remain constant while these parameters change.

The proposed feedback method can effectively compensate for the fluctuation and variation of the oscillation amplitude and, to some degree, the oscillation frequency drift which results from ambient temperature change, pump power fluctuation, and coupling gap change. This is possible because the optomechanical gain (G_{OM}) can be controlled by $\Delta\lambda_{\mathrm{det}}$ [3]. In other words, independent of the cause of variations, A_{osc} can be kept constant by adjusting $\Delta\lambda_{\mathrm{det}}$. We have evaluated the performance of the proposed technique using silica microtoroidal OMOs [1, 2, 13]. However, this technique is effective for all kinds of radiation-pressure-driven OMOs with different geometries and materials.

It is worth mentioning that the Brownian noise associated with thermal vibration of the mechanical mode as well as the relative intensity noise (RIN) and frequency noise of the pump laser, will also affect the OMOs' oscillation. However, as these are fast processes, their signature mainly appears as excess phase noise that broadens the linewidth of the optomechanical oscillation [19]. For given optical and mechanical quality factors, suppression of these noises is hard to achieve using external feedback loops and usually requires more advanced techniques (e.g., injection locking by a low noise oscillator), reducing the temperature and/or using a pump laser with lower noise.

3.2 Experimental demonstration

Figure 3.2 shows the experimental configuration used for the proof-of-concept demonstration. The silica microtoroid OMO [1, 2] is driven by a 1550 nm tunable laser (Velocity 6300-LN, New Focus) through a silica fiber taper, and the output is fed to a photodetector (Model 1811, New Focus); the photocurrent (RF oscillation) is detected by an RF power detector which converts RF input power to DC voltage with a slope of -25 mV/dB (ZX47-60-S+, Minicircuits), a DC block is used to eliminate the DC voltage corresponding to CW optical power. The detected voltage of the RF power detector is fed to the c ontrol system that generates the feedback signal to the tunable pump laser. A small part of the photocurrent is divided between an RF spectrum analyzer (for spectrum monitoring) and an oscilloscope (for temporal behavior and detuning monitoring). For this demonstration, we used a LabView program as the feedback controller since it allowed us to explore different control algorithms and fine-tune the corresponding parameters. Note that eventually the computer and the program can be replaced by a simple and compact PID controller for practical applications.

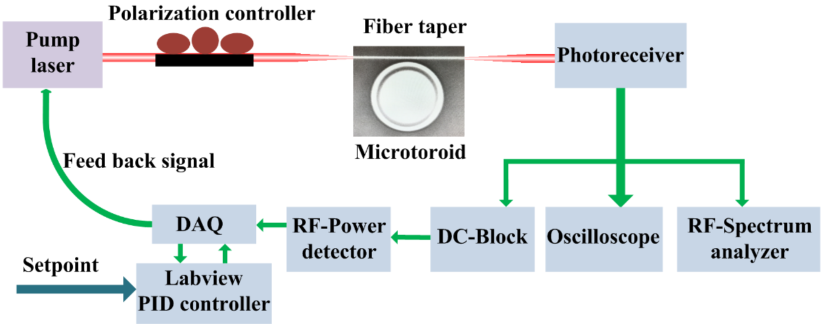

Fig. 3.2. Experimental setup used for testing the proposed stabilization technique.

The talk between the LabView program and the external equipment is through a Data Acquisition device (DAQ), it digitizes the incoming analog signal so that the computer (LabView) can interpret them, the DAQ then changes the computer-generated digital signal to analog signal for controlling the external equipment. Here, the LabView program converts the DC voltage to the oscillation amplitude (A_{osc}) which is used to generate a feedback signal through the PID block (also implemented in LabView). The control signal is fed back to the tunable laser to adjust the wavelength detuning ($\Delta\lambda$) to compensate for oscillation amplitude variations. The required wavelength change and, therefore, the PID parameters, for stabilizing the oscillation amplitude depend on the relation between $\Delta\lambda_{\mathrm{det}}$ and A_{osc} for the specific OMO under test. As such, initially we measured the relation between oscillation amplitude and wavelength detuning in the absence of the feedback. In this measurement, the power of the tunable pump laser is fixed, and the pump wavelength is scanned across the selected optical resonance while measuring A_{osc} using the oscilloscope.

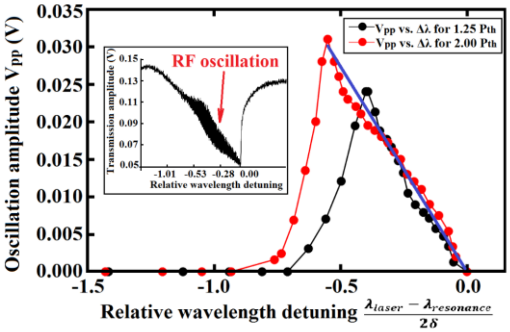

Fig. 3.3. Measured OMO oscillation amplitude A_{osc} plotted against normalized pump wavelength detuning for two levels of input pump power: $P_{\mathrm{pump}} = 1.25 \times P_{\mathrm{th}}$ and $P_{\mathrm{pump}} = 2 \times P_{\mathrm{th}}$. ($P_{\mathrm{th}}$ is the threshold pump power for optomechanical oscillation). The left inset is the transmitted optical power through the fiber-taper plotted against normalized wavelength detuning in the presence of optomechanical oscillation when $P_{\mathrm{pump}} = 1.25 \times P_{\mathrm{th}}$. For the measurement: $\lambda_0 \sim 1533$ nm; $Q_{\mathrm{loaded}} = 4.3 \times 10^6$; $f_{\mathrm{mech}} = 8.96$ MHz (the first radial mode) and $P_{\mathrm{th}} = 243$ µW.

Figure 3.3 shows A_{osc} plotted against normalized wavelength detuning ($\Delta\lambda_{\mathrm{det}}/2\delta$, where the 2δ is the loaded linewidth of the microtoroid OMO or $2\delta \sim \lambda_{\mathrm{resonance}}/Q_L$). For a given pump power, the linear range within negative or positive slopes can be used to maintain A_{osc} by controlling $\Delta\lambda_{\mathrm{det}}$. (In our experiment, we use the negative slope, the blue line in Fig. 3.3.) Once the PID parameters are adjusted based on the selected slope, the oscillation amplitude (or power) can be locked to the desired value by selecting the corresponding set point. The program calculates the error (derivation from the set point) and applies a correction voltage on the piezo stage of the tunable laser that controls the laser wavelength.

In order to test the performance of the proposed feedback loop, we used the proposed locking mechanism to stabilize two microtoroid OMOs while monitoring the oscillation amplitude and frequency. Figure 3.4(a) shows the measured oscillation amplitude for an OMO that oscillates at 8.96 MHz with and without a feedback loop with $P_{\mathrm{pump}} = 1.25 \times P_{\mathrm{th}}$. When the feedback is on (black trace), the oscillation amplitude is almost equal to the set point value 0.015 V (the detected voltage corresponding to the desired A_{osc}). In the absence of feedback (blue trace, when only intrinsic thermal optical feedback maintains $\Delta\lambda_{\mathrm{det}}$), the oscillation amplitude slowly deviates from the initial value (set by adjusting the pump power, coupling, and detuning) and, eventually, collapses to zero. Figure 3.4(b) shows the same measurement when $P_{\mathrm{pump}} = 2 \times P_{\mathrm{th}}$. As the pump power increased, the thermal locking becomes stronger, but still cannot prevent the slow drift of the oscillation amplitude (blue trace) in Fig. 3.4(b). Figure 3.4(c) shows the same measurement for another OMO that oscillates at 16.62 MHz when $P_{\mathrm{pump}} = 1.36 \times P_{\mathrm{th}}$.

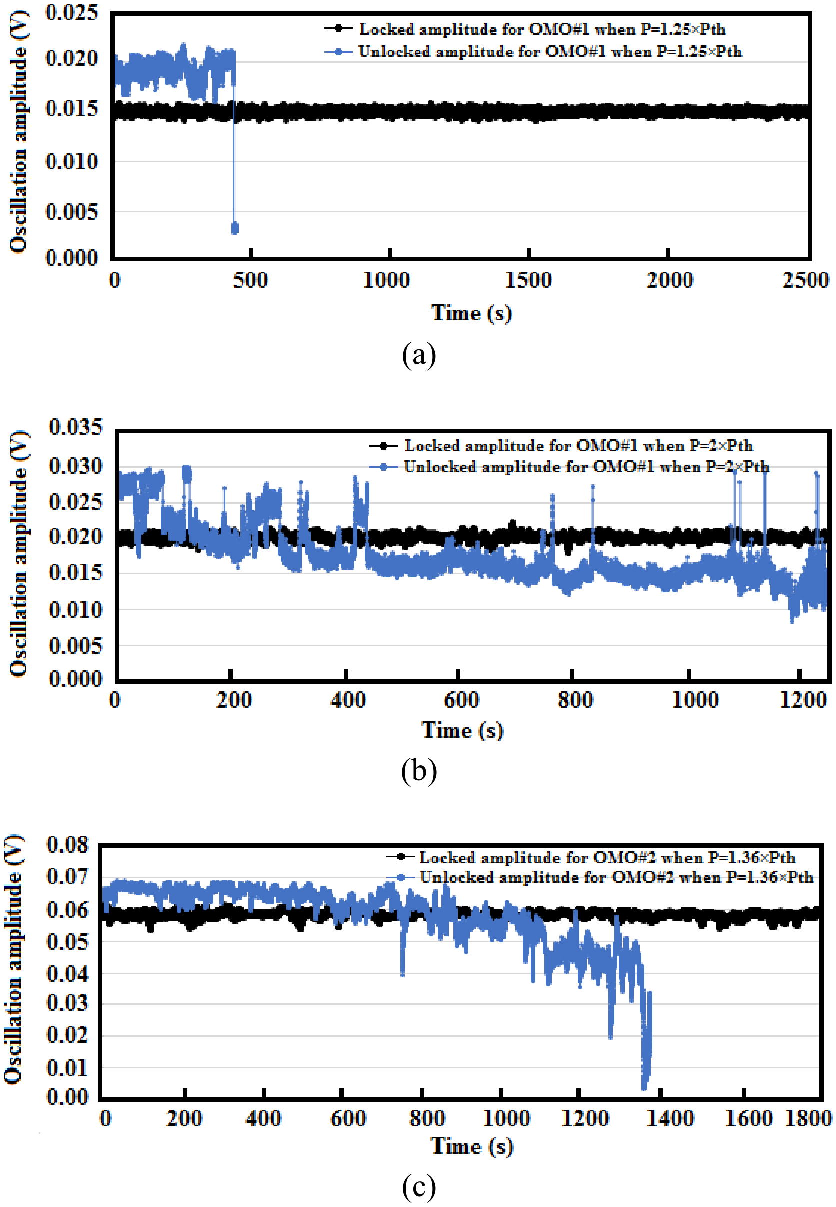

(a)

(b)

(c)

Fig. 3.4. Measured oscillation amplitude for different OMOs at various pump powers with and without feedback. (a) is the measured oscillation amplitude for OMO#1 with (black trace) and without (blue trace) feedback when $P_{\text{pump}} = 1.25 \times P_{\text{th}}$ and the setpoint is 0.015 V. (b) is the measured oscillation amplitude for OMO#1 with (black trace) and without (blue trace) feedback when $P_{\text{pump}} = 2 \times P_{\text{th}}$ and the setpoint is 0.02 V. (c) is the measured oscillation amplitude for OMO#2 with (black trace) and without (blue trace) feedback when $P_{\text{pump}} = 1.36 \times P_{\text{th}}$ and the setpoint is 0.06 V. For OMO#1: Diameter = 64 µm, $\lambda_0 \sim$ 1533 nm; $Q_{\text{loaded}} = 4.3 \times 10^6$; $f_{\text{mech}} = 8.96$ MHz and $P_{\text{th}} = 243$ µW. For OMO#2: Diameter = 64 µm, $\lambda_0 \sim$ 1557 nm; $Q_{\text{loaded}} = 8.3 \times 10^6$; $f_{\text{mech}} = 16.62$ MHz and $P_{\text{th}} = 30.95$ µW.

These measurements clearly show that this simple feedback mechanism can reduce oscillation amplitude fluctuations and enables long-term stability required for practical applications. The standard deviation of the measured oscillation amplitude in the unlocked case (before its sudden drop) is 7 to 10 times larger than that of the locked case. These results show that even at larger P_{pump}, the intrinsic thermal-optical feedback is not sufficient to prevent oscillation degradation and fluctuations.

We have also examined stabilizing the OMO using RF power (instead of oscillation amplitude) as the feedback parameter. Figure 3.5 shows the measured RF power when $P_{\text{pump}} = 1.25 \times P_{\text{th}}$ for OMO#1. As shown in the inset of Fig. 3.5, the measured relation between RF power and $\Delta\lambda_{\text{det}}$ is not as linear as the relation between A_{osc} and $\Delta\lambda_{\text{de}}$, but still it can be used to stabilize the OMO. This is important, as it allows one to directly use the output of the RF power detector (that is, a voltage proportional to RF power) as the feedback parameter. The proposed amplitude stabilization technique also reduces the OMO oscillation frequency variations due to the sensitivity of oscillation frequency to circulating optical power through an optical spring effect and optical absorption inside the cavity [13].

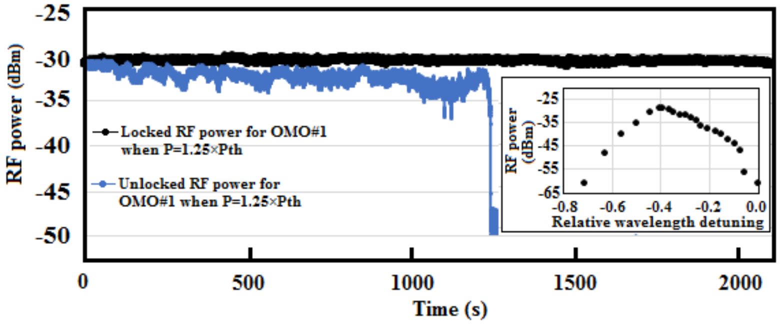

Fig. 3.5. Measured RF power for OMO#1 with (black trace) and without (blue trace) feedback when $P_{\text{pump}} = 1.25 \times P_{\text{th}}$ and the setpoint is 1.4 V. Note that here the RF power is the feedback parameter. The measured RF power is calculated from the output voltage of the RF power detector which has conversion factor of -25mV/dB. The inset shows the measured RF power plotted against the normalized pump wavelength detuning when $P_{\text{pump}} = 1.25 \times P_{\text{th}}$ for OMO#1.

Figure 3.6 shows the temporal variations of the OMO mechanical oscillation frequency in the presence (black trace) and absence (blue trace) of the feedback. The high-resolution measurement in the inset clearly shows that the feedback has reduced the frequency fluctuations from 900 to 300 Hz.

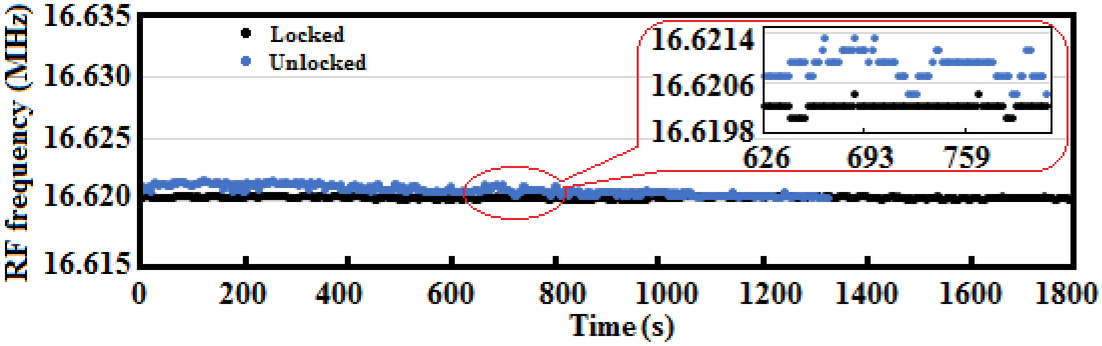

Fig. 3.6. Measured RF frequency for OMO#2 with (black trace) and without (blue trace) feedback, the set point is 0.06 V for the locked operation.

Temperature, pump power, and the coupling gap are the three main factors that affect the performance of OMOs. In order to demonstrate that the proposed feedback mechanism can compensate for the variations induced by these perturbations, we manually changed the ambient temperature, pump power, and the coupling gap for OMO#1 with and without the feedback loop and compared their impact on oscillation amplitude and frequency for each case.

3.3 Stability of OMO against temperature change

In order to verify that the proposed locking method can stabilize OMO in the presence of ambient temperature change, the OMO was placed in a box where the temperature inside the box was controlled by a heater, and monitored by a psychrometer (RH350, EXTECH Instruments) with temperature sensing resolution of 0.1°C.

Figure 3.7 shows OMO's performance when the ambient temperature was increased from 26.4 °C to 27.7 °C. The oscillation amplitude of the unlocked OMO changed dramatically and, eventually, collapsed at 27 °C while that of the locked one remained constant to 27.7 °C [Fig. 3.7(a)]. Figure 3.7(c) shows while the feedback loop did not completely suppress the OMO oscillation frequency variation, it reduced its magnitude by nearly 6 times compared to oscillation frequency variation of the free-running OMO (in the temperature range where it was still oscillating).

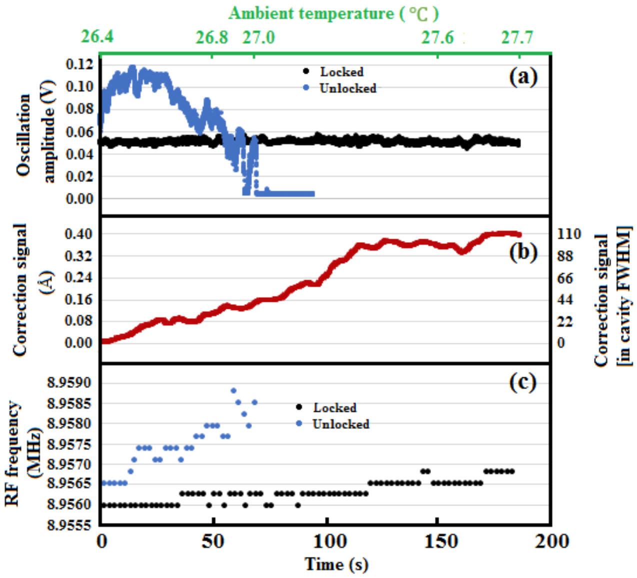

Fig. 3.7. (a) Measured oscillation amplitude with (black point) and without (blue point) feedback, (b) correction signal (red point) for the locked case and (c) the corresponding measured RF frequency with (black point) and without (blue point) feedback for OMO#1 when the ambient temperature increased from 26.4 °C to 27.7 °C.

3.4 Stability of the OMO against optical pump power variation

The effect of the pump power change on the stability of an OMO was tested by manually increasing the optical pump power using a fiber-optic attenuator and monitoring the oscillation amplitude and frequency of the OMO.

Figure 3.8 shows the OMO's performance when the pump power increased manually from 1.4 × P_{th} to 2.5 × P_{th} for OMO#1 under locked and unlocked conditions; for the free running (unlocked) OMO, the oscillation amplitude collapses when the pump power approached 2.3 × P_{th}. While the oscillation amplitude of the locked OMO remains constant even when the optical pump power is larger than 2.5 × P_{th}. The impact of the pump power variation on optomechanical oscillation frequency is relatively small, however still the oscillation frequency of the locked OMO is about 5 times smaller than that of the unlocked OMO (10^{-4} versus 5×10^{-4})

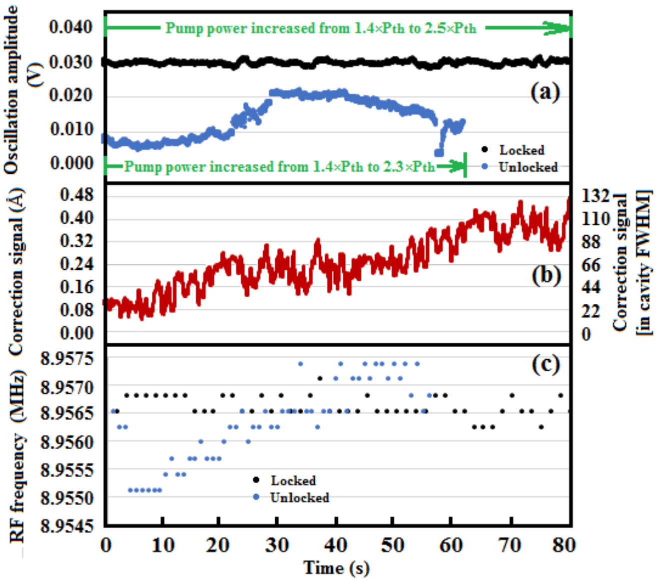

Fig. 3.8. (a) Measured oscillation amplitude with (black point) and without (blue point) feedback, (b) the correction signal (red point) for the locked case and (c) the corresponding measured RF frequency with (black point) and without (blue point) feedback for OMO#1 when the pump power increased from 1.4 × P_{th} to 2.5 × P_{th}. Note: the pump power is increased manually with a step size of ~0.05 × P_{th}.

3.5 Stability of the OMO against the coupling gap variation

In order to test the effect of the coupling gap change on the stability of the locked and free-running OMO, we manually decreased the coupling gap between the fiber taper and the microtoroid using a piezo stage with a resolution of 20 nm and monitor the output of OMO.

Figure 3.9 shows the OMO's performance when the coupling gap decreased by 260 nm for OMO#1 under locked and unlocked conditions. The mechanical frequency of the unlocked oscillator changes by 5 kHz and when the coupling gap decreased to 320 nm, it completely vanishes (not shown in the graph).

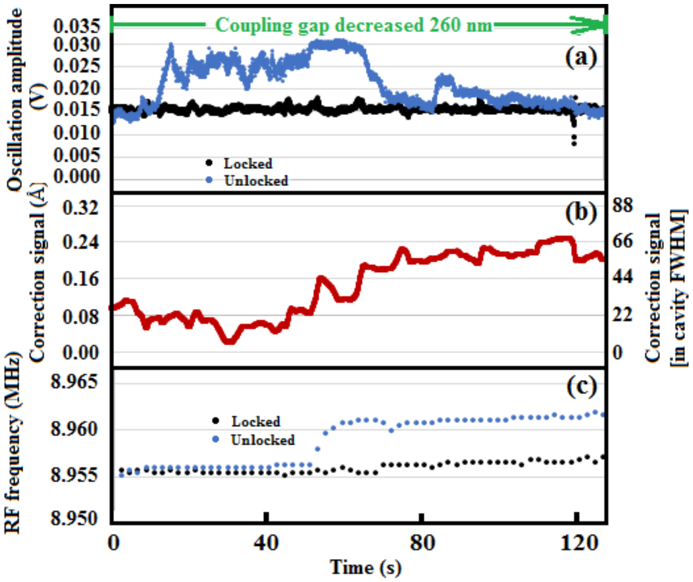

Fig. 3.9. (a) Measured oscillation amplitude with (black point) and without (blue point) feedback, (b) correction signal (red point) for the locked case and (c) the corresponding measured RF frequency with (black point) and without (blue point) feedback for OMO#1 when the coupling gap decreased by 260 nm. Note: the coupling gap is decreased manually with a step size of 20 nm.

Clearly the proposed feedback locking method enables effective locking of the oscillation amplitude to a desired value (set point) and protects it from temperature change, pump power variation, and coupling gap change. This technique can overcome relatively large variations in order to compensate for temperature, pump, and coupling gap changes; the laser wavelength has been detuned 110 × 2δ (where 2δ is the loaded linewidth of the selected optical mode) in Fig. 3.7(b), 110 × 2δ in Fig. 3.8(b), and 66 × 2δ in Fig. 3.9(b). As during these tests, the pump power and the coupling gap were changed manually with variable speed and through large jumps, the stable operation of the locked OMO verifies the fast response of the feedback mechanism which is required to correct both slow and sudden perturbations.

3.6 Summary

We have demonstrated a simple and effective locking method for stabilization of the oscillation amplitude of OMOs which requires only an RF power detector and a PID controller. Using the proposed mechanism, the oscillation amplitude can be locked to a desired value, and the RF frequency variations can be reduced without adding to the system cost and complexity. This feedback mechanism is effective in compensating for the effect of the temperature, pump power, and coupling gap variations. As such, this approach will pave the road for employment of OMOs in practical applications. For example, in chapter 6 of this thesis, it is demonstrated that OMO can simultaneously serve as acousto-optic transducer and frequency down-converter in underwater acoustic links; stabilization of OMO with the prescribed method here may improve the performance of the corresponding underwater acoustic links.

3.7 References

[1] H. Rokhsari, T. J. Kippenberg, T. Carmon, and K. J. Vahala, “Radiation-pressure-driven micro-mechanical oscillator,” Opt. Express., **13**(14), 5293-5301 (2005).

[2] H. Rokhsari, T. J. Kippenberg, T. Carmon, and K. J. Vahala, “Theoretical and Experimental Study of Radiation Pressure-Induced Mechanical Oscillations (Parametric Instability) in Optical Microcavities,” *IEEE* J. Sel. Top. Quantum Electron., **12**(1), 96-107 (2006).

[3] T. J. Kippenberg and K. J. Vahala, “Cavity Opto-Mechanics,” Opt. Express., **15**(25), 17172-17205 (2007).

[4] A. Gondarenko, J. S. Levy and M. Lipson, “High confinement micron-scale silicon nitride high Q ring resonator,” Opt. Express., **17**(14), 11366-11370 (2009).

[5] W. C. Jiang, X. Y. Lu, J. D. Zhang and Q. Lin, “High-frequency silicon optomechanical oscillator with an ultralow threshold,” Opt. Express., **20**(14), 15991-15996 (2012).

[6] S. Tallur, S. Sridaran, and S. A. Bhave, “A monolithic radiation-pressure driven, low phase noise silicon nitride opto-mechanical oscillator,” Opt. Express., **19**(24), 24522-24529 (2011).

[7] F. F. Liu, S. Alaie, Z. C. Leseman, and M. Hossein-Zadeh, “Sub-pg mass sensing and measurement with an optomechanical oscillator,” Opt. Express., **21**(17), 19555-19567 (2013).

[8] W. Y. Yu, W. C. Jiang, Q. Lin, and T. Lu, “Cavity optomechanical spring sensing of single molecules,” Nat. Commun., **7**, Art. no. 12311 (2016).

[9] M. Hossein-Zadeh and K. J. Vahala, “Photonic RF Down-Converter Based on Optomechanical Oscillation,” *IEEE* Photon. Technol. Lett., **20** (4), 234-236 (2008).

[10] F. F. Liu and M. Hossein-Zadeh, “Characterization of Optomechanical RF frequency Mixing/Down-Conversion and its Application in Photonic RF Receivers,” J. Lightwave. Technol., **32**(2), 309-317 (2014).

[11] T. Carmon, L. Yang, and K. J. Vahala, “Dynamical thermal behavior and thermal self-stability of microcavities,” Opt. Express., **12**(20), 4742-4750 (2004).

[12] J. Li, S. Diddams, and K. J. Vahala, “Pump frequency noise coupling into a microcavity by thermo-optic locking,” Opt. Express., **22**(12), 14559-14567 (2014).

[13] M. Hossein-Zadeh, H. Rokhsari, A. Hajimiri, and K. J. Vahala, “Characterization of a radiation-pressure-driven micromechanical oscillator,” Phys. Rev. A., **74**(2), Art. no. 023813 (2006).

[14] F. Liu and M. Hossein-Zadeh, “On the spectrum of radiation pressure driven optomechanical oscillator and its application in sensing,” Opt. Commun., **294**, 338-343 (2013).

[15] K. Huang and M. Hossein Zadeh, "Underwater Acoustic Signal Detection and Down-Conversion Using Optomechanical Resonance and Oscillation," in J. Lightwave. Technol., (2020).

[16] K. Huang and M. Hossein Zadeh, "Ultrasonic acousto-optical receivers based on optomechanical resonance and oscillation," *in Proc. CLEO.*, SF1J-5, San Jose, CA, USA, May, (2019).

[17] R. W. P. Drever, J. L. Hall, F. V. Kowalski, J. Hough, G. M. Ford, A. J. Munley, and H. Ward, “Laser phase and frequency stabilization using an optical resonator,” Appl. Phys. B., **31**, 97-105 (1983).

[18] T. W. Hansch and B. Couillaud, “Laser frequency stabilization by polarization spectroscopy of a reflecting reference cavity,” Opt. Commun., **35**(3), 441-444 (1980).

[19] H. Rokhsari, M. Hossein-Zadeh, Ali Hajimiri, and K. J. Vahala, “Brownian noise in radiation-pressure-driven micromechanical oscillators”, Appl. Phys. Lett., **89**(6), Art. no. 261109 (2006).

Chapter 4

Injection locking of optomechanical oscillators via acoustic waves

4.1 Introduction

In almost all applications of OMO (e.g., optical RF local oscillator, all-optical RF down-conversion [1, 2] and mass sensing [3, 4]), the stability of OMO and control over its phase and frequency are not only critical for the performance of the system, but also enable new functionalities. The frequency of an OMO is determined by its mechanical eigenmodes and therefore the microresonator size and structure. Typically, a single OMO can support few oscillation frequencies associated with mechanical modes that are strongly coupled to high quality (high-Q) optical modes of the cavity. These modes can be selected by adjusting the laser wavelength and coupling strength near optical resonant wavelengths with sufficient quality factor [1, 5, 6]. For an isolated OMO, fine tuning of each oscillation frequency over a limited range can be achieved by changing the optical power (through optical spring effect) as well as microresonator temperature [6, 7]. Alternatively, similar to other self-sustained oscillators, the oscillation frequency of OMO can be controlled by injection locking to another oscillator [8–11].

Injection locking that has been extensively studied in electronic [12, 13] and photonic oscillators (lasers) [14], not only provides control over the oscillation frequency and phase, but also enables synchronization of multiple oscillators to each other or to an external source. In general injection locking involves coupling (injecting) a periodic signal with a frequency close to the oscillation frequency into the oscillator. If the amplitude of the coupled signal is large enough, the frequency and phase of the oscillator are pulled and locked to that of the signal and therefore to the signal source. Basically, the injected signal generated by the “master” oscillator acts as a perturbation for the “slave” oscillator; so, the physical nature of the injected signal should be similar to one of the oscillating parameters in the slave oscillator. As such in electronic oscillators the injected signal can be an oscillating voltage, current or magnetic field and in lasers the injected signal is a coherent optical wave. Similarly, in an optomechanical oscillator the injected signal can be a modulated optical power (perturbing the circulating optical power), a periodic mechanical force, or a mechanical wave (perturbing the mechanical motion).

The first experimental observation of injection locking of an OMO was reported based on optical pump modulation [8], where the amplitude of the optical pump was partially modulated using an electro-optic modulator. Basically, a small portion of the input power that was modulated at a frequency near f_{OMO}, acted as the injection signal and the OMO was locked to the RF source that was driving the modulator. Later synchronization of multiple OMOs using this approach was theoretically analyzed [15] and experimentally demonstrated but only for few OMOs [10, 11]. While feeding a modulated optical pump to multiple OMOs in parallel or series configuration seems to be a trivial solution for synchronizing multiple OMOs, the fact that all these OMOs should have the same exact resonant optical wavelength, makes its practical implementation a very challenging task (in particular for oscillator networks). Fabrication of high-Q optomechanical cavities with the same exact resonant optical wavelengths is nearly impossible so these experiments require active thermal tuning of the corresponding optical cavities and therefore individual electrical contact with each OMO.

Recently it has been shown that OMO can be locked to an RF drive using electromechanical force directly applied on the OMO [16, 17]. This method uses a metallic electrode deposited on top of the OMO (in this case a toroidal silica microcavity) to convert the RF voltage to a modulated force. This approach suffers from several shortcomings: 1) deposition of metallic electrode on the optomechanical resonators not only makes the fabrication process complicated, but also degrades the optical and mechanical quality factor (this may explain the large threshold pump power in Ref. 17 that is more than one order of magnitude larger than similar OMOs). Clearly this problem is much more serious for nano scale optomechanical resonators such as zipper microcavities [18, 19], small microdisks [20] or spoke supported microrings [21] (as their optical and mechanical quality factors are extremely sensitive to the perturbation caused by any added structure). 2) In order to drive the electrodes, each OMO should be electrically connected to the RF source. While in a lab setting and for a single device the signal can be applied using special RF microprobes, in an integrated system the electric connection is a major challenge and limits the scalability of this technique.

In this chapter the first experimental observation of injection locking of OMO via acoustic waves and characteristics of the locked OMO are described and, we demonstrate that the acoustic waves, generated by an electromechanical oscillator, can stimulate the mechanical mode coupled to the optical resonance, they can also pull and lock the frequency and phase of the corresponding optomechanical oscillation to the frequency and phase of the electromechanical oscillator that generates them. We show injection locking can occur with an acoustic excitation that generates a mechanical amplitude modulation as small as 5% of the original optomechanically generated modulation (by radiation pressure). As long as the acoustic waves reaching the OMO can generate sufficient mechanical vibrations, the electromechanical transducer can be attached or fabricated at any location on the carrier chip without affecting the optomechanical properties of the OMO and interfering with its operation.

As such injection locking of OMOs via acoustic waves is superior to the previously reported techniques since by eliminating the need for physical contact with the microresonator and modulation of the optical pump power, it opens a wide range of possibilities for injection locking and synchronization of multiple OMOs using an external oscillator at reduced cost and complexity. Low power and large-scale injection locking and synchronization of OMOs may benefit many applications such as optomechanical RF signal processing, optical communication and sensing.

Beyond its engineering applications, this new technique can be used in fundamental studies in quantum measurement, quantum optomechanics and nonlinear dynamics of coupled oscillators where physical isolation is critical and phase/frequency control should be achieved with minimal interference with OMO's intrinsic properties and optical feedback.

For the proof of concept demonstration of this approach, we used a toroidal silica microcavity as the optomechanical resonator/oscillator and a piezoelectric transducer as the electromechanical oscillator. While silica microtoroid has been selected because of its simplicity, relatively low threshold power and phase noise in atmospheric pressure [6], with proper design the same approach can be used to injection lock nearly any OMO (down to nanoscale size) without the need to modify its structure.

Here we experimentally demonstrate and characterize the injection locking of two distinct mechanical modes of the selected microtoroidal OMO to an external piezoelectric transducer (PZT) via acoustic waves. Using a combination of finite element modeling for one of the modes and time-domain coupled differential equations, we verify that the behavior of the measured lock range as a function of RF input power fed to the PZT was in agreement with the classical theory of optomechanical oscillation. As such similar systems can be designed and optimized simply by finite element modeling of the acoustic energy exchange between the transducer and the selected mechanical mode and using the outcomes of the general coupled time domain differential equations governing the optomechanical oscillation.

4.2 Experimental setup and acoustic excitation configurations

Figure 4.1(a) shows the experimental arrangement used for characterizing the microtoroidal OMO and demonstration of injection locking via acoustic waves. Optical power from a tunable laser (λ_{laser} ~1550 nm) is coupled to high-Q Whispering-Gallery modes (WGMs) circulating inside the microtoroidal optical cavity using a standard tapered silica fiber [22–24]. The coupling gap between the tapered fiber and the microtoroid is precisely controlled with a nano-positioner. A photodetector (bandwidth = 150 MHz) is used to convert the optical power to electric signal for time and frequency domain analysis.

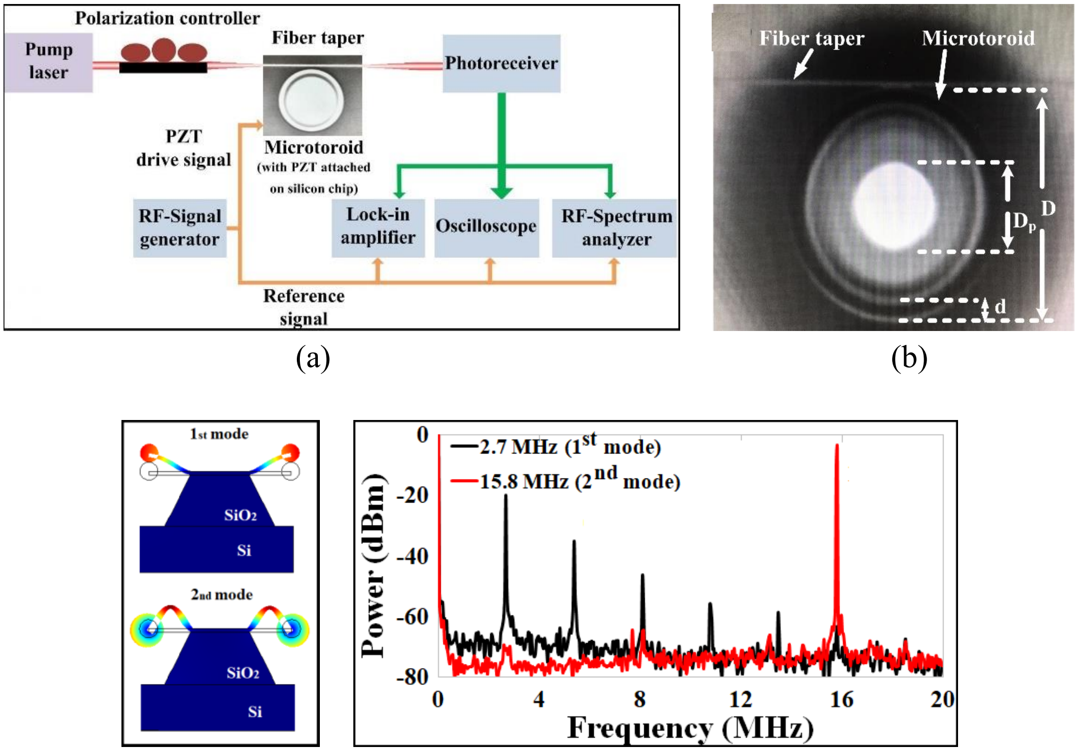

(a) (b)

(c) (d)

Fig. 4.1. (a) Experimental arrangement for the injection locking of OMO. (b) The top view micrograph of the silica microtoroid coupled to a silica fiber taper. The microtoroid has a major diameter of D = 76 μm and minor diameter of d = 9.7 μm, the supporting silicon pillar has diameter of D_p = 31.5 μm. (c) Mechanical deformation associated with mode-1 ($f_{OMO,1}$ = 2.7 MHz) and mode-2 ($f_{OMO,2}$ = 15.8 MHz), the modes' shape is calculated based on FEM using COMSOL software. (d) The measured RF spectrum of the transmitted optical power at $\Delta\lambda_1 = -0.38\lambda_1/Q_{L1}$ (black trace), $\Delta\lambda_2 = -0.42\ \lambda_2/Q_{L2}$ (red trace) corresponding to optomechanical oscillation of mode-1 with a frequency of 2.7 MHz and mode-2 with a frequency of 15.8 MHz, the higher harmonics that generated by the nonlinear optical transfer function of the cavity can be observed. The measured mechanical quality factor (Q_{mech}) is 119 for mode-1 and 360 for mode-2.

Using the standard OMO characterization procedure [6], in the absence of acoustic excitation, the high-Q WGMs with strongest coupling to two mechanical eigenmodes of the microtoroid were identified. Near each optical mode the coupling gap and wavelength detuning ($\Delta\lambda = \lambda_{laser} - \lambda_0$, λ_0: resonant wavelength of the corresponding optical mode) are optimized to obtain the minimum optomechanical threshold power (P_{th}) [22–25].

The first optomechanical mode oscillates at $f_{\mathrm{OMO,1}} = 2.7$ MHz and is excited by an optical mode with a resonant wavelength of $\lambda_{01} = 1559.1$ nm and loaded quality factor of $Q_{\mathrm{L1}} = 3.3 \times 10^{6}$. The second optomechanical mode oscillates at $f_{\mathrm{OMO,2}} = 15.8$ MHz and is excited by an optical mode with a resonant wavelength of $\lambda_{02} = 1558.7$ nm and loaded quality factor of $Q_{\mathrm{L2}} = 6.1 \times 10^{6}$. The measured threshold optical input power for exciting these oscillations were $P_{\mathrm{th,1}} = 90$ μW and $P_{\mathrm{th,2}} = 400$ μW, respectively. Figure 4.1(b) shows the top-view micrograph of the silica microtoroid used in this experiment. After careful measurement of microtoroid dimensions, we used Finite Element Modeling (COMSOL software) to identify the mechanical eigenmodes associated with the measured oscillation frequencies. Figure 4.1(c) shows the calculated mechanical deformation associated with these two modes indicating that mode-1 ($f_{\mathrm{OMO,1}} = 2.7$ MHz) is a flapping mode and mode-2 ($f_{\mathrm{OMO,2}} = 15.8$ MHz) is a breathing radial mode. Figure 4.1(d) shows the RF spectrum of the transmitted optical power when λ_{laser} was tuned near λ_{01} (black trace) and λ_{02} (red trace) while optical input power ($P_{\mathrm{o,in}}$) was larger than P_{th} for the corresponding mechanical modes. Both modes are coupled to the circulating optical power through radial component of the microtoroid displacement (ΔR). As such the modulation amplitude of the output optical signal is proportional to ΔR [6]. The estimated effective mass is $m_{\mathrm{eff}} = 40$ pg for the first mode and 360 pg for the second mode. Both mechanical modes were coupled to the optical mode with almost same optomechanical coupling coefficient of $g_{\mathrm{OM}} = 1.05$ GHz/nm estimated relative to the total displacement of the toroidal section (using the microtoroid dimensions and Finite Element Modeling). Note that the ability of exciting and monitoring two distinct optomechanical modes of the OMO is important to demonstrate the possibility of injection locking of two different modes and showing the dependence of locking strength on mechanical deformation for a given acoustic excitation.

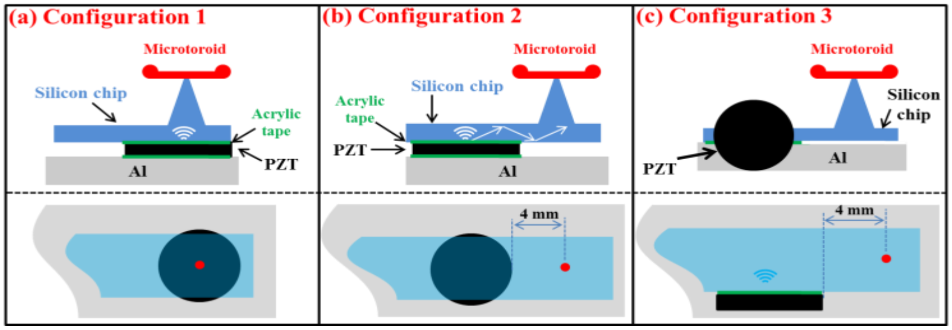

Fig. 4.2. Three configurations used to study the injection locking of OMO. (a) Configuration-1, the PZT is attached to the bottom side of the silicon chip right below the microtoroid. (b) Configuration-2, the PZT is attached to the bottom side of the silicon chip but 4 mm away from the microtoroid in the horizontal direction. (c) Configuration-3, the PZT is attached to the side edge of the silicon chip with 4 mm away from the OMO in the horizontal direction.

To study injection locking via acoustic waves, an external piezoelectric actuator is attached to the silicon chip that carries the OMO. The silicon chip has a dimension of 15 mm (L) × 4.5 mm (W) × 0.3 mm (H) and the piezoelectric actuator is a disk with a diameter of 20 mm and thickness of 0.2 mm. The selected piezo transducer (PZT) is designed to sustain mechanical oscillations through its thickness mode at a resonant frequency of 10.1 MHz. However, by adjusting the drive frequency it can oscillate at a wide frequency range from 2 to 16 MHz with slightly lower efficiency and with a FWHM linewidth of 26 Hz. We examined three configurations for exciting the mechanical modes of the microtoroid via acoustic waves generated by the PZT. These configurations are shown in Figs. 4.2(a)-(c): In configuration-1 (Fig. 4.2(a)), The PZT is attached to the bottom of the silicon chip right below the OMO, configuration-2 (Fig. 4.2(b)) is similar to configuration-1 but the PZT is moved 4 mm away from OMO; finally in configuration-3 (Fig. 4.2(c)) the PZT is rotated 90 degrees and is attached to the side of the silicon chip 4 mm away from the OMO.

In all configurations, the piezo transducer is attached to the silicon chip using an acrylic double-sided tape (thickness = 70 µm) and is driven by a sinusoidal wave generated by an RF source. For this proof-of-concept demonstration the acoustic impedance of the PZT is not matched to that of the silicon chip as such a relatively small portion of the acoustic energy produced by the PZT is transferred to the silicon chip (only 27% and 15% of the acoustic energy generated by the PZT is transmitted to the silicon chip at 2.7 MHz and 15.8 MHz, respectively). In principle using proper acoustic impedance matching layers between PZT and the chip 100% of the acoustic energy can be transferred to the silicon chip within the operational bandwidth of the PZT. For each optomechanical mode and configuration, the impact of the acoustic waves (generated by the PZT) on the OMO is evaluated by varying the power and frequency of the RF signal delivered to the PZT. The spectrum of the modulated output power and the relative phase between OMO and the RF signal are measured using an RF spectrum analyzer and a lock-in amplifier (as shown in Fig. 4.1(a)).

4.3 Experimental observation of OMO injection locking via acoustic waves

For the initial demonstration OMO injection locking was examined using configuration-2. Figure 4.3(a) shows the RF spectrum of the modulated optical output power near $f_{OMO,1}$ in the presence (red trace) and absence (black trace) of acoustic excitation when $P_{o.in} = 2 \times P_{th,1}$. Here the RF power delivered to the PZT (P_{PZT}) is – 40 dBm and its frequency ($= f_{PZT}$) is 1.7 kHz smaller than $f_{OMO,1}$.

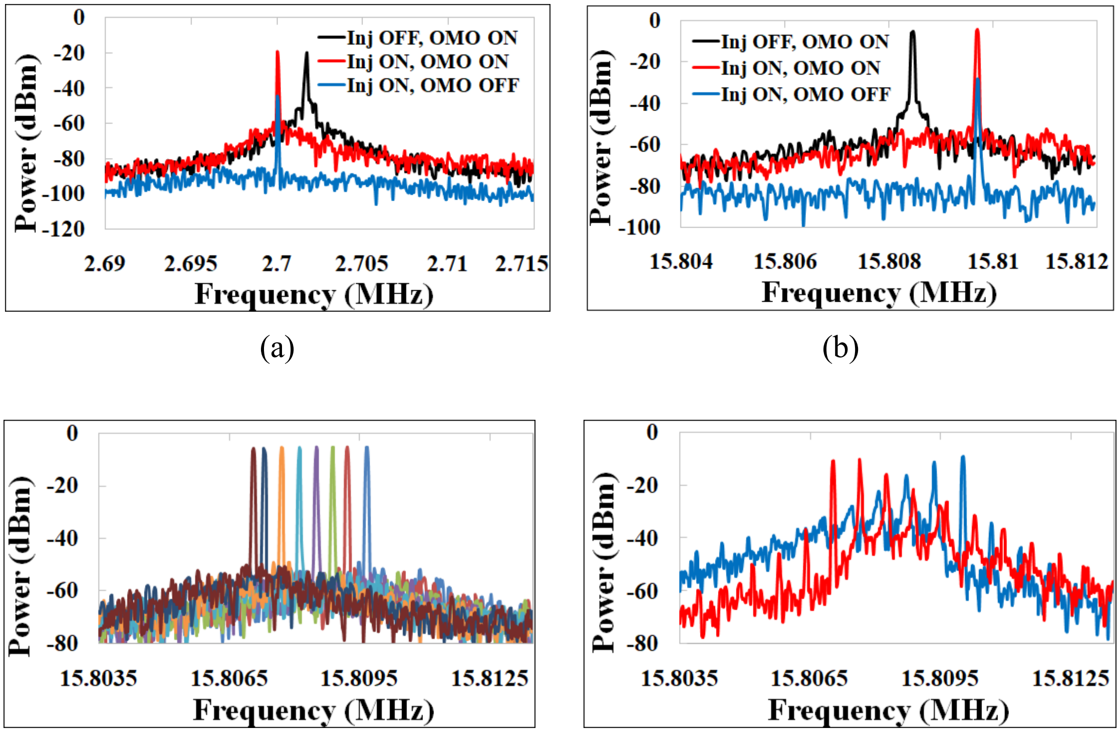

(a) (b)

(c) (d)

Fig. 4.3. Injection locking of mode-1 and mode-2 using configuration-2. (a) Measured spectrum of the optical power in the presence (red) and absence (black) of the injection signal (blue) for the 1st optomechanical mode. (b) Measured spectrum of the optical power in the presence (red) and absence (black) of the injection signal (blue) for the 2nd optomechanical mode. (c) Measured spectrum of the 2nd optomechanical mode tuned by the injection signal. (d) Measured spectrum of the 2nd optomechanical mode while the frequency of the injected signal is tuned slightly beyond the lock range. Note, in (a) $P_{PZT} =$ -40 dBm, $P_{o,in} = 2.0 \times P_{th,1}$ and $\eta = 0.138$. In (b) - (d) $P_{PZT} =$ -5 dBm, $P_{o,in} = 1.4 \times P_{th,2}$ and $\eta = 0.058$.

Figure 4.3(b) shows the RF spectrum of the optical output power near $f_{OMO,2}$ in the presence (red trace) and absence (black trace) of acoustic excitation when $P_{o.in} = 1.4 \times P_{th,2}$. Here the RF power delivered to the PZT (P_{PZT}) is – 5 dBm and its frequency ($= f_{PZT}$) is 1.24 kHz larger than $f_{OMO,2}$. It is apparent that the injected acoustic wave pulls $f_{OMO,1}$ and

$f_{OMO,2}$ and locks them to f_{PZT}. Note that in all these measurements not only a major portion of the acoustic energy is lost due to impedance mismatch (between the PZT and the chip) and material loss, but also only a small fraction of the total energy delivered to the chip couples to the desired mode.

As expected, the locking process reduced the OMO linewidth (from 400 Hz to 86 Hz). Note that oscillation linewidth of the locked OMO is still limited by the thermomechanical noise in the microtoroid structure. The measured linewidth of the acoustic wave generated by the PZT driven by the signal generator is about 26 Hz (measured directly using two identical PZTs, one as transmitter and the other as receiver). So even in the subthreshold regime the linewidth of the blue peak is limited by the thermo-mechanical noise in the microtoroid structure that is translated into optical domain through optical transfer function of the cavity.

For both modes we have also measured optical modulation spectrum due to excitation of the mechanical mode by the PZT (blue trace) by lowering $P_{o,in}$ below P_{th} (making the radiation pressure gain less than mechanical loss). At this power level the frequency of the modulated optical power is equal to that of the signal generator (that drives the PZT) and its amplitude is effectively proportional to the amplitude of the acoustic excitation. As shown later sub-threshold measurements allow us to quantify the radial motion induced by the acoustic excitation (ΔR_{PZT}) and its relationship with injection locking independent of the specific actuator and configuration used to transfer the acoustic energy. Figure 4.3(c) shows the spectrum of the optical output power near the frequency of the mode-2 at eight different injection frequencies. Here f_{PZT} is changed from $f_{OMO,2}$ -1.36 kHz to $f_{OMO,2}$ + 1.40 kHz. As expected within a frequency range (Δf_{lock} = 2.76 kHz) around $f_{OMO,2}$ (known as lock range) the injection locked optomechanical oscillation frequency is equal to f_{PZT} and follows its variations. Figure 4.3(d) shows the frequency pulling effect at the edge of the lock range (again for mode-2). When f_{PZT} is tuned slightly above and below the edge of the lock range, the oscillator is quasi-locked and the RF spectrum consists of a series of closely spaced decaying beat frequencies in the vicinity of $f_{OMO,2}$. This is a well-known effect that is studied in the context of electronic oscillators [12, 13] and is also observed in optically injection locked OMOs [8].

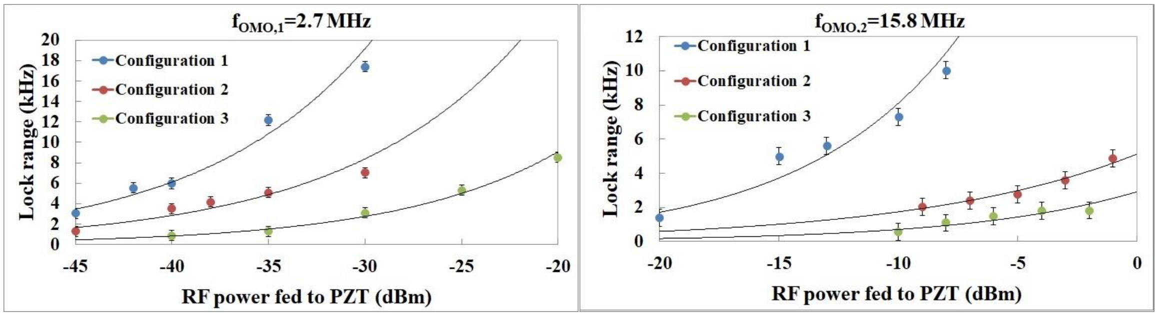

(a) (b)

Fig. 4.4. Measured lock-range for mode-1 (a) and mode-2 (b) as a function of P_{PZT} using configurations shown in Fig. 4.2. Note: the solid lines are exponential fit to the measured data, error bars along the vertical axis correspond to 2 × standard deviation (±500 Hz) for lock-range measurement.

We have carefully measured the lock-range for both mechanical modes injection locked to the PZT based on configurations shown in Fig. 4.2. Figure 4.4(a) and 4.4(b) show the measured lock range as a function of P_{PZT} for mode-1 and mode-2, respectively. The relation between RF power and injection strength for each configuration is complicated and requires a full 3D FEM analysis of the whole system (PZT + silicon chip + microtoroid

+ glue tape). However, the overall variation of the lock range for different modes and configurations can be explained based on the amplitude and the direction of mechanical vibrations generated by the PZT.

For the selected PZT, RF voltage stimulates its thickness mode, so configuration-1 and -2 generate mechanical vibrations along *z*-axis. As such for these configurations locking mode-2 requires more RF power compared to mode-1 because the vibrations along *z*-axis couple more efficiently to mode-1 compare to mode-2. Also, for both modes configuration-1 provides stronger injection compared to configuration-2 due to larger distance between PZT and OMO in configuration-2. Configuration-3 (where PZT is 90 degree rotated compared to configuration-2) provides the weakest injection as the resulting mechanical displacements are perpendicular to the displacement associated with mode-1 and mode-2.

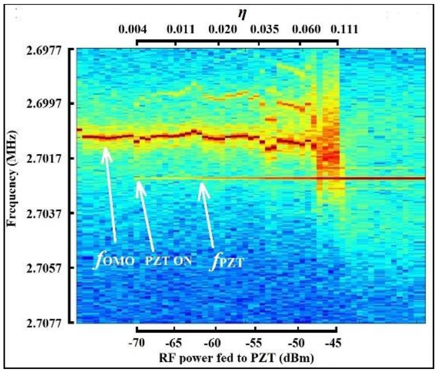

Fig. 4.5. RF spectrum of the OMO plotted against P_{PZT} and the relative displacement ratio η for the 1st mode and using configuration-2.

To show the dynamics of the locking process we have continuously monitored the oscillation frequency of mode-1 while increasing the input RF power at a fixed frequency offset. Figure 4.5 shows the measured spectrum of the OMO optical output power as a function of P_{PZT} and the corresponding values of η using configuration-2 when $f_{\mathrm{PZT}} - f_{\mathrm{OMO}} = 1.35$ kHz. As evident from the figure, above -65 dBm ($\eta > 0.011$) injection pulling begins and at ~-45 dBm ($\eta = 0.111$) the OMO is locked to the PZT.

4.4 Estimating lock range based on general theory of injection locking

Characterization of the lock range as a function of P_{PZT} (RF power delivered to the PZT) for a given configuration is important and useful for designing injection locked OMOs. However, in order to understand and evaluate the variation of lock range based on the general theory of injection locked oscillators (developed in the context of electronic oscillators), we need to characterize its behavior as a function of injection strength (as opposed to P_{PZT}). In electronic oscillators and optically injection locked OMOs this is an easy task because the injected signal and the force that drives self-sustained oscillations are identical (voltage and optical power respectively). However, when OMO is injection locked via acoustic waves, the injected signal is the RF power (or voltage) applied on the PZT while the driving force is the circulating optical power inside the cavity. Moreover, the strength of the mechanical stimulation of the corresponding mode strongly depends on the PZT characteristics and the configuration used to transport the acoustic wave to OMO.

In order to characterize the lock range as a function of injection strength independent of acoustic excitation efficiency in a specific configuration, we define the ratio between the effective force (F_{A}) inserted on the mechanical resonator by the acoustic wave and the optical force (F_{RP}) due to radiation pressure as $\eta = F_{\mathrm{A}}/F_{\mathrm{RP}}$. These forces can only be measured through the response of the corresponding mechanical mode and the resulting optical modulation. As shown in Ref. 6, in general the measured optical modulation depth (M) is related to the radial oscillation amplitude (ΔR) of the optical path length through $\Delta R = (M \times D)/(2 \times \Gamma \times Q_L)$ where Q_L is the loaded quality factor of the optical mode, M is the measured modulation depth, D is the diameter of the microtoroid and Γ is the corresponding modulation transfer function that is ~1 when $f_{OMO} << c/\lambda_0 Q_L$ (a condition valid for both modes studied here). As such we use relative radial oscillation amplitude ratio or $\Delta R_{PZT}/\Delta R_{RP}$ as η. Here ΔR_{RP} is the radial oscillation amplitude of the microtoroid driven by the radiation pressure ($P_{o,in} > P_{th}$) in the absence of external acoustic excitation ($P_{PZT} = 0$). ΔR_{PZT} is the radial oscillation amplitude of the microtoroid induced by the acoustic wave (generated by the PZT) in the absence of selfsustained optomechanical oscillations ($P_{o,in} < P_{th}$). In other words, ΔR_{PZT} and ΔR_{RP} are the radial oscillation amplitudes of the optical path length generated by acoustic energy and radiation pressure transferred to the corresponding mechanical mode respectively. Since below threshold the effective loss for a mechanical mode and therefore its response depend on $P_{o,in}$, η is equal to $\Delta R_{PZT}/\Delta R_{RP}$ only if ΔR_{PZT} is measured below but close to threshold so that mechanical loss is almost canceled by the optomechanical gain (similar to above threshold condition where ΔR_{RP} is measured). Note that above threshold ΔR is dominated by radiation pressure so ΔR_{PZT} has to be measured below threshold.

Using the above mentioned relation we have calculated ΔR_{RP} for each $P_{o,in}$ ($>P_{th}$) by measuring M when $P_{PZT} = 0$. Then for each P_{PZT} we calculated ΔR_{PZT} by measuring M while keeping $P_{o,in}$ below but close to threshold ($\sim 0.8 \times P_{th}$) to prevent radiation pressure driven oscillation. Since ΔR_{PZT} is a measure of the actual acoustic energy transferred to the corresponding mechanical mode, behavior of the lock range as a function of η is independent of efficiency of the PZT and acoustic energy transfer. Once the lock range is characterized as a function of η, finding the optimal configuration and actuation mechanism for minimizing the RF power required for achieving certain value of η can be addressed separately using acoustic-mechanical design and optimization techniques.

Based on general theory of injection locking for self-sustained electronic oscillators [8, 12, 13] and the above explanation, the lock range (Δf_{lock}) can be written as:

$$\Delta f_{lock} = \Delta f_{mech} \frac{\Delta R_{PZT}}{\Delta R_{RP}} [1 - (\frac{\Delta R_{PZT}}{\Delta R_{RP}})^2]^{-\frac{1}{2}}. \tag{4.1}$$

where the Δf_{mech} ($\approx f_{\mathrm{OMO}}/Q_{\mathrm{mech}}$) is the intrinsic linewidth of the passive mechanical resonator.

Figure 4.6(a) and 4.6(b) show the measured lock range as a function of η (= $\Delta R_{\mathrm{PZT}}/\Delta R_{\mathrm{RP}} = F_{\mathrm{A}}/F_{\mathrm{RP}}$) for the mechanical mode-1 (part-a) and mode-2 (part-b) using different acoustic excitation configurations. For the mode-1, $f_{\mathrm{OMO,1}} = 2.7$ MHz and $\Delta f_{\mathrm{mech}} =$ 23 kHz, for mode-2, $f_{\mathrm{OMO,2}} = 15.8$ MHz and $\Delta f_{\mathrm{mech}} = 44$ kHz. The solid lines are the theoretical prediction based on Eq. (4.1). The uncertainty of η is proportional to $[\Delta R_{\mathrm{PZT}} \times \delta(\Delta R_{\mathrm{RP}}) - \Delta R_{\mathrm{RP}} \times \delta(\Delta R_{\mathrm{PZT}})]/(\Delta R_{\mathrm{RP}})^2$. ΔR_{PZT} and ΔR_{RP} are calculated based on measured modulation depth and therefore detected modulated optical power ($P_{\mathrm{mod,RF}}$); so $\delta(\Delta R_{\mathrm{RP}})$ and $\delta(\Delta R_{\mathrm{PZT}})$ are proportional to $\delta P_{\mathrm{mod,RF}}$ that was about ±0.8 dBm (standard deviation) for all measurements. The error bars along vertical axis corresponds to 2 × standard deviation (±500 Hz) for lock range measurement.

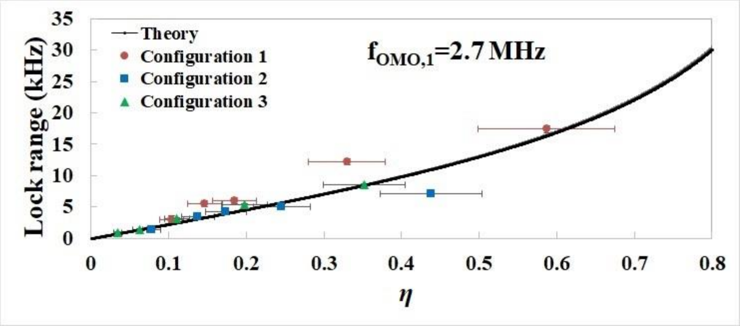

(a)

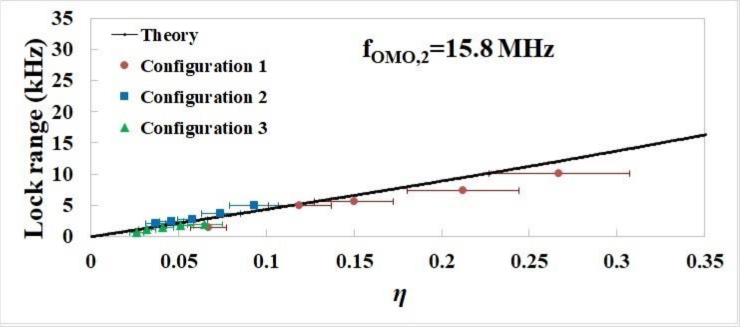

(b)

Fig. 4.6. Measured lock range plotted against the relative radial displacement ratio (η) based on different configurations for: (a) Mode-1 ($f_{OMO,1}$=2.7 MHz) and (b) Mode-2 ($f_{OMO,2}$ =15.8 MHz). The solid lines are theoretical estimation based on Eq. (4.1).

4.5 Phase locking of optomechanical oscillator via acoustic waves

In order to verify phase locking associated with the observed frequency locking between OMO and the RF oscillator, we have measured their phase difference using a lock-in amplifier (SR844, from Stanford Research). Figure. 4.7(a) and 4.7(c) show the temperal behavior of the measured phase difference between the RF signal driving the PZT and the OMO output ($\Delta\phi = \phi_{OMO} - \phi_{RF}$) in the presence (ON) and absence (OFF) of the injection signal when $f_{PZT} = f_{OMO}$. While based on basic injection locking theory [12, 13] the phase difference between OMO and the injected signal should be zero when $f_{PZT} = f_{OMO}$ (assuming P_{PZT} is large enough to lock the OMO), here $\Delta\phi$ is -100° and 90° at $f_{PZT} = f_{OMO}$. These phase off-sets are associated with delay between the injection signal (the acoustic excitation fed to the toroid) and the RF drive due to propagation through RF cables, response time of the PZT (RC time constant) and acoustic wave propagation from the PZT to the toroidal section of the microresonator. Figure 4.7(b) and 4.7(d) show the variation of $\Delta\phi$ as a function of frequency detuning ($\Delta f = f_{OMO} - f_{PZT}$) within 5.54 kHz and 2 kHz lock range.

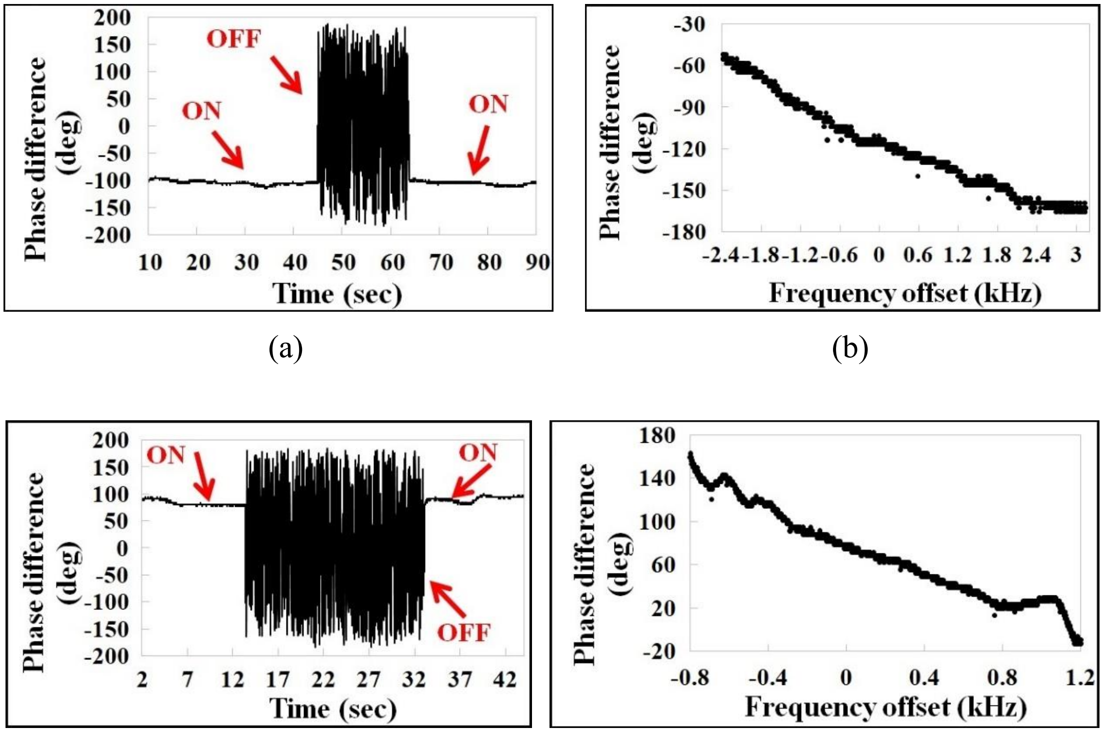

(a) (b)

(c) (d)

Fig. 4.7. Left column: temporal behavior of the measured phase difference between RF signal fed to PZT and the OMO optical output power ($\Delta\phi = \phi_{OMO} - \phi_{RF}$) in the presence (ON) and absence (OFF) of injection signal when $f_{PZT} = f_{OMO}$ for (a) the mode-1 measured using configuration-1 and (c) the mode-2 measured using configuration-2. Right column: Measured $\Delta\phi$ plotted against $f_{OMO} - f_{PZT}$ for (b) Mode-1 measured using configuration-1 and (d) Mode-2 measured using configuration-2. Here P_{PZT} = -42 dBm and η = 0.147 for (a) and (b), and P_{PZT} = -9 dBm and η = 0.037 for (c) and (d).

4.6 Modeling of injection locking using classical theory of the optomechancial oscillations and COMSOL FEM

We have used the time-domain classical theory of optomechanical oscillation [22, 23] to calculate the lock range as a function of the P_{PZT}. The optomechanical oscillation can be described by two coupled differential equations that govern the temporal variation of radial component of the microtoroid displacement and the circulating (resonant) optical power. These two equations are coupled through radiation pressure of the circulating optical power that acts as a radial force on the microtoroid and is controlled by the optical frequency detuning ($\Delta\omega_0 = \omega_{\mathrm{laser}} - \omega_0$, where ω_0 is the resonant frequency of the selected optical mode). The presence of an acoustic excitation is equivalent to an additional harmonic external force ($F_A(t) = F_{A0}\cos(\Omega_{\mathrm{PZT}}t)$) that is added to the optical force (radiation pressure). The resulting coupled differential equations can be written as:

$$m_{eff}\frac{d^2r}{dt^2} + b\frac{dr}{dt} + kr = \frac{2\pi|A(t)|^2}{c} + F_{A0}\cos\left(\Omega_{PZT}t\right). \tag{4.2}$$

$$\frac{dA}{dt} + A\left\{\frac{\alpha c}{n} - i\left[\Delta\omega_0 + \frac{\omega_0 r(t)}{R}\right]\right\} = iB\sqrt{\frac{\alpha c}{n\tau_0}}. \tag{4.3}$$

here m_{eff} is the effective mass associated with the radial component of the corresponding mechanical mode, r(t) is the radial displacement of the microtoroid, b is the mechanical dissipation (that can be inferred from the measured sub-threshold acoustic bandwidth), k is the spring constant, $|A(t)|^2$ is the circulating optical power, n is the refractive index of silica at 1550 nm wavelength, α is the optical loss in the cavity, R is the radius of the optical path (~radius of the microtoroid), B is the input pump field (normalized such that $|B|^2$ is the optical pump power). F_{A0} is the amplitude of the equivalent radial force corresponding to the acoustic excitation.

In order to calculate the optomechanical oscillation frequency as a function of the RF power that drives the PZT (P_{PZT}) we have calculated the relation between F_{A0} and P_{PZT}

using Finite Element Modelling (See **Appendix A**). Since modeling configuration-2 and -3 requires a relatively large model and therefore long simulation time, we have limited our calculation to mode-1 excited via configuration-1. The cylindrical symmetry of configuration-1 allows reducing the simulated zone without significant impact on the outcome. The amplitude of the radial force inserted on the microtoroid when the PZT is driven at $\Omega_{\mathrm{PZT}} = 2\pi f_{\mathrm{OMO},1}$ can be written as (the derivation is in **Appendix A**):

$$F_{A0} = 3.3 \times 10^{-9} \times 10^{(P_{PZT}/20)}. \tag{4.4}$$

here P_{PZT} is in dBm and it has been assumed that impedance of the RF source and the PZT are 50 and ~32 Ω respectively (based on the actual PZT and signal generator used in our experiment).

Figure 4.8(a) shows the calculated lock range as a function of P_{PZT} using Eqs. (4.2) - (4.4). The red dots are experimental results for the 1st mode and configuration-1 (extracted from Fig. 4.4). The good agreement between experimental and calculated results shows the validity of our assumptions and therefore the usefulness of this simple model for predicting the locking behavior of the optomechanical systems. Figure 4.8(b) shows the calculated the phase difference between $F_A(t)$ and $r(t)$ ($= r_0\cos(\Omega_{\mathrm{PZT}}t + \gamma)$) for mode-1 and configuration-1 using the same equations, here $P_{\mathrm{PZT}} = -42$ dBm, and all parameters are the same as that used in the experiment to obtain Figs. 4.7(a) and 4.7(b).

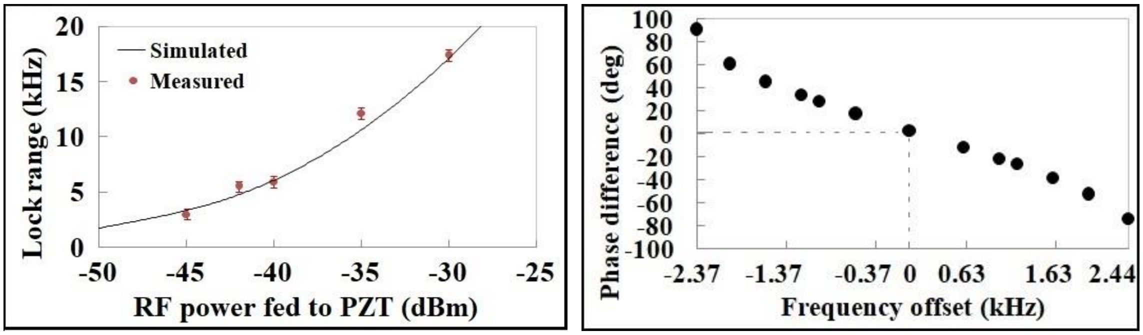

(a) (b)

Fig. 4.8. (a) Calculated (solid line) and measured (red dots) lock-range for mode-1 injection-locked using configuration-1. Here, $b = 0.92\times10^{-6}$ kg/s, $n = 1.46$, pump laser frequency is fixed 0.38 FWHM larger than the resonant frequency of the toroid, so $\Delta\omega_0 = 0.38(\omega_0/Q_{L1})$, ω_0 can be inferred from λ_{01}. Error bars along vertical axis correspond to 2 × standard deviation (±500 Hz) for the lock range measurement. (b) Calculated phase difference between the F_A(t) and r(t) for mode-1 and configuration-1 using Eqs. (4.2) - (4.4), here $P_{PZT} = -42$ dBm.

Note that in the experiment we measured the phase difference ($\Delta\phi$) between r(t) and V_{RF}(t) ($=V_{RF,0}\cos(\Omega_{PZT}t-\theta)$), so although the behavior of the simulated (Fig. 4.8(b)) and measured (Fig. 4.7(b)) results are in good agreement, unlike the measured phase offset, the simulated phase offset is zero ($\gamma = 0$ at $f_{PZT} = f_{OMO,1}$). While the relation between amplitude of F_A(t) and V_{RF}(t) can be estimated using Finite Element Modeling, their phase difference ($\Delta\phi$) involves more advanced modeling tools and computational resources, so by using $\Delta\phi = \gamma$ instead of $\Delta\phi = \gamma + \theta$ in our simulation we have ignored the delay between the RF voltage applied on the PZT and the acoustic excitation experienced by the microtoroid (we assume $\theta = 0$).

4.7 Summary

An OMO can be locked to an electromechanical transducer via acoustic waves transmitted by the electromechanical transducer and received by the OMO. Even without acoustic impedance matching and optimizing the energy transfer between the transducer and the OMO, a lock range of 17 kHz has been achieved with only 1 microwatt (-30 dBm) RF power. We expect the required RF power for a carefully designed impedance matched system to be significantly lower. For example, by eliminating the acoustic reflection between PZT and the silicon chip in configuration-1 (using an impedance matching layer), mode-1 can be locked within 17 kHz range with an RF power as low as 270 nano watts. Note that even in the absence of acoustic loss only a small portion of the transmitted acoustic energy is absorbed by the OMO (due to the small interaction cross-section of the OMO). As such with the same level of RF power multiple OMOs on a chip can be locked to a single RF source. Moreover, employing on-chip electromechanical transducers based on piezo electric thin films and interdigitated electrodes, enables excitation of various types of surface acoustic waves that may transfer the acoustic energy to the OMO more efficiently. Additionally, integrated acoustic waveguides and photonic crystals can be used to improve the directivity of the acoustic energy transferred to the target OMO. Using this approach, the acoustic energy from one transducer can be distributed among several OMOs or multiple transducers can be independently locked to groups of OMOs. These possibilities combined with the fact that injection locking via acoustic waves does not require power hungry optical modulators and direct physical contact with the OMO, makes this approach superior to the previously demonstrated techniques (based on optical modulation and direct application of electrostatic force) in particular for locking nanoscale OMOs and synchronization of OMO networks. While the physics and behavior of a network of synchronized OMOs has yet to be explored, theoretical studies on network of synchronized oscillators has revealed very interesting properties that are promising for communication and sensing applications. For example, it has been shown that the frequency precision of a network of regenerative oscillators perturbed by *N* independent noise sources is improved by a factor of *N* [26].

While we did not measure the phase-noise of the locked OMO (due to lack of access to a phase-noise analyzer), based on previous results (injection locking both based on optical modulation [8] and direct electrostatic force [17]), it is clear that in addition to synchronization and frequency control, injection locking via acoustic wave can reduce the phase noise of the OMO proportional to the power and phase noise of the RF source that generates the acoustic wave [27, 28].

As evident from Eq. (4.1), the lock range for an acoustically injection locked OMO is limited by its mechanical quality factor. The tradeoff between the lock range and mechanical loss (and therefore the threshold power) in the system is fundamental and may impose a limitation for certain applications. However, we expect synchronization to be more important than wide range frequency tuning in most applications. For example, it has reported that the phase difference between two synchronized oscillators, which that is highly sensitive to the frequency mismatch between oscillators, can be used to detect the changes of certain physical parameters [29, 30] (also see chapter 7); considering that single OMO has been used for sensing [3, 4], acoustically injection locked OMO, by looking at the phase difference change caused by the measurand, could exhibit enhanced sensitivity for sensing when compared with single OMO based sensor which looks at the frequency change caused by the measurand [31]. Besides, injection locking of OMO via acoustic wave may enable the possibility to selectively control the optomechanical gain for different mechanical modes; In other words, one may be able to select the dominant mode of an OMO (from a family of modes supported by OMO), by changing the frequency of the injected acoustic signal. The selected optomechanical mode may dominate the OMO spectrum even after turning off the acoustic excitation; in such case OMO can potentially serve as a type of "non-volatile" optomechanical memory [32] or enabling the exploration of normally inaccessible stable dynamical attractors of the system [33, 34].

4.8 Reference

[1] M. Hossein-Zadeh, and K. J. Vahala, "Photonic RF down converter based on optomechanical oscillation," *IEEE* Photon. Technol. Lett., **20**(4), 234-236 (2008).

[2] F. F. Liu and M. Hossein-Zadeh, "Characterization of Optomechanical RF frequency Mixing/Down-Conversion and its Application in Photonic RF Receivers," J. Lightwave. Technol., **32**(2), 309-317 (2014).

[3] F. Liu, S. Alaie, Z. C. Leseman, and M. Hossein-Zadeh, "Sub-pg mass sensing and measurement with an optomechanical oscillator," Opt. Express., **21**(17), 19555–19567 (2013).

[4] W. Yu, W. C. Jiang, Q. Lin, and T. Lu, "Cavity optomechanical spring sensing of single molecules," Nat. Commun., **7**, Art. no. 12311 (2016).

[5] H. Rokhsari, T. J. Kippenberg, T. Carmon, and K. J. Vahala, "Theoretical and experimental study of radiation pressure induced mechanical oscillations (parametric instability) in optical microcavities," *IEEE* J. Sel. Top. Quantum. Electron., **12**(1), 96-107 (2006).

[6] M. Hossein-Zadeh, H. Rokhsari, A. Hajimiri, and K. J. Vahala, "Characterization of a radiation-pressure-driven micromechanical oscillator," Phys. Rev. A., **74**(2), Art. no. 023813 (2006).

[7] K. Huang and M. Hossein-Zadeh, "Direct stabilization of optomechanical oscillators," Opt. Lett., **42**(10), 1946–1949 (2017).

[8] M. Hossein-Zadeh and K. J. Vahala, "Observation of injection locking in an optomechanical rf oscillator," Appl. Phys. Lett., **93**(19), Art. no. 191115 (2008).

[9] J. J. Zheng, Y. Li, N. Goldberg, M. McDonald, X. S. Luan, A. Hati, M. Lu, S. Strauf, T. Zelevinsky, D. A. Howe, and C. W. Wong, "Feedback and harmonic locking of slot-type optomechanical oscillators to external low-noise reference clocks," Appl. Phys. Lett., **102**(14), Art. no. 141117 (2013).

[10] E. Gil-Santos, M. Labousse, C. Baker, A. Goetschy, W. Hease, C. Gomez, A. Lemaître, G. Leo, C. Ciuti, and I. Favero, "Light-Mediated Cascaded Locking of Multiple Nano-Optomechanical Oscillators," Phys. Rev. Lett., **118**(6), Art. no. 063605 (2017).

[11] M. Zhang, S. Shah, J. Cardenas, and M. Lipson, "Synchronization and phase noise reduction in micromechanical oscillator arrays coupled through light," Phys. Rev. Lett., **115**(16), Art. no. 163902 (2015).

[12] R. Adler, "A study of locking phenomena in oscillators," *in Proc. IEEE Conference*, **61**(10), 1380–1385 (1973).

[13] B. Razavi, "A study of injection locking and pulling in oscillators," *IEEE* J. Solid-state Circuits., **39**(9), 1415–1424 (2004).

[14] H. L. Stover and W. H. Steier, "Locking of laser oscillators by light injection," Appl. Phys. Lett., **8**(4), 91–93 (1966).

[15] T. Li, T. Y. Bao, Y. L. Zhang, C. L. Zou, X. B. Zou, and G. C. Guo, "Long-distance synchronization of unidirectionally cascaded optomechanical systems," Opt. Express., **24**(11), 12336–12348 (2016).

[16] E. Amitai, N. Lörch, A. Nunnenkamp, S. Walter, and C. Bruder, "Synchronization of an optomechanical system to an external drive," Phys. Rev. A., **95**(5), Art. no. 053858 (2017).

[17] C. Bekker, R. Kalra, C. Baker, and W. P. Bowen, "Injection locking of an electro-optomechanical device," Optica, **4**(10), 1196–1204 (2017).

[18] J. Chan, M. Eichenfield, R. Camacho, and O. Painter, "Optical and mechanical design of a zipper photonic crystal optomechanical cavity," Opt. Express., **17**(5), 3802-3817 (2009).

[19] H. Kaviani, C. Healey, M. Wu, R. Ghobadi, A. Hryciw, and P. E. Barclay, "Nonlinear optomechanical paddle nanocavities," Optica, **2**(3), 271-274 (2015).

[20] W. C. Jiang, X. Lu,J. Zhang, and Q. Lin, "High-frequency silicon optomechanical oscillator with an ultralow threshold," Opt. Express., **20**(14), 15991-15996 (2012).

[21] S. Tallur, S. Sridaran and S. A. Bhave, "A monolithic radiation pressure driven, low phase noise silicon nitride opto-mechanical oscillator," Opt. Express., **19**(24), 24522-24529 (2011).

[22] H. Rokhsari, T. J. Kippenberg, T. Carmon, and K. J. Vahala, "Radiation pressure driven micro-mechanical oscillator," Opt. Express., **13**(14), 5293-5301 (2005).

[23] T. Carmon, H. Rokhsari, L. Yang, T. J. Kippenberg, and K. J. Vahala, "Temporal Behavior of Radiation-Pressure-Induced Vibrations of an Optical Microcavity Phonon Mode," Phys. Rev. Lett., **94**(22), Art. no. 223902 (2005).

[24] T. J. Kippenberg, H. Rokhsari, T. Carmon, A. Scherer, and K. J. Vahala, "Analysis of Radiation-Pressure Induced Mechanical Oscillation of an Optical Microcavity," Phys. Rev. Lett., **95**(3), Art. no. 033901 (2005).

[25] T. J. Kippenberg, and K. J. Vahala, "Cavity Opto-Mechanics," Opt. Express., **15**(25), 17172-17205 (2007).

[26] M. C. Cross, "Improving the frequency precision of oscillators by synchronization," Phys. Rev. E., **85**(4 Pt 2), Art. no. 046214 (2012).

[27] E. Shumakher and G. Eisenstein, "On the noise properties of injection locked oscillators," *IEEE* Trans. Microw. Theory Tech., **52**(5), 1523–1537 (2004).

[28] P. Maffezzoni and D. D'Amore, "Phase noise reduction in oscillators via small signal injection," *IEEE* Trans. Circ. Syst., **58**(10), 2498–2507 (2011).

[29] J. Juillard, A. Bonnoit, N. Barniol, A. Uranga, and G. Vidal-Álvarez, "A novel architecture for differential resonant sensing," Procedia Engineering, **87**, 1573-1576 (2014).

[30] J. Juillard, A. P. Prache, and N. Barniol, “Analysis of Mutually Injection-Locked Oscillators for Differential Resonant Sensing,” *IEEE* T. CIRCUITS-I., **63**(7), 1055-1066 (2016).

[31] K. Huang, and M. Hossein-Zadeh, “Detection and Sensing with Homogenous and Heterogeneous Coupled Oscillatory Systems,” Early Access, *IEEE* Sens. J., (2020).

[32] M. Bagheri, M. Poot, M. Li, W. P. H. Pernice, and H. X. Tang, “Dynamic manipulation of nanomechanical resonators in the high-amplitude regime and non-volatile mechanical memory operation,” Nat. Nanotechnol., **6**, 726-732 (2011).

[33] F. Marquardt, J. G. E. Harris, and S. M. Girvin, “Dynamical multistability induced by radiation pressure in high-finesse micromechanical optical cavities,” Phys. Rev. Lett., **96**(10), Art. no. 103901 (2006).

[34] A. G. Krause, J. T. Hill, M. Ludwig, A. H. Safavi-Naeini, J. Chan, F. Marquardt, and O. Painter, “Nonlinear radiation pressure dynamics in an optomechanical crystal,” Phys. Rev. Lett., **115**(23), Art. no. 233601 (2015).

Chapter 5

Acousto-optical transducer with optomechanical gain

5.1 Introduction

High sensitivity acoustic transducers are essential for a large variety of applications such as sonar systems, hydrophones, non-destructive evaluation of structures, medical imaging and diagnosis. While most commercial sensors use piezoelectric crystals for acousto-electric transduction, during the past two decades a significant amount of effort has been dedicated to the development of their optical counterparts [1-10]. These efforts have been fueled by the need for reduced size, cost and weight (in particular for sensor arrays) and eliminating the susceptibility to electromagnetic interference [1]. Fiber Bragg gratings (FBGs), miniaturized Fabry-Perot resonators and to a lesser extent other optical microcavities have been used for converting the acoustic energy to optical amplitude modulation [1-10]. The resonant nature of these configurations results in the sensitivity of the transmitted/reflected optical output power to the optical path length modulation induced by the acoustic perturbation. In the acousto-optical sensors based on FBGs [3–6], acoustic wave generates a strain field that modulates the refractive index (through photoelastic effect) and the grating period of the fiber (through the applied strain). As a result, the Bragg wavelength and the reflectance (or the transmittance) of the FBG will be modulated proportional to the acoustic wave amplitude. In acoustic transducers that use Fabry-Perot (FP) or other microcavities [7–10], acoustic wave modulates the cavity boundary and therefore the resonance frequencies of the cavity; at a fixed laser wavelength this resonant frequency modulation manifests itself as modulation of the reflected (or transmitted) optical power proportional to the acoustic wave amplitude.

In all the above mentioned platforms, the amplitude of modulated optical power for a given acoustic excitation scales linearly with the optical input power to the system.

As described in chapter 2, optomechanical resonators (OMRs) can sustain optical and mechanical resonance within the same structure and enable the strong coupling between them through radiation pressure and displacement of the cavity boundary [11–15]; as such they are natural candidates for acousto-optical transduction. In this chapter we explore the performance of optomechanical resonator (OMR) as an acousto-optical transducer in a regime where the radiation pressure is large enough to reduce the mechanical damping but does not exceed the threshold level for self-sustained optomechanical oscillation.

We estimate the acousto-optical response of an OMR using a theoretical framework developed based on time domain equations for the sub-threshold OMR and the general optical transfer function of the optical cavity (described in chapter 2). By adding the main sources of noise (i.e., thermo-mechanical, rin noise and photodetection noise), we also estimate the signal-to-noise ratio for a given acoustic pressure amplitude incident on the OMR, as a function of the characteristics of the laser, the OMR and the photodetector used in the detection system.

We show that when in the aforementioned regime, the acoustically induced optical modulation scales exponentially with the optical input power. As such by using a high quality (high-*Q)* OMR and the radiation pressure assisted acoustic detection, the required optical power for generating a target optical modulation depth by a given acoustic amplitude can be significantly reduced compared to conventional acousto-optical transducers (where mechanical damping and optical power are decoupled). While here we use a high-*Q* silica microtoroidal OMR for the proof of concept demonstration, a similar behavior is expected using other types of OMRs.

5.2 Experimental characterization of acousto-optical transduction assisted by optomechanical gain

Figure 5.1(a) shows the experimental arrangement used for characterizing the acousto-optical response of the microtoroidal OMR. The silica microtoroid is fabricated using a process described in chapter two. The silica microtoroid has a major diameter of D = 60 μm, minor diameter of d = 7 μm, and it is attached on top of a silicon pillar. The silicon pillar that has a shape close to a truncated cone, a diameter of D_p = 25 μm at the point of contact with the microtoroid and a height of 35 μm. The silica microtoroid and the silicon pillar are fabricated on a rectangular silicon chip (20 mm by 5 mm) with a thickness of 300 μm. Figure 5.1(b) shows the mechanical deformation associated with the first mechanical mode of the microtoroid calculated using finite element modeling (FEM). In our experiment, acoustic excitation frequency (f_A) is tuned to the resonant frequency of this mode (f_{mech} = 5.78 MHz). The optical power from a tunable laser (λ_{laser} ~ 1550 nm) is coupled to a high-*Q* Whispering-Gallery mode (WGM) of the microtoroidal optical cavity using a tapered silica fiber [12, 14]. The coupling gap between the tapered fiber and the microtoroid is controlled with a nanopositioner. The polarization and power of the pump laser are controlled using a polarization controller and a tunable attenuator. 10% of this output optical power is directed to an optical power meter to monitor the power level and 90% is fed to the fiber taper and coupled to the OMR. The transmitted optical power through the fiber taper is directed to a photodetector that generates a voltage proportional to the received optical power. This photo-voltage is measured using an oscilloscope and an electrical spectrum analyzer to characterize the optical modulation induced by the acoustic excitation.

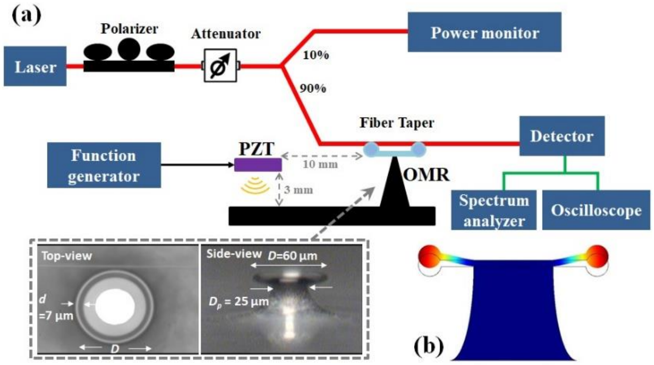

Fig. 5.1. (a) Experimental arrangement used for characterizing the OMR based acousto-optical transducer. The inset is the micrograph of the silica microtoroid. (b) Calculated mechanical deformation associated with the 1st mechanical mode of the OMR which has a resonant frequency f_{mech}=5.780 MHz (the deformation and the resonant frequency were calculated using finite element modeling).

The acoustic wave only excites one of the mechanical modes of microtoroid that has resonant frequency almost equal to that of the acoustic wave. As illustrated in Fig. 5.1(b) the resulting mechanical motion modulates the radius of the microtoroid and hence the optical path length and the transmitted optical power. Note that the mechanical resonant frequency of the fiber taper is much lower (kHz range) and therefore its movement due to acoustic wave is negligible. As such the only dominant response of the system to the incident acoustic wave is the modulation of the resonant frequency of the optical WGM inside the OMR.

First, we measured the optomechanical properties of the OMR in the absence of acoustic excitation. The selected optical WGM mode had a loaded optical quality factor ($Q_L = \lambda_{WGM}/\delta\lambda_L$) of 8.3×10^6 and the first mechanical mode had a quality factor (Q_{mech}) of 578. The threshold power (P_{th}) for self-sustained optomechanical oscillation of this mode (at 5.78 MHz) was 68 μW. Using these measurements and FEM modeling we estimated an effective mass (m_{eff}) of 400 pg, the optomechanical coupling factor (g_{OM}) of 6.4 GHz/nm and vacuum optomechanical coupling rate (g_0) of 386 Hz for the first mechanical mode coupled to the selected WGM. To measure the acoustic response, a piezoelectric disk (PZT) with dimension of Ø10 mm × 0.4 mm was placed at a vertical distance of 3 mm above the chip and 10 mm away from the OMR. The PZT had a resonance frequency of $f_{PZT} \sim 5.62$ MHz corresponding to its thickness mode; as such the acoustic wave was emitted mainly perpendicular to the chip (see Fig. 5.1(a)). The PZT was driven by a function generator and its oscillation amplitude was almost constant within the measurement range of 5.5 MHz to 6.0 MHz.

The acoustic pressure applied on the silicon chip by the PZT is estimated using FEM (COMSOL software). Figure 5.2(a) shows a plot of the simulated pressure field distribution when an RF power of -10 dBm (P_{PZT} = -10 dBm) excites the thickness mode of the PZT. Figure 5.2(b) shows the pressure on the silicon chip right below the PZT (red point in Fig. 5.2(a)) plotted against RF input power (P_{PZT}) from the function generator.

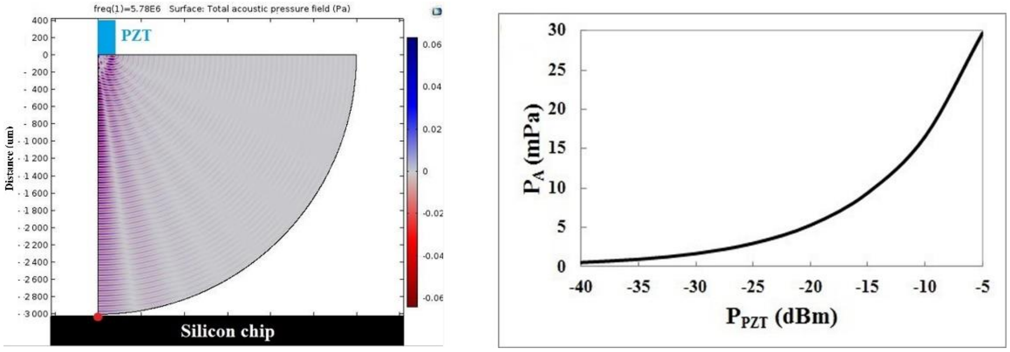

(a) (b)

Fig. 5.2. (a) Simulated acoustic pressure distribution in air generated by the PZT when P_{PZT} = -10 dBm and f_{A} = 5.780 MHz. (b) Calculated acoustic pressure amplitude (P_{A}) on the top surface of the silicon chip right below the PZT (red point in part-a) plotted against P_{PZT}.

Next, the acoustic response of the system was characterized by measuring the acoustically induced optical modulation depth near the mechanical resonance at different acoustic pressures and optical input power levels (P_{in}). For all measurements the laser was blue detuned from the cavity resonance with a normalized detuning ($\Delta\lambda = (\lambda_{\mathrm{laser}} - \lambda_{\mathrm{res}})/\delta\lambda_{\mathrm{laser}}$) of about -0.7. Figure 5.3(a) shows the detected voltage (which is proportional to the optical modulated optical power) as a function of the normalized input optical power ($P_{\mathrm{in}}/P_{\mathrm{th}}$) when acoustic pressure amplitude is 16.56 mPa. The response is measured at $f_{\mathrm{A}} = f_{\mathrm{mech}}$, $f_{\mathrm{mech}} \pm 1$ kHz and $f_{\mathrm{mech}} \pm 2$ kHz.

The solid lines in Fig. 5.3(a) are the calculated results based on the coupled differential equations that govern the dynamics of optical and mechanical modes in OMR [12–16]. The exponential growth of the detected voltage with optical input power (especially when $f_{\mathrm{A}} = f_{\mathrm{mech}}$) is a signature of the optomechanical gain (as elaborated in section 5.3). Note that in the absence of optomechanical gain, the modulated optical power at a given acoustic pressure amplitude grows linearly with P_{in} (as evident from previously reported results for acousto-optical transducers based on FBG and FP [3–9]).

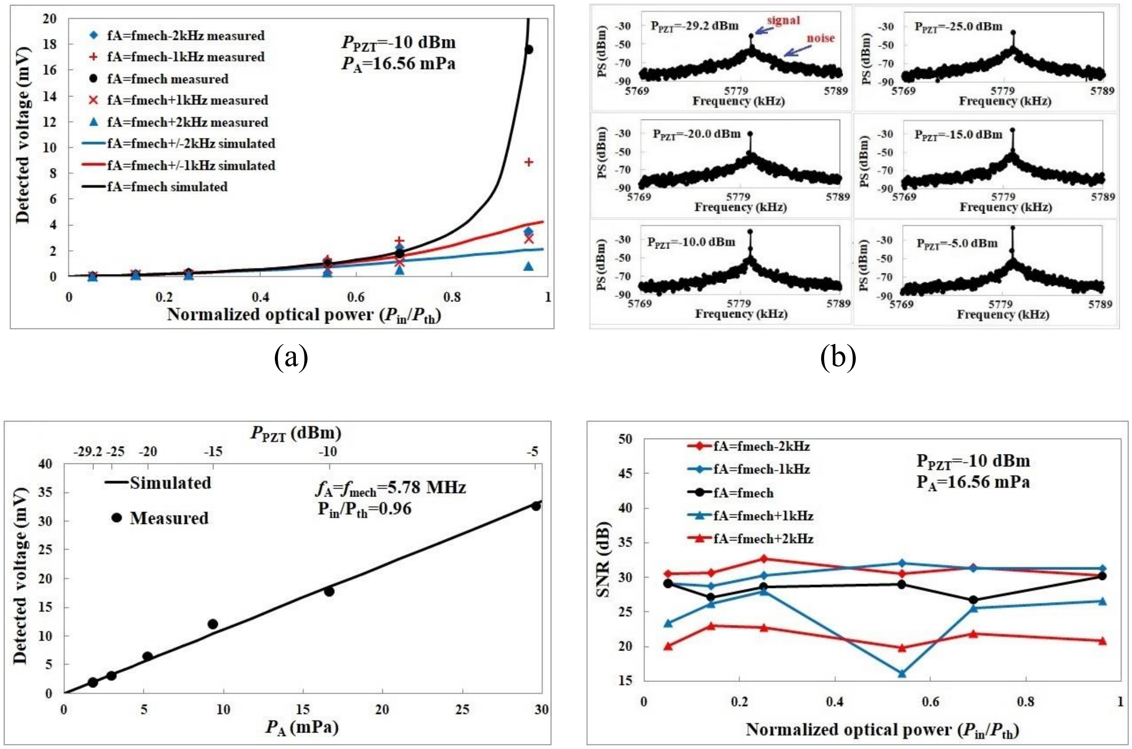

(a) (b)

(c) (d)

Fig.5.3. (a) Measured (dots) and simulated (solid lines) voltage as a function of the normalized input optical power at different acoustic frequencies (f_A). (b) Measured power spectrum (PS) as a function of the acoustic pressure amplitude (different PZT drive power) on the silicon chip when acoustic frequency f_A = 5.780 MHz and optical power P_{in} = $0.96P_{\mathrm{th}}$. (c) Measured (dots, peak values in Fig. 5.3(b)) and calculated (solid line) voltage signal plotted against the incident acoustic pressure amplitude. (d) Measured SNR as a function of the normalized optical power at different PZT drive frequency.

Figure 5.3(a) also shows that the acousto-optical response rapidly decays when the acoustic frequency is detuned away from f_{mech} (due to the narrow linewidth of the optomechanical gain). Figure 5.3(b) shows the measured power spectrum (PS) of the modulated output of the OMR as a function of the acoustic pressure amplitude that impinges on the silicon surface right below the PZT transducer (red point in Fig. 5.2(a)). Here the sensitivity of the system is maximized by increasing the optical input power to

$P_{\text{in}} = 0.96 \times P_{\text{th}}$. The amplitude of the signal, that appears as a peak (at $f_A = 5.78$ MHz) above the background noise, is proportional to acoustic pressure amplitude. Figure 5.3(c) shows the detected peak voltages (from Fig. 5.3(b)) plotted against the incident acoustic pressure amplitude (the solid line is calculated). The maximum sensitivity of the transducer is estimated to be 1.11 V/Pa. Given the photodetector response (4.2×10^4 V/W) and the detected optical power level in the absence of acoustic excitation ($P_{\text{det}} \sim 3\ \mu$W) in this measurement, the OMR can generate a modulation depth ($P_{\text{mod}}/P_{\text{det}}$) of 14% induced by a pressure wave with an amplitude of 16 millipascal. Figure 5.3(d) shows the measured signal-to-noise ratio (SNR) as a function of normalized optical power when the acoustic pressure is 16.56 mPa.

5.3 Analysis of the performance of OMR based acousto-optical transducer

In this section, the response and noise performance of the OMR based acousto-optical transducer are analyzed using a modified equation of motion for the mechanical mode (in the presence of thermal noise and optomechanical coupling) and the optical transmission function of the optical microresonator.

5.3.1 Acousto-optical transduction in OMR

1) *Mechanical motion of the OMR*

As described in chapter 2, when the optical pump power is below the threshold optical power ($P_{\text{in}} < P_{\text{th}}$), the optomehcanical gain is not sufficient to induce the self-sustained oscillation and the dynamics of the mechanical mode can be described by the harmonic oscillator equation where the damping factor is replaced with an effective damping factor (Γ_{eff}) decreases as P_{in} is increased due to optomechanical gain [11]:

$$m_{eff}\frac{d^2r(t)}{dt^2} + m_{eff}\Gamma_{eff}\frac{dr}{dt} + m_{eff}\Omega_m^2 r(t) = F_{appl}. \tag{5.1}$$

$$\Gamma_{eff} = \Gamma_m(1 - \frac{P_{in}}{P_{th}}). \tag{5.2}$$

F_{appl} is the sum of all the forces applied on the OMR; in the experiment described above, it includes the forces induced by acoustic signal, thermal (Brownian) noise and Back action noise.

1.1) *Motion caused by acoustic signal*

The relation between the equivalent acoustic force (F_{A}) and the RF power provided to the PZT (P_{PZT}) is (see **Appendix A**):

$$F_A(f) = C \times 10^{\frac{P_{PZT}(f)}{20}}. \tag{5.3}$$

here $C = (\eta/\zeta)/\sqrt{10}$, where $\zeta = d_{\text{r0}}/F_{\text{A0}}$ and $\eta = d_{\text{r0}}/V_{\text{RF,0}}$. ζ and η can be approximated using the method described in **Appendix A**. The amplitude of the mechanical oscillation induced by the equivalent acoustic force can be written as:

$$r_A(f) = \frac{F_A(f)}{m_{eff}\sqrt{((2\pi f_m)^2-(2\pi f)^2)^2+(2\pi f)^2{\Gamma_{eff}}^2}}. \tag{5.4}$$

where m_{eff} and f_{m} are the effective mass and the frequency of the excited mechanical mode of the OMR.

1.2) *Motion caused by thermal Brownian noise*

As mentioned in chapter 2, the thermal Brownian force can be expressed as:

$$F_{th} = \sqrt{4K_B BT m_{eff}\Gamma_m}. \tag{5.5}$$

note here, the B is the resolution bandwidth of the electrical spectrum analyzer that used for the measurement. The resulting thermo-mechanical excitation amplitude can be written as:

$$r_{th}(f) = \frac{\sqrt{4K_B BTm_{eff}\Gamma_m}}{m_{eff}\sqrt{((2\pi f_m)^2-(2\pi f)^2)^2+(2\pi f)^2{\Gamma_{eff}}^2}}. \tag{5.6}$$

1.3) *Motion caused by Back action noise*

As described in chapter 2, the mechanical noise associated with back action noise can be expressed as:

$$r_{ba} = \frac{2\hbar g_{OM}}{m_{eff}}\sqrt{\frac{2n_{cav}}{\kappa_{tot}}}\frac{1}{\sqrt{((2\pi f_m)^2-(2\pi f)^2)^2+(2\pi f)^2{\Gamma_{eff}}^2}}. \tag{5.7}$$

2) *Derivation of the acousto-optical transduction of OMR*

Using the coupled mode theory (CMT) [17], it can be shown that the optical transmission through a waveguide that is coupled to a WGM microresonator can be written as [16]:

$$T(\Delta) = \frac{(\frac{\omega_0}{2Q_e}-\frac{\omega_0}{2Q_0})^2+\Delta^2}{(\frac{\omega_0}{2Q_e}+\frac{\omega_0}{2Q_0})^2+\Delta^2}. \tag{5.8}$$

where ω_0 is the resonant frequency of the WGM, $\Delta = \omega_{laser} - \omega_0$ is the laser-cavity frequency detuning, ω_{laser} is the frequency of the input optical wave, Q_e is the external quality factor and Q_0 is the intrinsic quality factor. If the OMR operates in the sideband unresolved regime ($\omega_0 \ll \kappa = \omega_{laser}/Q_0$), the intra-cavity field and hence the field transmitted through the cavity, adiabatically changes according to variation of $\Delta = \omega_{laser} - \omega_0$ induced by the radial component of the mechanical displacement (r). In an OMR detuning and mechanical displacement are related through, $\delta\Delta = g_{OM} \times r$. As such, the optical transmission change ΔT induced by a shift of the cavity resonance frequency can be estimated as:

$$\Delta T = \frac{dT}{d\Delta}\delta\Delta. \tag{5.9}$$

given that $P_{out} = T \times P_{in}$, the modulated transmitted optical power ($P_{m,o}$) that induced by r and received by the photodetector can be written as:

$$P_{m,o}(f) = \frac{dT}{d\Delta}\eta_{in}P_{in}g_{OM}r(f). \tag{5.10}$$

here, the η_{in} is the optical power transmission efficiency from the OMR cavity to the photodetector and P_{in} is the optical pump power. If the photodetector has a transimpedance gain of R_V (unit: V/W) and the generated photovoltage is measured using an electrical spectrum analyzer (ESA) with input impedance Z, the power spectral (PS, with unit: dBm) of the photoengraved electric power can be written as:

$$PS(f) = 10 \cdot log[\frac{(R_V P_{m,o}(f))^2}{Z} \cdot 1000]. \tag{5.11}$$

Using Eqs. (5.10) and (5.11) while replacing the r with the radial displacement induced by acoustic signal r_A, back action noise r_{ba} or thermal Brownian noise r_{th}, transmitted optical power modulation and the PS associated with the acoustic excitation, thermal noise and back action noise can be calculated separately.

5.3.2 Signal to noise ratio of the OMR based acousto-optical transducer

Eqs. (5.4), (5.6), (5.7), (5.10), and (5.11) can be used to estimate the PS of the OMR output in the presence of equivalent acoustic force (due to the incident acoustic pressure), thermal Brownian noise and back action noise. In addition to thermal and back action noise, the intensity noise (rin noise) of the laser that provides the optical input power to the OMR and the photodetection noise also contribute in the total noise in the OMR based acousto-optical transducer.

The laser intensity noise can be quantified using relative intensity noise. The resulting variation of the optical output power incident on the photodetector $\langle \delta P_{\mathrm{rin}} \rangle$ is related to *RIN* through:

$$\langle \delta P_{rin} \rangle = \langle P_{\mathrm{det}} \rangle^2 \times 10 \times 10^{\frac{RIN}{10}} \times B. \qquad (5.12)$$

where P_{det} is the instantaneous optical power incident on the photodetector. The measured electrical power spectrum due to laser intensity noise can be expressed as:

$$PS_{RIN}(f) = 10 \cdot log[\frac{(R_V\sqrt{\langle \delta P_{rin}^2 \rangle})^2}{Z} \cdot 1000]. \qquad (5.13)$$

The photodetection noise comprises shot noise and the noise associated with the amplification of the detected photocurrent (thermo-electric noise). The variation of the photocurrent associated with shot noise ($\delta i^2_{\mathrm{shot}}$) can be written as:

$$\langle \delta i_{shot}^2 \rangle = \frac{2h\nu_l \langle P_{det} \rangle}{\eta_e} \times B. \qquad (5.14)$$

with the electrical power spectrum as:

$$PS_{shot}(f) = 10 \cdot log[\frac{(R_V\sqrt{\langle \delta i_{shot}^2 \rangle})^2}{Z} \cdot 1000]. \qquad (5.15)$$

here, ν_l is the frequency of the received optical photons, and η_e is the quantum efficiency of the photo detector. The total noise associated with the electronic circuit that receives and amplifies the photocurrent can be estimated using the noise equivalent power (NEP) of the photodetector.

$$\langle \delta P_{NEP}^2 \rangle = NEP^2 \times B. \tag{5.16}$$

with the electrical power spectrum as:

$$PS_{NEP}(f) = 10 \cdot log[\frac{(R_V\sqrt{\langle \delta P_{NEP}^2 \rangle})^2}{Z} \cdot 1000]. \tag{5.17}$$

Figure 5.4(a) shows the calculated (solid lines) and measured (orange dots) RF spectrum of the electrical noise power generated by an OMR based acousto-optical transducer in the absence of acoustic excitation (F_A= 0) when optical input power (P_{in}) is 0.14 × P_{th}. The properties of the laser, photodetector and OMR used in this transducer are summarized in Table 1.

Table 5.1. Parameters for the OMR based acousto-optical transducer experiment.

Parameter	m_{eff}	Γ_m	P_{th}	Ω_m	k_B	B
Value	400 pg	$2\pi\times12$ kHz	68 μW	$2\pi\times5.78$ MHZ	1.38×10^{-23} m^2 kg s^{-2} K^{-1}	11.2 Hz
Parameter	g_{OM}	C	Q_e	Q_0	ω_0	R_v
Value	6.4 GHz/nm	160 pN/V	2.8×10^7	1.2×10^7	$2\pi\times192$ THz	42000 V/W
Parameter	η_{in}	T	Z	RIN	NEP	η_e
Value	0.047	300 K	50 Ω	-118 dBc/Hz	2.5 pW/$\sqrt{Hz}$	0.76

Figure 5.4(a) shows the calculated RF spectrum associated with individual noise mechanisms that contribute in the total noise. Note that thermal and back action noise are indirectly measured through their impact on the transmitted optical power (modulated by mechanical displacement), as such their frequency dependence is similar to the opto-mechanical transfer function. Figure. 5.4(b) shows the calculated and measured electrical noise power spectrum of the same OMR based acousto-optical transducer at several values

of optical input power (P_{in}). As expected, the total noise increases proportional to optical input power and is dominated by thermal Brownian noise.

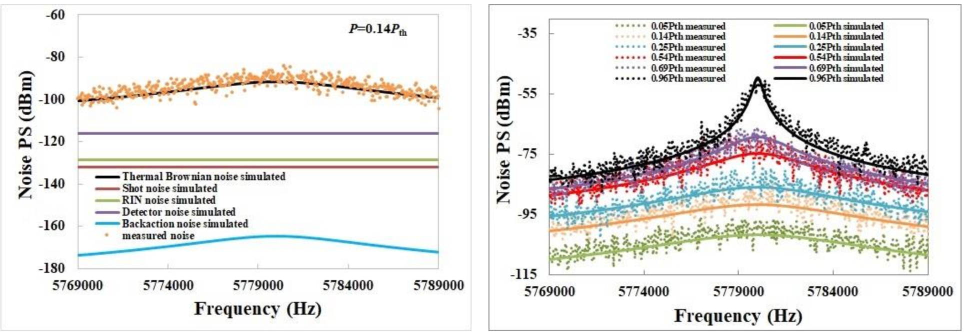

(a) (b)

Fig. 5.4. Calculated and measured noise spectrum of the optical power transmitted through OMR based acousto-optical transducer in the absence of acoustic excitation. (a) The noise generated via different noise mechanisms (calculated) and the measured total noise when $P_{\mathrm{in}} = 0.14P_{\mathrm{th}}$. (b) Calculated and measured total noise at various pump powers with $P_{\mathrm{th}} = 68\ \mu\mathrm{W}$.

As evident from Fig. 5.4(b) increasing the optical power, results in larger average noise that is amplified within a narrow bandwidth (around f_{OMO}) due to the increased optomehcanical gain (similar to experimentally observed behavior reported in Fig. 5.3(a) and (b)).

Figure. 5.5 shows the calculated and measured electrical power spectrum of the transducer in presence of acoustic excitation at different levels of optical input (pump) power and different acoustic frequencies. The colored dotted lines are the measured spectra while the black dots and the solid line are the calculated signals and the noise spectra respectively (calculated separately). For the most part, the measure and calculated spectra are in good agreement. However, in some spectra the measured signal is larger than the calculated signal when $f_{\mathrm{PZT}} < f_{\mathrm{mech}} = 5.780$ MHz and smaller than the calculated signal when $f_{\mathrm{PZT}} > f_{\mathrm{mech}}$. This is because for calculated signals the acoustic energy transfer efficiency is considered to be frequency independent and equal to value calibrated at the single frequency value $f_{\mathrm{PZT}} = f_{\mathrm{mech}} = 5.780$ MHz; in the experiment however, the frequency dependence of the impedance mismatch results in less loss at frequencies lower than 5.78 MHz and more at frequencies larger than 5.78 MHz.

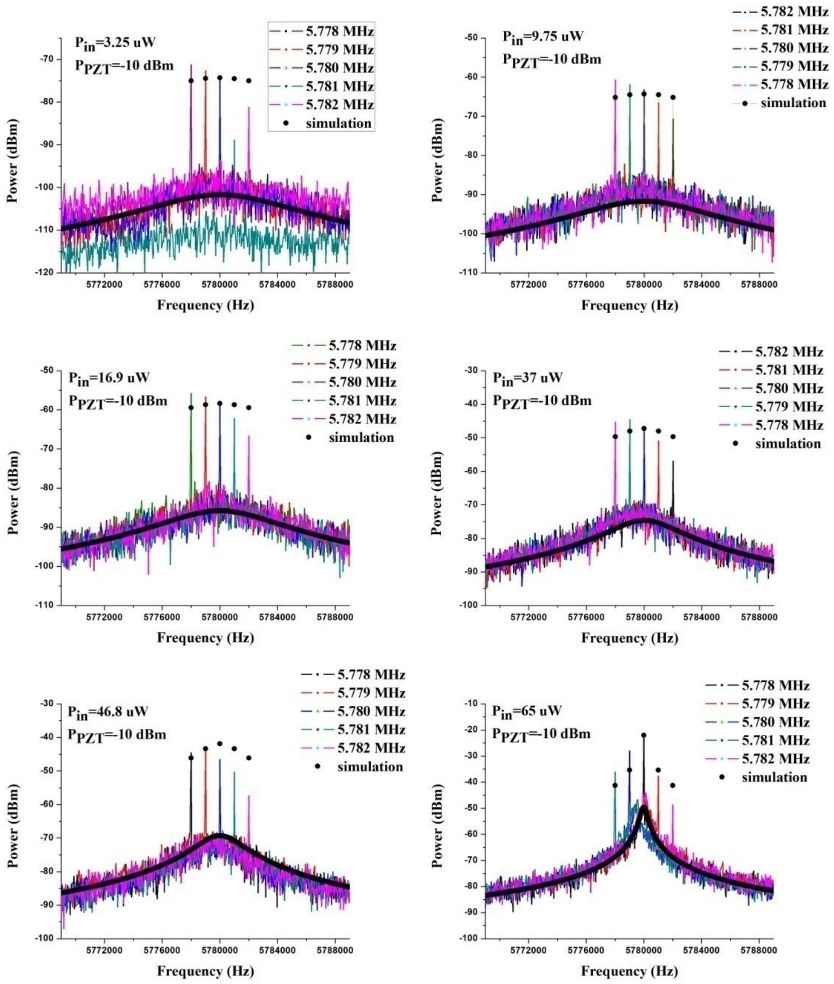

Fig. 5.5. Power spectrum of the transducer in the presence of acoustic excitation calculated and measured at different levels of optical input (pump) power and different acoustic frequencies when P_{PZT}=10 dBm. The colored dotted lines are the measured spectra while the black dots and the solid lines are the calculated signals and the noise spectra respectively (calculated separately).

Figure 5.6 shows calculated signal-to-noise ratio (SNR) at $f_{\mathrm{PZT}} = f_{\mathrm{A}} = f_{\mathrm{mech}}$, $f_{\mathrm{mech}} \pm$ 1kHz, $f_{\mathrm{mech}} \pm$ 2 kHz plotted versus normalized optical power. At very low optical power

($P_{in}/P_{th} < 0.1$) the noise is dominated by photodetector noise and *RIN* noise, for higher power levels, where the contribution of optomechanical gain becomes relevant, thermal noise becomes dominant (also shown from the calculations presented in Fig. 5.4).

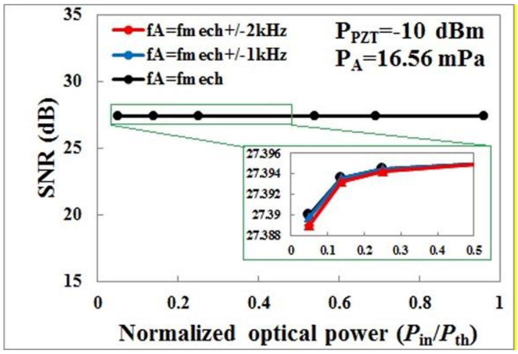

Fig. 5.6. Calculated signal-to-noise ratio (SNR) at $f_{PZT} = f_A = f_{mech}$, f_{mech} ± 1kHz, f_{mech} ± 2 kHz (where f_{mech} = 5.780 MHz) plotted versus normalized optical power.

As evident from Fig. 5.6, similar to the experimentally measured data shown in Fig. 5.3(d), SNR is almost independent of the input optical power indicating that optomechanical gain enhances the thermal noise and the acoustic excitation equally. Note that in contrast to Fig. 5.3(d), in Fig. 5.6 SNR is independent of optical input power and frequency. The small variations observed in the measured SNR (at different frequencies and optical input powers) are associated with the optical coupling instabilities during the measurement that result in optomechanical gain variations (in particular the large variation at f_{mech}+1 kHz) and the frequency dependence of acoustic impedance mismatch that has been ignored in the calculations. An SNR of 27 dB with an acoustic pressure amplitude of 16.5 mPa means that the ultimate limit of detection (LoD) for the OMR tested here is about 33 μPa. Ideally this limit can be obtained with a detected optical power level of 3 μW, given the optical losses in system, the required input optical power can be 30 μW (which is also limited by the P_{th}). We believe modifying the design of the silicon substrate for optimal acoustic impedance matching, larger interaction cross-section and more efficient energy transfer to the OMR can improve the performance another order of magnitude.

5.4 Comparison between OMR based acousto-optical transducer and other types of acousto-optical transducers

The response of the transducers that use optical resonance for translating a given acoustic pressure amplitude (P_A) to optical modulation, the sensitivity can be expressed as the optical modulation depth:

$$Modulation\ depth = P_{mod} / P_{tot} = \eta_{AO} \times P_A \times S$$

where η_{AO} (=$d\lambda_{res}/dP_A$ unit: nm/Pascal) is the acoustically induced resonant wavelength change and S (=$dT/d\lambda_{res}$ unit:1/nm) is the optical transmission slope. P_{mod} and P_{tot} are the modulated and total detected optical powers respectively. This definition is independent of the photodetector response and allows for a fair comparison among different acousto-optical transducers. S is a fixed number for a selected mode of a specific optical cavity at a given laser detuning ($\Delta\lambda = \lambda_{laser} - \lambda_{res}$). η_{AO} depends on the mechanical response of the transducer and the strength of acousto-optical coupling but typically it is independent of P_{tot} (or P_{in}) in previous reported acousto-optical transducers [3-9]. In the OMR used in our experiment the large optical quality factor of the cavity not only results in a large S but also enables strong mutual coupling between mechanical and optical modes. When the laser wavelength is blue detuned from the optical resonance ($\Delta\lambda < 0$), this optomechanical coupling manifests itself as optomechanical gain or reduction of the effective mechanical damping factor (Γ_{eff}) according to Eq. (5.2).

As such for OMR η_{AO} becomes proportional to the optical power making the optical modulation depth dependent on P_{in}. In other words, the optical power not only serves as a high sensitivity readout but also amplifies the acoustic response. To our knowledge none of the acousto-optical transducers reported so far (primarily based on FBG and FP) exhibited such behavior.

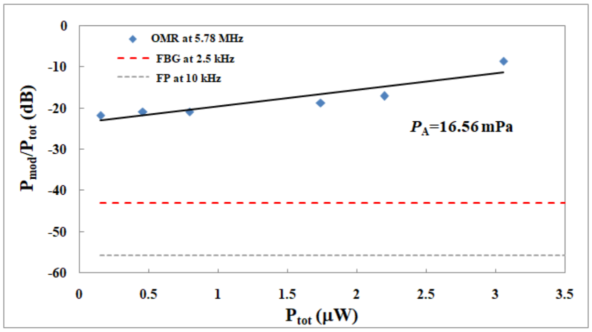

Fig. 5.7. The measured modulation depth (ratio between modulated optical power and the power impinged on the photo-detector) versus the power impinged on the photo-detector at fixed acoustic pressure for an FBG based transducer [6], a Fabry-Perot based transducer [8] and the microtoroidal OMR (this work), the solid curves/lines are fitted to the measured data.

Figure 5.7 shows the modulation depth plotted against P_{tot} for the microtoroidal OMR and two previously reported optical hydrophones [6, 8] used as examples. For FBG and FP based acousto-optical transducers, modulation depth is estimated based on the measured response reported in Refs. 6 and 8, respectively. Here the acoustic pressure amplitude is fixed however the responses in each case are measured at optimal frequencies for each device. The FBG does not support optomechanical gain and the low optical quality factor of the FP resonator (three orders of magnitude smaller than that of the microtoroid OMR) also makes the optomechanical gain negligible. As such η_{AO} and therefore the response of both transducers is independent of optical power.

As evident from Fig. 5.7, even at low optical powers (where $\Gamma_{\mathrm{eff}} \approx \Gamma_0$) microtoroidal outperforms the other two transducers simply due to its large optical quality factor (resulting in large S) and large mechanical response (resulting in large η_{AO}). Effectively for a given acoustic pressure amplitude and target level of modulated optical power (P_{mod}), OMR requires 4 and 2 orders of magnitude smaller optical power compared to the selected FP and FBG based transducers [6, 8], respectively. As such OMR can provide high sensitivity with extremely low power consumption.

Unfortunately, the bandwidth of the optomechanical gain is limited by the quality factor of the mechanical mode of the OMR and therefore the high acousto-optical sensitivity is only provided within a narrow bandwidth near the mechanical resonant frequency. Another evident limitation of the OMR based transducers is the fact that its input optical power (and therefore optical power modulation) is limited by the onset of optomechanical oscillation. This means that one cannot increase the modulated optical power beyond certain level by increasing the optical power. However, given the performance of modern low-noise photodetectors still a reasonably large SNR can be obtained.

5.5 Summary

In this chapter we have studied the radiation pressure assisted acousto-optical transduction in an optomechanical resonator (OMR). We have shown that high optical quality factor combined with strong coupling between optical and mechanical modes of an

OMR results in very high sensitivity to acoustic excitation with frequency equal to the frequency of one of the mechanical modes of the OMR. The sensitivity, that manifests itself as a large acoustically induced optical modulation, is a result of the high sensitivity of the optical transmission to mechanical deformation as well as optical reduction of the effective mechanical loss via radiation pressure. The proof of principle experiment based on a silica microtoroid OMR has shown that even without optimal acoustic design, 14% modulation depth can be induced by an acoustic pressure amplitude of less than 16 mPa. For a given acoustic excitation the microtoroidal transducer can generate the same level of modulated optical power as previously demonstrated acousto-optical transducers (e.g. FBG and FP based) with as large as four orders of magnitude lower input optical power. However, the maximum achievable modulated optical power is limited by the onset of self-sustained optomechanical oscillations. As such the OMR based acousto-optical transducer is suitable where very low power consumption is a critical factor. While the intrinsically narrow bandwidth of this transducer is a major limitation in general underwater sensing applications (where a flat and wide frequency response is required), for under water communication its ultra-high sensitivity and low power consumption are extremely useful. Note that the frequency of microtoroidal OMR can be lowered by increasing the microtoroid diameter; microtoroid based transducers with frequencies within 1-10 MHz range can be used for short distance and high data rate communication and those with frequencies within 100-1000 kHz can be used for longer distance and lower data rate.

5.6 References

[1] J. G. V. Teixeira, I. T. Leite, S. Silva, and O. Frazão,"Advanced fiber acoustic sensors," Photonic Sensors, **4**(3), 198-208 (2014).

[2] X. Y. Bo, D. P. Zhou, C. Baker, and L. Chen, "Recent development in the distributed fiber optic acoustic and ultrasonic detection," *IEEE* J. Lightwave Technol., **35**(16), 3256-3267 (2017).

[3] Q. Zhang, Y. P. Zhu, X. G. Luo, G. G. Liu, and M. Han, "Acoustic emission sensor system using a chirped fiber Bragg grating Fabry-Perot interferometer and smart feedback control," Opt. Lett., **42**(3), 631-634 (2017).

[4] G. Lee, D. A. Scripka, B. Wagner, N. N. Thadhani, Z. T. Kang, and C. J. Summers, "Design and fabrication of distributed Bragg reflector multilayers for dynamic pressure sensing," Opt. Express., **25**(22), 27067-27076 (2017).

[5] D. C. Seo, D. J. Yoon, I. B. Kwon, and S. S. Lee "Sensitivity enhancement of fiber optic FBG sensor for acoustic emission," *in Proc. SPIE Smart Structures and Materials + Nondestructive Evaluation and Health Monitoring*, 729415, San Diego, CA, USA (2009).

[6] C. Li, X. B. Peng, H. Zhang, C. Wang, S. C. Fan, and S. Q. Cao, "A sensitivity enhanced flexible acoustic sensor using polished fiber Bragg-Grating," Measurement, **117**, 252-257 (2017).

[7] J. Ma, W. Jin, H. L. Ho, and J. Y. Dai, "High sensitivity fiber tip pressure sensor with grapheme diaphragm," Opt. Lett., **37**(13), 2493-2495 (2012).

[8] J. Ma, H. F. Xuan, H. L. Ho, W. Jin, Y. H. Yang, and S. C. Fan, "Fiber optic Fabry-Perot acoustic sensor with multilayer grapheme diaphragm," *IEEE* Photon. Technol. Lett., **25**(10), 932935 (2013).

[9] Z. F. Gong, K. Chen, X. L. Zhou, Y. Yang, Z. H. Zhao, H. L. Zhou, and Q. X. Yu, "High sensitivity Fabry-Perot interferometric acoustic sensor for low frequency acoustic pressure detections," J. Lightwave Technol., **35**(24), 5276-5279 (2017).

[10] O. Kilic, M. J. F. Digonnet, G. S. Kino, and O. Solgaard, "Miniature photonic crystal hydrophone optimized for ocean acoustics," J. Acoust. Soc. Am., **129**(4), 1838-1850 (2011).

[11] H. Rokhsari, T. J. Kippenberg, T. Carmon, and K. J. Vahala, “Radiation pressure driven micro-mechanical oscillator,” Opt. Express., **13**(14), 5293-5301 (2005).

[12] T. Carmon, H. Rokhsari, L. Yang, T. J. Kippenberg, and K. J. Vahala, "Temporal Behavior of Radiation-Pressure-Induced Vibrations of an Optical Microcavity Phonon Mode," Phys. Rev. Lett., **94**(22), Art. no. 223902 (2005).

[13] T. J. Kippenberg, H. Rokhsari, T. Carmon, A. Scherer, and K. J. Vahala, “Analysis of Radiation-Pressure Induced Mechanical Oscillation of an Optical Microcavity,” Phys. Rev. Lett., **95**(3), Art. no. 033901 (2005).

[14] M. Hossein-Zadeh, H. Rokhsari, A. Hajimiri, and K. J. Vahala, “Characterization of a radiation-pressure-driven micromechanical oscillator,” Phys. Rev. A., **74**(2), Art. no. 023813 (2006).

[15] E. Verhagen, S. Deleglise, S. Weis, A. Schliesser, and T. J. Kippenberg, “Quantum-coherent coupling of a mechanical oscillator to an optical cavity mode,” Nature, **482**, 63-67 (2012).

[16] G. C. Righini *et al.*, “Whispering gallery mode microresonators: Fundamentals and applications,” Ricista. Del. Nuovo. Cimento., **34**(7), 435-488 (2011).

[17] H. Haus, “Waves and Fields in Optoelectronics,” (Prentice-Hall) 1984.

Chapter 6

Underwater acoustic signal detection and down conversion using optomechanical resonance and oscillation

6.1 Introduction

As described in chapter 5, nearly all optical hydrophones demonstrated to date use fiber Bragg gratings (FBG) and to a lesser extent miniaturized Fabry–Pérot (FP), photonic crystal (PC) and circular microcavities [1-5]. To achieve the desired acoustic sensitivity (comparable to the PZT based transducers), FBGs are usually wrapped around a mandrel or encapsulated in thick polymer coatings and require a relatively high level of optical power to generate a reasonable SNR [6]. So, while FBG based optical hydrophones have already enabled fabrication of remotely interrogated hydrophone arrays, there is still a need for further reduction of weight, size and power consumption for more efficient and larger hydrophone arrays. On the other hand, the miniaturized resonant optical hydrophones that provide high sensitivity in a small footprint, still consume a relatively high level of optical power. In chapter 5 it was shown that the optomechanical gain in optomechanical resonators (OMRs) can result in high sensitivity acousto-optical transduction when the optical input power to OMR (P_{in}) is below the threshold power required for self-sustained oscillation (P_{th}, typically less than 1 mW) [7]. As such using an OMR the required optical power for generating a given optical modulation amplitude can be significantly reduced compared to existing optical hydrophones where the impact of the optical power on mechanical damping is negligible. This property along with low power consumption and small size make OMR an excellent candidate for underwater applications where reduced size, weight, and power consumption (SWaP) are important [8-15]. SWaP is particularly critical for underwater autonomous vehicles (UAVs) and large aperture sensor arrays due to constraints imposed by the lifetime of the power source, limited space, and hydrodynamic drag [16-18]. The resonant nature of OMR based acoustic transducers limits their sensitivity to a relatively narrow bandwidth near the mechanical resonant frequency; as such these transducers are good candidates for receiver design in multichannel underwater communication links where the information in each channel is carried by a different ultrasonic carrier. Using several carriers with different frequencies increases the total information transfer capacity of the link beyond the bandwidth limitations of these transducers. An added benefit of this approach is the isolation from the relatively high level of low frequency noise that exists in the sea [19, 20].

In this chapter, we first examine the performance of subthreshold OMR as a hydrophone in an ultrasonic underwater link based on a modulated ultrasonic carrier. Next we show that when $P_{\mathrm{in}} \geq P_{\mathrm{th}}$, the resulting self-sustained oscillation of the so-called optomechanical oscillator (OMO) [21] directly down-converts the intermediate frequency (IF) or baseband signal from the ultrasonic carrier and eliminates the need for RF local oscillator (LO) and mixer in the receiver. The fact that in both cases the optical input power level is in sub-mW range and in the case of OMO an additional (~10 mW) power is saved (by eliminating the LO) makes OMR and OMO based acousto-optical receivers very attractive for underwater applications.

6.2 Theoretical analysis of the OMR/OMO based acoustic receiver in underwater acoustic links

In the examples presented in this chapter, a high-quality factor (high-Q) silica toroidal microcavity on a silicon chip [22] is used for the proof of concept demonstration of OMR/OMO performance as acousto-optical transducers/acoustic receiver in ultrasonic underwater links; however similar performance can be expected from other kinds of OMRs that mentioned in chapter 2 [23-26].

The operational principle of acoustic signal detection and down conversion in OMR and OMO is shown in Fig. 6.1. We assume that the acoustic signal is an RF carrier (with a frequency f_C) modulated by a baseband signal (with a frequency f_b). The acoustic wave is normally incident to the bottom of the chip that carries the microresonator (Fig. 6.1(a)). The acoustic carrier frequency is equal to the frequency of the first mechanical mode (f_{mech}) of the microcavity (shown in the inset); while by adjusting the frequency, an acoustic wave can excite any of the mechanical modes, at normal incidence the acoustic energy most effectively couples to the fundamental mode. When the optical input power (P_{in}) is coupled to one of the Whispering Gallery modes (WGMs) of the microcavity with radius R_0, the radial component of the acoustically induced mechanical displacement of the toroid $r(t)$, modulates the resonant frequency of the WGM ($\omega_0' = \omega_0 + \omega_0 r/R_0$, where ω_0 is the cold cavity WGM frequency) and therefore the transmitted optical power P_{out}. r is induced by two forces, *optical radiation pressure force* (F_{rad}) and *equivalent acoustic pressure force* (F_A). By tuning the frequency of the input power ($\omega_p = 2\pi v$) to a frequency larger than ω_0,

F_{rad} results in optomechanical gain (G_{OM}) that decreases the effective mechanical damping [21].

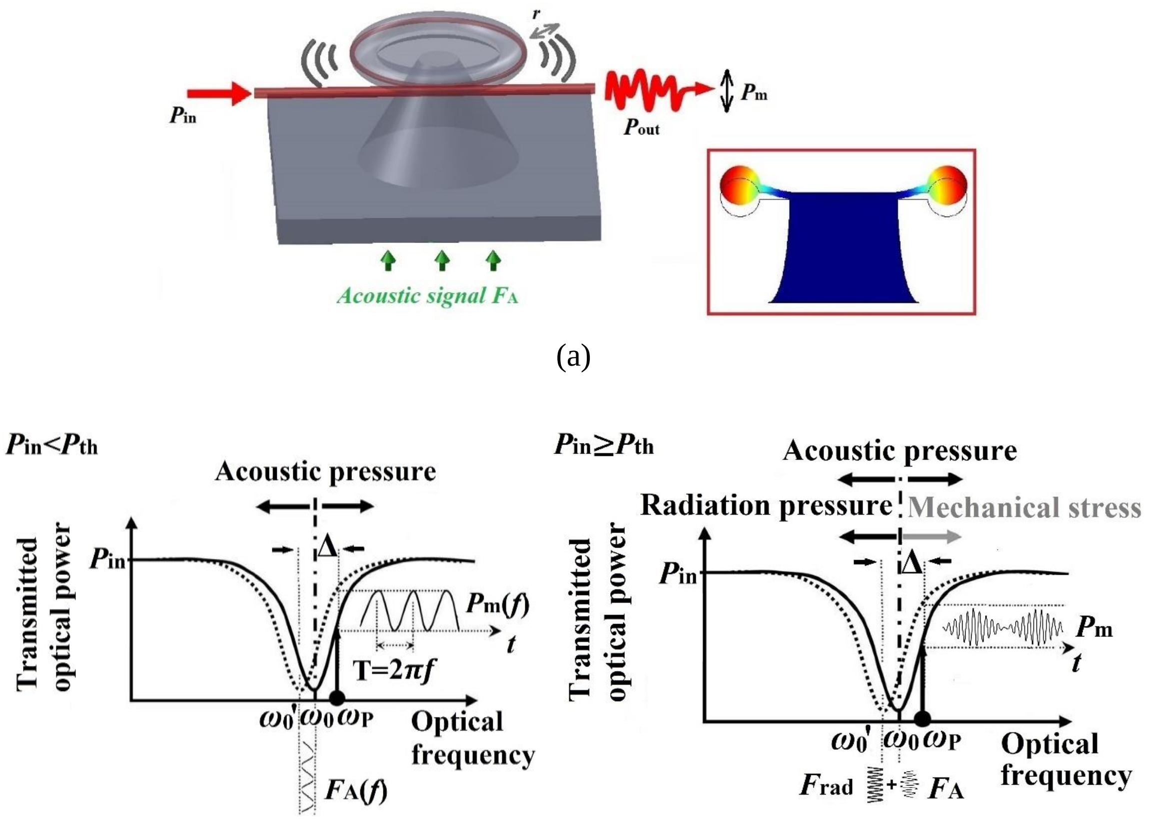

(a)

(b) (c)

Fig. 6.1. (a) Schematic diagram showing mechanical excitation of a toroidal OMR by a normally incident acoustic wave. The red line is the optical waveguide (in this case fiber-taper) coupled to the OMR. The inset is FEM simulation of the fundamental mechanical mode of the OMR (flapping motion). Operational principle of the device based on optical transfer function (OTF): (b) OMR functioning as an acousto-optical transducer and (c) OMO simultaneously functioning as acousto-optical transducer, RF local oscillator and mixer. F_A: Equivalent acoustic pressure force, F_{rad}: Radiation pressure force, P_m: Modulated optical power, r: radial component of the cavity displacement, Δ: the detuning between the pump frequency ω_P and the real time cavity resonance ω_0'.

When $P_{in} < P_{th}$, the reduced mechanical loss only makes the structure more sensitive to external acoustic excitation [7]. Figure 6.1(b) shows the Lorentzian shape optical transfer function (OTF) of the corresponding WGM; in this case the instantaneous frequency detuning $\Delta(= \omega_P - \omega_0') \propto F_A$ and OMR simply modulates P_{out} proportional to the incident acoustic signal strength but with an efficiency much larger than its FBG or FP based counterparts [7]. Since a linear response is required, ω_P should be tuned to the linear section of the optical transfer function. The detected signal will be a modulated carrier (a copy of the original signal) so the baseband (or IF) has to be down converted in electrical domain using an RF mixer and local oscillator. When $P_{in} \geq P_{th}$, the radiation pressure force induces self-sustained oscillation of the cavity at a frequency which is almost equal to f_{mech} (referred to as optomechanical oscillation frequency or f_{OMO}).

Clearly in the presence of optomechanical oscillation the signature of the single tone acoustic excitation at $f_A = f_{OMO}$ in the transmitted optical power is negligible. In this case r (and therefor Δ) is proportional to $F_A + F_{rad}$ (see Fig. 6.1(c)). During optomechanical oscillation the large variation of Δ involves the nonlinear part of the OTF and generates components proportional to $F_A \times F_{rad}$ in the spectrum of P_{out} (due to $(F_A + F_{rad})^2$ terms). As a result, P_{out} will be also modulated at f_b and the corresponding signal can be extracted simply by low pass filtering of the detected signal, so OMO simultaneously functions as an acousto-optical transducer and down-converter. Initial alignment of ω_P to the nonlinear section of the OTF can enhance the strength of the nonlinearity and therefore efficiency of the down-conversion [27]. It is worth mentioning that this mechanism is different from optomechanical down-conversion of baseband from a modulated optical pump in an OMO (described in detail in Ref. 28). In the latter case the received optical signal and the optomechanical oscillation are naturally multiplied and the nonlinearity of the OTF does not play a major role.

Figure 6.2(a) and 6.2(b) illustrate the signal flow in the spectral domain for the acousto-optical link based on OMR and OMO respectively.

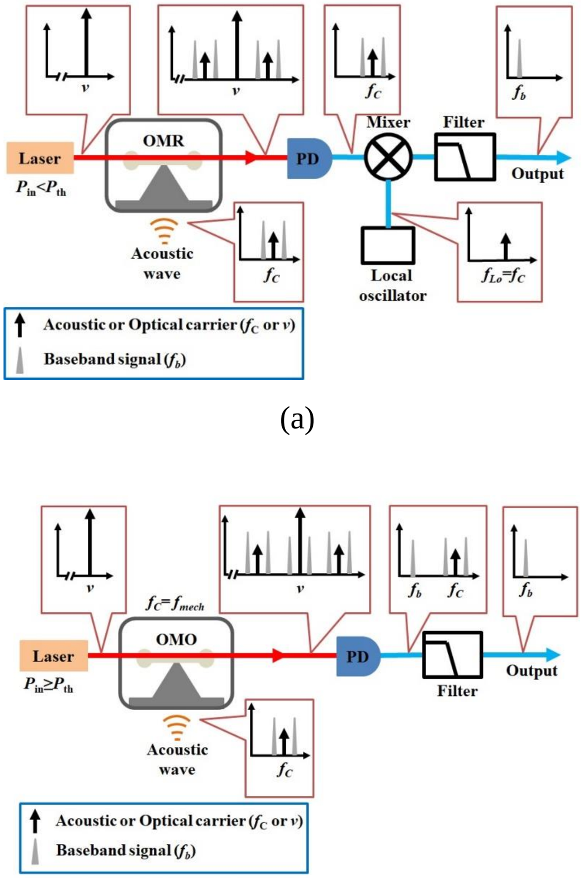

(a)

(b)

Fig. 6.2. (a) Signal flow in the OMR based acousto-optical link. (b) Signal flow in the OMO based acousto-optical link.

The dynamics of OMR/OMO driven by a modulated acoustic carrier signal (qualitatively explained above) can be numerically analyzed by solving the coupled differential equations governing the mechanical and the optical modes of the microcavity:

$$m_{eff}\frac{d^2r(t)}{dt^2}+m_{eff}\Gamma_0\frac{dr(t)}{dt}+m_{eff}\Omega_m^2r(t) = \frac{2\pi|E(t)|^2n}{c}+F_A[1+m\,cos(\Omega_b t)]cos(\Omega_b t). \tag{6.1}$$

$$\frac{dE(t)}{dt} + E(t)\left\{\frac{\alpha c}{n} - i\left[\Delta_0 + \frac{\omega_0 r(t)}{R_0}\right]\right\} = iB\sqrt{\frac{\alpha c}{n\tau_0}}. \tag{6.2}$$

$$E_{out}(t) = \left(1 - \frac{\tau_0 \alpha c}{2n}\right)B + i\sqrt{\frac{\tau_0 \alpha c}{n}}E(t). \tag{6.3}$$

where m_{eff} is the effective resonator mass for radial motion, $r(\mathrm{t})$ is the radial displacement of the microtoroid, $\mathit{\Gamma}_0$ is the mechanical damping factor, Ω_{m} (= $2\pi f_{\mathrm{mech}}$) is angular frequency of the microtoroid's excited mechanical mode. $E(t)$ is the circulating optical field amplitude in the cavity, n is the refractive index of the cavity, c is the speed of light in vacuum, α is the optical loss in the cavity, $\mathit{\Delta}_0 = \omega_{\mathrm{P}} - \omega_0$ is the preset optical frequency detuning, R_0 is radius of the toroidal microcavity, B is the input pump field, τ_0 is the round trip time of the cavity and E_{out} is the optical field coupled out of the microtoroidal cavity. Eq. (6.1) governs the motion of the mechanical cavity driven by the two forces, the first term on the right-hand side corresponds to Radiation pressure force induced by the circulating optical power, the second term is proportional to the equivalent radial acoustic force (F_{A}) which is proportional to the incident acoustic pressure (P_{A}) [29]. Here the carrier frequency Ω_{C} (= $2\pi f_{\mathrm{C}}$) is modulated by a baseband signal ($\Omega_{\mathrm{b}} = 2\pi f_{\mathrm{b}}$) with a modulation index m. Eq. (6.2) governs the dynamics of the circulating optical field in the microcavity and Eq. (6.3) is the total optical output field [30].

6.2.1 Theoretical analysis of the OMR based acousto-optical transducer in underwater acoustic links

When $P_{\mathrm{in}} < P_{\mathrm{th}}$, the optomechanical gain is not sufficient to induce the self-sustained oscillation and the optomechanical dynamics can be described by a harmonic mechanical oscillator where the effective damping factor ($\varGamma_{\mathrm{eff}}$) linearly decreases with P_{in} due to optomechanical gain [31]:

$$m_{eff}\frac{d^2r(t)}{dt^2} + m_{eff}\varGamma_{eff}\frac{dr(t)}{dt} + m_{eff}\varOmega_m^2 r(t) = F_A[1 + m\cos(\varOmega_b t)]\cos(\varOmega_C t)$$
$$= F_A\cos(\varOmega_C t) + \frac{m}{2}F_A\cos[(\varOmega_C + \varOmega_b)t] + \frac{m}{2}F_A\cos[(\varOmega_C - \varOmega_b)t]$$
$$= F_1(\varOmega_1) + F_2(\varOmega_2) + F_3(\varOmega_3). \tag{6.4}$$

$$\varGamma_{eff} = \varGamma_0\left(1 - \frac{P_{in}}{P_{th}}\right). \tag{6.5}$$

Subsequently the radial displacement induced by each frequency component of the incident acoustic wave ($\varOmega_{\mathrm{i}}$, i =1, 2, 3) can be written as:

$$r(\varOmega_i) = \frac{F_i(\varOmega_i)}{m_{eff}\sqrt{(\varOmega_m^2 - \varOmega_i^2)^2 + \varOmega_i^2\varGamma_{eff}^2}} = \chi(\varOmega_i, P_{in})\frac{F_i(\varOmega_i)}{m_{eff}}. \tag{6.6}$$

here χ is the mechanical susceptibility which depends on the acoustic frequency and the input optical power. The resulting variation in the transmitted optical power (T) can be calculated using the optical transfer function of the microcavity [32, 33]:

$$T(\Delta) = 1 - \frac{\omega_0^2}{Q_0Q_e}\frac{1}{\left(\frac{\omega_0}{2Q_e} + \frac{\omega_0}{2Q_0}\right)^2 + \Delta^2}. \tag{6.7}$$

Here Q_0 is the intrinsic quality factor of the corresponding optical mode, Q_{e} is the external quality factor which is limited by the optical attenuation due to the waveguide resonator coupling loss. We assume the OMR operates in the unresolved sideband regime, where $\Omega_{\mathrm{m}} << \omega_0/Q_0$ (in our experiment $\Omega_{\mathrm{m}} = 2\boldsymbol{\pi} \times f_{\mathrm{m}} = 2\boldsymbol{\pi} \times 4.61$ MHz, $\omega_0/\mathrm{Q}_0 = 2\boldsymbol{\pi} \times 121.61$ MHz), T adiabatically follows the variations of detuning through $\delta T = [\mathrm{d}T/\mathrm{d}\varDelta] \times \delta\varDelta$ where $\delta\varDelta = g_{\mathrm{OM}} \times r(\Omega_{\mathrm{i}})$ and g_{OM} is the optomechanical coupling coefficient of the OMR. Therefore, the modulated optical output power at each frequency can be written as:

$$P_m(\Omega_i) = \frac{dT}{d\Delta}\eta P_{in} g_{OM} r(\Omega_i). \tag{6.8}$$

The coefficient η characterizes the transmission loss from microcavity to the photodetector. Using Eqs. (6.6) - (6.8), $P_m(\Omega_i)$ can be expressed as:

$$P_m(\Omega_i) = \left(\frac{2\omega_0^2\Delta}{Q_0 Q_e\left[\left(\frac{\omega_0}{2Q_e}+\frac{\omega_0}{2Q_0}\right)^2+\Delta^2\right]^2}\right)(\eta P_{in} g_{OM})\left(\frac{F_i(\Omega_i)}{m_{eff}\sqrt{(\Omega_m^2-\Omega_i^2)^2+\Omega_i^2\Gamma_{eff}^2}}\right). \tag{6.9}$$

This equation shows that, as opposed to conventional acousto-optical transducers, the modulation amplitude at each frequency component or $P_m(\Omega_i)$ grows super linearly proportional to P_{in} (because Γ_{eff} in the denominator of the last term linearly decreases with P_{in}). According to Eq. (6.9), the spectral components of the acoustic signal are independently mapped to optical domain (see Fig. 6.2(a)); as such the spectrum of P_{out} is proportional to the spectrum of F_A or acoustic signal. Subsequently, the amplitude of the down-converted baseband signal can be calculated considering the photodetector response (β), conversion loss of the RF mixer (L_c) and the RF modulation index (m). Figure 6.3(a) shows the calculated down converted signal amplitude plotted versus normalized optical input power (P_{in}/P_{th}) for three different values of mechanical qualify factor Q_m (= Ω_m/Γ_0).

Here the acoustic wave is suppressed carrier signal with an amplitude of 0.2 Pa (corresponding to F_A = 27 pN). All parameters are selected based on experimental values (see the figure caption, and the experimental result will be discussed in section 6.3.1). When $P_{in}/P_{th} < 0.2$, optomechanical gain is negligible ($\Gamma_{eff} \approx \Gamma_0$) and P_m is proportional to P_{in} [2, 34].

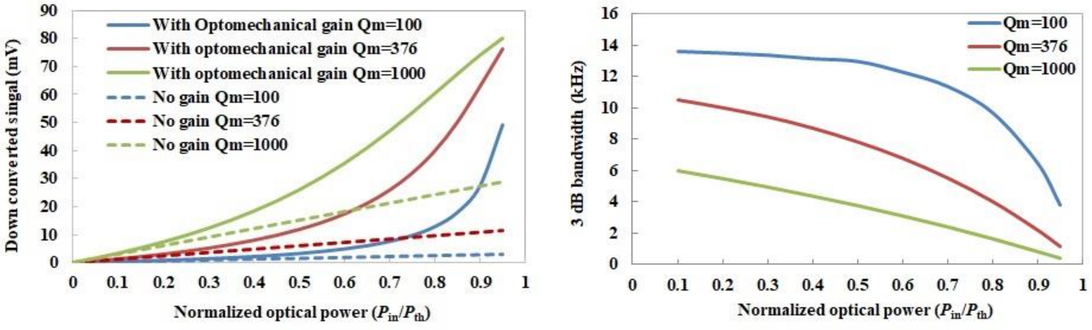

(a) (b)

Fig. 6.3. (a) Estimated performance of the OMR as an acousto-optical transducer in the acoustic link: (a) rms voltage of the down converted signal at different values of Q_m. The dashed lines are the estimated performance in the absence of optomechanical gain ($\Gamma_{eff}=\Gamma_0$). (b) Simulated bandwidth plotted vs. normalized optical input power for different values of Q_m. Here, $\eta = 0.047$, $g_{OM} = 2\boldsymbol{\pi}\times 3.21$ GHz/nm, $f_C = f_{mech} = 4.61$ MHz, $f_b = 1$ kHz, $F_A = 27$ pN (corresponding to acoustic pressure $P_A = 0.2$ Pa), $\beta = 4.2\times10^4$ V/W, $m = 21.08$, $L_c = -4.7$ dB, $\Delta_0 = 0.4 \times \omega_0/Q_L$, λ_0=1555.4 nm, $P_{th} = 539$ µW, $Q_0 = 1\times10^7$, $Q_L = 6.1\times10^6$, $m_{eff} = 580$ ng (the values are chosen based on the actual parameters in our experiments, see section 6.3.1).

When $P_{in}/P_{th} > 0.2$, the optomechanical gain results in near exponential growth of P_m with P_{in}. The dashed lines are the estimated values in the absence of optomechanical gain ($\Gamma_{eff} = \Gamma_0$). As such compared to conventional acousto-optical transducers OMR consumes less power to generate a given signal level. Figure 6.3(b) shows the simulated 3 dB bandwidth vs. normalized optical power for different values of Q_m. These plots suggest that the operational bandwidth of the transducer is limited by the mechanical resonance. As usual there is a bandwidth penalty associated with the higher sensitivity; however, by employing several carriers a multi-channel receiver comprising of several OMRs can support faster data rates. Note that even when P_{in} is much lower than P_{th} and the optomechanical gain is negligible, just the combination of low loss optical and mechanical modes make an OMR based acousto-optical transducer more sensitive and efficient than the conventional FBG and FP based acousto-optical transducers [7].

6.2.2 Theoretical analysis of the OMO based acousto-optical transducer in underwater acoustic links

In the above threshold region, the response of radiation pressure driven OMO to a modulated acoustic signal should be evaluated by directly solving Eqs. (6.1) - (6.3). To show the feasibility of the direct down-conversion we have calculated optical modulation ($\delta P_{out} \propto |\delta E_{out}|^2$ that is equivalent to P_m) induced by a suppressed carrier acoustic signal.

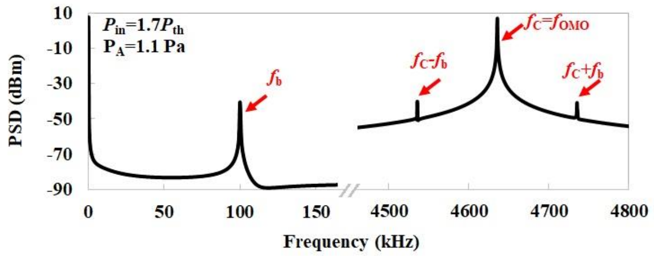

(a)

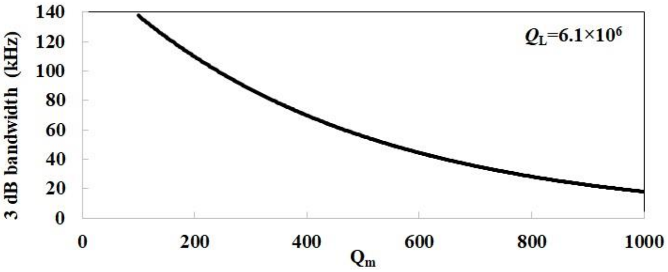

(b)

Fig. 6.4. (a) Simulated spectrum of the OMO's output in the presence of modulated acoustic pressure force F_A = 148 pN (corresponding to acoustic pressure P_A = 1.1 Pa). The discontinuity between high and low frequency is made on purpose to help observing both part of spectrum with high resolution. (b) Simulated bandwidth of the down converted signal versus the mechanical quality factor Q_m. Here the values of all parameters are identical to those used in Fig. 6.3 except that f_b is 100 kHz.

Figure 6.4(a) shows the simulated spectrum of δP_{out} (the values of all parameters are identical to the ones used in section 6.2.1 except that f_b = 100 kHz here). Since the optomechanical oscillation is much larger than the acoustically induced modulation the sidebands look very small. Here P_A is 1.1 Pa. As expected, the mixing process in the optomechanical domain also generates a component at f_b in the spectrum of δP_{out}. Figure 6.4(b) shows the bandwidth vs. quality factor of the mechanical mode when quality factor of the optical mode is $Q_L = 6.1\times10^6$, in our simulation the down conversion bandwidth for the OMO is still determined by the mechanical quality factor.

Note that analyzing the general behavior of the 3dB down-conversion bandwidth for the OMO based receiver (as a function of detuning and optical pump power) is complicated partly due to the fact that the location of the sidebands affect the oscillation amplitude of the OMO; in other words it cannot be assumed that OMO's oscillation amplitude is independent of the received signal.

6.3 Experimental demonstration of the OMR/OMO based acoustic receiver in underwater acoustic links

For the proof of principle demonstration, we used high-Q silica toroidal microcavities (fabricated on a silicon chip) as the OMR and OMO [22]. Figure 6.5(a) and 6.5(b) show the experimental arrangements used to characterize the performance of the acousto-optic receivers based on OMR ($P_{in} < P_{th}$) and OMO ($P_{in} \geq P_{th}$) respectively. In both arrangements, a narrow linewidth tunable laser (1550 nm) generates the input optical power (P_{in}) that is coupled into and out of the microcavity through a fiber taper. The optical output power (P_{out}) is fed to a photodetector with responsivity (β) of 4.2×10^4 V/W. The carrier chip is encapsulated so that it can be immersed in water but to increase the distance from the transducer here only the bottom part is immersed so that the silicon chip is in direct contact with water. The silicon chip has dimensions of 18 × 5 × 0.3 mm^3 for both experiments. The modulated acoustic carrier is generated by mixing a local oscillator (frequency = f_c) with the baseband signal (frequency = f_b) in an RF mixer. The resulting suppressed carrier signal (with an index of m = 21.08) is fed to an encapsulated piezoelectric transducer (PZT) that is placed at the bottom of a container 10 cm away from the silicon carrier chip. The frequency of the acoustic carrier (local oscillator) is equal to the frequency of the mechanical mode (f_{mech}) of the OMR or OMO.

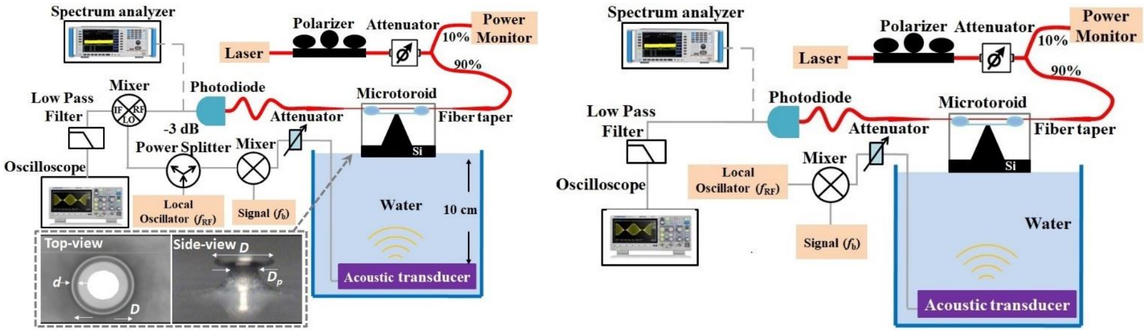

(a) (b)

Fig. 6.5. Experimental arrangements (acousto-optical link) for testing the performance of OMR and OMO based acousto-optical receivers. (a) $P_{in} < P_{th}$ (OMR based receiver); here OMR functions only as an acousto-optical transducer. The inset shows the top and side view of the toroidal microcavity. (b) $P_{in} \geq P_{th}$ (OMO based receiver); here the OMO simultaneously functions as acousto-optical transducer, RF local oscillator and RF mixer. In both cases $D = 125$ µm, $D_p = 80$ µm, $d = 12$ µm, $f_m = 4.61$ MHz, $Q_m = 376$, $P_{th} = 539$ µW and the size of the silicon chip is 18 mm (L) × 5 mm (W) × 0.3 mm (H).

In the first configuration shown in Fig. 6.5(a), where $P_{in} < P_{th}$, the OMR only functions as a sensitive acousto-optical transducer. So, in order to extract the baseband signal from the acoustic carrier the detected signal is mixed with the original local oscillator in an RF mixer. In the second configuration, shown in Fig. 6.5(b), $P_{in} \geq P_{th}$ and the self-oscillation of OMO performs the RF down-conversion in optical domain; as a result a baseband component (f_b) appears in the detected signal that can be separated from the main signal simply by using a low-pass RF filter (without the need for local oscillator and mixer at the receiver end). Note that down-conversion in OMO happens only if f_{OMO} (= f_{m}) is equal to the carrier frequency (f_{C}).

6.3.1 Underwater acoustic link based on OMR acousto-optical transducer

Figure 6.6(a) shows the measured amplitude of the measured down-converted signal plotted against normalized optical input power ($P_{\mathrm{in}}/P_{\mathrm{th}}$) for the link shown in Fig. 6.5(a) where an OMR ($P_{\mathrm{in}} < P_{\mathrm{th}}$) transducer is used in the receiver.

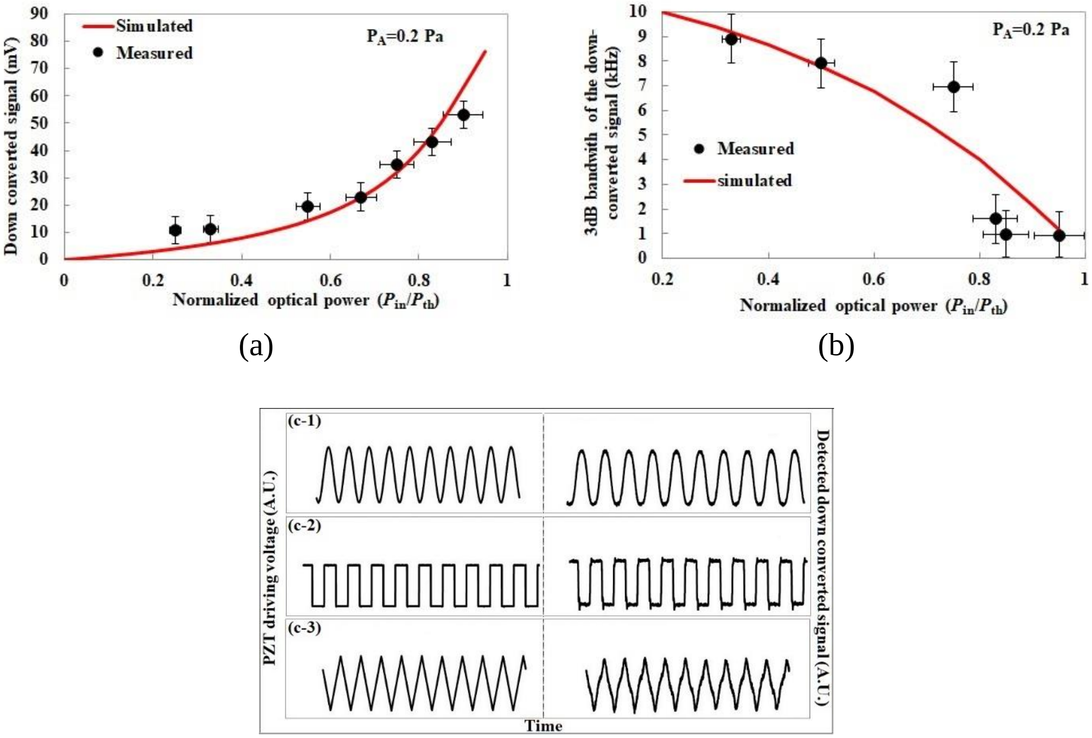

(a) (b)

(c)

Fig. 6.6. Performance of the OMR based receiver ($P_{\mathrm{in}} < P_{\mathrm{th}}$). (a) Simulated (red line) and measured (black points) rms voltage of the down-converted signal versus $P_{\mathrm{in}}/P_{\mathrm{th}}$. (b) Simulated (red line) and measured (black points) 3 dB bandwidth of the receiver. The parameters for the simulations are the same as the Fig. 6.3 and $Q_{\mathrm{m}} = 376$. (c) The original (left) and the corresponding received baseband waveforms (right) of the OMR based underwater acoustic link. The frequency and acoustic pressure amplitude (P_{A}) for the sinusoidal, square and triangular waves are: (4 kHz, 0.2 Pa), (100 Hz, 0.25 Pa), (1 kHz, 0.16 Pa),).

In this link, f_C = 4.61 MHz and a single tone baseband with f_b = 1 kHz. The red line is the simulated value based on Eq. (6.9) and characteristic of the RF mixer used in the experiment. The exponential growth is a signature of the presence of optomechanical gain in OMR.

Figure 6.6(b) shows the simulated (red line) and measured bandwidth of the down-converted signal for the OMR based receiver (that, as expected, is limited by the bandwidth of the mechanical mode). The deviation of the measured data from the simulation is partially due to non-flat spectral response of the PZT. The minimum acoustic pressure at which a measurable down-converted signal can be generated is about 0.1 mPa.

In order to examine the fidelity of the OMR based underwater acoustic link, we recorded the temporal variation of the received baseband signal for three different types of input basebands. The left column of Fig. 6.6(c) shows the temporal variation of the input baseband signals (c-1: sinusoidal wave with frequency of 4 kHz; c-2: Square wave with frequency of 100 Hz; and c-3: Triangle wave with frequency of 1kHz) before mixing with the RF carrier. After mixing (up-conversion) the resulting RF signal drives the PZT in the water (see Fig. 6.5(a)), the output optical power of the OMR is converted to an RF voltage by the photodetector and then mixed with a local oscillator (same oscillator used for up converting the baseband signal) to down-convert the baseband signal. Subsequently a low pass RF filter removes the high frequency components (transmitted and generated by the mixer), and the down converted signal is monitored using an oscilloscope. The right column of Fig. 6.6(c) shows the temporal variation of the down-converted signals. The negligible distension of the received signals indicate that the performance of the OMR is satisfactory.

6.3.2 Underwater acoustic link based on OMO acousto-optical transducer

As discussed in section 6.2.2, an OMO can simultaneously receive (i.e., modulated the optical carrier proportional to the amplitude of incident acoustic signal) and down-convert the based band signal. As such the configuration shown in Fig. 6.5(b) the receiver only comprises an OMO, a photodetector and a low pass RF filter. The down converted signal is monitored using an electrical spectrum analyzer. Figure 6.7(a) shows the spectrum of the RF signal (f_C = 4.61 MHz and f_b = 100 kHz) used to drive the PZT transducer. Figure 6.7(b) shows measured spectrum of P_{out} when $P_{in} = 0.9P_{th}$. Note that while in the original RF signal the carrier is suppressed, the natural thermal vibration of the OMR has boosted the amplitude at f_C, however this small thermal excitation won't coherently mix with the original signal. That is why no signal is observed at f_b. Figure 6.7(c) shows the measured spectrum of P_{out} when $P_{in} = 1.7P_{th}$ (~900 μW). In this case optomechanical oscillation generates a strong amplitude modulation at f_C; here the coherent mixing of the carrier generated through optomechanical oscillation and the sidebands has generated a baseband component (the left panel). So only 0.9 mW of optical input power has generated a down-converted signal with an SNR >20 dB with no need for RF oscillator and mixer after the photodetector.

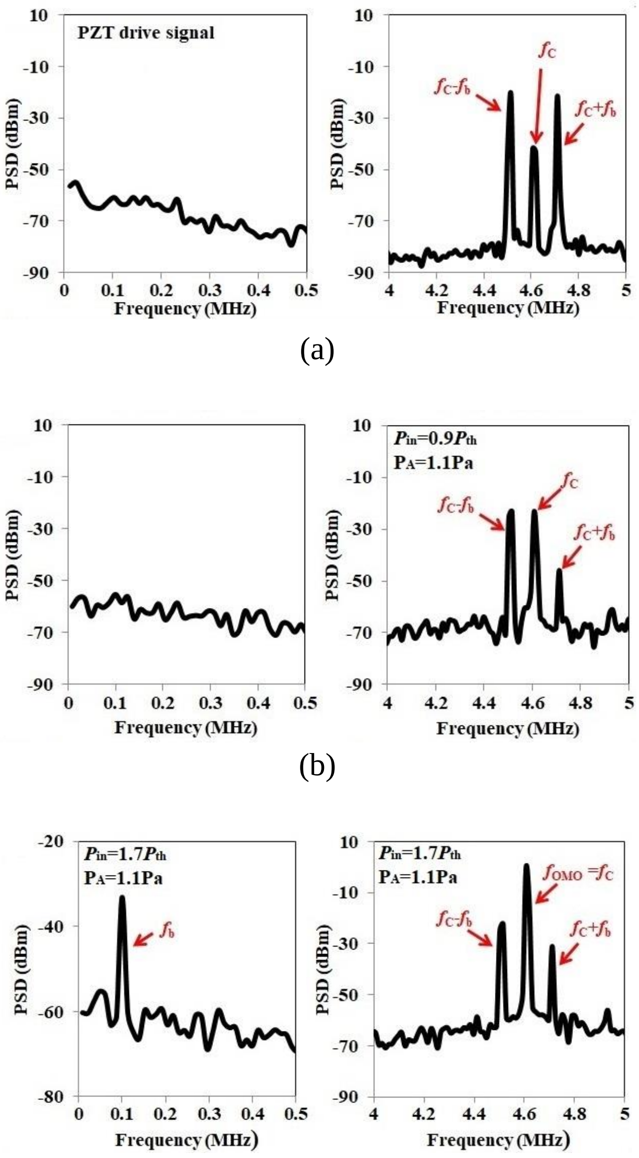

(a)

(b)

(c)

Fig.6.7. (a) Spectrum of the suppressed carrier signal that drives the PZT. Here f_C = 4.61 MHz and f_b = 100 kHz. (b) The spectrum of P_{out} when $P_{in} = 0.9 \times P_{th}$ (~450 μW). (c) The spectrum of P_{out} when $P_{in} = 1.7 \times P_{th}$ (~900 μW). The left panel (0-0.5 MHz) and the right panel (4-5 MHz) are separated to help observing the carrier and baseband signals with high resolution. The resolution bandwidth for these measurements was 3 kHz.

Qualitatively Fig. 6.7(c) and Fig. 6.4(a) are in good agreement (i.e. the location of the frequency components and their relative amplitude almost match); however, near carrier frequency (f_{OMO}), the simulated background level in Fig. 6.4(a) is much larger than the actual noise floor in Fig. 6.7(c). This difference is due to limited resolution in our simulation. Note that in Eqs. 6.1 - 6.3 (used for generating Fig. 6.4(a)), noise has not been taken into account and the background level observed in the simulated data is a numerical artifact and does not carry any information. It is worth mentioning that in the measured spectrum the two side bands (located near f_{OMO}) have slightly different amplitudes. This asymmetry is due to frequency dependence of the acoustic impedance as well as the frequency response of the acoustic transducer used to generate the acoustic waves (its response at $f_{OMO} - f_b$ is about 1 dB larger than its response at $f_{OMO} + f_b$).

Figure 6.8 shows the measured down-converted signal amplitude as a function of normalized optical power (P_{in}/P_{th}) for OMO based receiver ($P_{in} \geq P_{th}$) when $f_c = f_{OMO} = 4.61$ MHz and $f_b = 100$ kHz. The slight difference between the measured and simulated results is due to variation of the preset frequency detuning (Δ_0) during the measurement. In the above threshold experiment, we have not been able to accurately measure the 3dB bandwidth due to the limited working bandwidth of the PZT transducer; however, we expect the bandwidth to be limited by the mechanical mode as predicted in Fig. 6.4(b).

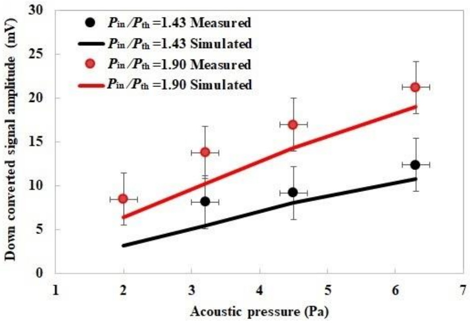

Fig. 6.8. The measured rms voltage of the down-converted baseband signal versus normalized optical power for OMO based receiver ($P_{in} \geq P_{th}$).

Unfortunately, due to executive noise in our system we were not able to record the temporal behavior of the down converted signal using the oscilloscope. So while the functionality of the OMO based underwater acoustic link has been verified by the presence of the down converted signal on the electrical spectrum analyzer (Fig. 6.7), we were not able to evaluate the fidelity of the down-converted signal as we did for OMR based underwater acoustic link experiment.

Our experimental observation indicates that the frequency pulling and injection locking [29] may impose a lower limit on the baseband (or IF) frequency. While evaluating the ultimate limit requires more investigation, in a similar case where the received signal was used to modulate the pump instead of inducing mechanical vibration, audio data was successfully down converted from a high frequency carrier [28].

6.4 Frequency considerations for the OMR/OMO based acoustic receiver in underwater acoustic links

The mechanical resonance frequencies of typical toroidal microcavities that have a diameter between 50 and 100 micron varies between 2 to 100 MHz. This frequency range is considered high for direct (without a carrier) underwater communication. While the preferred acoustic frequency varies depending on the application, generally for underwater wireless communication, the acoustic frequency is between 10 kHz to several megahertz. Lower frequencies are more suitable for long range communication as they experience less absorption in sea water [35]. Meanwhile, lower frequencies suffer from bandwidth restriction, ambient noise and multipath effects [19, 36]. High frequency waves that are generally used for short range communication with high channel capability can overcome the multipath effect and are immune from the ambient noise that exist in the sea water [15, 37]. Past research work has already demonstrated the feasibility of using 1 MHz acoustic waves to realize 60 ~ 100 meters undersea wireless communication links [38, 39]. As such typical toroidal microcavities can be employed in short-range underwater communication.

It is also possible to fabricate toroidal microcavities with frequencies in kHz range by making their diameter larger and the pillar size smaller. Figure 6.9 shows the simulated mechanical frequency of the fundamental mechanical mode of the toroidal microcavity versus the membrane length (D/2 - D_p/2). We believe, the toroid based acousto-optical transducers with kHz range operational frequency can significantly enhance the performance (sensitivity and power consumption) of kilometers range underwater links.

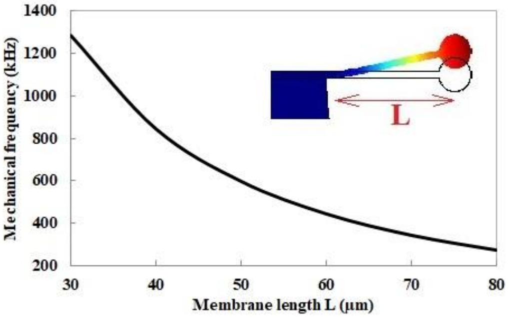

Fig. 6.9. Simulated mechanical frequency versus the radial cavity length for the first flapping mode for microtoroid resonator, the simulation is processed by using COMSOL multi-physics software.

Beyond toroidal microcavities, several other chip scale optomechanical microcavities, that support lower resonant frequencies, can be used as acousto-optical transducers. For example, those designed based on photonics-crystals can be resonate/oscillate at frequencies as low as tens of kilohertz [33, 40] and still provide efficient optomechanical transduction [41].

6.5 Packaging acousto-optical transducers based on microtoroidal OMRs/OMOs

In order to be used in practical applications, microtoroid based acousto-optical transducers have to be properly packaged. The package design for these transducers should take into account two major requirements: 1) the package should be completely sealed to protect the microtoroid and the fiber-taper from water and moisture (that are detrimental to the quality factor of the microtoroid and the optical transmission of the fiber-taper). The package should stay sealed at pressure levels associated with the operation depth of the hydrophone. In the meantime, the package should support fiber-optic input and output ports. 2) Due to small size of the OMR, its acoustic cross-section (i.e., the effective area that interacts with acoustic waves) is very small. In order to increase the amount of acoustic energy received by the OMR (and therefore the sensitivity of the transducer), the package should be designed to capture more acoustic energy and efficiently transfer it to the acousto-optical transducer. The first requirement alone is relatively easy to satisfy; for example, the silicon chip that carries the microtoroid can be placed in a small sealed box while the input and output sections of the fiber–taper pass through two small holes provided on the box. The small clearance between the hole and the fiber (<50 micron) can be easily sealed using specialized glue. The second requirement is much more challenging as it requires efficient acoustic transmission from water to the package and from the package to the silicon chip. As such, here we propose a possible design strategy that may be used to address the second requirement.

We propose a package comprising an acoustic lens that enables focusing the acoustic waves received by a relatively large area (~20× larger than the silicon chip that carries the OMR) to the OMR [42, 43]. In addition to focusing the acoustic energy, the proposed design enables acoustic impedance matching between the sea water and the silicon chip. For example, at 5 MHz, the acoustic impedance of sea water is about 1.48 MRayl while the acoustic impedance of silicon chip is about 19.7 MRayl; so if the silicon chip directly receives the acoustic waves from sea water (similar to the configurations used in the demonstrations described above), the impedance mismatch results in 74% reflection of the acoustic energy at the interface between sea water and silicon.

Figure 6.10 shows an example of the proposed packaging design that uses a biconcave acoustic lens to focus the acoustic pressure on the silicon chip that carries the microtoroid. The lens is optimized for focusing the acoustic waves having a frequency equal to that of the mechanical mode of the microtoroid used for acousto-optical transduction. In this design, an acoustic impedance matching layer is attached to (or deposited) the bottom side of the silicon chip so that nearly all the energy of the focused acoustic wave can be transferred to the silicon chip without any reflection.

In the specific design shown in Fig. 6.10(a), the microtoroid has a major diameter of 104 μm, a minor diameter of 12 μm and a pillar diameter of 76 μm. This design is optimized for exciting the fundamental mode of this microtoroid that has a frequency of 5

MHz. The acoustic lens is made of acrylic resin, its diameter is 20 mm and radius of the curvature is also 20 mm. The silicon based microtoroid is encapsulated in a container made of Schott glass, the bottom side of the silicon chip is covered by an impedance matching layer composed of araldite glue [44], that is also used to attach the glass container to the base of the glass container. The glass container is attached to an acrylic ring that is attached to the lens using four pillars (where the ring, the pillar and the lens are all machined as one part). Figure 6.10(b) shows a 3D illustration of the package. The thickness of the araldite glue between the silicon chip and the glass container, and the thickness of the glass container, can be selected to match the impedance of the focused incident wave (transmitted through water) and the impedance of the acoustic wave transmitted in the silicon chip. Basically, the glass layer and the glue layer together act as an anti-reflection layer. Using the method presented in Ref. [45], the optimal thickness of the glue is determined to be 43 μm + N × 262 μm, and the optimal thickness of the Schott glass is determined to be 65 μm + N × 491 μm (where N is an integer). Note that, given the acoustic loss in the glass and glue, a smaller N results in lower insertion loss. Figure 6.10(a) also shows the calculated acoustic pressure field distribution (using FEM method), resulted from an acoustic plane wave incident to the lens. As evident from the figure, all the energy captured by the lens aperture, is focused on the silicon chip. Fig. 6.10(c) shows the acoustic pressure level along the propagation direction before and after the acoustic lens. In this simulation, absorption and scattering in the acoustic lens are ignored. According to this simulation, the acoustic pressure level received by the microtoroid, can be 12 dB larger than the acoustic pressure of the incident wave.

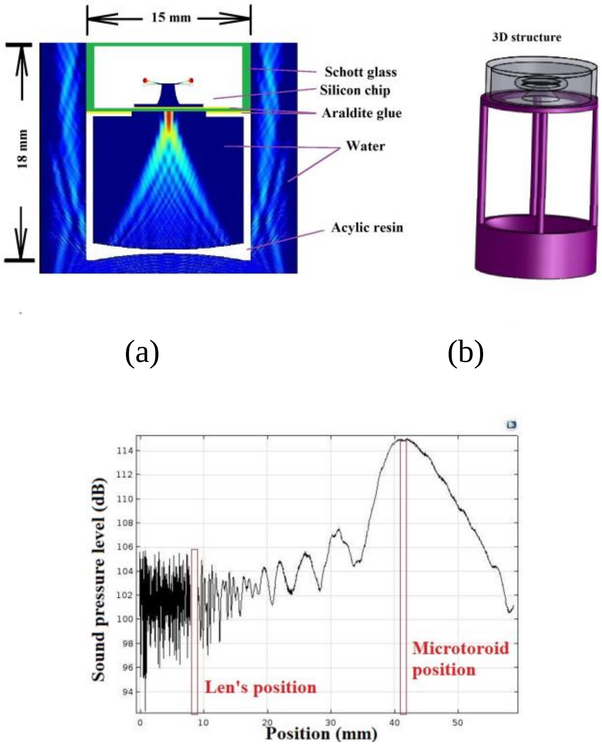

(a) (b)

(c)

Fig. 6.10. A package design for an optical hydrophone based on microtoroidal OMR. This design comprises an acoustic lens. (a) The proposed design and the simulated distribution of acoustic pressure field resulting from incident acoustic plane wave. (b) A 3D illustration of the design shown in part-a.(c) The acoustic pressure plotted along the propagation direction of the incident wave. Note: the microtoroid on the silicon chip is magnified for clarity.

6.6 Summary

In this chapter, we demonstrated the application of strong optomechanical coupling and resulting gain in acousto-optical transduction and frequency mixing in the context of underwater signal transmission with ultrasonic carrier frequencies. We have shown that OMR can function as a narrow-band and high sensitivity acousto-optical transducer with low power consumption. We also demonstrated that when pumped above threshold, OMO can down convert the baseband signal from the ultrasonic carrier without the need for RF oscillator and mixer resulting in unprecedented level of simplicity and power consumption for ultrasonic receiver design. In both OMR and OMO based receivers the down-converted signal with an SNR larger than 20 dB was generated with sub-milliwatt optical input power. While our calculations and measurements have revealed some of the basic properties of OMO/OMR based acoustic receivers, still many parameters in these systems have to be investigated. Dynamic range, behavior of the 3B down-conversion bandwidth (as a function of various parameters) are examples of issues that will be the subject of future studies and publications.

We have also proposed a packaging strategy that not only protects the OMR (or OMO), but also increases the sensitivity of the acousto-optical transducer, by increasing the effective acoustic cross section of the device and providing an impedance matching layer to increase the acoustic energy delivered to the OMR.

This work may pave the way for further development of this new application of cavity optomechanics and exploiting the unique properties of optomechanical resonators and oscillators that for the most part have remained untapped. Given the rapid progress towards design and fabrication of high performance monolithic optomechanical micro-cavities, the proposed approach can be used to fabricate compact and low power acousto-optical receivers for multichannel underwater acoustic signal detection and processing.

6.7 References

[1] S. Campopiano *et al*., "Underwater Acoustic Sensors Based on Fiber Bragg Gratings," Sensors, **9**(6), 4446-4454 (2009).

[2] P. Morris, A. Hurrell, A. Shaw, E. Zhang, and P. Beard, "A Fabry–Pérot fiber-optic ultrasonic hydrophone for the simultaneous measurement of temperature and acoustic pressure," J. Acoust. Soc. Am., **125**(6), 3611-3622 (2009).

[3] O. Kilic, M. J. F. Digonnet, G. S. Kino, and O, Solgaard, "Miniature photonic-crystal hydrophone optimized for ocean acoustics," J. Acoust. Soc. Am., **129**(4), 1837-1850 (2011).

[4] F. Monifi *et al*., "Ultrasound sensing using a fiber coupled silica microtoroid resonator encapsulated in a polymer," in Proc. *IEEE* Photonics Conference, Bellevue, WA, USA, 2013, pp. 215-216.

[5] C. Zhang, S. L. Chen, T. Ling, and L. J. Gao, "Review of imprinted polymer microrings as ultrasound detectors: Design, Fabrication, and Characterization," *IEEE* Sens. J., **15**(6), 3241-3248 (2015).

[6] J. H. Cole, C. Kirkendall, A. Dandridge, G. Cogdell, and T. G. Giallorenzi, "Twenty-five years of interferometric fiber optic acoustic sensors at the naval research laboratory," J. Wash. Acad. Sci., **90**(3), 40-57 (2004).

[7] K. Huang, and M. Hossein-Zadeh, "Acousto-Optical transducer with optomechanical gain," *IEEE* Photon. Techno. Lett., **30**(22), 1960-1963 (2018).

[8] J. A. Bucaro, and H. D. Dardy, "Fiber-Optic hydrophone," J. Acoust. Soc. Am., **62**(5), 1302-1304 (1977).

[9] A. K. Talwar, and D. K. Srivastava, "Fibre optics in undersea applications," Def. Sci. J., **34**(1), 85-96 (1984).

[10] A. Hurrell and P. Beard, "Piezoelectric and fibre-optic hydrophones," in *Ultrasonic Transducers*, K. Nakamura, Ed. Oxford, U.K.: Woodhead Publishing, 2012, pp. 621–622.

[11] S. Bilek, "Ultra low noise fiber optic acoustic sensor for underwater applications," M.S. thesis, The Grad school of Eng. and Sc., Bilkent Univ., Çankaya/Ankara, Turkey, (2015).

[12] J. Y. Ma, M. R. Zhao, X. J. Huang, H. Bae, Y. Y. Chen, and M. Yu, “Low cost, high performance white-light fiber-optic hydrophone system with a trackable working point,” Opt. Express., **24**(17), 19008-19019 (2016).

[13] J. G. V. Teixeira, I. T. Leite, S. Silva, and O. Frazão, “Advanced fiber-optic acoustic sensors,” Photonics Sensors, **4**(3), 198-208 (2014).

[14] C. Jan, W. Jo, M. J. F. Digonnet, and O. Solgaard, “Photonic-Crystal-Based fiber hydrophone with sub-100 μPa/√Hz pressure resolution,” *IEEE* Photon. Techno. Lett., **28**(2), 123-126 (2015).

[15] I. F. Akyildiz, D. Pompili, and T. Melodia, “Underwater acoustic sensor networks: research challenges,” Ad. Hoc. Networks., **3**(3), 257-279 (2005).

[16] J. D. Holmes, and A. Kukulya, “Characteristics of an autonomous underwater vehicle with a towed hydrophone array,” in *Proc. IEEE OCEANS conf.*, Boston, MA, USA, 2006, pp. 1-5.

[17] G. B. Jacobs, “Laser hydrophone and virtual array of laser hydrophones,” U.S. Patent 5504719A, Sep. 19, 1974.

[18] J. D. Holmes, W. M. Carey, J. F. Lynch, A. E. Newhall, and A. Kukulya, “An autonomous underwater vehicle towed array for ocean acoustic measurements and inversions,” in *Proc. IEEE* OCEANS *Conf.*, Brest, France, 2005, pp. 1058-1061.

[19] P. H. Dahl, J. H. Miller, D. H. Cato, and R. K. Andrew, “Underwater ambient noise,” Acoust. Today., **2**, 23-33 (2007).

[20] C. M. G. Gussen, P. S. R. Diniz, and L. R. Campos, “A survey of underwater wireless communication technologies,” J. Commun. Inf. Sys., **31**(1), 242–255 (2016).

[21] H. Rokhsari, T. J. Kippenberg, T. Carmon, and K. J. Vahala, “Radiation pressure driven micro-mechanical oscillator,” Opt. Express., **13**(14), 5293-5301 (2005).

[22] M. Hossein-Zadeh, and K. J. Vahala, "Optomechanical oscillator on a silicon chip", Invited paper, *IEEE* J. Sel. Top. Quantum Electron., special issue on Silicon Photonics, **16**(1), 276-287 (2010).

[23] X. Jiang, M. Wang, Mark C. Kuzyk, T. Oo, Gui-Lu Long, and H. Wang, “Chip-based silica microspheres for cavity optomechanics,” Opt. Express., 23(21), 27260-27265 (2015).

[24] M. Hermouet *et al*., "1 million-Q optomechanical microdisk resonators for sensing with very largescale integration," in *Proc. SPIE 10491, Microfluidics, BioMEMS, and Medical Microsystems XVI*, San Francisco, CA, USA, 2018, pp. 1-4.

[25] T. Tetsumoto, and T. Tanabe, "High-Q silica zipper cavity with strong opto-mechanical coupling for optical radiation pressure driven directional switching," in *IEEE* Photonics Conference San Diego, CA, USA 2014, pp. 126-127.

[26] A. Grine *et al*., "Frequency noise of silicon nitride optomechanical oscillators with integrated waveguides," in *Proc. International conference on optical MEMs and nanophononics*, Lausanne, Switzerland, 2018, pp. 18-19.

[27] F. Liu, and M. Hossein-Zadeh, "On the spectrum of the radiation-pressure -driven optomechanical oscillator and its application in sensing," Opt. Commun., **294**, 338-343 (2013).

[28] F. Liu, and M. Hossein-Zadeh, "Characterization of Optomechanical RF frequency Mixing/Down-Conversion and its Application in Photonic RF Receivers", *IEEE* J. LightWave. Techno., **32**(2), 309-317 (2014).

[29] K. Huang, and M. Hossein-Zadeh, "Injection locking of optomechanical oscillators via acoustic waves," Opt. Express., **26**(7), 8275-8288 (2018).

[30] M. L. Gorodesky, and V. S. Ilchenko, "Optical microsphere resonators: optimal coupling to high-Q whispering-gallery modes," J. Opt. Soc. Am. B., **16**(1), 147-154 (1999).

[31] T. Carmon, H. Rokhsari, L. Yang, T. J. Kippenberg and K. J. Vahala, "Temperal behavior of radiation-pressure-induced vibrations of an optical microcavity phonon mode," *Phys. Rev. Lett*., **94**(22), Art. no. 223902 (2005).

[32] G. C. Righini et al., "Whispering gallery mode microresonators: Fundamentals and applications," Ricista. Del. Nuovo. Cimento., **34**(7), 435-488 (2011).

[33] A. G. Krause, M. Wigner, T. D. Blasius, Q. Lin, O. Painter, "A high-resolution microchip optomechanical accelerometer," Nature, **6**, 768-772 (2012).

[34] C. Li, X. B. Peng, H. Zhang, C. Wang, S. C. Fan, and S. Q. Cao, "A sensitivity enhanced flexible acoustic sensor using polished fiber Bragg grating," *Measurement*, **117**, 252-257 (2018).

[35] M. Stojanovic, “On the relationship between capacity and distance in an underwater acoustic communication channel,” in *Proc. WUWNet’06 Proceedings the 1st ACM international workshop on Underwater networks*, Los Angeles. CA, USA, 2006. pp. 41-47.

[36] M. Stojanovic, “Underwater acoustic communications,” *in Proc. Electron/International.*, Boston, MA, USA, 1995, pp. 435-440.

[37] T. J. Hajenko and C. R. Benson, “The high frequency underwater acoustic channel,” in *Proc. IEEE OCEANS Conference.*, Sydney, NSW, Australia, 2010, pp. 1-3.

[38] A. Kaya and S. Yauchi, “An acoustic communication system for subsea robot,” in *IEEE OCEANS Conference*, Seattle, WA, USA, 1989, pp. 765-770.

[39] J. Younce, A. Singer, T. Riedl, B. Landry, A. Bean, and T. Arikan, “Experimental results with HF underwater acoustic modem for high bandwidth applications,” in *49th Asilomar Conference on Signals, Systems and Computers*, Pacific Grove, CA, USA, 2015, pp. 248-252.

[40] Y. J. Huang, J. G. F. Flores, Z. Cai, M. Yu, D-L Kwong, G. Wen, L. Churchill, C. W. Wong, “A low frequency chip-scale optomechanical oscillator with 58 kHz mechanical stiffening and more than 100th- order stable harmonics,” Scientific Reports, **7**, Art. no. 4383 (2017).

[41] J. Zheng, Y. Li, M. S. Aras, A. Stein, K. L. Shepard, *and* C. W. Wong, “Parametric optomechanical oscillations in two-dimensional slot-type high-Q photonic crystal cavities,” Appl. Phys. Lett., **100**(21), Art. no. 211908 (2012).

[42] T. Nakamura, Y. Sato, T. Kamakura, and T. Anada, “Sound pressure field focused using biconcave acoustic lens for normal incidence,” Jpn. J. Appl. Phys., **43**(5B), 3163-3168 (2004).

[43] J. T. Welter, S. Sathish, D. F. Christensen, P. G. Brodrick, J. D. Heebl and M. R. Cherry, “Focusing of longitudinal ultrasonic waves in air with an aperiodic flat lens,” J. Acoust. Soc. Am., **130**(5) 2789-2796, (2011).

[44] H. Davies, "A review of some of the characteristics of epoxy resins used in electrical components," Proceedings of the IEE - Part B: Electronic and Communication Engineering, **109**(21), 259-265 (1962).

[45] D. Callens, C. Bruneel and J. Assaad, “Matching ultrasonic transducer using two matching layers where one of them is glue,” NDT&E International, **37**(8), 591-596 (2004).

Chapter 7

Dynamics of coupled oscillators and their applications in sensing

7.1 Introduction

Resonators and oscillators are key elements in a wide variety of natural and manmade systems. As such understanding and exploiting their dynamics both as isolated devices and members of coupled systems has been the subject of intensive investigation for more than a century. The advent of optomechanical resonators (OMRs) that support strong coupling between optical and mechanical modes resulting in self-sustained optomechanical oscillations, has created new opportunities for device development and implementation of coupled oscillatory systems.

For decades, the dynamics of coupled oscillators remains a subject of active investigation. Many theoretical papers reported important findings in the context of coupled homogeneous oscillators [1-7] and heterogeneous oscillators [8-10]. However, experimental work is needed to verify theoretical predictions against noise mechanisms, parasitic effects, and unexpected coupling mechanisms. Experimental research has considered coupled homogeneous oscillators in various domains, such as biological oscillators [11], optical oscillators [12, 13], electrical oscillators [14-16], optomechanical oscillators [17], chemical oscillators [18], mechanical oscillators [19], optoelectronic oscillators [20, 21] and so on. While several experimental works have dealt with coupled homogeneous oscillators, a relatively unexplored area is the study of interactions between physically dissimilar oscillators [22-24].

Instances of coupled heterogeneous oscillators may be found in many biological systems. An example is provided by the cardiorespiratory interactions between the lungs and the heart, with each having different temporal variations; the respiratory oscillation is near sinusoidal [25], while the heartbeat has a more complex behavior that may vary due to a disease or other factors. The lungs may be considered as a single oscillator [26] while the heart is composed of numerous oscillating cells [27, 28]. There is scientific evidence that arrhythmia and other cardiac disorders are associated with changes in other oscillations in the body, such as neuronal and circadian [29, 30].

It is therefore important to understand how physically dissimilar oscillators interact with each other and what are the possible causes for dramatic changes in their dynamics. Unfortunately, experimentation with biological systems is not easy due to the weak and irregular nature of their interactions [22] and most importantly due to the inherent difficulty of isolating the oscillating entities and quantifying their coupling. As such, experimental platforms based on non-biological systems may provide a proxy for much more complex biologically systems and pave the way toward a better understanding of their behavior. For example, Prasad *et al*. observed a phase-flip bifurcation, or a transition from in-phase synchrony to out-of-phase synchrony as the coupling delay between two oscillators is increased in an electrical circuit [31]; later, Adhikari *et al*. observed similar transitions in neuron models involving a large number of interacting neurons [32].

In this chapter the outcomes of the experimental and theoretical studies on coupled physically dissimilar oscillators are presented. The studies include characterization of the dynamics (synchronization, bifurcation, chaos and so on) of the coupled oscillatory systems as well as exploring their applications (i.e., sensing).

More specifically, the coupling oscillatory systems include Colpitts oscillators (a type of electronic oscillator), optoelectronic oscillators (OEOs) and optomechanical oscillators (OMOs). The fundamental differences between these oscillators make the resulting systems highly heterogenous with interesting dynamical behavior. These systems may have different natural frequencies: typically, kHz ~ MHz, kHz ~ GHz, and ~MHz in the Colpitts oscillators, OEOs, and OMOs, respectively. Some features of the oscillators we studied here are listed in table 7.1.

Table 7.1 The oscillators studied in this chapter.

Oscillators	Kind	Log_{10}(fre (Hz))	Oscillation nature
OMO	Optomechanics	5-8	Mechanical, Optical
OEO	Optoelectronics	4-9	Electrical, Optical
Colpitts	Electronics	4-9	Electrical

7.2 Cluster synchronization in coupled Colpitts oscillators

Because the complexity of the OMOs and OEOs, direct coupling and exploration of them are not easy and which need experimental and theoretical working experience. Considering the simple feature and well-developed models of the Colpitts oscillators, the first system selected for our study includes four identical coupled Colpitts oscillators. This first study lays the path for building and studying more complex oscillatory systems based on OMOs and OEOs. Moreover, the specific configuration used to couple four Colpitts oscillator supports interesting dynamics that was not observed before.

By coupling eletrical Colpitts oscillators, we are the first to study cluster synchronization in a fully analog symmetrical multilayer network with both diffusive and non-diffusive coupling. Despite its simplicity, this analog electronic system not only represents the smallest multilayer network with multiple symmetries but also captures the uncertainties and fluctuations present in real and more complex physical systems. We describe the possible cluster synchronizations of the system as we vary coupling parameters. We experimentally observe and theoretically characterize clusters of nodes that synchronize on different time evolutions. The system is fully analog, where other studies have used a computer interface to implement coupling [33, 34, 35].

7.2.1 Observation of Cluster synchronization in coupled Colpitts oscillators

Electronic circuits are ideal test beds for the study of nonlinear behavior in networks [36]; we choose to use coupled four classical Colpitts oscillators.

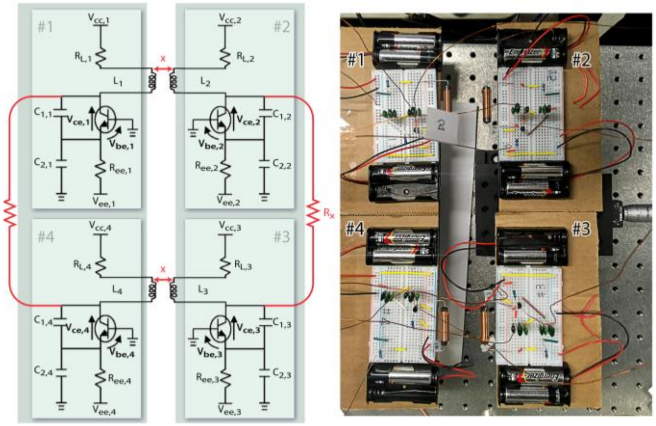

(a) (b)

Fig. 7.1. Experimental setup for the cluster synchronization in multilayer networks. (a) Ring of four Colpitts oscillators coupled to their neighbors via resistor R_x and mutual magnetic coupling between the tank inductors, controlled by the inductor separation x. From upper left going clockwise, oscillators 1, 2, 3, and 4. Internal connections of each Colpitts are represented in black, coupling between Colpitts is shown in red. (b) A photography of the system.

As shown in the Fig. 7.1, the Colpitts oscillator is a simple electronic oscillator based on a bipolar junction transistor (BJT) that uses two center-tapped capacitors in series with a parallel inductor as its resonance tank circuit.

The single Colpitts oscillator can be described by:

$$C_1\frac{dV_{ce}}{dt} = I_L - I_C. \tag{7.1}$$

$$C_2\frac{dV_{be}}{dt} = -\frac{V_{ee}+V_{be}}{R_{ee}} - I_b - I_L. \tag{7.2}$$

$$L\frac{dI_L}{dt} = V_{cc} - V_{ce} + V_{be} - I_L R_L. \tag{7.3}$$

where V_{ce} is the voltage drop between the collector and the emitter of the transistor, V_{be} is the voltage drop between the base and the emitter of the transistor. V_{cc} and V_{ee} are applied voltages with values of 3.2 V and -1.6 V, respectively. I_{b} and I_{c} are the current of the base and the collector, respectively. The transistor operates in two regimes, forward active and cutoff. We can describe this behavior with a piecewise function [37]:

$$I_b = \begin{cases} 0 & , V_{be} < V_{th} \\ \frac{V_{be}-V_{th}}{R_{on}}, & V_{be} \geq V_{th} \end{cases}, \qquad I_c = \beta_f I_b \ . \tag{7.4}$$

We use a 2N2222 transistor. V_{th} = 0.75 V is the threshold voltage, R_{on} = 325 Ω is the resistance, and β_{f} = 200 is the current gain of the transistor. We create a multilayer network with the four Colpitts oscillators connected by two kinds of coupling, resistive and magnetic, following the schematic in Fig. 7.1. The proposed circuit can be seen as a two-layer network. Each layer contains two oscillators, with resistive intralayer coupling; the magnetic coupling forms the interlayer coupling, as shown in Fig. 7.2. Because the oscillators in the two layers are identical, the multilayer network can be flattened to obtain a multidimensional network.

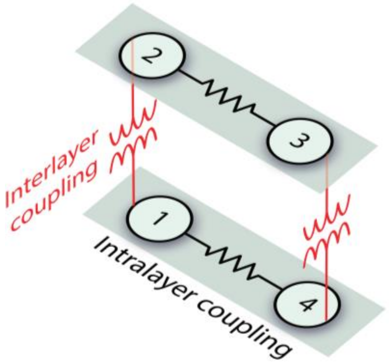

Fig. 7.2. Visualization of multidimensional network as a multilayer network. Nodes 2 and 3 belong to one layer, and nodes 1 and 4 belong to the other. Resistive coupling is intralayer coupling; magnetic coupling is interlayer coupling.

The four nodes, each a Colpitts oscillator, form a ring with coupling alternating between resistive and magnetic. We achieve resistive coupling by connecting the collectors of transistors in pairs of oscillators through a resistor R_x; we tune the coupling by connecting resistors of the desired value. To achieve magnetic coupling, we bring the inductors of two nodes sufficiently near, such that the mutual inductance M_{ij} becomes large enough; we tune the coupling by changing the inductor separation distance x. The dynamics of the network shown in Fig. 7.1 and 7.2 is:

$$C_{1,i}\frac{dV_{ce,i}}{dt} = I_{L,i} - I_C\left(V_{be,i}\right) + \frac{1}{R_x}\sum_{j=1}^{N} \Re_{ij}\left[\left(V_{ce,j} - V_{ce,i}\right) - \left(V_{be,j} - V_{be,i}\right)\right]. \qquad (7.5)$$

$$C_{2,i}\frac{dV_{be,i}}{dt} = -\frac{V_{ee}+V_{be,i}}{R_{ee,i}} - I_b\left(V_{be,i}\right) - I_{L,i} - \frac{1}{R_x}\sum_{j=1}^{N} \Re_{ij}\left[\left(V_{ce,j} - V_{ce,i}\right) - \left(V_{be,j} - V_{be,i}\right)\right].$$

7.6)

$$L_i\frac{dI_{L,i}}{dt} = V_{cc} - V_{ce,i} + V_{be,i} - I_{L,i}R_{L,i} - \sum_{j=1}^{N} M_{ij}\mathfrak{M}_{ij}\frac{dI_{L,j}}{dt}. \qquad (7.7)$$

where i =1,…4 is the index of the oscillator, L_i is the inductance, $C_{1,i}$, $C_{2,i}$ are the capacitances of the circuit components (see Fig. 7.1), $V_{ce,i}$ is the voltage drop between the collector and the emitter of the transistor, and $V_{be,i}$ is the voltage drop between the base and the emitter. V_{cc} and V_{ee} are applied voltages, I_b and I_c are the current of the base and the collector, respectively. These two currents are the nonlinear terms in the system, they are zero below a threshold voltage and increase linearly above this cutoff as manifested in Eq. (7.4). In a BJT these currents are related through $\beta = \Delta I_c = \Delta I_b \approx I_c = I_b$, where β is the BJT amplification factor. The magnitudes of the resistive and magnetic coupling coefficients are $1/R_x$ and $M_{ij} = k\sqrt{L_i L_j}$, respectively. k characterizes the mutual inductance and is roughly proportional to $1/x^2$, k is positive if the currents induced by mutual and self-inductance are in phase and negative if they are antiphase. Note that the resistive and magnetic couplings are different in nature and therefore enter the dynamic equations in different forms. Resistive coupling is diffusive and affects the current. Magnetic coupling is non-diffusive, differential [38], and affects the voltage. The adjacency matrices $\boldsymbol{\mathfrak{R}}$ and $\boldsymbol{\mathfrak{M}}$ describe how the oscillators are connected to one another by resistive and magnetic coupling, respectively. In our four-member ring network, $\boldsymbol{\mathfrak{R}}$ and $\boldsymbol{\mathfrak{M}}$ are:

$$\mathfrak{R} = \begin{bmatrix} 0 & 0 & 0 & 1 \\ 0 & 0 & 1 & 0 \\ 0 & 1 & 0 & 0 \\ 1 & 0 & 0 & 0 \end{bmatrix}. \tag{7.8}$$

$$\mathfrak{M} = \begin{bmatrix} 0 & 1 & 0 & 0 \\ 1 & 0 & 0 & 0 \\ 0 & 0 & 0 & 1 \\ 0 & 0 & 1 & 0 \end{bmatrix}. \tag{7.9}$$

In order to calibrating the magnetical coupling strength, we have to measure the relationship between inductor separation, x, and mutual inductance, M_{ij}, we first measured the inductances L_1 and L_2 of the two inductors. We then connect the first inductor (L_1) and a resistor to a signal generator which applies a sinusoidal voltage with known amplitude. The frequency of the signal we used is 100 kHz, which is comparable with the frequencies of the Colpitts oscillator investigated in the paper. We then aligned the second inductor (L_2) to the first inductor and varied the distance x. We measure the current in the first inductor, $I_{L,1}$, and the induced voltage in the second inductor, $V_{L,2}$. With the relationship $V_{L,2} = M_{1,2}\dot{I}_{L,1}$ and $M_{1,2} = k\sqrt{L_1 L_2}$, we can derive k. Figure 7.3 shows the experimental measurements of k versus the inductor separation. We found that $k = 27.4/x^2 + 0.014$, where x is the center-to-center separation of the inductors in millimeters.

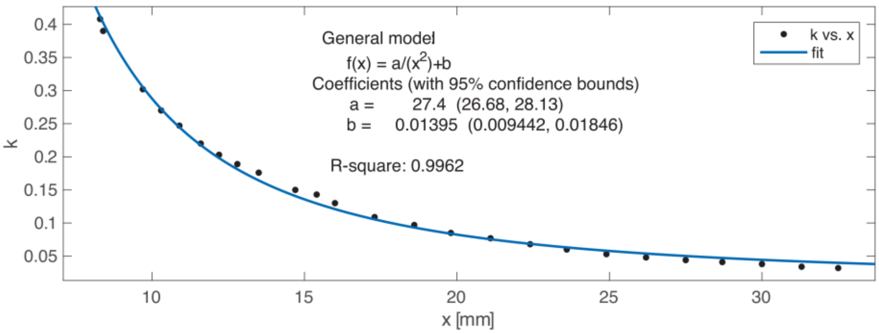

Fig. 7.3. Experimental fitting of the mutual induction M versus the inductor separation x. On the vertical axis we report the value of the parameter $k = M_{1,2}/\sqrt{L_1 L_2}$,

The parameters for the components used in the experiment are listed in table 7.2.

Table 7.2. Experimental values of Colpitts oscillator parameters

Parameter	Osc#1	Osc#2	Osc#3	Osc#4
R_L (Ω)	27.4	27.4	27.3	27.3
R_{ee} (Ω)	74.9	75.1	74.8	75.2
L (μH)	97.06	93.02	95.42	96.80
C_1 (nF)	61.29	63.10	59.17	58.91
C_2 (nF)	62.27	60.42	61.03	60.86

After calibration, we measured the magnetic coupling range achievable for the setup. The oscillators 2 and 3 (see Fig. 7.1(b)) are mounted on a caliper, we can set x precisely and identically for both inductor pairs. Due to physical constraints of the system (for example, once the inductors are touching, they can't get any closer), magnetic coupling is restricted to the range $0.03 < |k| < 0.4$.

By inspection of the four-node system (Fig. 7.1), we observe three symmetries present in the multilayer network, i.e., three permutations of the nodes which leave the network unchanged:

(1) vertical symmetry, permuting 1 with 4 and 2 with 3;

(2) 180° rotation, permuting 1 with 3 and 2 with 4;

(3) horizontal symmetry, permuting 1 with 2 and 3 with 4.

These permutations, along with the identical permutation (that maps each node to itself), form a mathematical group $\mathcal{G}$ that we call *the symmetry group of the multilayer network*. Subgroups of $\mathcal{G}$ define possible cluster patterns [39].

We performed experiments at five values of R_x (27 Ω, 300 Ω, 510 Ω, 750 Ω, and 1000 Ω) and varied k from -0.03 to -0.4 for the parallel inductor configuration and from 0.03 to 0.4 for the antiparallel inductor configuration. To detect the presence of multiple attractors, we first increase then decrease k, guided by the theoretically predicted hysteresis between the periodic in-phase and the periodic antiphase solutions. The top left-hand panel of Fig. 7.4 shows the cluster state observed at each experimental measurement. Figure 7.4 shows broad agreement between our experimental and theoretical results. Each of the four cluster types (reported in the bottom boxes of Fig. 7.4) observed experimentally is predicted by the theoretical analysis. The system exhibits bi-stability between the fully synchronized state [(A), gray] and the vertical two-cluster state [(C), pink] for large ranges of k and R_x. We observe the fully synchronized solution for large positive magnetic coupling and small negative coupling; we observe the vertical two cluster solution for small positive and large negative coupling. Near $k = 0.12$, we see the quasiperiodic vertical two-cluster state [(D), magenta]. At $k = 0.05$ and $R_x = 27\ \Omega$, we observe the vertical two-cluster with a phase separation near π=2 rad [(B), turquoise].

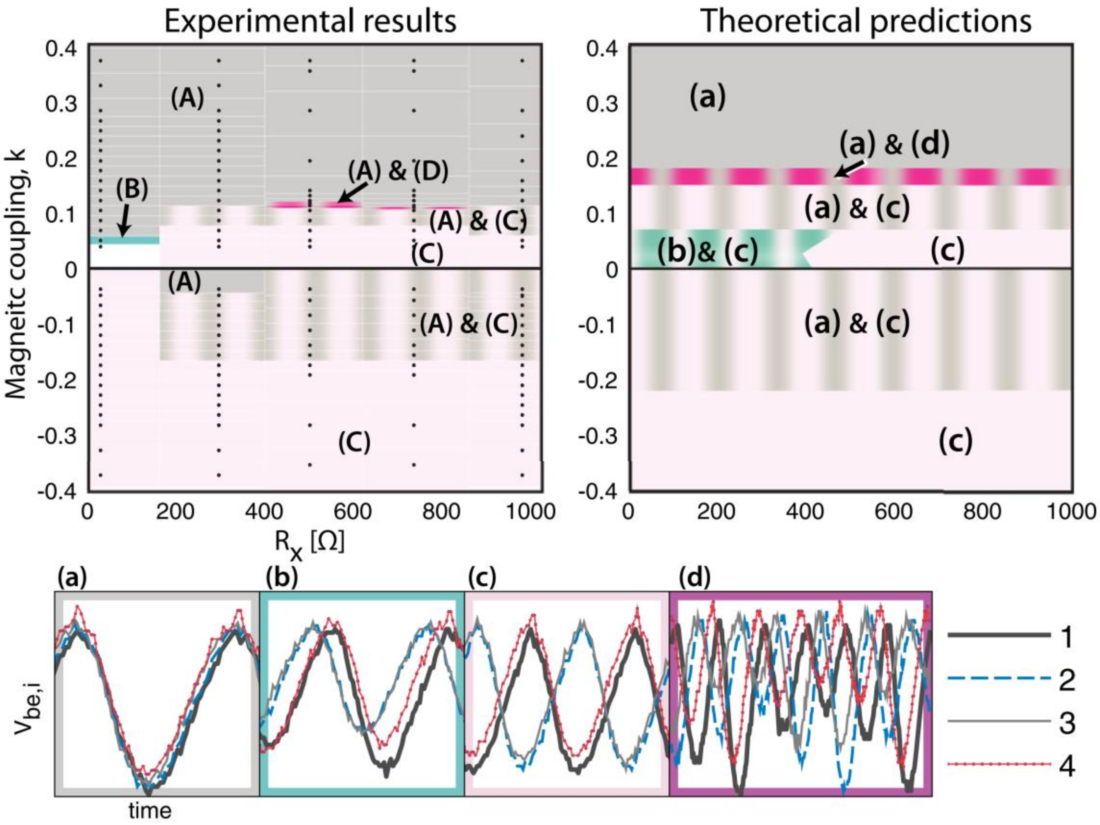

Fig. 7.4. Comparison between experimental results and theoretical predictions. Capital letters in figure indicate experimental observations; lowercase letters indicate theoretical predictions. [(A), (a), gray] one-cluster state; [(C), (c), pink] vertical two-cluster state; [(B), (b), turquoise] vertical two-cluster state, two-cluster with a phase offset up to π/ 2; [(D), (d), magenta] quasi-periodic solution of the vertical two-cluster state; [white] no stable frequency locking. Stripes of two colors represent bi-stability between the two states represented by each color. (Top left) Experimentally observed cluster states. Black dots represent individual experimental measurements; we infer a color mesh from these results. (Top right) Theoretical prediction of cluster states. (Bottom) Experimental time series of $V_{be}(t)$ demonstrating clusters corresponding to the theoretical predictions.

7.2.2 Importance of this work

This work is the first study on cluster synchronization in multilayer networks with symmetries. We show that a small network with well-understood periodic Colpitts oscillators exhibits rich dynamical behavior such as bi-stability, hysteresis, and quasi-periodicity. This is the first experimental observation of a clustered quasiperiodic state. The coworkers on this work [40] did a lot of analysis that innovatively combines bifurcation analysis and the computation of transverse Lyapunov exponents, allowing us to overcome limitations of each individual approach. First, unlike the bifurcation analysis of the full system, our approach can handle multiple symmetries using standard software [41, 42]. Second, compared to the computation of transverse Lyapunov exponents alone, it can find any possible cluster pattern even in the presence of multiple attractors of the quotient networks. The interplay of theory and experiments was essential for an in-depth phenomenological understanding of the system behavior; experiments allowed us to understand which theoretically predicted cluster states were observable, while theory helped us identify hard to find cluster states. Note that even though we have applied our analysis to a very simple multilayer network, it is possible to scale the described approach to networks with any numbers of nodes or layers. This scaling is nontrivial and requires the definition of the group of symmetries of a multilayer network; Our work shows how different interaction layers influence the overall state of the system; applications of the described theory can be found in a variety of fields where patterned behavior and multilayer systems arise. The method requires three ingredients: (1) a dynamical system describing the network, (2) multiple kinds of interactions, and (3) patterned behavior. Understanding the dynamical behavior of symmetric multilayer networks may play an important role in the design and development of neuromorphic computational systems [43]. To our knowledge, none of the studies on neuromorphic systems has considered dissimilar interactions between nodes, which seems to be an essential feature of most biological networks such as the brain [44] as well as a contributor to the overall robustness of a system [45, 46].

7.3 Theoretical investigation of the coupled OMO and OEO

Both optomechanical oscillator (OMO) and optoelectronic oscillator (OEO) can be considered as hybrid oscillator. OMO's operation involves an optical mode and a mechanical mode [47] and its output is optical power modulated by the cavity's mechanical oscillation. OEO involves the optical signal, optical delay and electric voltage [48]. OEO's output can be modulated optical power or modulated eletrical signal (before or after the photodiode in the OEO loop). The coupling between OMO and OEO can be achieved using both optical and electrical signals. Compared to eletrical coupling, optical coupling eliminates the use of electrical components and the electro-optical modulators, which makes the system less complicated and free from the electromagnetic interference. However, the challenge for optical coupling is the fact that the OMO only works when the optical wavelength matches the resonant wavelength of an optical mode.

Figure 7.5(a) is the configuration of the coupled OMO and OEO system, while Fig. 7.5(b) is the proposed circuits of the coupled system.

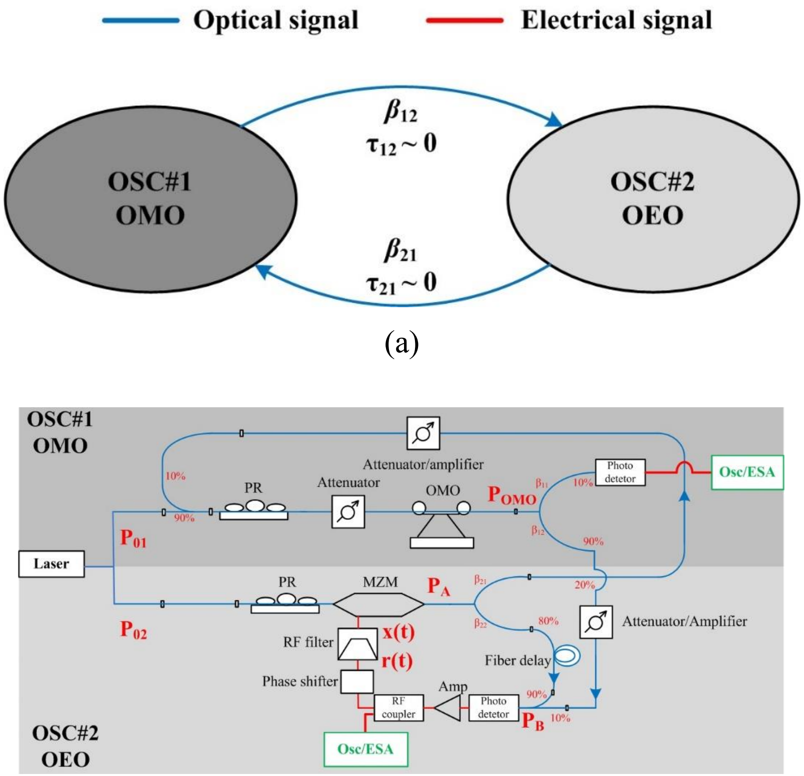

(a)

(b)

Fig. 7.5. (a) The configuration and (b) circuits for proposed experimental setup of the coupled OEO and OMO system.

Here a microtoroidal OMO and a single loop fiber delayed OEO are used. In Fig. 7.5(b) the OMO and the OEO are coupled through the optical fibers (via optical signal), the attenuator (or optical amplifier) in each coupling path is used to control the coupling strengths by controlling the transmitted optical power. The β_{12} and β_{21} represent the coupling strengths from OMO to OEO and from OEO to OMO. The coupling strength β_{12} is defined as the ratio between the optical power coupled from the OMO to OEO and the optical power in the OEO loop before coupling, the coupling strength β_{21} is defined as the ratio between the optical power coupled from the OEO to OMO and the optical power in the OMO loop before coupling.

Here we assume the coupling delay τ_{12}, τ_{21} is zero ($\ll 1/f \sim 0.2\mu s$, generally $f \sim 5$

MHz is the OMO and OEO oscillation frequency) if the fibers that connect the OMO and OEO are not too long ($\ll$ 41 m, 41 m corresponds to a delay of ~ 0.2 μs).

In Fig. 7.5(b) the optical power from a 1550 nm laser is split into the OMO and OEO loops by using a 50/50 fiber coupler. In the OMO loop 10% of the optical output from the OMO is directed to a photodetector for monitoring and 90% is directed to the photodetector in the OEO loop through an optical power attenuator or amplifier as coupled power. In the OEO loop 20% of the optical output from the Mach-Zander modulator (MZM) is directed to the OMO through a fiber and an optical attenuator or amplifier as coupled power, another 80% of the optical power is feed back to the photodetector inside the OEO loop. The eletrical output of the OEO can be coupled out from the RF coupler and directed to an oscilloscope (Osc) and an eletrical spectrum analyzer (ESA) for monitoring.

The dynamics of single OMO and OEO have been theoretically investigated in Refs. [49] and [50]. The state equations of the coupled OMO and OEO can be derived with the inspiration from these two research papers and maybe written as:

$$\Delta\omega(t) = \Delta\omega_0 + \frac{r(t)}{R_0}\omega_0. \tag{7.10}$$

$$B(t) = \sqrt{P_{01}(t) + \beta_{21}P_{02}cos^2(x(t) + \emptyset_0)}. \tag{7.11}$$

$$P_{OMO}(t) = |\left(1 - \frac{\tau_0\alpha c}{2n}\right)B(t) + i\sqrt{\frac{\tau_0\alpha c}{n}}A(t)|^2. \tag{7.12}$$

$$m_{eff}\frac{d^2r}{dt^2} + b\frac{dr}{dt} + kr = \frac{2\pi n}{c}|A(t)|^2. \tag{7.13}$$

$$\frac{dA}{dt} + A\left[\frac{\alpha c}{n} - i\Delta\omega(t)\right] = iB(t)\sqrt{\frac{\alpha c}{n\tau_0}}. \tag{7.14}$$

$$\frac{dx}{dt} = -\left(\frac{1}{\tau_L} + \frac{1}{\tau_H}\right)x(t) - \frac{1}{\tau_L}u_2(t) + \frac{1}{\tau_L}RG(\beta_{22}P_{02}cos^2(x(t-\tau) + \emptyset_0) + \beta_{12}P_{OMO}(t)). \tag{7.15}$$

$$\frac{du_2}{dt} = \frac{1}{\tau_H} x(t). \tag{7.16}$$

The first five equations describe the dynamics of OMO and the last two describe the dynamics of the OEO. The coupling terms (β_{12}, β_{21}) are included in Eq. (7.11) and Eq. (7.15). Here, r is the radial displacement of the OMO; $\Delta\omega_0 = \omega_L - \omega_0$ is the pre-set detuning between the pump laser frequency ω_L and the optical resonant frequency ω_0 of the OMO; R_0 is the radius of the microcavity (microtoroid); $\Delta\omega$(t) is the real time frequency detuning between the pump frequency and OMO optical resonant frequency; B(t) is the real time optical field coupled into the OMO; P_{01} is the optical input (pump) power to the OMO from the laser; P_{02} is the optical input (pump) power to OEO from the laser; $\O_0$ is the fixed phase set by the bias voltage of the MZM; P_{OMO} is the output power of OMO; α is the internal optical loss in the OMO (which defines its intrinsic quality factor); τ_0 is the roundtrip time of the photon inside the OMO; n is the refractive index of the microtoroid; A(t) is the optical field inside OMO; m_{eff} is the effective mass of the OMO's mechanical mode; b is the corresponding mechanical dissipation; k is the spring constant of the OMO; x(t) is the output voltage of the RF filter; u_2 is a state vector of the filter system; τ_L and τ_H are the time constants used to construct band pass filters in the OEO loop; R is the responsivity of the photodetector in the OEO loop; G is the gain of the OEO loop; τ is the total time delay of the OEO loop.

Based on typical OMOs and OEOs that can be fabricated in the lab, we choose the parameters' values of the OMO and OEO as listed in Table 7.3 for our simulation.

Table 7.3 Parameters of the OMO and OEO used in the simulation

Parameters	P_{01}	P_{02}	f_{OMO}	τ	τ_L	τ_H
Values	300 μW	50 μW	5.455 MHz	5.7 μs	15.9 ns	159 ns
Parameters	$Ø_0$	λ_0	$\Delta\omega_0$	R_0	R	G
Values	-π/4	1461 nm	8.87×10^7 rad	29 μm	1 V/W	3×10^4

1) *The OMO injection locking the OEO*

First, we assume $\beta_{21} = 0$ and solving the Eqs. (7.10) ~ (7.16). Figure 7.6 shows the frequency of the OEO ($\omega_{02}/(2\pi)$) and OMO ($\omega_{01}/(2\pi)$) plotted against β_{12}. As we can see the OEO is pulled toward and final injection locked to the OMO when increasing the coupling strength β_{12}.

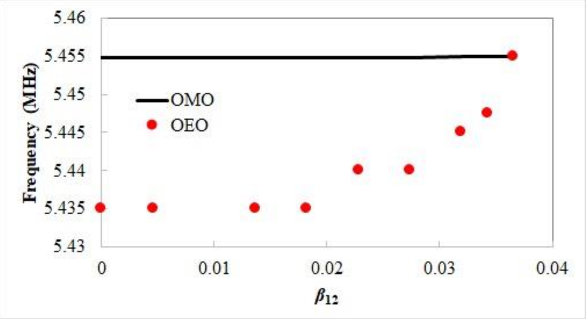

Fig. 7.6. Simulated frequency of OMO and OEO plotted against β_{12}.

2) *The OEO injection locking the OMO*

Next we assume $\beta_{12} = 0$ and solving the equation system. Figure 7.7 shows the frequency of the OMO and OEO plotted against β_{21}.

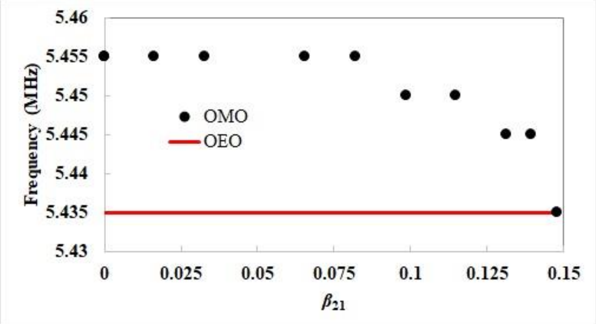

Fig. 7.7. Simulated frequency of OMO and OEO plotted against β_{21}.

3) *The OEO and OMO are bilaterally coupled*

Now both the coupling strengths (β_{12}, β_{21}) are larger than zero, one of the interesting phenomena of the coupled OMO and OEO versus changing coupling strength β_{12} and β_{21} is shown in Fig. 7.8. The intrinsic frequency (prior to coupling) of the OEO and OMO are $f_{\text{OEO,i}} = 5.43$ MHz, and $f_{\text{OMO,i}} = 5.46$ MHz. The figure shows that the OMO and OEO are synchronized when $\beta_{12} = 0.05$ and $\beta_{21} = 0$, with increasing the β_{21} alone the frequency of the synchronized system shifts up and then desynchronize with the frequency of the two oscillators start to move to the opposite directions when β_{21} is larger than 0.13.

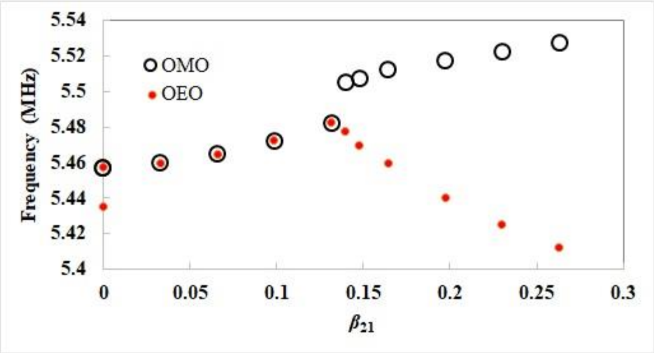

Fig. 7.8. Simulated frequency of OMO and OEO versus β_{21} when β_{12} is fixed at 0.05.

The experimental implementation of the configuration shown in Fig. 7.5(b), is complicated and challenging. The only access to one tunable narrow linewidth laser (required to tune the wavelength to an optical mode of the OMO) with an output optical power less than 7 mW plus the optical loss associated with multiple fiber couplers used in this configuration, this laser power was not sufficient to pump both OMO and OEO, the power will not be enough to pump the OMO for the loss caused by the fiber couplers. As such we weren't able to experimentally verify the above mentioned outcomes.

7.4 The investigation of coupled Colpitts oscillator and OMO

The eletrical Colpitts oscillator used here is the same as the Colpitts oscillator used in section 7.2.1. Considering the only electrical signal in the Colpitts loop as well as the optical signal and eletrical signal in the OMO loop, it is possible to couple these two oscillators electrically. It also possible to revise the Colpitts oscillator by integrating a photodiode to the Colpitts circuits so that the OMO and the Colpitts can be coupled either electrically or optically.

7.4.1 Electrical coupling to a Colpitts oscillator

Before coupling the Colpitts oscillator and the OMO, we have to test which part of the Colpitts oscillator can be used for accepting injected signal. The electronics circuit of the single typical Colpitts oscillator together with the value of the parameters used in our test is shown in Fig. 7.9. The capacitor C_{12} and C_{22} are tunable with the capacitance tunable between 20 pF and 600 pF. In order to couple another oscillator to a Colpitts oscillator, a port should be identified through which an external signal can control the dynamics of the Colpitts. Typically the possible connection ports of the Colpitts circuit that can be used for injection of external voltage or current are the collector port (C), emitter port (E) and base port (B) of the transistor (as shown in Fig. 7.9), basically, injecting the current to the base port could be the most efficient way to perturb the Colpitts oscillator because the current in the base port can get amplified in the transistor provided that the injected current can enter the base port. However, for this typical Colpitts oscillator the base port is grounded, so only the collector port and the emitter port may be used to couple external signals.

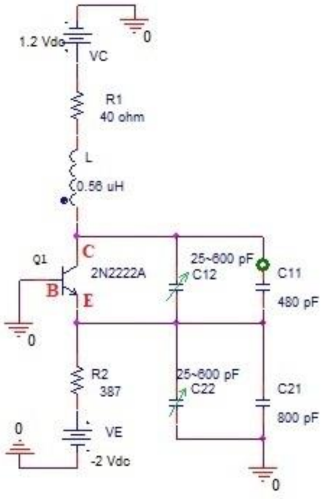

Fig. 7.9. The electrical Colpitts oscillator with the value of the parameters.

We quantify the coupling (or perturbation) efficiency by measuring the locking range of the Colpitts oscillator for given strength of injected signal. As such the coupling efficiency can be measured by injection locking of Colpitts to a harmonic (e.g., generated by a function generator).

1) *Injection locking the Colpitts oscillator through the collector port*

First, we measure lock range of the Colpitts oscillator by injecting the signal to the collector port, the circuit of the setup is shown in Fig. 7.10, the output of the function generator (a sinusoidal voltage) is fed to a homemade voltage buffer and then transmitted to the Colpitts oscillator through the collector port of the transistor. A resistor with value $R_C = 2180\ \Omega$ is used as the coupling resistor. The buffer used here makes the coupling unidirectional (from the function generator to the Colpitts oscillator).

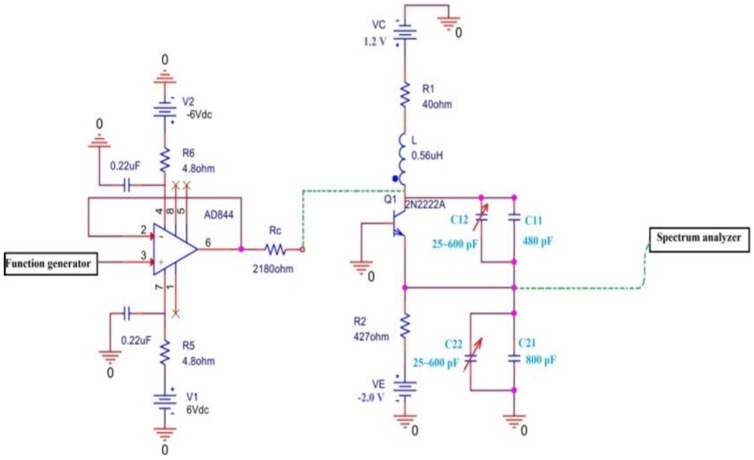

Fig. 7.10. Injection locking of the Colpitts oscillator to a function generator. The injected signal passes through a voltage buffer and then enters the Colpitts oscillator through the collector port. Signal of the Colpitts oscillator is monitored through the emitter port using an eletrical spectrum analyzer.

The oscillation frequency of the Colpitts oscillator can be approximated using the equation:

$$f_{Col} = \frac{1}{2\pi\sqrt{L\frac{C_1C_2}{C_1+C_2}}}. \tag{7.17}$$

The state equation of this system shown in Fig. 7.10 may be written as:

$$C_1\frac{dV_{C1}}{dt} = I_L - I_C + \frac{V_{inj}-(V_{C1}+V_{C2})}{R_C}. \tag{7.18}$$

$$C_2\frac{dV_{C2}}{dt} = \frac{V_E-V_{C2}}{R_2} + I_B + I_L + \frac{V_{inj}-(V_{C1}+V_{C2})}{R_C}. \tag{7.19}$$

$$L\frac{dI_L}{dt} = V_C - V_{C1} - V_{C2} - I_LR_1. \tag{7.20}$$

$$I_B = \begin{cases} 0 & -V_{C2} \le V_{THM} \\ \frac{-V_{C2}-V_{THM}}{R_{ON}} & -V_{C2} > V_{THM} \end{cases}. \tag{7.21}$$

$$I_C = h_{FE}I_B. \tag{7.22}$$

Where V_{inj} is the injected voltage that enters the collector port of the transistor.

2) *Injection locking the Colpitts oscillator through the emitter port*

The second configuration is to injection locking the Colpitts oscillator through the emitter port of the transistor, which is shown in Fig. 7.11. In the setup, the sinusoidal signal generated by the function generator passes though the buffer and the coupling resistor, then injected to the emitter port, the eletrical spectrum analyzer is connected to the collector port of the transistor for monitoring.

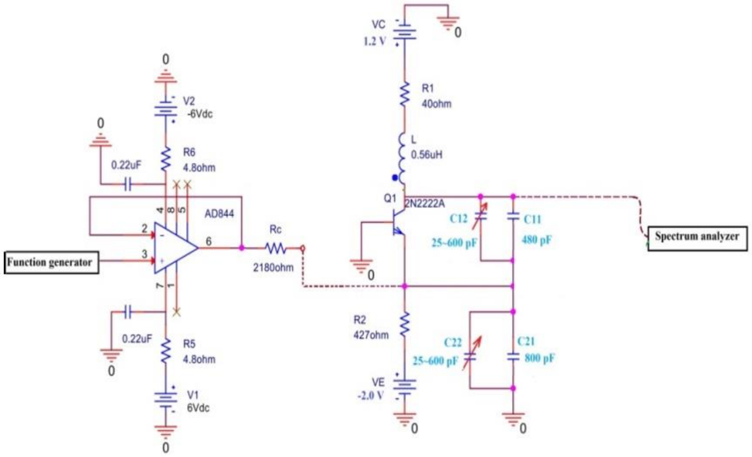

Fig. 7.11. Injection locking of the Colpitts oscillator to a function generator. The signal generated by the function generator passes through a home-made voltage buffer and then directed to the Colpitts oscillator through the emitter port. Signal of the Colpitts oscillator is monitored through the collector port using an eletrical spectrum analyzer.

The state equations of the configuration shown in Fig.7.11 may be written as:

$$C_1 \frac{dV_{C1}}{dt} = I_L - I_C. \tag{7.23}$$

$$C_2 \frac{dV_{C2}}{dt} = \frac{V_E - V_{C2}}{R_2} + I_B + I_L + \frac{V_{inj} - V_{C2}}{R_C}. \tag{7.24}$$

$$L \frac{dI_L}{dt} = V_C - V_{C1} - V_{C2} - I_L R_1. \tag{7.25}$$

$$I_B = \begin{cases} 0 & -V_{C2} \le V_{THM} \\ \frac{-V_{C2} - V_{THM}}{R_{ON}} & -V_{C2} > V_{THM} \end{cases}. \tag{7.26}$$

$$I_C = h_{FE} I_B. \tag{7.27}$$

The measured lock range versus the injected signal strength (rms voltage) for the mentioned two coupling configurations is plotted in Fig. 7.12, we can see that more efficient perturbation could be achieved through the emitter port.

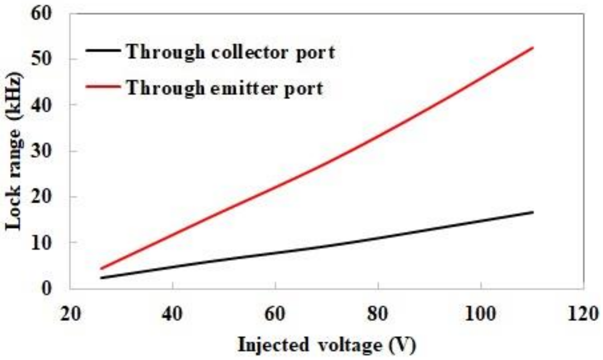

Fig. 7.12. The measured lock range vs. injected signal strength by injecting the signal to the collector port (black line) and emitter port of the transistor (red line).

7.4.2 Optical coupling to Colpitts oscillator

In order to optically couple a Colpitts oscillator to optically assisted oscillators such as OMO or OEO, the Colpitts oscillator should have an optical input port through which an optical signal can affect its dynamics. We have provided such port, by adding a photodiode into the Colpitts oscillator circuit. To examine the efficiency of the optical coupling, we used a modulated optical power to injection locking Colpitts oscillator to a signal generator through the added optical port.

Two possible configurations to integrate the photodiode into the Colpitts oscillator and using modulated optical signal to injection locking the Colpitts is shown in Fig. 7.13.

In Fig. 7.13(a) the photodiode is added between the DC voltage supply and the base port of the transistor while in Fig. 7.13(b) the photodiode is connected between the DC voltage supply and the collector port. The optical power from a laser passes through a Mach-Zadeh modulator (MZM) driven by a function generator, and the modulated optical power is fed to the photodiode, the optical power is converted to photocurrent in the photodiode and perturbs the Colpitts oscillator.

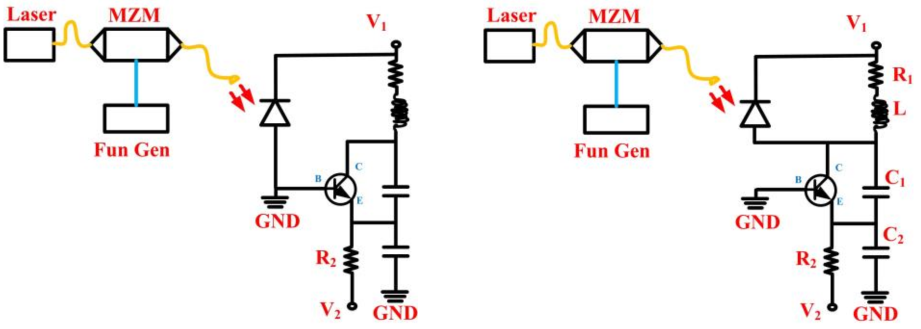

(a) (b)

Fig. 7.13. Modulated optical power is fed to a photodiode integrated with the Colpitts oscillator to enable optical coupling. (a) photodiode is added between the DC voltage supply and the base port. (b) photodiode is added between the DC voltage supply and the collector port. Here, $V_1 = +1.5$ V, $V_2 = -1.5$ V, $R_1 = 40\ \Omega$, $R_2 = 426\ \Omega$, L = 2.2 µH, $C_1 = 363\ \Omega$, $C_2 = 657\ \Omega$. MZM DC bias voltage is 3.1 V.

Figure 7.14 shows the measured locking range of the Colpitts oscillator at different injected photocurrent strengths (peak-peak current) for the first configuration (shown in Fig. 7.13(a)). In the measurement the laser output power is 20 µW, the modulated optical (current) strength can be achieved by changing the RF power applied on the MZM.

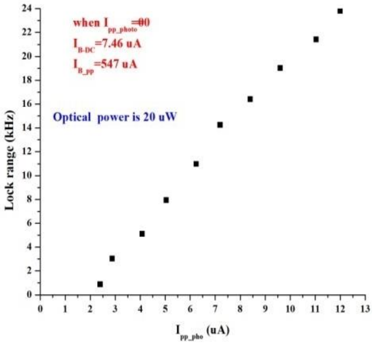

Fig. 7.14. Measured lock range of the Colpitts oscillator shown in Fig. 7.13(a).

The injection locking efficiency for the second configuration (shown in Fig. 7.13(b)) was too low and is not plotted here. For the second configuration, when optical power is 27 µW and modulated photocurrent is $I_{pp\_pho} = 28.8$ µA, the lock range is 1.5 kHz, when the modulated photocurrent is $I_{pp\_pho}=35.0$ µA, the lock range is 2.7 kHz. In conclusion, the Colpitts circuit shown in Fig. 13(a) could be a potential configuration of coupling Colpitts oscillator with other oscillators optically.

7.4.3 Electrical coupling between OMO and a Colpitts oscillator

1) *The OMO unidirectionally coupled to the Colpitts oscillator*

In our first demonstration we inject the electrical signal generated by converting the output of an OMO in a photodetector (PD) to a Colpitts oscillator through the emitter port (that was shown to support efficient locking, see section 7.4.11). Figure 7.15 shows the configuration used to unidirectionally couple OMO to a Colpitts oscillator. The optical output of the OMO is fed to a photodector (PD) where it converted to photovoltage, this voltage is transferred through a buffer (to avoid reverse coupling) and then injected to the emitter port of the transistor through the coupling resistor R_C. The values of the eletrical components are labelled in the figure. For the OMO, $\lambda_0 = 1555.0$ nm, $f_{OMO} = 4.718$ MHz, the optical pump power is $P = 670$ μW, $Q_m = 210$, $m_{eff} = 52$ ng.

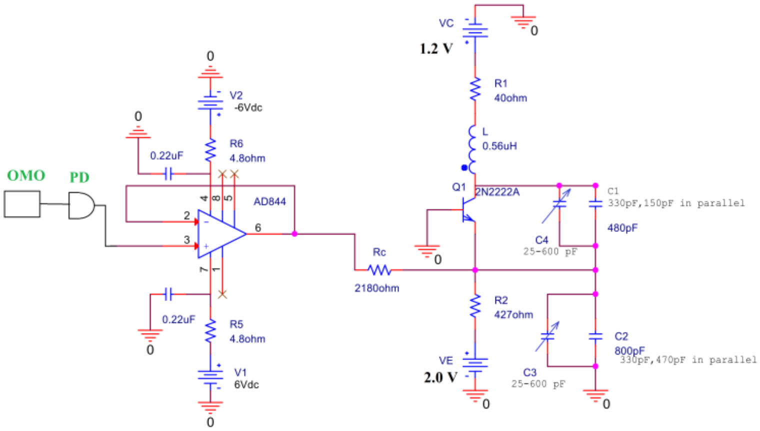

Fig. 7.15. The OMO unidirectionally coupled to the Colpitts oscillator.

Before coupling, the waveform and spectrum of the OMO is measured at an optical pump power of $P = 670$ μW; the waveform of the OMO is measured after the PD (red line) and after the coupling resistor (R_C) (black line), both of which are shown in Fig.7.16(a). The spectrum of the OMO (PD output) is shown in Fig. 7.16(b), Figures 7.16(c) and 7.16(d) are the measured waveforms and spectrum of the Colpitts oscillator respectively.

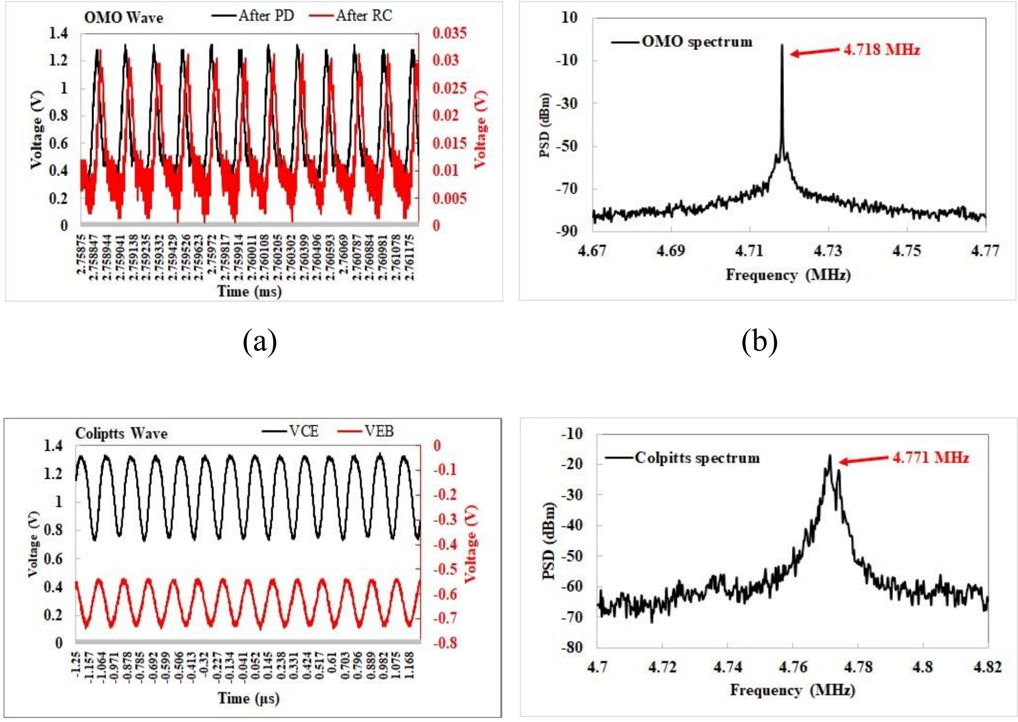

(a) (b)

(c) (d)

Fig. 7.16. The measured output of the two oscillators before coupling. (a) Waveform of the OMO measured after the PD (red line) and measured after the coupling resistor R_C (black line), (b) Spectrum of the OMO measured after the PD, (c) measured waveform of the Colpitts oscillator (black line is the waveform measured across the capacitor C_1 and C_2, red line is the waveform measured across the capacitor C_2), (d) measured spectrum of the Colpitts oscillator. Here $R_C = 2180\ \Omega$, optical pump power is 670 µW.

Figure 7.17(a) shows the output of the OMO (black trace), that is measured after PD and the measured voltage V_{CE} (red line) of the Colpitts oscillator when the Colpitts oscillator is injection locked to the OMO. Here V_{CE} has a peak-to-peak value of ~500 mV (same as Fig. 7.16(c)), V_{EB} has a peak-to-peak value of ~200 mV (not shown here). The output of OMO has peak-to-peak voltage of ~1.1 V (measured after PD) and ~30 mV (measured after the R_C, not shown here). The measured lock range for this system is 7 kHz. Figure 7.17(b) shows the spectrum of the Colpitts oscillator before (black line) and after injection locking (red line). As we can see here the Colpitts oscillator frequency spectrum can be "cleaned" by the OMO using injection locking method, the linewidth of the Colpitts oscillator is 7 kHz before injection locking and 30 Hz after injection locking.

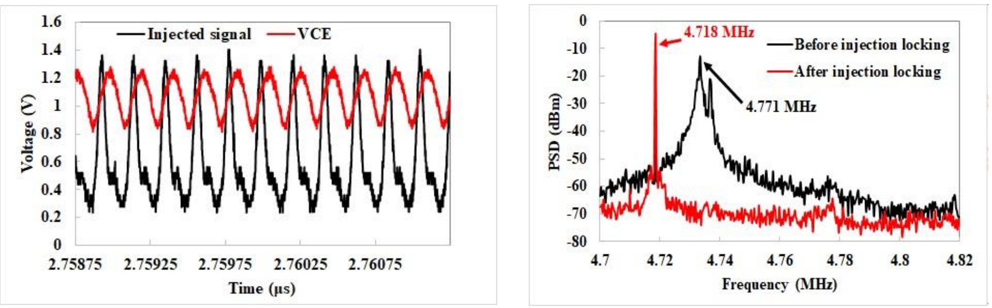

(a) (b)

Fig. 7.17 (a) After injection locking, the waveform of the OMO (black line) measured after the PD and the waveform of the Colpitts oscillator V_{CE} (red line), (b) the spectrum of the Colpitts oscillator before (black line) and after injection locking (red line).

The measured lock range is shown in Fig. 7.18, here the V_{EB} has peak to peak voltage value of ~200 mV prior to injection locking, the *x* axis is the peak-peak voltage of the OMO measured after R_c.

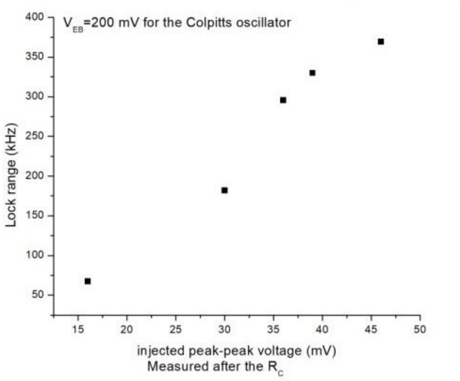

Fig. 7.18. Measured lock range vs. injected peak-peak voltage.

2) *The Colpitts oscillator unidirectionally coupled to the OMO*

Figure 7.19 shows the circuit of the setup we used to study the unidirectional perturbation on OMO induced by the Colpitts oscillator. The voltage from the collector port of the Colpitts oscillator is injected to the RF port of the MZM in the OMO loop through a buffer, the buffer has unit gain and maintains unidirectional coupling.

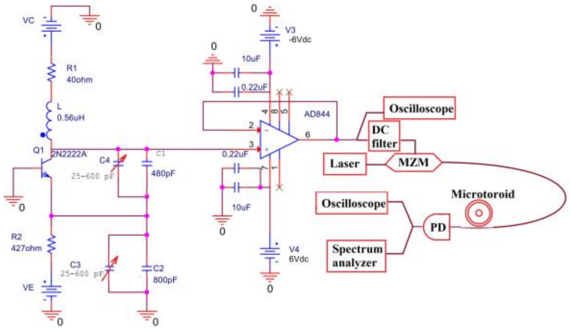

Fig. 7.19. The Colpitts oscillator unidirectional coupled to the OMO.

In this experiment, the MZM is working on its quadrature point, the DC bias voltage is 2.4 V, the parameters for the OMO are $\lambda_0 = 1556.0$ nm, $f_{\mathrm{OMO}} = 5.55$ MHz, the optical pump power is $P = 700$ μW, $Q_{\mathrm{m}} = 108$, $m_{\mathrm{eff}} = 49$ ng, the drive voltages of the Colpitts oscillator are $V_C = 1.2$ V and $V_E = -3.4$ V.

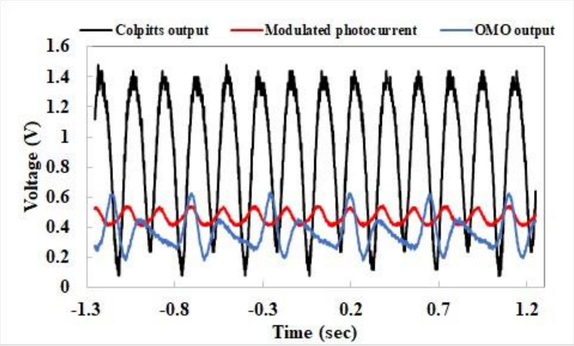

Fig. 7.20. The output of the Colpitts oscillator measured after the buffer (black line). The photovoltage (measured after MZM using a photodetector with responsivity of 4.2×10^4 V/W) of the modulated optical power by using the Colpitts oscillator to modulate the MZM (red line). The output of the OMO prior to coupling measured with the same photodetector, with responsivity of 4.2×10^4 V/W (blue line).

Figure 7.20 shows the waveform of the Colpitts oscillator in black line, this voltage waveform is measured after the buffer, this voltage is then directed to the MZM and modulate the optical power, the red line shows the modulated optical power detected by a photodetector (responsivity of 4.2×10^4 V/W). The blue line shows the voltage output of the OMO when it is uncoupled (no Colpitts voltage is injected) by directing the optical output of the OMO to a photodetector (responsivity of 4.2×10^4 V/W).

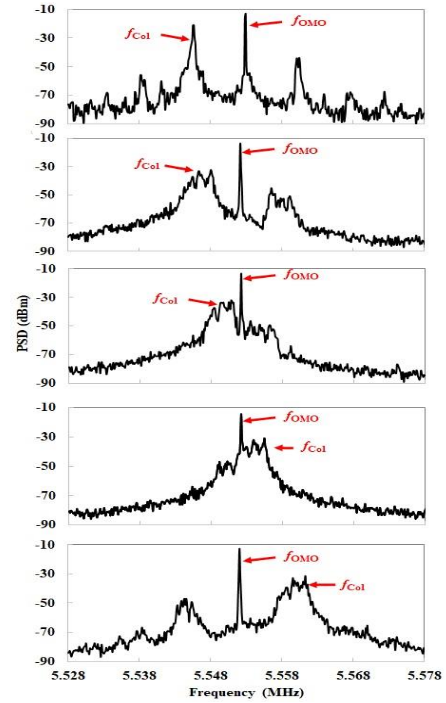

Fig. 7.21. The output spectrum of the Colpitts that is unidirectionally coupled to the OMO. The spectrum of the OMO and the Colpitts oscillator when the frequency of the Colpitts oscillator is tuned across the OMO frequency by changing the value of the tunable capacitors C_3 and C_4.

Next we inject the modulated voltage into the RF port of the MZM and measure the spectrum of the OMO vs. different Colpitts oscillation frequency (Only the Colpitts oscillation frequency is tuned by adjusting the value of the two tunable capacitors C_3 and C_4 here, as shown in Fig. 7.19). The spectrum of the OMO and the Colpitts is plotted in

Fig. 7.21. As we can see in Fig. 7.21 when tuning the frequency of the Colpitts oscillator across the frequency of the OEO, no talk between the two oscillators in the spectrum is observed.

In this preliminary experiment, we did not observe any interesting phenomenon. Judging by the spectrum the Colpitts oscillator cannot affect the OEO at all. The reason maybe that the linewidth of the Colpitts oscillator is much larger than that of the OMO; therefore its energy is distributed over a wide frequency range and density of the coupled power to OMO (that can be only affected with signals having a frequency within its narrow linewidth) is too weak to affect the OMO (i.e., pull the OMO's frequency).

7.5 Experimental observations of synchronization between bidirectionally coupled OEO and Colpitts oscillators

In this section, we experimentally study the complex dynamics of two physically dissimilar oscillators bidirectionally coupled using two different types of coupling mechanisms. Specifically, an OEO is coupled to a Colpitts oscillator via optical power and the Colpitts oscillator is coupled back to the OEO via electrical voltage. Like other delayed feedback oscillators, OEO can be configured to generate a wide variety of waveforms with differing degrees of complexity. In particular, at large optical pump power, OEO can exhibit high dimensional chaotic behavior [51-54]. Colpitts oscillator, which has been extensively used for investigation of various dynamical phenomena, is an electronic oscillator based on an LC tank. This oscillator can also exhibit a rich dynamical behavior including periodic oscillation, period doubling and chaotic oscillations [55-58]. We investigate and characterize phase synchronization and generalized chaos synchronization in the coupled OEO-Colpitts system.

7.5.1 Experiment design

Figure 7.22(a) shows the configuration of the mutually coupled OEO and Colpitts circuits where the red line indicates optical coupling and the black line indicates electrical coupling. The parameters κ_{12} and κ_{21} represent the strength of the optical and electrical coupling, respectively. Figure 7.22(b) shows the implementation of the coupled OEO-Colpitts system used in our experiment. The OEO (oscillator system in the top shaded region) is fabricated using a simple single loop architecture with an optical delay line consisting of 1 km single mode optical fiber. The optical pump power is generated by a narrow linewidth (~ 0.5 MHz) fiber coupled semiconductor laser at a wavelength of 1.55 μm. After passing through a polarization controller, the pump power is fed into a Mach-Zehnder modulator (MZM) where the transmitted optical power through the MZM is a nonlinear function of the applied voltage on the RF port of the MZM. Light exiting the modulator passes through a 1 km long single mode optical fiber and then is converted to voltage by a photodiode (PD1). The resulting voltage signal passes through an RF combiner and then amplified by an RF amplifier, the amplified signal is filtered by an RF filter and the loop is closed by feeding back the filtered signal to the RF port of the MZM. A small portion (-19 dB) of the RF power circulating in the OEO loop is coupled out by an RF coupler and fed to one of the four channels (channel #1) of an oscilloscope (Osc) (TDS2024B, Tektronix, 4 channels, 200 MHz bandwidth, 2GS/s sample rate) and an electrical spectrum analyzer (ESA) (N9320B, Keysight, 9 Hz~3 GHz range, 10 Hz to 1 MHz RBW) for monitoring the temporal and spectral characteristics of the OEO.

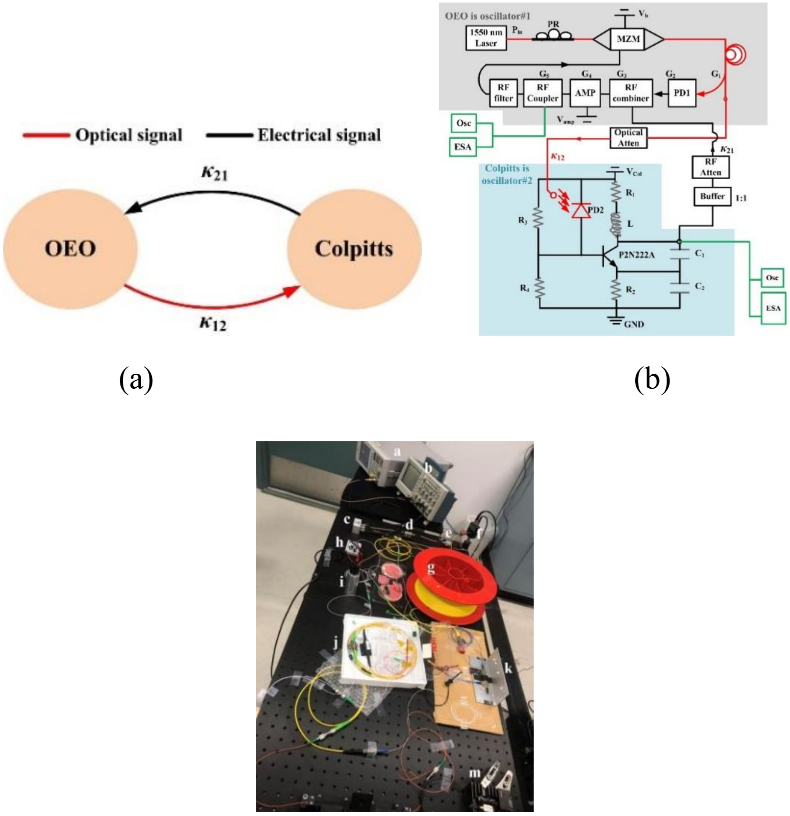

(a) (b)

(c)

Fig. 7.22. (a) Schematic of the bidirectionally coupled OEO and Colpitts oscillator, the OEO is coupled to the Colpitts oscillator through optical power while the Colpitts oscillator is coupled to the OEO through voltage. κ_{12} and κ_{21} are the coupling strengths. (b) Circuit diagram of the bidirectionally coupled OEO and Colpitts oscillator. The circuits in green are the oscilloscope (Osc) and electrical spectrum analyzer (ESA) for the wave and frequency spectrum monitoring. Here, P_{in} is optical pump power of the OEO, V_b is the DC bias voltage of the Mach-Zehnder modulator (MZM), G_1 is the coupling loss of the fiber coupler, G_2 is the voltage gain of the photodiode (PD1), G_3 is the voltage loss of the RF combiner, G_4 is the voltage gain of the RF amplifier, G_5 is the voltage loss of the RF coupler, V_{col} is the drive voltage of the Colpitts oscillator, L is the inductor, R_1, R_2, R_3, and R_4 are the resistors, C_1, C_2 are the capacitors, the transistor is P2N222A NPN transistor, and a photodiode (PD2) is biased between the voltage supply and the base port of the transistor with the responsivity as β. (c) The experimental setup that includes: a: ESA, b: Osc; c: RF Coupler; d: AMP; e: RF Combiner; f: PD1; g: Fiber delay; h: The PCB board contains Colpitts oscillator, Buffer and PD2; i: RF Attenuator; j: Optical Attenuator; k: MZM and m: Laser.

The Colpitts oscillator circuit comprises an LC tank and an NPN bipolar transistor configured as a common emitter amplifier. The LC tank consists of one inductor (L) and two capacitors (C_1 and C_2). A photodiode (PD2) is connected between the collector port and base port of the transistor to enable optical coupling to the Colpitts. The same oscilloscope (through channel #2) and electrical spectrum analyzer are used to monitor the waveform and frequency spectrum of the Colpitts from the collector port of the transistor.

In order to couple the OEO to the Colpitts oscillator, half of the circulating optical power in the OEO loop is directed to PD2 using a 1×2 50/50 fiber optical directional coupler. The coupled optical power is converted to photocurrent in PD2 and distributed to the base port of the transistor because of the bias network constructed using R_3 and R_4. The photocurrent that entered the base port gets amplified in the transistor together with the Colpitts intrinsic current and then circulate inside the LC tank. The magnitude of the coupled optical power and so the resulting photocurrent can be adjusted by a tunable fiber optical attenuator.

To couple the Colpitts oscillator to the OEO, a portion of the RF voltage from the collector port of the transistor is unidirectionally directed to the RF power combiner placed in the OEO loop using an electronic buffer and an RF power attenuator. This coupled RF voltage will be combined with the OEO intrinsic RF voltage in the RF combiner and then circulate inside the OEO loop. The magnitude of the coupled RF voltage is controlled by the tunable RF attenuator. As such OEO and Colpitts are mutually coupled via two different types of coupling mechanisms where both couplings are unidirectional and adjustable.

Using the coupled system shown in Fig. 7.22(b) we have investigated the synchronization of the mutually coupled OEO and Colpitts oscillators in the two distinctive regimes which are 1) OEO and Colpitts both oscillate periodically before coupling, 2) OEO and Colpitts both oscillate chaotically before coupling. The values of the system parameters are adjusted (as listed in Tables 7.4 and 7.5) to ensure that the OEO and Colpitts operate in these two distinct regimes prior to coupling.

We define κ_{12}, the coupling strength from the OEO-to-Colpitts, as the ratio between the average photocurrent induced by the optical power incident on the PD2 and the average base current of the Colpitts oscillator before coupling. We define κ_{21}, the coupling strength from Colpitts-to-OEO, as the ratio between the injected average voltage from the Colpitts oscillator and the intrinsic average voltage of the OEO before coupling.

7.5.2 Phase synchronization

In this section, the value of the various parameters that control the behavior of the OEO and the Colpitts oscillator are chosen such that, before coupling, both oscillators oscillate periodically. These values are listed in table 7.4.

Figure 7.23 shows the waveforms and the spectrum generated by the OEO and Colpitts under test, when the two oscillators are decoupled ($\kappa_{12} = \kappa_{21} = 0$) and both oscillate periodically. The intrinsic oscillation frequencies of the OEO ($f_{\text{OEO-i}}$) and the Colpitts oscillator ($f_{\text{Col-i}}$) are 296.87 kHz and 304.15 kHz, respectively.

Table 7.4. Parameters for the OEO and Colpitts for them to oscillate periodically when they are uncoupled

Parameter	P_{in} (μW)	V_b (V)	G_1	G_2 (V/W)	G_3	G_4
Value	53.3	3.2	0.5	22670	-0.5	57
Parameter	G_5	V_{amp} (V)	V_{col} (V)	L (μH)	R_1 (Ω)	R_2 (Ω)
Value	0.92	9	3	22	60.56	88.93
Parameter	R_3 (Ω)	R_4 (Ω)	C_1 (μH)	C_2 (μH)	β (A/W)	
Value	75.90	300.60	29	39	0.96	

The difference between these frequencies are selected such that synchronization can be achieved with accessible coupling strengths. As evident from the plots, OEO's output carries more noise and the output of Colpitts has a DC voltage shift of +2 Volts.

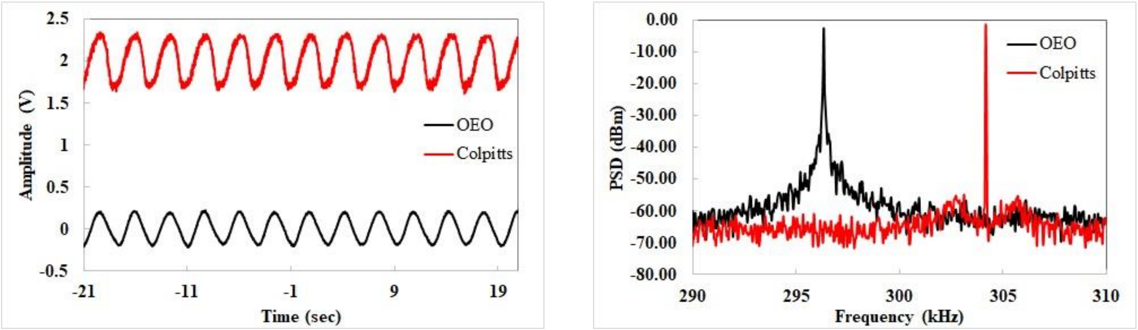

(a) (b)

Fig. 7.23. (a) Waveform of the OEO (black) and Colpitts oscillator (red) and (b) spectrum of the OEO (black) and the Colpitts oscillator (red) when they are running separately ($\kappa_{12} = \kappa_{21} = 0$).

The behavior of the coupled oscillatory system is characterized by monitoring the oscillation frequency of each oscillator as the unidirectional coupling coefficients (κ_{12} and κ_{21}) are changed. Figure 7.24(a) shows the oscillation frequency of OEO (f_{OEO}) and Colpitts (f_{Col}) plotted against $\kappa_{21}$for different values of κ_{12}. The solid dots are the measured values of f_{OEO} while hollow squares are the measured values of f_{Col}. κ_{21} is varied between 0 and 0.014 while κ_{12} is varied between 0 and 0.172. These ranges are selected such that the transitions between asynchronous and synchronous oscillations can be captured. For each value of κ_{12}, as κ_{21} increases the f_{OEO} and f_{Col} are pulled toward each other until at a certain value of κ_{21} they collapse into one single value that gradually grows by further increasing κ_{21}.

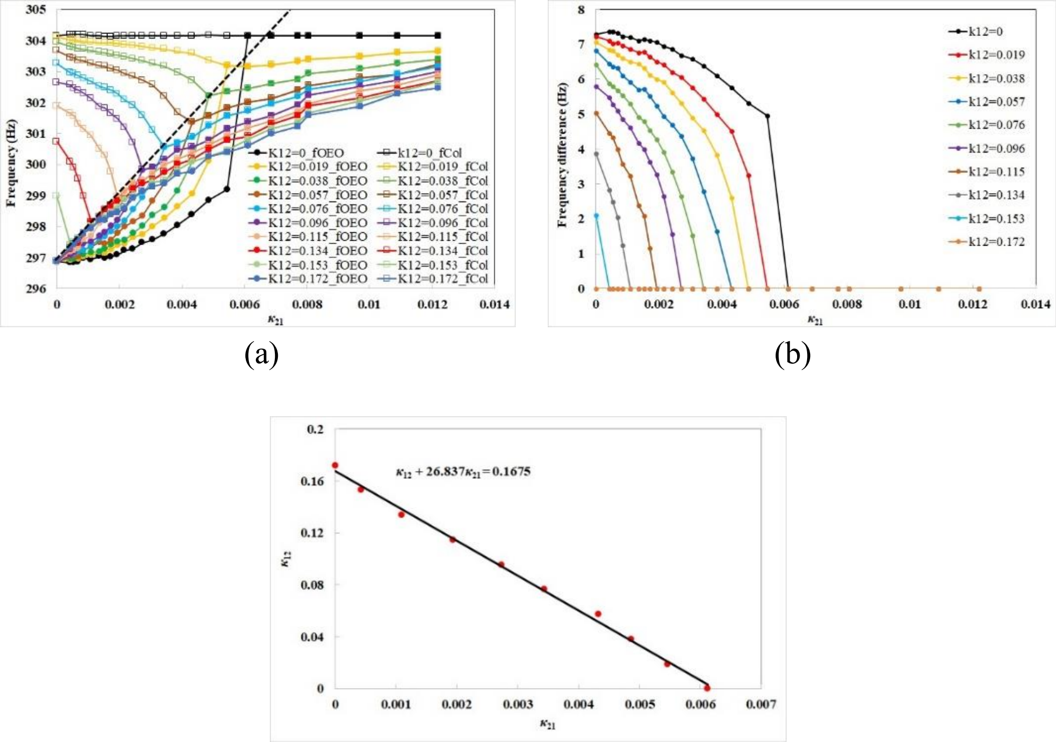

(a) (b)

(c)

Fig. 7.24. Route to phase synchronization in the coupled OEO and the Colpitts oscillator. (a) Frequency of the OEO and Colpitts oscillator vs. coupling strengths (κ_{12}, κ_{21}), (b) the frequency difference Δf ($= f_{\mathrm{Col}} - f_{\mathrm{OEO}}$) vs. coupling strengths, and (c) the relation between the two coupling strengths (κ_{12}, κ_{21}) when the coupled OEO and Colpitts oscillator are just synchronized, the solid line is the linear fit of the data points.

In Fig. 7.24(a) the trace of the black dots and black squares show that when $\kappa_{12} = 0$, f_{OEO} (black dots) is unidirectionally pulled up toward $f_{\mathrm{Col\text{-}i}}$ as κ_{21} is increased, and at $\kappa_{21} = 0.00612$ collapses to $f_{\mathrm{Col\text{-}i}}$. Here the sudden rise of f_{OEO} from $\kappa_{21} = 0.00546$ to $\kappa_{21} = 0.00612$ is artificially induced by the resolution of the κ_{21} variable while performing the measurement (due to the 1 dB attenuation step of the RF power attenuator used here).

Similarly, the trace of the hollow squares with different colors on y-axis, where $\kappa_{21} = 0$, shows f_{Col} is unidirectionally pulled down toward $f_{\mathrm{OEO\text{-}i}}$ as κ_{12} is increased, and collapses to $f_{\mathrm{OEO\text{-}i}}$ at $\kappa_{12} = 0.172$. When both κ_{12} and κ_{21} are larger than zero, f_{OEO} and f_{Col} are pulled toward each other and collapse to a single oscillation frequency f_s between the $f_{\mathrm{OEO\text{-}i}}$ and $f_{\mathrm{Col\text{-}i}}$ (i.e., the intrinsic oscillation frequencies of OEO and Colpitts) at a particular value of κ_{12} for a given value of κ_{21}. The synchronization process can be visualized by plotting the frequency difference between the OEO and Colpitts ($\Delta f = f_{\mathrm{Col}} - f_{\mathrm{OEO}}$). Figure 7.24(b) shows Δf plotted versus κ_{21} for different values of κ_{12}. We see that, Δf is a monotonically decreasing function of both coupling strengths and becomes zero at particular values of κ_{12} and κ_{21} referred to as critical values ($\kappa_{12,\mathrm{C}}$ and $\kappa_{21,\mathrm{C}}$). The black dashed line in Fig. 7.24(a) shows a near linear relation between f_s and $\kappa_{21,\mathrm{C}}$.

Since each $\kappa_{21,\mathrm{C}}$ is associated with a unique $\kappa_{12,\mathrm{C}}$, a functional relation can be found between these critical values in the form $\kappa_{21,\mathrm{C}} = F(\kappa_{12,\mathrm{C}})$ or $\kappa_{12,\mathrm{C}} = F^{-1}(\kappa_{21,\mathrm{C}})$. Figure 7.24(c) shows the measured values of $\kappa_{12,\mathrm{C}}$ plotted against $\kappa_{21,\mathrm{C}}$. A match between measured data points and a linear fit reveals a linear relationship between $\kappa_{21,\mathrm{C}}$ and $\kappa_{12,\mathrm{C}}$ in the form $\kappa_{12,\mathrm{C}} + 26.837\kappa_{21,\mathrm{C}} = 0.1675$. This means that the κ_{21} is 26.837 times more effective than κ_{12} in pulling the oscillation frequencies toward each other. In other words, one may define an equivalent coupling strength $\kappa_{\mathrm{eq}} = \kappa_{12,\mathrm{C}} + 26.837\kappa_{21,\mathrm{C}}$ for this coupled oscillatory system where $\kappa_{\mathrm{eq}} \geqslant 0.1675$ is the required condition for $\Delta f = f_{\mathrm{OEO}} - f_{\mathrm{Col}}$ to be zero. The measured linewidth of the free running OEO is 300 Hz and the measured linewidth of the free running Colpitts is 15 Hz, the linewidth of the OEO is almost 26 times larger than the linewidth of the Colpitts. For general mutually coupled oscillators in accordance with simple Adler or Kuramoto model, the pulling strength of the target oscillator is proportional to the product of the coupling strength (κ_{ij}) and the target oscillator's linewidth [59-61], this means the oscillator with smaller linewidth is more resistive to be pulled and so needs higher injection strength. This may just explain the higher efficiency of κ_{21} compared to κ_{12} in pulling the oscillation frequencies (OEO is easier to be pulled by Colpitts, while in comparison, Colpitts is more difficult to be pulled by OEO).

While $\Delta f = 0$ is usually an indication of synchronized oscillation (in the context of injection locking), however in order to better characterize synchronization we have also measured the phase difference between OEO and Colpitts. Figure 7.25 shows the variation of the measured phase difference between the synchronized OEO and Colpitts oscillator (φ_{Col} - φ_{OEO}) as the coupling strengths are changed. The positive phase difference indicates that the Colpitts oscillator is leading the OEO. As shown in Fig. 7.25, the phase difference increases both by increasing κ_{12} and increasing κ_{21}.

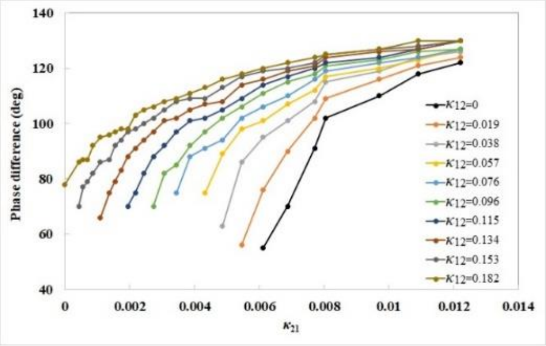

Fig. 7.25. The measured phase difference (φ_{Col} - φ_{OEO}) between the synchronized OEO and Colpitts oscillator at different coupling strengths κ_{12} and κ_{21}.

7.5.3 Generalized chaos synchronization

In this section, the control parameters of the OEO and the Colpitts oscillator are chosen such that they both oscillate chaotically before coupling. The values of these parameters are listed in Table 7.5.

Table 7.5. Parameters for the OEO and Colpitts for them to oscillate chaotically when they are uncoupled

Parameter	P_{in} (μW)	V_b (V)	G_1	G_2 (V/W)	G_3	G_4
Value	224.2	3.2	0.5	22670	-0.5	57
Parameter	G_5	V_{amp} (V)	V_{col} (V)	L (μH)	R_1 (Ω)	R_2 (Ω)
Value	0.92	9	5	95	20.67	387
Parameter	R_3 (Ω)	R_4 (Ω)	C_1 (μH)	C_2 (μH)	β (A/W)	
Value	65.30	183.57	50.8	50.8	0.96	

Figure 7.26(a) shows the measured waveforms generated by the isolated ($\kappa_{12} = \kappa_{21} = 0$) chaotic OEO and the Colpitts oscillator and Fig. 7.26(b) shows their measured frequency spectrum. The gray trace in Fig. 7.26(b) is the measured background noise of the electrical spectrum analyzer in the absence of an input. The black and red traces are the measured spectrum for the OEO and the Colpitts oscillator, respectively. The measured spectrum for both oscillators comprises a few sharp peaks superimposed on a broad background; such features are typically considered the signature of chaos in power spectrum of an oscillator [62-64]. Using the measured waveforms, we have extracted the two largest Lyapunov exponents (LEs) for the OEO and the Colpitts oscillator. The Lyapunov exponents are $LE_{1,OEO} = 1.36 \times 10^6$ bit/sec, $L_{E2,OEO} = 2.90 \times 10^5$ bit/sec for the

OEO and $LE_{1,Col} = 8.41 \times 10^4$ bit/sec, $LE_{2,Col} = -1.39 \times 10^5$ bit/sec for the Colpitts oscillator [65]. The largest LE for the OEO is almost twenty times larger than the largest LE for the Colpitts oscillator; this difference is in agreement with the measured spectrum in Fig. 7.26(b) where OEO's spectrum is extended to much larger frequencies compared to that of the Colpitts oscillator. The fact that the two largest LEs of the OEO are both positive, indicates that the OEO is hyperchaotic. The fact that the largest LE of the Colpitts is positive while the second largest LE is negative indicates that the Colpitts oscillator is chaotic but not hyperchaotic [66].

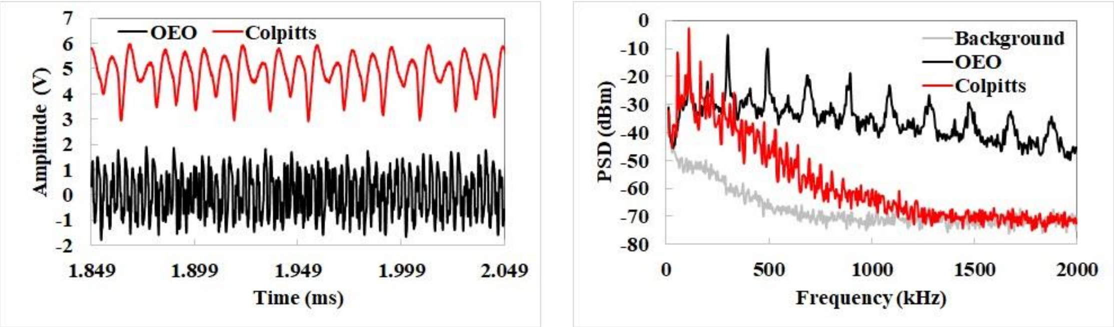

(a) (b)

Fig. 7.26. (a) Measured waveform of the OEO (black) and the Colpitts oscillator (red), and (b) measured frequency spectrum of the OEO (black) and the Colpitts oscillator (red) when they are uncoupled ($\kappa_{12} = \kappa_{21} = 0$). The gray line in part-b, is associated with the background noise of the ESA used for these measurements (when there is no input to the ESA).

Next, in order to investigate the emergence of synchronization as a function of the coupling strengths; the two oscillators are mutually coupled and the coupling strengths (κ_{12} and κ_{21}) are increased. Generally, one can characterize synchronization using two standard techniques, namely, correlation function and the generalized return plots [67, 68]. We introduce the correlation function $S(\Delta t)$ between two time-varying parameters $x_1(t)$ and $x_2(t)$ as:

$$S(\Delta t) = \frac{\langle x_1(t)x_2(t-\Delta t)\rangle}{\sqrt{\langle x_1^2(t)\rangle\langle x_2^2(t)\rangle}}. \tag{7.28}$$

where ⟨•⟩ indicates a time average over an extended period of time, here x_1(t) is the OEO output voltage subtracted by its mean value (x_1(t) = V_{OEO}(t) - $\overline{V_{OEO}}$) and x_2(t) is the Colpitts output voltage subtracted by its mean value (x_2(t) = V_{Col}(t) - $\overline{V_{Col}}$) We search for the time shift Δt at which the correlation between the outputs of OEO and Colpitts is maximized. The maximum value of *S* is typically referred to as correlation degree.

Figure 7.27 shows the correlation degree (max{*S*(Δt)}) calculated at several values of coupling strengths (κ_{12}, κ_{21}) that happened at certain time shift Δt. We can see, as the coupling strengths increase, the correlation degree increases rapidly from 0.1 (when $\kappa_{12} = \kappa_{21} = 0$) until it reaches a saturation value ~0.8 (when $\kappa_{12} > 0.53$ and $\kappa_{21} > 0.04$). Note that while when the two oscillators are isolated, the correlation degree should be zero, the experimentally measured signal have a correlation degree of $S = 0.1$ when $\kappa_{12} = \kappa_{21} = 0$. It is believed that is due to unwanted coupling through electromagnetic radiation and antenna effects associated with wires, and other electrical components used in the experimental setup.

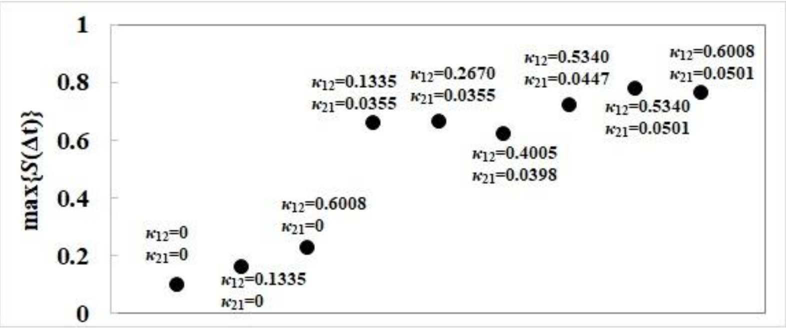

Fig. 7.27. Correlation degree (max{*S*(Δt)) calculated for different values of κ_{12} and κ_{21} that achieved at certain time shift Δt.

The large correlation (~0.8) between the outputs of the OEO and the Colpitts oscillator at large coupling strengths indicates the two oscillators are essentially synchronized [67]. To further investigate the onset of synchronization between these originally chaotic oscillators, in Fig. 7.28 *S*(Δt) is plotted versus Δt (time shift) when $\kappa_{12} = \kappa_{21} = 0$ and when $\kappa_{12} = 0.6008$, $\kappa_{21} = 0.0501$. As mentioned before, the weak correlation shown in Fig. 7.28(a) is due to the parasitic electromagnetic coupling. Figure 7.28(b) shows that appearance of sharp peaks at $\Delta t = n \times \tau$ ($n = 1, 2, 3, \ldots$) where $\tau \sim 0.0073$ ms.

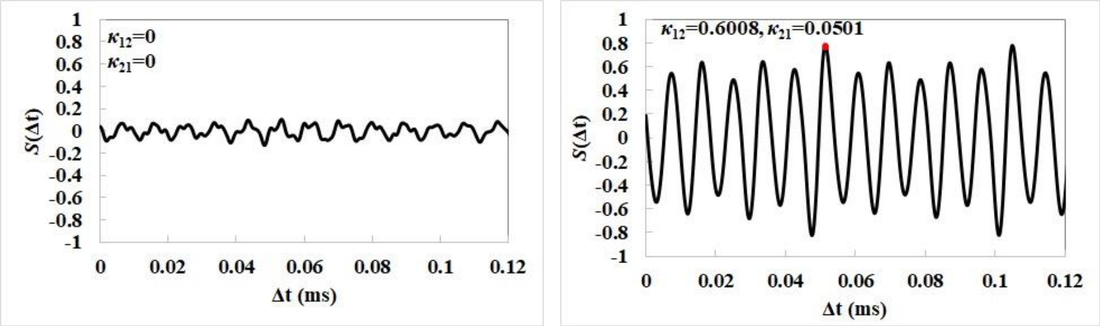

(a) (b)

Fig. 7.28. Correlation function between the OEO and the Colpitts oscillator when (a) $\kappa_{12} = \kappa_{21} = 0$ and (b) $\kappa_{12} = 0.6008$, $\kappa_{21} = 0.0501$.

The largest peak of $S(\Delta t)$ (marked by a red dot in Fig. 7.28(b)) indicates synchronized chaotic oscillation. This peak has a magnitude of 0.77 and it appears at Δt = 0.051 ms.

We also did the similarity measure of the x_1(t) and x_2(t-Δt) when $\kappa_{12} = 0.6008$, $\kappa_{21} = 0.0501$ using the function:

$$Dist(x_1(t), x_2(t-\Delta t)\,) = \sqrt{\sum_t |x_1(t) - x_2(t-\Delta t)|^2}. \tag{7.29}$$

Figure 7.29 shows the measured similarity at various time delay. Same as the result obtained by using correlation function analysis, one of the local minima occurs at Δt = 0.051 ms, at which the synchronization happens.

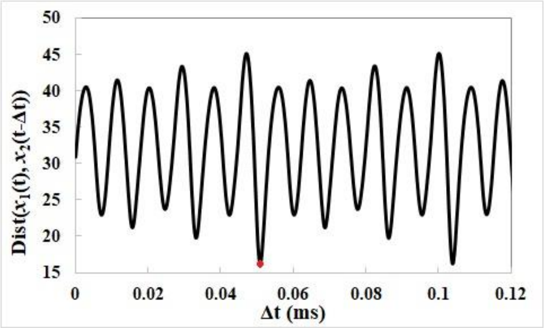

Fig. 7.29. Similarity function for coupled OEO and Colpitts oscillator (both operating in chaotic regime) when $\kappa_{12} = 0.6008$, $\kappa_{21} = 0.0501$.

The temporal variation of the corresponding output signals (when $\kappa_{12} = 0.6008$, $\kappa_{21} = 0.0501$) is shown in Fig. 7.30(a). Figure 7.30(b) shows $x_1(t)$ and $x_2(t\text{-}0.05\text{ms})$. The overlap and coincidence of the maxima and minima of one wave form with a time shifted version of the other waveform observed here, is known as achronal generalized synchronization [13, 68]. Figure 7.30(c) shows a generalized return plot where $x_1(t)$ is plotted against $x_2(t\text{-}0.05\text{ms})$. As evident from the plot the oscillation amplitudes are confined within a narrow region that is extended approximately along a 45° direction. The dynamical properties of this achronal state originate from the bidirectional coupling of the two physically dissimilar subsystems. It is worth noting that the achronal state is not a perfectly synchronized state of the coupled system; such state may only exist for coupled periodic oscillators [67, 68]. The spectrum of the coupled chaotic system under generalized synchronization is shown in Fig. 7.30(d), which still consists of broad spectrum with many sharp peaks.

When the OEO and Colpitts oscillator are synchronized (for $\kappa_{12} = 0.6008$, $\kappa_{21} = 0.0501$), we measured the two largest LEs for the system with $\text{LE}_1 = 2.28 \times 10^5$ bit/sec and $\text{LE}_2 = -1.55 \times 10^5$ bit/sec. Both the spectrum and the LEs indicate that the system is chaotic.

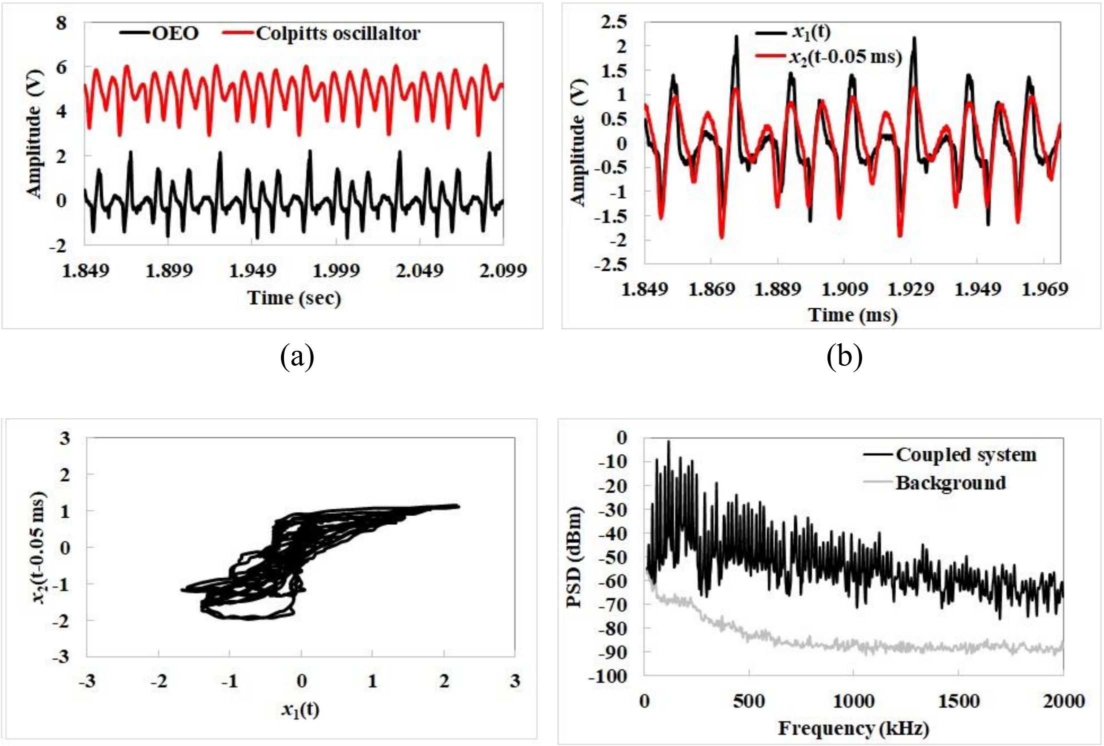

(a) (b)

(c) (d)

Fig. 7.30. Characterization of output signals generated by the synchronized OEO and Colpitts oscillator when both oscillators are operating in chaotic regime, here $\kappa_{12} = 0.6008$ and $\kappa_{21} = 0.0501$. (a) The output waveform extracted from the OEO (black) and Colpitts oscillator (red). (b) The time trace of x_1(t) and x_2(t-0.05 ms). (c) The generalized return plot for of x_1(t) and x_2(t-0.05 ms). (d) The frequency spectrum of the OEO measured through the output port of the RF coupler in the OEO loop shown in Fig. 1(b). The gray line in part-d is the background noise spectrum of the ESA (in the absence of input). Here x_1(t) is the output waveform of OEO subtracted with its mean value and x_2(t-0.05 ms) is the output waveform of the Colpitts oscillator subtracted with its mean value and then shift with a time of 0.05 ms.

We have calculated the two largest LEs for the coupled system based on the signal measured through the RF coupler in OEO loop (see Fig. 7.22-b) at different values of κ_{12} and κ_{21}. We have found that as the coupling strengths increase, the system transitions from hyperchaos to chaos. For example, when $\kappa_{12} = 0.1335$ and $\kappa_{21} = 0.0355$, the two largest LEs of the system are $LE_1 = 4.98 \times 10^5$ bit/sec and $LE_2 = 8.80 \times 10^4$ bit/sec, indicating the system is in hyperchaotic regime. When the $\kappa_{12} = 0.6008$ and $\kappa_{21} = 0.0501$, (with the attractor is shown in Fig. 7.30-c), the system becomes chaotic with the two largest LEs measured as $LE_1 = 2.28 \times 10^5$ bit/sec and $LE_2 = -1.44 \times 10^5$ bit/sec.

Figure 7.31(a) and (b) show the largest and the second largest LE of the coupled system as a function of κ_{12} and κ_{21} respectively. As evident from the plots, the largest LE (part-a) decreases from 1.36×10^6 bit/sec when $\kappa_{12} = \kappa_{21} = 0$ to 2.28×10^5 bit/sec when $\kappa_{12} = 0.6008$ and $\kappa_{21} = 0.0501$, while the second largest LE (par-b) decreases from 2.90×10^5 bit/sec when $\kappa_{12} = \kappa_{21} = 0$ to -1.55×10^5 bit/sec when $\kappa_{12} = 0.6008$ and $\kappa_{21} = 0.0501$. Additionally, Figure 7.31(b) shows a gradual transition of the second largest LE from positive to negative values in a certain region of κ_{12}-κ_{21} plane indicating a gradual transition from hyperchaos to chaos.

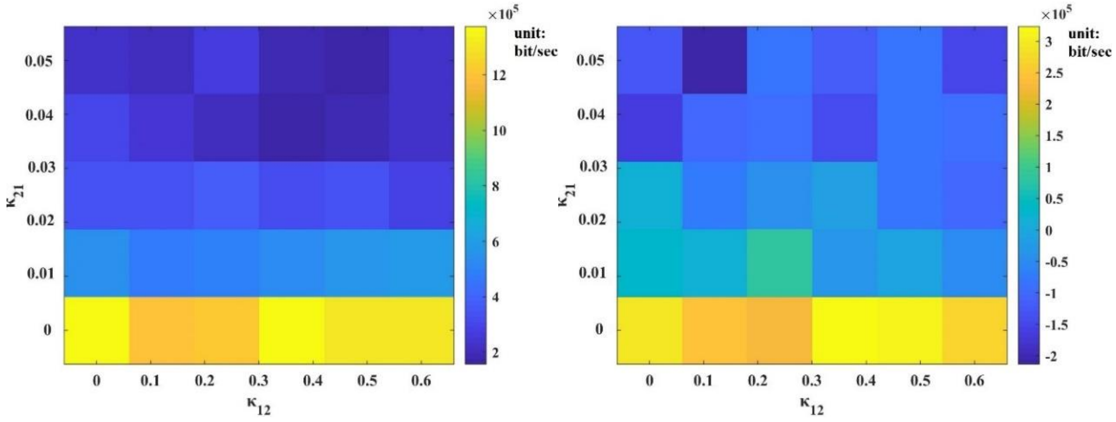

(a) (b)

Fig. 7.31. Variation of the two largest Lyapunov exponents (LEs) of the measured OEO output as a function of coupling strengths (κ_{12} and κ_{21}). (a) Contour plot of the largest LE. (b) Contour plot of the second largest LE.

7.5.4 Importance of this work

In this work, we have experimentally studied the behavior of a coupled oscillatory system comprising two physically dissimilar oscillators coupled bidirectionally through two different coupling mechanisms. More specifically we have characterized the behavior of a coupled system wherein an optoelectronic oscillator (OEO) is coupled to a Colpitts oscillator via optical power, and the Colpitts is coupled back to the OEO via RF voltage. The experimental arrangement, selected coupling mechanisms, measurement strategy and the results obtained in this paper, may pave the way toward designing new experiments that enable characterizing coupled systems that involve coupling between a larger variety and larger number of oscillators. Understanding the complex dynamics of such highly heterogeneous systems, is critical for many disciplines of science and engineering.

7.6 Detection and sensing with homogenous and heterogeneous coupled oscillatory systems

Oscillators have been extensively used for various sensing applications. In particular for sensing and measuring physical parameters that can affect their oscillation frequency (e.g. mass, temperature, humidity, etc.). Typically the interaction of the measurand with the resonator or the feedback loop of the oscillator results in a change in the oscillation frequency; subsequently the magnitude of the measured frequency change can be used to extract the strength of the interaction with the measurand that is typically proportional to the magnitude of the measurand (e.g. mass, temperature, number of molecules,…). Frequency based sensing using a single oscillator has been the subject of extensive investigation. For example, electrical oscillators have been used for mass sensing [69], humidity sensing [70], load sensing [71], etc. Mechanical oscillators have been used for mass sensing [72, 73], charge detection [74], gas and pressure sensing [75], etc.

Optomechanical oscillators have been used for mass sensing [76, 77]. Optoelectronic oscillators have been used for temperature sensing [78 79], distance [80], load and strain [81] measurement, refractive index sensing [82] and thermos-optical coefficient measurement [83].

To a lesser extent, synchronized coupled oscillators have been also considered for sensing applications. Juillard *et al* [84, 85] showed that the phase difference between the two oscillators synchronized through mutual coupling is highly sensitive to the mismatch between the oscillators and can be used to detect the changes of certain physical parameters. It has been demonstrated that the amplitude change of the antisymmetric vibrational mode of two coupled cantilevers (micromechanical oscillators) is more sensitive than frequency change of single cantilever to the added mass on one of them [86]. Spletzer *et al* [87] have shown that the amplitude of both symmetric and antisymmetric modes of two coupled cantilevers exhibits higher sensitivity than the frequency change of each one of them when upon adding a mass. Barbarossa *et al* [88] theoretically showed that a sensor based on a network of synchronized oscillators exhibits higher reliability than a sensor based on a single oscillator because the SNR of the sensor can be improved by the oscillator nodes. Beyond sensing, coupled oscillators have been also used in image sensors where nodal phase change in a network of 32×32 synchronized oscillators was used for imaging [89]. In almost all of these experimentally demonstrated sensing systems, the sensor includes two identical oscillators, which before coupling have the exact same oscillation frequency. Once they are coupled, either two distinctive modes with two different frequencies emerge or the two oscillators are synchronized. The amplitude change of one of these two emerged modes or the phase difference between the synchronized oscillators is then used as a sensing parameter to detect a change induced by perturbing a parameter in one of them.

The sensing mechanism and coupled oscillatory system studied here, is based on two oscillators that when they are decoupled, have close but non-identical oscillation frequencies. These oscillators can be physically similar or dissimilar, but their oscillation frequencies are close enough so that after mutual or unidirectional coupling, they become synchronized. We demonstrate that when these two oscillators are coupled (mutually or unidirectionally) and their coupling is adjusted such that the coupled system is at the synchronization edge , the frequency difference between them can be used for enhanced sensing of an external perturbation affecting one of the oscillators (hereafter referred to as the “detector oscillator”). When a measurand perturbs a parameter of the detector oscillator, that changes its oscillation frequency, the two oscillators become desynchronized and their oscillation frequencies split. This frequency splitting can be converted to a measurable beat frequency that is proportional to the perturbation strength (i.e., the magnitude of the target measurand). We show that the variation of the beat frequency is much larger than the oscillation frequency shift of the isolated detector oscillator induced by the same type and magnitude of perturbation.

Previously the beat frequency generated by oscillation of two coupled mechanical modes of a single resonator (e.g., a single crystal) has been used for force and temperature sensing [90, 91]. In some other examples, the beat frequency between excited modes of two mechanical resonators fabricated on the same substrate has been used for temperature sensing [92]. In those systems, the coupling between the modes was naturally provided through the mechanical structure resulting in simultaneous perturbation of both modes by the measurand. As such, to make the beat frequency sensitive to a perturbation, the frequency of each mode had to be affected differently. Moreover, since in such configurations the coupling factor is determined by the structure, preparation of the system in a specific oscillatory state (e.g., synchronization edge) can be very challenging. Note that in other kinds of oscillators that support multimodal oscillations (e.g., optomechanical oscillators and optoelectronic oscillators [93, 94]), the response of each mode to a perturbation is an inherent property of the system and cannot be easily manipulated to provide significantly different response (to support a large beat frequency change up on exposure to a measurand).

Here, we first derive a general theory that explains the enhanced sensitivity provided by the coupled oscillatory system (compared to single oscillator sensors), then we demonstrate its validity by building and testing two oscillatory systems: 1) two non-identical mutually coupled electronic oscillators and 2) an optoelectronic oscillator unidirectionally coupled (injection locked) to an electronic oscillator.

7.6.1 General theory

In this section, we theoretically analyze the performance of an oscillatory sensing system comprising two non-identical coupled oscillators that may be physically similar or dissimilar. The coupling strengths considered here are weak; in other words, the injected signal from one to the other oscillator is much smaller than the oscillation amplitude of the oscillator that receives the signal ($s_{\mathrm{inj}}/s_{\mathrm{int}} \ll 1$). With this assumption, the oscillation amplitude variation induced by coupling can be ignored, and the interaction between the two oscillators may be described by the well-known *Kuramoto* model [95-97]. As such the dynamic of the coupled oscillatory system can be captured by the coupled differential equations governing the phase of each oscillators:

$$\frac{d\theta_1}{dt} = \omega_{01} + \kappa_1 \sin(\theta_2 - \theta_1). \tag{7.30}$$

$$\frac{d\theta_2}{dt} = \omega_{02} + \kappa_2 \sin(\theta_1 - \theta_2). \tag{7.31}$$

where θ_1, θ_2 are the phases of the two oscillators, κ_1, $\kappa_2 \geq 0$ are the coupling strengths, and ω_{01}, ω_{02} are their isolated oscillation frequencies, ω_{01}, ω_{02} are close enough to support synchronization between the two oscillators (here we assume $\omega_{01} \geq \omega_{02}$). This simple phase model has been reported to be useful in predicting the behavior of a large variety of coupled oscillators [97], for example, it has been used in modelling biological oscillators [96], electrical oscillators [98, 99], chemical oscillators [100, 101], mechanical oscillators [102, 103] and optical oscillators [104, 105].

Using Eqs. (7.30) and (7.31) the temporal variation of the phase difference between the two coupled oscillators can be written as:

$$\frac{d(\theta_1 - \theta_2)}{dt} = (\omega_{01} - \omega_{02}) - (\kappa_1 + \kappa_2)\sin(\theta_1 - \theta_2). \tag{7.32}$$

If the two oscillators are synchronized, the temporal variation of their phase difference is zero, so Eq. (7.32) is simplified as:

$$(\omega_{01} - \omega_{02}) = (\kappa_1 + \kappa_2)\sin(\theta_1 - \theta_2). \tag{7.33}$$

Eq. (7.33) shows that the necessary condition for synchronization is:

$$|(\omega_{01} - \omega_{02})| \le (\kappa_1 + \kappa_2). \tag{7.34}$$

that is essentially the condition for Eq. (7.33) to have a real solution. In Eq. (7.34) equal sign corresponds to the frequency difference that for a given coupling can be considered the *synchronization edge*; meaning that a change in the original frequency difference or the coupling strength will desynchronize the two oscillators.

Under this condition the coupled system responds to an external perturbation (applied on one of the oscillators) with the highest level of sensitivity. Here we consider that oscillator #1 is the detector oscillator that is perturbed (a change induced in one or more parameters that determine its oscillation frequency). We assume that the magnitude of the perturbation is small enough such that the induced change in the oscillation frequency of the isolated oscillator (ω_{01}') is linearly proportional to the perturbation strength and can be written as

$$\omega_{01}' = \omega_{01} + \epsilon S. \tag{7.35}$$

where S is the strength of the perturbing signal and ϵ is the proportionality constant. Using Eq. (7.35), Eq. (7.32) is modified as:

$$\frac{d(\theta_1 - \theta_2)}{dt} = (\omega_{01}' - \omega_{02}) - (\kappa_1 + \kappa_2)\sin(\theta_1 - \theta_2). \tag{7.36}$$

This equation is similar to Adler's equation that was developed in context of electronic oscillators [106].

We now introduce a phase variable $\varphi(t) = \exp(j(\theta_1 - \theta_2))$ to capture the phase difference of the coupled oscillators. Using this phase variable, Eq. (7.35) can be rewritten as:

$$\frac{d\varphi}{dt} = -\frac{\kappa_1+\kappa_2}{2}\varphi^2 + j(\omega_{01}{}' - \omega_{02})\varphi + \frac{\kappa_1+\kappa_2}{2}. \tag{7.37}$$

following procedures similar to those presented in Refs. [99] and [107], the solution for φ(t) may be expressed as:

$$\varphi(t) = \frac{\sigma_2 - C\sigma_1 e^{j\sqrt{(\omega_{01}{}'-\omega_{02})^2-(\kappa_1+\kappa_2)^2 t}}}{1-\mathrm{C}e^{j\sqrt{(\omega_{01}{}'-\omega_{02})^2-(\kappa_1+\kappa_2)^2 t}}}. \tag{7.38}$$

where C is a constant, and σ_1, σ_2 are defined as:

$$\sigma_1 = j\left(\frac{\omega_{01}{}'-\omega_{02}}{\kappa_1+\kappa_2} + \sqrt{\left(\frac{\omega_{01}{}'-\omega_{02}}{\kappa_1+\kappa_2}\right)^2 - 1}\right). \tag{7.39}$$

$$\sigma_2 = j\left(\frac{\omega_{01}{}'-\omega_{02}}{\kappa_1+\kappa_2} - \sqrt{\left(\frac{\omega_{01}{}'-\omega_{02}}{\kappa_1+\kappa_2}\right)^2 - 1}\right). \tag{7.40}$$

Eq. (7.38) indicates that φ(t) is a harmonically oscillating parameter with an oscillation frequency equal to:

$$\omega_{\mathrm{B}} = \omega_{01\mathrm{c}} - \omega_{02\mathrm{c}} = \sqrt{(\omega_{01}{}' - \omega_{02})^2 - (\kappa_1 + \kappa_2)^2}. \tag{7.41}$$

where ω_{01c} and ω_{02c} are the oscillation frequencies of the two coupled oscillators after perturbing the detector oscillator. ω_B is essentially the beat frequency that can be extracted from the oscillatory systems by subtracting the output frequency of the two coupled oscillators (in practice, ω_B can be generated using a frequency mixer followed by a low pass filter).

If the coupled system is tuned to oscillate at the *synchronization edge* (i.e. $\kappa_1 + \kappa_2 = \omega_{01} - \omega_{02}$), Eq. (7.41) can be written as:

$$\omega_{\mathrm{B}} = \sqrt{(\omega_{01} + \epsilon S - \omega_{02})^2 - (\kappa_1 + \kappa_2)^2} = \sqrt{(\epsilon S)^2 + 2(\omega_{01} - \omega_{02})\epsilon S}.$$

(7.42)

A comparison between Eq. (7.35) (the oscillation frequency shift for the isolated detector oscillator) and Eq. (7.42) (the beat frequency for the coupled system) shows ω_B is much larger than ϵS, especially when the perturbing signal is very weak (i.e. $\epsilon S \ll \omega_{01} - \omega_{02}$). One can define an enhancement factor as the ratio between the beat frequency ω_B and the frequency shift $\omega_{01}' - \omega_{01}$ as:

$$\eta = \frac{\sqrt{(\epsilon S)^2 + 2(\omega_{01} - \omega_{02})\epsilon S}}{\epsilon S} = \sqrt{1 + 2\frac{\omega_{01} - \omega_{02}}{\epsilon S}}. \tag{7.43}$$

7.6.2 Experiment design

In order to test the proposed sensing scheme and validate the corresponding theory, we fabricated two different kinds of oscillators to detect two different measurands. The first experiment uses two mutually coupled Colpitts electronic oscillators to detect a current change in one of them (more specifically optically induced current change or a photocurrent). The second experiment uses an optoelectronic oscillator (OEO) injection locked to an electronic oscillator to detect the temperature change that affects the OEO’s optical time delay. For both measurements we compare the frequency shift of the isolated detector oscillator (that in the first case can be one of the two Colpitts and in the second case is the OEO) with the frequency difference between the two coupled oscillators (beat frequency), for a given change in the measurand (photocurrent and temperature). We also calculate the frequency shift for the isolated detector oscillator, beat frequency for the coupled system and the sensitivity enhancement using Eqs. (7.35), (7.42), and (7.43) and show that the calculated results are in good agreement with the experimental results.

7.6.3 Using Colpitts oscillators to detect DC current

Figure 7.32 shows the first coupled oscillatory system that consists of two resistively coupled Colpitts oscillators. Each oscillator uses an NPN bipolar transistor configured as a common emitter amplifier, and an LC tank as the feedback. The oscillation frequency of the first oscillator (#1) is f_{C1} = 398.20 kHz and its oscillation linewidth is 11.94 Hz. The oscillation frequency of the second oscillator (#2) is f_{C2} = 395.00 kHz and its linewidth is 12.60 Hz. This system is used to compare the sensitivity of the oscillation frequency of a single oscillator and beat frequency of a coupled system to a current change applied to the base port of the first oscillator (serving as the detector oscillator).

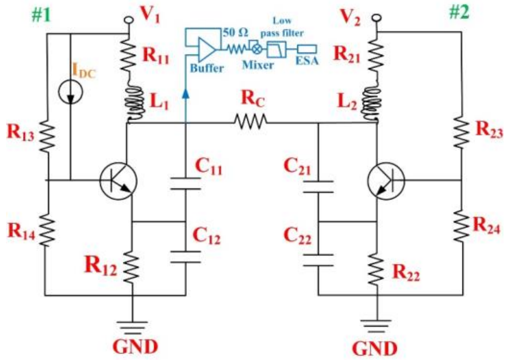

Fig. 7.32. Two resistively coupled Colpitts oscillators used to detect a DC photocurrent (I_{DC}) applied to the base port of the first oscillator (serving as the detector oscillator). The blue circuit is used to generate the beat frequency and its output is measured using an electric spectrum analyzer (ESA). Here, V_1 = 3 V, L_1 = 16 μH, R_{11} = 33 Ω, R_{12} = 68 Ω, R_{13} = 83 Ω, R_{14} = 327 Ω, C_{11} = 27 nF, C_{12} = 33 nF, V_2=3 V, L_2 = 22μH, R_{21}= 33 Ω, R_{22} = 69 Ω, R_{23} = 75 Ω, R_{24} = 325 Ω, C_{21} = 31 nF, C_{22} = 21 nF, and R_c = 3500 Ω.

Firstly, we use oscillator #1 (as a single isolated oscillator) to detect the DC photocurrent generated by a photodiode. The magnitude of the DC current is controlled by changing the intensity of the incident light. The black dots in Fig. 7.33 are the measured data points for the frequency change (Δf_{C1}) plotted against the applied photocurrent (I_{DC}).

The oscillation frequency is monitored through the collector port of the transistor using a buffer circuit (to make sure the measurement does not affect the oscillation). Next, oscillator #1 (the detector oscillator) is coupled to the oscillator #2. The two oscillators are bidirectionally coupled through a resistor R_C that can be selected according to desired coupling strength.

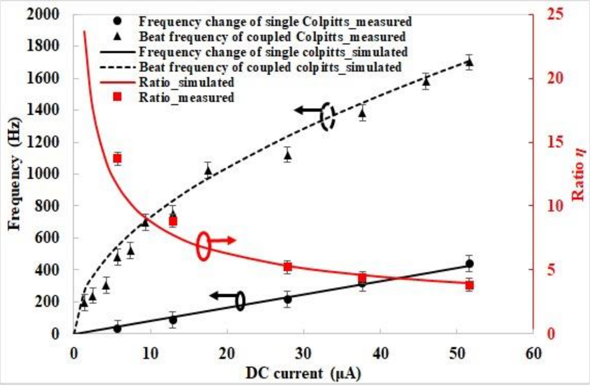

Fig. 7.33. Response of a single isolated Colpitts oscillator and a coupled Colpitts oscillating system to induced current change in one of the oscillators. Black dots and black triangles are the measured values of Δf_{C1} and f_B plotted against applied photocurrent (I_{DC}) respectively. The squares are the measured values for $\eta = f_B/(\Delta f_{C1})$. The lines are the calculated values for f_B (dashed black), Δf_{C1} (solid black) and η (solid red) using Eqs. (7.34), (7.41), and (7.42) for $\epsilon = 2\boldsymbol{\pi} \times 8.3184$ Hz/μA (extracted from the measured values of Δf_{C1}) and $\omega_{01} - \omega_{02} = 2\boldsymbol{\pi} \times 3200$ Hz.

For the system in Fig. 7.32 when R_C is 3500 Ω, the coupled oscillatory system will oscillate at the *synchronization edge* (as defined by Eq. (7.34)). Here the ratio between the amplitude of the injected current through R_C to each oscillator and amplitude of the intrinsic current flowing in the oscillator (I_{inj}/I_{int}) is 1.3×10^{-4}. Once a system oscillating at the *synchronization edge* is prepared, the photocurrent is induced only in the base port of oscillator #1 by illuminating the photodiode connected between V_1 and the base port of the transistor. In this case the readout circuit (blue circuit in Fig. 7.32) includes a mixer and a low-pass filter (in addition to the buffer) that together they generate an output proportional to Sin(ω_Bt). The frequency of this signal (f_B) is monitored using an electric spectrum analyzer.

The triangles in Fig. 7.33 are the measured values of f_B plotted against applied photocurrent (I_{DC}). The squares in the same figure are the calculated ratio (η) between measured beat frequency (f_B) and the measured frequency shift (Δf_{C1}). The solid lines are the calculated values of f_B, Δf_{C1} and η using Eqs. (7.35), (7.42), and (7.43) for $\epsilon = 2\boldsymbol{\pi} \times 8.3184$ Hz/µA (extracted from the measurement) and measured value of $\omega_{01} - \omega_{02} = 2\boldsymbol{\pi} \times 3200$ Hz. It is worth mentioning that when the photocurrent is too small (less than 6 µA) the resulting frequency shift (Δf_{C1}) in the single Colpitts oscillator is not detectable since its magnitude is in the same order or smaller than the oscillation linewidth. However, the magnitude of f_B of the coupled system is large enough to be resolved. As such the limit of detection (LoD) for the coupled system is significantly larger compared to the single oscillator system (~500 times larger based on the linewidth of the Colpitts oscillator).

7.6.4 Using OEO to detect temperature change

The second coupled oscillatory system studied here is a heterogeneous system consisting of an optoelectronic oscillator (OEO) [48] injection locked to an electronic oscillator. Figure 7.34 shows the schematic diagram of the coupled oscillatory system. The electronic oscillator is a commercially available signal generator (HP, 8648B). The OEO that serves as detector oscillator, is fabricated using a simple single loop architecture with an optical delay line consisting of 1 km of single mode fiber. The RF filter in the OEO feedback loop has been selected to force OEO to oscillate at 10.5650 MHz. The measured linewidth of the resulting oscillation is 16.09 Hz. Here the measurand is temperature and the affected OEO parameter is the optical delay. As such the fiber optic delay has been enclosed in a chamber so that the temperature of the entire loop can be controlled with an electrical heater placed inside the chamber. A Commercial psychrometer (EXTECH, RH350) with temperature sensing resolution of 0.1°C, is used to characterize the temperature.

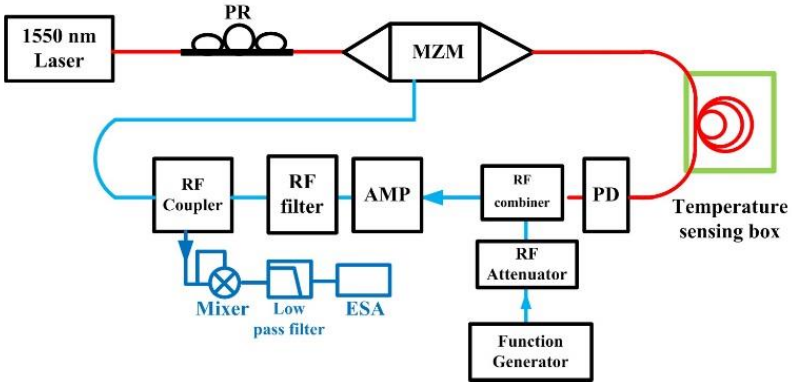

Fig. 7.34. A coupled heterogeneous oscillatory system consisting of an OEO injection locked (unidirectionally coupled) to an electronic oscillator, the fiber-optic delay loop is enclosed in a temperature-controlled chamber. The blue circuit is used to generate the beat frequency and its output is measured using an electric spectrum analyzer (ESA).

First, we measure the oscillation frequency change (Δf_{OEO}) of the isolated OEO as a function of the temperature of the optical delay. In this experiment the oscillating RF power inside the OEO is monitored using a direction RF coupler that couples 19 dB of the RF power circulating in OEO's feedback loop out. The readout circuit for the single oscillator characterization only includes a buffer that isolates the ESA from the feedback loop. The black dots in Fig. 7.35 are the measured oscillation frequency of the free running OEO as a function of the temperature of fiber optic delay.

Next, the output RF power of a tunable electronic oscillator is fed to OEO's feedback loop using a 3-port RF combiner as shown in Fig. 7.34. The strength of the coupling is adjusted by tuning the oscillation frequency of the electronic oscillator and controlling the magnitude of the coupled (injected) RF power using a tunable RF attenuator. When the frequency of the electronic oscillator is 10.5687 MHz and the ratio between injected voltage amplitude and the intrinsic oscillating voltage amplitude of the OEO (V_{inj}/V_{int}) is 0.02, the coupled system oscillates at the *synchronization edge*. Similar to the previous experiment, a mixer and a low-pass filter are used after the buffer to generate an output proportional to $\mathrm{Sin}(\omega_B t)$ without affecting the oscillation of the system (see the blue circuit in Fig. 7.34). The resulting beat frequency is monitored using an ESA.

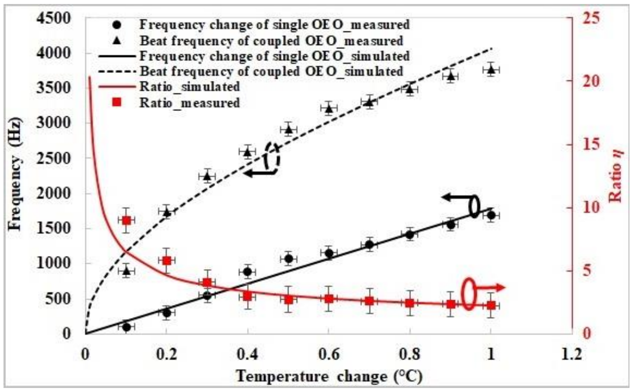

Fig. 7.35. Single and coupled OEO is used to detect the temperature change in the chamber containing the fiber-optic delay, Black dots and black triangles are the measured values of Δf_{OEO} and f_B plotted against the temperature, respectively. The squares are the measured values for $\eta = f_B/(\Delta f_{OEO})$. The lines are the calculated values for f_B (dashed black), Δf_{OEO} (solid black) and η (solid red) using Eqs. (7.35), (7.42), and (7.43). Here $\epsilon = 2\boldsymbol{\pi} \times 1794.20$ Hz/ °C, and $\omega_{01} - \omega_{02} = 2\boldsymbol{\pi} \times 3700$ Hz.

The black triangles in Fig. 7.35 are the measured values of the beat frequency (f_B) at different temperatures. The red squares are the magnitude of the enhancement ratio (η) calculated based on measured frequencies (f_B, Δf_{OEO}). The solid lines are the calculated values of f_B, Δf_{OEO} and η using Eqs. (7.35), (7.42), and (7.43) for $\epsilon = 2\boldsymbol{\pi} \times 1794.20$ Hz/°C (extracted from the measurement) and measured value of ω_{01}-$\omega_{02} = 2\boldsymbol{\pi} \times 3700$ Hz. As expected, the temperature sensitivity of the beat frequency is much larger than that of the single OEO oscillation frequency change. In particular between 0 and 0.1°C, η can be as large as 20. Note that the smallest data point measured is limited by the resolution of our temperature sensor and it is not related to the limit of detection of the system.

7.6.5 Discussion of the proposed sensor

The sensing method described above relies on the fact that the perturbation of the sensor oscillator increases the difference between the intrinsic oscillation frequencies of the two oscillators. So assuming the two oscillators are synchronized and the coupling coefficients are selected so that the system is at the synchronization edge, two scenarios are possible: 1) the intrinsic oscillation frequency of the sensor oscillator is larger than the other oscillator; in this case the perturbation should increase the frequency of the sensor oscillator. 2) the intrinsic oscillation frequency of the sensor oscillator is smaller than the other oscillator; in this case the perturbation should decrease the frequency of the sensor oscillator. Given that the oscillation frequency of any oscillator is selectable by design, once the response of the sensor oscillator to a target measurand is known, the frequency of any other oscillators can be selected to provide maximum sensitivity to a change in the target measurand in a given direction. Clearly, this requirement imposes a limit on the direction or sign of the measurand change; in other words, if the system is designed to detect an increase in certain measurand with highest sensitivity (initially synchronized at synchronization edge), then it will be insensitive to the decrease of that measurand. Alternatively, the system may be tuned such that initially it is not right at the synchronization edge so that the beat frequency is present even in the absence of a measurand change; in this case the system may detect both an increase and decrease of the measurand but with a lower sensitivity.

Since the limit of detection (LoD) of the proposed oscillatory sensor system is ultimately limited by the smallest measurable beat frequency, the signal-to-noise ratio (SNR) of the beat signal may impose a bound on the limit of detection beyond the limit defined by the resolving power of the frequency measurement system. Our preliminary theoretical analysis and experimental observations indicate that the amplitude of the beat signal decreases as the perturbation (and therefore the beat frequency) becomes smaller. Given that generally (at least in electronic circuits) the level of noise increases at lower frequencies (e.g., due to $1/f$ noise mechanisms), we expect the SNR to degrade as the magnitude of the perturbation decreases. A comprehensive study and analysis of the amplitude variations of the beat frequency and the noise in such system is beyond the scope of this paper but it should be considered as an important limitation in particular for applications where a low LoD is required.

Generally, the temperature dependence of the oscillation frequency can be different for the two coupled oscillators in the sensing system. As such if temperature of the oscillators varies during the measurement, the measured value of the beat frequency cannot be used to accurately monitor a change in the measurand (due to residual shift resulted from temperature variations). This problem can be mitigated by stabilizing the temperature of the oscillators (by active control) and thermally isolating them from the sensing element of the sensor oscillator that is used to detect the measurand (e.g., the fiber delay in the OEO).

Another possible limitation of the proposed method is the fact that the beat frequency is much smaller than the oscillation frequencies of the individual oscillator. As such, depending on the frequency measurement system used (e.g., a frequency counter, RF spectrum analyzer, and the like), measuring small changes in a small beat frequency may require longer integration time compared to the time required for monitoring the frequency of isolated oscillators. This factor should be taken into account when evaluating the enhanced sensitivity provided by the coupled system.

7.6.6 Importance of this work

The enhanced sensitivity and the fact that the oscillatory system and the sensing mechanism used in this work support dissimilar oscillators with slightly different frequencies, suggest that this work may become an effective technique in many applications. The tolerance for small frequency difference between two oscillators is an advantage over previously demonstrated systems, since fabrication of oscillators with identical oscillation frequencies (a prerequisite of most previously demonstrated systems), is a challenging task. The heterogeneous systems may provide the added benefit of simultaneous detection of small perturbations of physically distinctive measurands (e.g., temperature, optical power, current, magnetic field, etc.).

The proposed approach is particularly suitable for detection of extremely small perturbations where the frequency shift of a single oscillator may be screened by noise, but the high sensitivity of the beat frequency change in the proposed coupled oscillatory systems is large enough to be measured (resulting in significantly lower limit of detection).

While the variation of the beat frequency in a coupled oscillatory system is inherently nonlinear, for detecting small changes around a background value or starting from a zero perturbation, the sensitivity can be approximated by linear slope. Moreover, in many applications only detection (as opposed to measurement) of a small change of a parameter is the objective, in which case the nonlinearity of the response becomes irrelevant. An example of such applications is detection of small quantity of hazardous molecules (in particular in gaseous state) and triggering an alarm when the detected signal exceeds a pre-set threshold.

7.7 Summary

In this chapter we investigated the dynamics of certain coupled homogeneous and heterogeneous oscillatory systems and some of their applications. The oscillators included in our studies were optomechancial oscillator, Colpitts oscillator and optoelectronic oscillator.

First, we experimentally investigated the cluster synchronization in a multilayer network of four electrical Colpitts oscillators with two interaction layers. We observed the appearance of several cluster states; to our knowledge, the clustered quasiperiodic state was observed for the first time. This work was also the first experimental study of a multilayer network of oscillators with dissimilar coupling between layers. This outcome may provide some insight for understanding clustering in various multilayer systems.

In our second study, we investigated certain aspect of coupling between optoelectronic oscillator, optomechanical oscillator and Colpitts oscillator. Simulation of the coupled optoelectronic oscillator and optomechancial oscillator showed that once the two oscillators are synchronized, further increasing the coupling strength may destroy the synchronization and push the frequencies of the two oscillators to the opposite directions, this is a very unusual but interesting phenomenon, which needs experimental verification and detailed investigation. In addition, we theoretically and experimentally studied the coupling between the optomechanical oscillator and Colpitts oscillator. We found that the noisy spectrum of a Colpitts oscillator can be "cleaned" once injection locked to a high quality optomechancial oscillator (the linewidth of the Colpitts oscillator can be narrowed from tens of kilohertz to 30 Hertz), this finding might be helpful in some MEMS devices as well as certain electronic circuits and systems. Chip based electrical oscillators are widely used in various applications, however electronic oscillators that use an LC tank on a chip generally exhibit poor quality factor compared to those with quatz crystal resonator (note that high frequency quatz crystals are not practical and cannot be integrated with on-chip circuits [108, 109]). In contrast, high frequency and high quality optomechanical oscillator are CMOS compatible and can be fabricated on a chip [110, 111]. So, it is plausible to integrate the OMOs and electronic oscillators on a single chip and injection lock the on-chip electronic oscillators to OMOs to achieve high quality electronic oscillation at higher frequencies.

Next, we experimentally studied the complex dynamics of bidirectionally coupled optoelectronic oscillator and electrical Colpitts oscillator via two different coupling mechanisms. More specifically, we coupled an optoelectronic oscillator to a Colpitts oscillator via optical coupling and coupled back the Colpitts oscillator to the optoelectronic oscillator using a voltage. We investigated and observed phase synchronization and generalized chaos synchronization in the resulting coupled oscillatory system. The phase synchronization was observed when both oscillators were initially pre-set to oscillate in periodical regime (before coupling), while the generalized chaos synchronization was observed if both oscillators were pre-set to oscillate in chaotic regime (when isolated). In the periodical regime we observed simple linear relationship between the values of coupling factors at which a transition to phase synchronization occur. In the chaotic regime, we observed a chaos to hyperchaos transition associated with the synchronization. This work is one of the first experimental studies on the synchronization of two physically dissimilar coupled oscillators.

Finally, we studied the potential application of a coupled oscillatory system in sensing and detection. We theoretically demonstrated that the beat frequency generated by a coupled oscillatory system comprising two originally synchronized similar or dissimilar oscillators is highly sensitive to a weak perturbation of the frequency of one of the oscillators. Based on the well-known *Kuramoto model*, we analytically showed that the variation of the beat frequency resulted from the desynchronization of the coupled oscillators induced by external perturbation is much larger than the frequency shift of a single oscillator exposed to the same level of perturbation. The theoretical predications were validated by experimental measurements of the response of two different coupled oscillatory systems to external perturbation: 1) Two bidirectionally coupled electronic

Colpitts oscillators, when a photo induced current is applied to one of them. 2) An electronic oscillator unidirectionally coupled to an optoelectronics oscillator (OEO), when the temperature of the delay line of the OEO is changed.

In conclusion, coupled oscillatory systems, particularly when they are heterogenous, support many interesting phenomena that are worth exploring. The outcomes of these studies may benefit many related studies and may also find applications in unexpected domains.

7.8 References

[1] M. Dolnik and I. R. Epstein, "Coupled chaotic chemical oscillators," Phys. Rev. E., **54**(24), 3361-3368 (1996).

[2] B. Blasius, E. Montbrio, and J. Kurths, "Anomalous phase synchronization in populations of nonidentical oscillators," Phys. Rev. E., **67**(3), Art. no. 035204(R) (2003).

[3] P. Woafo and H. G. Enjieu Kadji, "Synchronized states in a ring of mutually coupled self-sustained electrical oscillators," Phys. Rev. E., **69**(4), Art. no. 046206 (2004).

[4] D. M. Abrams, and S. H. Strogatz, "Chimera States for Coupled Oscillators," Phys. Rev. Lett. **93**(17), Art. no. 174102 (2004).

[5] O. V. Popovych, S. Yanchuk, and P. A. Tass, "Delay- and Coupling-Induced Firing Patterns in Oscillatory Neural Loops," Phys. Rev. Lett., **107**(22), Art. No. 228102 (2011).

[6] A. Xuereb, C. Genes, and A. Dantan, "Strong Coupling and Long-Range Collective Interactions in Optomechanical Arrays," Phys. Rev. Lett., **109**(22), Art. no. 223601 (2012).

[7] K. M. Hannay, D. B. Forger. and V. Booth, "Macroscopic models for networks of coupled biological oscillators," Sci. Adv., **4**(8), Art. no. e1701047 (2018).

[8] L. J. Pei, L. X. Duan, and H. Y. Liu, “Dynamics of the Coupled Lorenz-Rössler Systems,” in *2010 International Workshop on Chaos-Fractal Theories and Applications*, Kunming, Yunnan, CN, Oct (2010).

[9] P. K. Roy, C. Hens, I. Grosu, and S. K. Dana, “Engineering generalized synchronization in chaotic oscillators,” Chaos, **21**(1), Art. No. 013106 (2011).

[10] G. Tanaka, K. Morino, H. Daido, and K. Aihara, “Dynamical robustness of coupled heterogeneous oscillators,” Phys. Rev. E., **89**(5), Art. no. 052906 (2014).

[11] Guevara, M. R., Glass, L. & Shrier, A. “Phase-locking, period-doubling bifurcations and irregular dynamics in periodically stimulated cardiac cells,” Science, **214**(4527), 1350–1353 (1981).

[12] R. Roy, and K. S. Thornburg, “Experimental Synchronization of Chaotic Lasers,” Phys. Rev. Lett., **72**(13), 2009-2012 (1994).

[13] T. Heil, I. Fischer, and W. Elsässer, J. Mulet, and C. R. Mirasso, “Chaos Synchronization and Spontaneous Symmetry-Breaking in Symmetrically Delay-Coupled Semiconductor Lasers,” Phys. Rev. Lett., **86**(5), 795 (2001).

[14] H. D. I. Abarbanel, N. F. Rulkov, and M.l M. Sushchik, “Generalized synchronization of chaos: The auxiliary system approach,” Phys. Rev. E., **53**(5), 4528-4535 (1996).

[15] R. Banerjee, D. Ghosh, E. Padmanaban, R. Ramaswamy, L. M. Pecora, and S. K. Dana, “Enhancing synchrony in chaotic oscillators by dynamic relaying,” Phys. Rev. E., **85**(2), Art. no. 027201 (2012).

[16] K. A. Blaha, K. Huang, F. D. Rossa, L. Pecora, M. Hossein-Zadeh, and F. Sorrentino, “Cluster Synchronization in Multilayer Networks: A Fully Analog Experiment with LC Oscillators with Physically Dissimilar Coupling,” Phys. Rev. Lett., **122**(1), Art. No. 014101 (2019).

[17] G. Heinrich, M. Ludwig, J. Qian, B. Kubala, and F. Marquardt, “Collective Dynamics in Optomechanical Arrays,” Phys. Rev. Lett., **107**(4), Art. no. 043603 (2011).

[18] M. R. Tinsley, S. Nkomo, and K. Showalter, “Chimera and phase-cluster states in populations of coupled chemical oscillators,” Nat. Physics., **8**, 662–665 (2012).

[19] M. Bagheri, M. Poot, L. R. Fan, F. Marquardt, and H. X. Tang, “Photonic Cavity Synchronization of Nanomechanical Oscillators,” Phys. Rev. Lett., **111**(21), Art. No. 213902 (2013).

[20] C. R. S. Williams, T. E. Murphy, R. Roy, F. Sorrentino, T. Dahms, and E. Scholl, “Experimental Observations of Group Synchrony in a System of Chaotic Optoelectronic Oscillators,” Phys. Rev. Lett., **110**(6), Art. No. 064104 (2013).

[21] C. R. S. Williams, F. Sorrentino, T. E. Murphy, and R. Roy, “Synchronization states and multistability in a ring of periodic oscillators: Experimentally variable coupling delays,” Chaos, **23**(4), Art. no. 043117 (2013).

[22] C. Schäfer, M. G. Rosenblum, J. Kurths, and H. H. Abel, “Heartbeat synchronized with ventilation,” Nature, **392**, 239–240 (1998).

[23] I. Ozden, S. Venkataramani, M. A. Long, B. W. Connors, and A. V. Nurmikko, “Strong Coupling of Nonlinear Electronic and Biological Oscillators: Reaching the “Amplitude Death” Regime,” Phys. Rev. Lett., **93**(15-8), Art. no. 158102 (2004).

[24] C. Droin, E. R. Paquet, F. Naef, “Low-dimensional dynamics of two coupled biological oscillators,” Nat. Phys., **15**, 1086–1094 (2019).

[25] A. Pikovsky, M. Rosenblum, and J. Kurths. “Synchronization. A Universal Concept in Nonlinear Sciences,” Cambridge University Press, Cambridge, (2001).

[26] A. B. Dubois, A. W. Brody, D. H. Lewis, and B. F. Burgess, “Oscillation mechanics of lungs and chest in man,” J. Appl. Physiol., **8**(6) 587-594 (1956).

[27] A. J. Connolly, W. E. Finkbeiner, P. C. Ursell, R. L. Davis, “Chapter 8 - Microscopic Examination,” Elsevier, (2016).

[28] Y. Lan et al., “Noise-induced synchronous stochastic oscillations in small scale cultured heart-cell networks,” Chin. Phys. B., **20**(2), Art. no. 020508 (2011).

[29] C. Foerch, H. W. Korf, H. Steinmetz, M. Sitzer, and A. S. Hessen, “Abrupt shift of the pattern of diurnal variation in stroke onset with daylight saving time transitions,” Circulation, **118**(3), 284-290 (2008).

[30] P. Franco, D. Verheulpen, F. Valente, I. Kelmanson, Alainde Broca, S. Scaillet, J. Groswasser, and A. Kahn. “Autonomic responses to sighs in healthy infants and in victims of sudden infant death,” Sleep Med., **4**(6), 569-577 (2003).

[31] A. Prasad, S. K. Dana, R. Karnatak, J. Kurths, B. Blasius, and R. Ramaswamy, “Universal occurrence of the phase-flip bifurcation in time-delay coupled systems,” Chaos, **18**(2), Art. no. 023111 (2008).

[32] B. M. Adhikari, A. Prasad, and M. Dhamala, “Time-delay-induced phase-transition to synchrony in coupled bursting neurons,” Chaos, **21**(2), Art. no. 023116 (2011).

[33] R. Sevilla-Escoboza, I. Sendiña-Nadal, I. Leyva, R. Gutiérrez, J. M. Buldú, and S. Boccaletti, “Interlayer synchronization in multiplex networks of identical layers,” Chaos: An Interdisciplinary Journal of Nonlinear Science, **26**(6), Art. no. 065304 (2016).

[34] I. Leyva, R. Sevilla-Escoboza, I. Sendiña-Nadal, R. Gutiérrez, J. M. Buldú, and S. Boccaletti, “Inter-layer synchronization in non-identical multi-layer networks,” Sci. Rep., **7**, Art. no. 45475 (2017).

[35] L. Pecora, F. Sorrentino, A. Hagerstrom, T. Murphy, and R. Roy, “Cluster synchronization and isolated desynchronization in complex networks with symmetries,” Nat. Commun., **5**, Art. no. 4079 (2014).

[36] M. Frasca, L. Gambuzza, A. Buscarino, and L. Fortuna, “Synchronization in Networks of Nonlinear Circuits,” Spinger International Publishing, Cham, Switzerland, (2018).

[37] M. Kennedy, “On the relationship between the chaotic Colpitts oscillator and Chua’s oscillator," *IEEE* Trans. Circuits Syst. I., **42**(6), 376-379 (1995).

[38] M. Wickramasinghe, and I. Z. Kiss, “Synchronization of electrochemical oscillators with differential coupling,” Phys. Rev. E **88**(6), Art. no. 062911 (2013).

[39] C. R. S. Williams, F. Sorrentino, T. E. Murphy, and R. Roy, “Synchronization states and multistability in a ring of periodic oscillators: Experimentally variable coupling delays,” Chaos: An Interdisciplinary Journal of Nonlinear Science, **23**(4), Art. no. 043117 (2013).

[40] K. A. Blaha, K. Huang, F. D. Rossa, L. Pecora, M. Hossein-Zadeh, and F. Sorrentino, “Cluster Synchronization in Multilayer Networks: A Fully Analog Experiment with LC Oscillators with Physically Dissimilar Coupling,” Phys. Rev. Lett., **122**(1), Art. no. 014101 (2019).

[41] E. J. Doedel, A. R. Champneys, F. Dercole, T. Fairgrieve, A. Yu, B. Oldeman, R. Paffenroth, B. Sandstede, X. Wang, C. Zhang et al., Auto-07p: Continuation and bifurcation software for ordinary differential equations, (2012).

[42] A. Dhooge, W. Govaerts, and Y. A. Kuznetsov, "Matcont: a MATLAB package for numerical bifurcation analysis of ODEs," ACM Trans. Math. Softw., **29**(2), 141-164 (2003).

[43] J. Cosp, J. Madrenas, E. Alarcon, E. Vidal, and G. Villar, "Synchronization of Nonlinear Electronic Oscillators for Neural Computation," *IEEE* Trans. Neural Networks., **15**(5),1315-1327 (2004).

[44] A. E. Pereda, "Electrical synapses and their functional interactions with chemical synapses," Nat. Rev. Neurosci.,**15**, 250-263 (2014).

[45] M. Scheffer, S. R. Carpenter, T. M. Lenton, J. Bascompte, W. Brock, V. Dakos, J. van de Koppel, I. A. van de Leemput, S. A. Levin, E. H. van Nes, M. Pascual, and J. Vandermeer, "Anticipating Critical Transitions," Science, **338**(6), 344-348 (2012).

[46] M. Alberti, "Cities that Think like Planets: Complexity, Resilience, and Innovation in Hybrid Ecosystems," University of Washington Press, Seattle, (2016).

[47] T. J. Kippenberg, H. Rokhsari, T. Carmon, A. Scherer, and K. J. Vahala, "Analysis of Radiation-Pressure Induced Mechanical Oscillation of an Optical Microcavity," Phys. Rev. Lett., **95**(3), Art. no. 033901 (2005).

[48] X. S. Yao and L. Maleki, "Optoelectronic microwave oscillator," J. Opt. Soc. Am. B., **13**(8), 1725-1735 (1996).

[49] T. Carmon, H. Rokhsari, L. Yang, T. J. Kippenberg, and K. J. Vahala, "Temporal behavior of radiation pressure induced vibrations of an optical microcavity phonon mode," Phys. Rev. Lett., **94**(22), Art. no. 223902 (2005).

[50] T. E. Murphy, A. B. Cohen, B. Ravoori, K. R. B. Schmitt, A. V. Setty, F. Sorrentino, C. R. S. Williams, E. Ott and R. Roy "Complex dynamics and synchronization of delayed-feedback nonlinear oscillators," Phil. Trans. R. Soc. A., **368**(1911), 343-366 (2010).

[51] Y. K. Chembo, L. Larger, H. Tavernier, R. Bendoula, E. Rubiola, and P. Colet, "Dynamic instabilities of microwaves generated with optoelectronic oscillators," Opt. Lett., **32**(17), 2571-2573 (2007).

[52] Y. K. Chembo, L. Larger, and P. Colet, “Nonlinear dynamics and spectral stability of optoelectronic microwave oscillators,” *IEEE* J. Quant. Electron., **44**(9), 858-866 (2008).

[53] M. Peil, M. Jacquot, Y. K. Chembo, L. Larger, and T. Erneux, “Routes to chaos and multiple time scale dynamics in broadband bandpass nonlinear delay electro-optic oscillators,” Phys. Rev. E., **79**(2), Art. no. 026208 (2009).

[54] K. E. Callan, L. Illing, Z. Gao, D. J. Gauthier, and E. Schöll, “Broadband chaos generated by an optoelectronic oscillator,” Phys. Rev. Lett., **104**(11), Art. no. 113901 (2010).

[55] M. P. Kennedy, “Chaos in the Colpitts oscillator,” *IEEE* Trans. Circuits. Systems., **41**(11), 771-774 (1994).

[56] O. D. Feo, G. M. Maggio, “Bifurcations in the Colpitts oscillator: From theory to practice,” Int. J. Bifurcat. Chaos., **13**(10), 2917-2934 (2003).

[57] J. Kengne, J. C. Chedjou, G. Kenne, and K. Kyamakya, “Dynamical properties and chaos synchronization of improved Colpitts oscillators,” Commun. Nonlinear. Sci. Numer. Simulat., **17**(7), 2914 (2012).

[58] L. K. Kana, A. Fomethe, H. B. Fotsin, E. T. Wembe, and A. I. Moukengue, “Complex dynamics and synchronization in a system of magnetically coupled Colpitts oscillators,” J. Nonlinear Dyn., **2017**, Art. no. 5483956 (2017).

[59] R. A. York, P. Liao, and J. J. Lynch, "Oscillator Array Dynamics with Broadband N-Port Coupling Networks," *IEEE* Trans. Microw. Theory Tech., **42**(11) 2040-2045 (1994).

[60] B. Razavi, "A Study of Injection Locking and Pulling in Oscillators," *IEEE* J. Solid-State Circuits., **39**(9), 1415-1424 (2004).

[61] A. Mirzaei, H. Darabi, "Mutual pulling between two oscillators," *IEEE* J. Solid-State Circuits., **49**(2), 360-372 (2014).

[62] D. Farmer, J. Crutchfield, H. Frochling, N. Packard, and R. Shaw, “Power spectra and mixing properties of strange attractors,” International Conference on Nonlinear Dynamics, New York, NY, Dec. 17-21, (1979).

[63] R. S. Dumont, and P. Brumer, “Characteristics of power spectra for regular and chaotic systems,” J. Chem. Phys., **88**(3), 1481-1496 (1988).

[64] M. C. Valsakumar, S. V. M. Satyanarayana, and V. Sridhar, “Signature of chaos in power spectrum,” Pramana - J. Phys., **48**(1), 69-85 (1997).

[65] M. Sano, and Y. Sawada, “Measurement of the Lyapunov Spectrum from a Chaotic Time Series,” Phys. Rev. Lett., **55**(10), 1082-1085 (1985).

[66] A. Čenys, A. Tamaševičius, A. Baziliauskas, R. Krivickas, and E. Lindberg, “Hyperchaos in coupled Colpitts oscillators,” Chaos. Soliton. Fract., **17**(2-3), 349-353 (2003).

[67] J. Mulet, C. Mirasso, T. Heil, and I. Fischer, “Synchronization scenario of two distant mutually coupled semiconductor lasers,” J. Opt. B: Quantum Semiclass. Opt., **6**(1), 97-105 (2004).

[68] J. K. White, M. Matus, and J. V. Moloney, “Achronal generalized synchronization in mutually coupled semiconductor lasers,” Phys. Rev. E., **65**(3), Art. No. 036229 (2002).

[69] A. T. Nimal, M. Singh, U. Mittal, and R. D. S. Yadava, “A comparative analysis of one-port Colpitt and two-port Pierce SAW oscillators for DMMP vapor sensing,” Sensors and Actuators B: Chemical, **14**(1), 316-325 (2006).

[70] M. Z. Yang, C. L. Dai, and D. H. Lu, “Polypyrrole Porous Micro Humidity Sensor Integrated with a Ring Oscillator Circuit on Chip” Sensors, **10**(11), 10095-10104 (2010).

[71] Y. C. Ahn, and H. Guckel, “Resonant Microbeam Electronic Oscillators for strain sensing,” Sensors and Materials, **12**(4), 175-203 (2000).

[72] J. Chaste, A. Eichler, J. Moser, G. Ceballos, R. Rurali, and A. Bachtold, “A nanomechanical mass sensor with yoctogram resolution,” Nat. Nanotechnol., **7**, 301-304 (2012).

[73] Y. T. Yang, C. Callegari, X. L. Ekinci, and M. L. Roukes, “Zeptogram-Scale Nanomechanical Mass Sensing,” Nano. Lett., **6**(4), 583-586 (2006).

[74] A. N. Cleland, and M. L. Roukes, “A nanometre-scale mechanical electrometer,” Nature, **392**, 160-162 (1998).

[75] X. B. Guo, Y. B. Yi, and S. Pourkamali, “Thermal-Piezoresistive Resonators and Self-Sustained Oscillators for Gas Recognition and Pressure Sensing,” *IEEE* Sens. J., **13**(8), 2863-2872 (2013).

[76] F. F. Liu, S. Alaie, Z. C. Leseman, and M. Hossein-Zadeh, “Sub-pg mass sensing and measurement with an optomechanical oscillator,” Opt. Express., **21**(17), 19555-19567 (2013),

[77] W. Y. Yu, W. C. Jiang, Q. Lin, and T. Lu, “Cavity optomechanical spring sensing of single molecules,” Nature. Commun., **7**, Art. no. 12311 (2016).

[78] Y. P. Wang, J. J. Zhang, and J. P. Yao, “An Optoelectronic Oscillator for High Sensitivity Temperature Sensing,” *IEEE*. Photon. Technol. Lett., **28**(13), 1458-1461 (2016).

[79] S. X. Chew, X. K. Yi, C. J. Wu, L. W. Li, L. Nguyen, and R. Minasian, “Optoelectronic Oscillator Based Sensor Using an On-Chip Sensing Probe,” *IEEE*. Photonics J., **9**(2), Art. no. 5500809 (2017).

[80] T. Zhang, J. Zhu, T. Guo, J. Wang, and S. Ye, “Improving accuracy of distance measurements based on an optoelectronic oscillator by measuring variation of fiber delay,” Appl. Opt., **52**(15), 3495-3499 (2013).

[81] M. Li, W. Li, J. Yao, and J. Azaña, “Femtometer-Resolution Wavelength Interrogation Using an Optoelectronic Oscillator,” in Proc. *IEEE* Photon. Conference, Burlingame, CA, USA, pp. 298-299 (2012).

[82] L. D. Nguyen, K. Nakatani, and B. Journet, “Refractive Index Measurement by Using an Optoelectronic Oscillator,” *IEEE* Photon. Technol. Lett., **22**(12), 857-859 (2010).

[83] O. Terra, “Optoelectronic oscillations for thermo-optic coefficient measurement of optical fibers,” Measurement Science and Technology, **30**(3), Art. no. 035205 (2019).

[84] J. Juillard, A. Bonnoit, N. Barniol, A. Uranga, and G. Vidal-Álvarez, “A novel architecture for differential resonant sensing,” Procedia Engineering, **87**, 1573-1576 (2014).

[85] J. Juillard, A. P. Prache, and N. Barniol, “Analysis of Mutually Injection-Locked Oscillators for Differential Resonant Sensing,” *IEEE* T. CIRCUITS-I., **63**(7), 1055-1066 (2016).

[86] E. Gil-Santos, D. Ramos, A. Jana, M. Calleja, A. Raman, and J. Tamayo, “Mass Sensing Based on Deterministic and Stochastic Responses of Elastically Coupled Nanocantilevers,” Nano. Lett., 9(12), 4122-4127 (2009).

[87] M, Spletzer, A. Raman, A. Q. Wu, and X. F. Xu, “Ultrasensitive mass sensing using mode localization in coupled microcantilevers,” Appl. Phys. Lett., **88**(25), Art. no. 254102 (2006).

[88] S. Barbarossa, and F. Celano, “Self-organizing sensor networks designed as a population of mutually coupled oscillators,” in *IEEE 6th workshop on single processing advances in wireless communications*, New York, NY, USA, pp. 475-479 (2005).

[89] J. Kowalski, M. Strzelecki, and H. Kim, “Implementation of a Synchronized Oscillator Circuit for Fast Sensing and Labeling of Image Objects,” Sensors, **11**(4), 3401-3417 (2011).

[90] J. R. Vig, “Temperature-Insensitive Dual-Mode Resonant Sensors-A Review,” *IEEE* Sens. J., **1**(1), 62-68 (2001).

[91] Z. Y. Wang, H. Z. Zhu, Y. G. Dong, and G. P. Feng, “A Thickness-Shear Quartz Resonator Force Sensor with Dual-Mode Temperature Compensation,” *IEEE* Sens. J., **3**(4), 490-496 (2003).

[92] C. M. Jha, G. Bahl, R. Melamud, S. A. Chandorkar, M. A. Hopcroft, B. Kim, M. Agarwal, J. Salvia, H. Mehta and T. W. Kenny, “CMOS-Compatible Dual-Resonator MEMS Temperature Sensor with Milli-Degree Accuracy,” in *Transducers 2007 Internation Solid-State Sensors, Actuators and Microsystems Conference*. Lyon, France, pp. 229-232 (2007).

[93] W. H. P. Nielsen, Y. Tsaturyan, C. B. Møller, E. S. Polzik, and A. Schliesser, “Multimode optomechanical system in the quantum regime,” PNAS, vol. 114, no. 1, pp. 62-66, Jan. 2017.

[94] Z. Y. Xie, S. Y. Li, H. Z. Yan, X. D. Xiao, X. P. Zheng, and B. K. Zhou, “Tunable dual frequency optoelectronic oscillator with low intermodulation based on dual-parallel Mach-Zehnder modulator,” Opt. Express., **24**(26), 30282-30288 (2016).

[95] Y. Kuramoto, and H. Araki, “Self-Entrainment of a population of coupled non-linear oscillators.” International symposium on mathematical problems in theoretical physics, **39**, 420-422 (2005).

[96] S. H. Strogatz, “Human sleep and circadian rhythms: a simple model based on two coupled oscillators,” J. Math. Biol., **25**(3), 327-347 (1987).

[97] S. H. Strogatz, “From Kuramoto to Crawford: exploring the onset of synchronization in populations of coupled oscillators,” Physica D, 143(1-4), 1-20 (2000).

[98] B. Razavi, “Mutual injection pulling between oscillators,” in *IEEE* 2006 Custom Intergrated Circuits Conference. San Jose, CA, USA, 2006, pp. 1-4.

[99] A. Mirzaei, and H. Darabi, “Mutual pulling between two oscillators,” *IEEE* J. Solid - State Circuits., **49**(2), 360-372 (2014).

[100] I. Z. Kiss, Y. M. Zhai, and J. L. Hudson, “Emerging coherence in a population of chemical oscillators,” Science, **296**(5573), 1676-1678 (2002).

[101] I. Z. Kiss, Y. M. Zhai, and J. L. Hudson, “Predicting Mutual Entrainment of Oscillators with Experiment-Based Phase Models,” Phy. Rev. Lett., **94**(24), Art. no. 248301 (2005).

[102] G. Heinrich, M. Ludwig, J. Qian, B. Kubala, and F. Marquardt, “Collective Dynamics in Optomechanical Arrays,” Phy. Rev. Lett., **107**(4), Art. no. 043603 (2011).

[103] D. Mertens, and R. Weaver, “Synchronization and stimulated emission in an array of mechanical phase oscillators on a resonant support,” Phys. Rev. E., **83**(4), Art. no. 046221 (2011).

[104] G. Kozyreff, A. G. Vladimirov, and P. Mandel, “Global coupling with time delay in an array of semiconductor lasers,” Phy. Rev. Lett., **85(**18), Art. no. 3809 (2000).

[105] M. Nixon, M. Friedman, E. Ronen, A. A. Friesem, N. Davidson, and I. Kanter, “Synchronized Cluster Formation in Coupled Laser Networks,” Phy. Rev. Lett., **106**(22), Art. no. 223901 (2011).

[106] R. Adler, "A study of locking phenomena in oscillators", *Proc. IEEE,* **61**, 1380-1385 (1973).

[107] A. Mirzaei, and A. A. Abidi, “The Spectrum of a Noisy Free-Running Oscillator Explained by Random Frequency Pulling,” *IEEE* T CIRCUITS-I., **57**(3), 642-653 (2010).

[108] S. H. Zhou, J.-P. Zeng, Q. Xiong, Y. Zeng, “Study and design of integrated crystal oscillator,” *in Proc. International Conference on Wireless Communications & Signal Processing*, Nanjing, CN, Nov, (2009).

[109] H. iKutsuwada, S. Watanabe, M. Sohgawa, T. Abe, “Fabrication of a true-Gaussian-shaped quartz crystal resonator,” Sensors and Actuators A: Physical, **260**, 58-61 (2017).

[110] X. K. Sun, K. Y. Fong, C. Xiong, W. H. P. Pernice, and H. X. Tang, “GHz optomechanical resonators with high mechanical Q factor in air,” Opt. Express., **19**(20), Art. no. 22316 (2011).

[111] S. Tallur, S. Sridaran, and S. A. Bhave, “A monolithic radiation-pressure driven, low phase noise silicon nitride opto-mechanical oscillator,” Opt. Express., **19**(24), 24522-24529 (2011).

Chapter 8

Future directions

8.1 Injection locking of OMO via surface acoustic waves (SAWs)

As is discussed in chapter 3, injection locking of OMO via acoustic waves can be a very efficient non-contact method for synchronizing one or more OMOs with another type of oscillator. As such, many applications such as RF signal processing, optical communication and sensing may benefit from this method. In the proof-of-demonstration experiment, we used a bulk PZT transducer attached to the carrier chip of the OMO to generate acoustic signal to injection lock the OMO. However, in a monolithically integrated chip, the bulk transducer may be replaced with on-chip electromechanical transducers based on piezo electric thin films and interdigitated electrodes that not only result in more compact systems, but also enable excitation of various types of surface acoustic waves (SAWs) that may transfer the acoustic energy to selected modes of the OMO more efficiently. Moreover, integrated acoustic waveguides and phononic crystals can be used to improve the directivity of the acoustic energy transfers to the target OMO. With this approach, the acoustic energy from one transducer can be distributed among several OMOs or multiple transducers can be independently locked to groups of OMOs.

In the past few years high quality factor optomechanical cavities have been already fabricated on single crystal Lithium Niobate ($LiNbO_3$) [1]; since $LiNbO_3$ is also a piezoelectric material that can serve as a substrate for SAW devices [2], a possible monolithic system may include optomechanical cavities and SAW devices fabricated on a single LiNbO$_3$ chip. Acoustic waveguides can also be fabricated on the same chip to redirect or concentrate the acoustic energy to the target OMOs [3, 4]. Figure 8.1 (a) shows an example of surface acoustic wave generated by a SAW device calculated based on finite element modeling (FEM) using a commercial software (COMSOL); here the SAW generator is a interdigital transducer (IDT) formed from Al electrode deposited on a LiNbO$_3$ substrate (the characteristic frequency of this IDT, that is determined by the period of the Al electrodes, is 9.58 MHz). Figure 8.1(b) is a schematic diagram showing of toroidal microcavity on the same substrate.

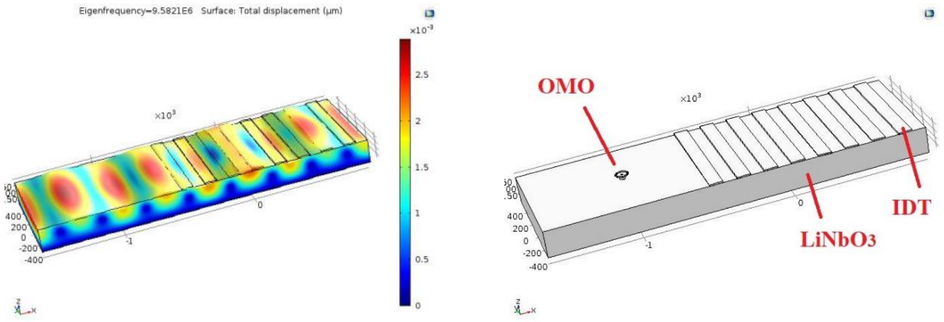

(a) (b)

Fig. 8.1. (a) Surface acoustic wave generated by an IDT, and (b) Microtoroidal cavity integrated with the SAW generator shown in part-a.

8.2 Performance of OMR/OMO based acoustic receiver

In chapter 5 and 7 we demonstrated the application of strong optomechanical coupling and the resulting gain in acousto-optical transduction and down conversion in the context of acoustic transducer and underwater acoustic link. While our calculations and measurements have revealed some of the basic properties of OMR/OMO based acoustic receivers, still many parameters in these systems needs to be investigated. Some related future directions may include:

1) *Improving Acoustic transmission efficiency and the device packaging*

As mentioned in chapter 6, The large impedance mismatch between the cavity material (e.g., silicon) and the acoustic signal transfer medium (e.g., sea water) results in significant insertion loss of the acoustic energy due to reflection at the interface between silicon and water. Meanwhile the small size of the cavity device (~ hundreds micron) limits its capability of capturing acoustic energy. In the example discussed in chapter 6 (section 6.5), a combination of acoustic impedance matching, and acoustic concentration were proposed to overcome this problem. Similar configuration with a more compact form factor may be implemented to fabricate more practical acousto-optical transducers based on OMR. Clearly, the efficiency of acoustic energy transfer cannot be addressed independent of packaging.

2) *Measuring the bandwidth and dynamic range of the OMR/OMO based acoustic receiver*

Dynamic range is one of the important characteristics of an acousto-optical transducer. However, measuring the dynamic range of the OMR/OMO based acoustic receiver needs a carefully designed setup, that can resolve problems like fiber taper vibration caused by the acoustic wave during the measurement. Bandwidth is another important characteristic of an acoustic transducer. Considering the injection locking can happen at certain frequency range with certain acoustic power in the OMO based acoustic receiver, characterization of the bandwidth of the OMO based acoustic receiver is a challenging task and requires a good acoustic source with wide flat spectrum.

8.3 Photoacoustic imaging using OMR

Noninvasive laser-based diagnostic and imaging techniques have been subject of research and development for several decades. Photoacoustic imaging is a relatively new technique that has demonstrated great potential for visualization of the internal structures and function of soft tissue [5, 6] and it has particularity shown great potential for small animal imaging [7]. This imaging technique is based on selective of absorption of light in certain biological materials and subsequent generation of acoustic waves that may be used to form an image. A pulsed or modulated laser source illuminates a sample volume and the absorbed optical energy produces thermal variations and therefore pressure waves generated by expansion and contraction of the volume in which light is absorbed. The generated acoustic waves can be detected by ultrasound transducers positioned outside the sample in order to determine their origin and create an image of the points from which the acoustic waves emerge. For example, because of the large difference between optical absorption at certain wavelengths (i.e., 488 nm) between blood and surrounding tissue, the ultrasound wave induced by the laser irradiation at 488 nm may be used for the imaging the microvascular system. Typical acoustic imaging techniques use a short-pulsed laser source to irradiate the sample. In 2004, a novel frequency domain photoacoustic imaging methodology has been proposed [8], in which the acoustic wave is generated by periodic modulation of the laser source. It has been shown that frequency-domain approaches yield higher signal-to-noise ratios than time-domain approaches [9].

As demonstrated in this thesis, OMR shows enhanced modulation depth than any other type of opto-acoustic transducers at fixed optical power. In addition, the modulation depth of the OMR’s detection increases proportional to level of the optical pump power (due to optomechanical gain). So, it should be possible to reduce the power consumption and enhance the efficiency of photoacoustic imaging by using an OMR transducer instead of other optical transducers or piezoelectric transducers.

8.3.1 Preliminary experimental work for acousto-optical imaging using OMR

Photoacoustic imaging was demonstrated upon different samples by using different laser wavelengths, the main considerations are the cost, laser intensity and the sample’s absorption of the laser power. Table 8.1 shows some typical photoacoustic imaging experiments for imaging different samples with different wavelengths.

We have designed an experimental setup for proof of demonstration of photo-acoustic imaging system based on microtoroidal OMR. We selected a laser with a wavelength of 488 nm as the optical source. Such a wavelength is absorbed in samples such as sutures made of Nylon, Silk, Polyester, Polypropylene, Catgut with diameters of 150 μm and 200 μm as well MEH-PPV powder dissolved in toluene solution (which has peak absorption in 488 nm [19]).

Figure 8.2 shows the experimental setup that we built to test microtoroid OMR acoustic transducer for photoacoustic imaging. The sample is placed inside an acoustic gel and on top of a thin cover glass with thickness of 170 μm. The laser light is focused on the sample using a microscope objective (UPLFLN 20X, from Olympus) that generates a beam waist with a diameter of 1 μm.

Table. 8.1. Various photoacoustic imaging experiments

Approach type	Sample	Wavelength	Transducer	References
Frequency domain	Rubber in water	1064 nm	PZT PanametricsV382	[8]
Pulsed laser	Microvascular of rat	584 nm	PZT array	[10]
Pulsed laser	Chicken breast	650 nm	PZT L8-4, Philips Healthcare	[11]
Frequency domain	Agar phantom	808 nm	PZT V382, Olympus-NDT	[12]
Pulsed laser	Human hair, Black ink	532 nm	PZT V323, Panametrics-NDT	[13]
Pulsed laser	Blood flow in zebrafish	532 nm	$LiNbO_3$	[14]
Frequency domain	Castor/Mineral/Olive oil and Glycerin	1210 nm	PZT V382, Panametrics, Olympus	[15]
Frequency domain	Indocyanine Green aqueous solution	785 nm	PZT UST,Olympus NDT	[16]
Frequency domain	Chromium line and blood smear	405 nm	Onda, needle hydrophone: HNC 1000	[17]
Frequency domain	Suture and eyeball/suture/vasculature of zebrafish larva	488 nm	PZT SONAXIS, Besancon	[18]
Frequency domain	Sutures (Nylon, Silk, Polyester, Polypropylene, Catgut) and MEH-PPV in toluene	488 nm	OMR On Si chip	Our work

In the experiment, the maximum average optical power from the 488 nm laser (QFLD-488-10SAX, from QPhotonics) incident on the objective lens is about 7 mW so a fluence as large as 0.4 MW/cm^2 could be generated on the sample (note that in practical applications, the maximum fluence allowed is limited by the ANSI safety standards and should be less than 200 mW/cm^2). In order to scan the sample to obtain the image, the cover glass was attached to a computer-controlled translation stage with the horizontal travel resolution of 29 nm.

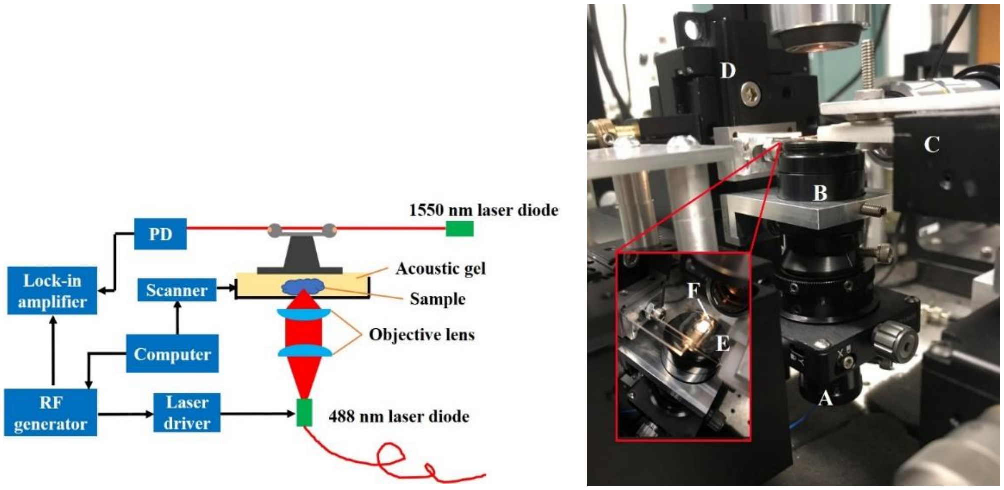

(a) (b)

Fig. 8.2. (a) Experimental configuration designed for proof-of-concept demonstration of photoacoustic imaging using a microtoroidal OMR. (b) Photograph of the experimental setup. A: 488 nm laser; B: Objective; C: Computer controlled high resolution translation stage; D: Manual controlled translation stage; E: Cover glass with sample and F: OMR on silicon chip. (the region shown in red rectangle is magnified for better visibility).

An RF function generator was used to modulate the output optical power of the laser with sinusoidal wave. A modulation depth of 100% was achieved at a modulation frequency of 100 kHz, and with modulation depth of 76% was achieved at a modulation frequency of 10 MHz (that is equal to the frequency of one of the mechanical eigen modes of the OMR). The optical output of the OMR is converted to voltage signal using a fast photodetector with transimpedance gain of 4.2×10^4 V/W. The output signal was measured using a Lock-in amplifier (SR844, Stanford Research Systems). The microtoroid cavity used here has major diameter D = 110 μm; minor diameter d = 10 μm; pillar diameter D_p = 70 μm; and fundamental mode frequency f_{mech} = 10 MHz, the $Q_{tot} = 3.1 \times 10^6$ and Q_m = 238; the silicon chip has dimension of 150 mm × 45 mm × 0.35 mm.

8.3.2 Problems and the possible solutions

We have examined several samples including Nylon, Silk, Polyester, Polypropylene, Catgut with diameters of 150 μm and 200 μm as well as MEH-PPV dissolved in toluene. Unfortunately, after many attempts, we did not observe any photoacoustic signal. One possible reason can be the strong thermal noise generated near the mechanical frequency of the selected OMR. Further investigation is required to find the origin of the problem and the experiment should be systematically repeated with OMRs with higher optical and mechanical quality factors. Moreover, the alignment of the focused laser beam with the sample should be revisited. Unfortunately, we were not able to continue the experimental work as our lab was closed due to a pandemic (COVID-19).

8.4 Dynamics of two coupled heterogenous oscillators

As mentioned earlier, the dynamic of coupled heterogeneous oscillators may have applications in sensing [20] and may benefit study of oscillatory living system [21]. In chapter 7 some of the basic aspects of the physics and dynamics of relatively simple coupled heterogeneous oscillatory systems were presented; however, there are still many interesting aspects remaining that require further investigation. For example:

1) *Coupling function of two coupled heterogeneous oscillators*

Several theoretical approaches have been reported in the literatures to analyze coupled homogeneous oscillators, for example, some are based on dynamical equations [22, 23] and some are based on group-theoretical approach [24, 25]. The most commonly employed method is to work directly with the differential equations describing the coupled oscillators—i.e., the Oregonator model for BZ reaction [26], the Kirchhoff's law for coupled Colpitts oscillators [27]. However, it is generally difficult to determine the differential equations governing the dynamics of coupled oscillatory systems in biological systems, especially coupled heterogeneous biological systems.

A complementary, and perhaps a more promising approach, is using a phase model. Such approach has been used to study the dynamics of various coupled homogeneous systems [28-30]. To the best of our knowledge, there is no effort reported to build a phase model for coupled heterogeneous oscillators. Considering that the coupled heterogeneous oscillatory system involves dissimilar oscillators with different working mechanisms and dissimilar coupling mechanisms which makes the study on it very complicated. So, building a phase model applicable for such system is very necessary to simplify the research process.

2) *Numerical study of the coupled OEO and electrical Colpitts oscillator*

In chapter 7, we experimentally studied the dynamics of the coupled OEO and electrical Colpitts oscillator, we found that a simple linear relationship exists between the two coupling mechanisms in phase synchronization regime. We also observed a transition from chaotic synchronization regime to hyperchaotic synchronization regime in that system. A comprehensive theoretical study of the system may reveal more interesting phenomena that may have been missed in current experiments. Verification and explanation of these phenomena may lead to discovery of new properties only found in heterogeneous oscillatory systems.

8.5 References

[1] W. C. Jiang and Q. Lin, "Chip-scale cavity optomechanics in lithium niobate," Sci. Rep., **6**, Art. no. 36920 (2016).

[2] M. K. Hu and F. L. Duan, "Design, fabrication and characterization of SAW devices on LiNbO3 bulk and ZnO thin film substrates," Solid-State Electronics, **150**, 28-34 (2018).

[3] K. J. Fang, M. H. Matheny, X. S. Luan, and O. Painter., "Optical transduction and routing of microwave phonons in cavity-optomechanical circuits," Nat. Photon., **10**, 489-496 (2016).

[4] E. Wadbro, R. Udawalpola, and M. Berggren, "Shape and topology optimization of an acoustic horn–lens combination," J. Comput. Appl. Math., **234**(6), 1781-1787 (2010).

[5] G. Langer, B. Buchegger, J. Jacak, T. A. Klar, and T. Berer, "Frequency domain photoacoustic and fluorescence microscopy," Biomed. Opt. Express., **7**(7), Art. no. 262884 (2016).

[6] S. Kellnberger, *et al.*, "Optoacoustic microscopy at multiple discrete frequencies," Light Sci. Appl., **7**, Art. no. 109 (2018).

[7] N. Baddour, "Theory and analysis of frequency-domain photoacoustic tomography," J. Acoust. Soc. Am., **123**(5), 2577-2590 (2008).

[8] Y. Fan, A. Mandelis, G. Spirou, and I. A. Vitkin, "Development of a laser photothermoacoustic frequency-swept system for subsurface imaging: Theory and experiment," J. Acoust. Soc. Am., **116**(6), 3523–3533 (2004).

[9] J. F. De Boer, B. Cense, B. H. Park, M. C. Pierce, G. J. Tearney, and B. E. Bouma, "Improved signal-to-noise ratio in spectral-domain compared with time-domain optical coherence tomography," Opt. Lett., **28**(21), 2067–2069 (2003).

[10] R. J. Zemp, et al., “Photoacoustic imaging of the microvasculature with a high-frequency ultrasound array transducer,” J. Biomedical Optics, **12**(1), Art. no. 010501 (2007).

[11] C. Kim, et al., “Deeply penetrating in vivo photoacoustic imaging using a clinical ultrasound array system,” Biomed. Opt. Express., **1**(1), 278-284 (2010).

[12] S. Kellnberger, et al., “In vivo frequency domain optoacoustic tomography,” Opt. Lett., **37**(16), 3423-3425 (2012).

[13] Y. Gao, J. Rong, and X. Y. Jing, “The Effect of Different Center Frequency of Transducers on the Photoacoustic tomography,” in *IEEE International Conference on Medical Imaging Physics and Engineering*, 315-318 (2013).

[14] J. Park, et al., “High frequency photoacoustic imaging for in vivo visualizing blood flow of zebrafish heart,” Opt. Express., **21**(12), 14636-14642 (2013).

[15] S. Liang, et al., “The application of frequency-domain photoacoustics to temperature-dependent measurements of the Grüneisen parameter in lipids,” Photoacoustics, **11**, 56-64 (2018).

[16] P. LeBoulluec, H. L. Liu, and B. H. Yuan., “A cost-efficient frequency-domain photoacoustic imaging system,” Am. J. Phys., **81**(9), Art. no. 712 (2013).

[17] G. Langer, *et al*., “Frequency domain photoacoustic and fluorescence microscopy,” Biomed. Opt. Express., **7**(7), 2692-2702 (2016).

[18] S. Kellnberger, *et al*., “Optoacoustic microscopy at multiple discrete frequencies,” Light Sci. Appl., **7**, Art. no. 109 (2018).

[19] S. Y. Quan, F. Teng, *et al*., “Solvent and concentration effects on fluorescence emission in MEH-PPV solution,” Eur. Polym. J., **42**(1), 228-233 (2006).

[20] K. Huang, and M. Hossein-Zadeh, “Detection and Sensing Using Coupled Oscillatory Systems at the Synchronization Edge,” Early Access, *IEEE* Sens. J., (2020).

[21] K. Huang, F. Sorrentino, and M. Hossein-Zadeh, “Experimental observation of synchronization between two coupled physically dissimilar oscillators,” under review.

[22] S. C. Manrubia, A. S. Mikhailov, and D. H. Zanette, “Emergence of Dynamical Order: Synchronization Phenomena in Complex Systems,” World Scientific, Singapore, (2004).

[23] Y. Kuramoto, Chemical Oscillation, “Wave, and Turbulence,” Springer-Verlag, Berlin, (1984).

[24] M. Golubitsky, I. Stewart, and D. G. Schaeffer, “Singularities and Groups in Bifurcation Theory,” **69**, Springer, New York, (1988).

[25] A. Takamatsu, R. Tanaka, H. Yamada, T. Nakagaki, T. Fujii, and I. Endo, “Spatiotemporal Symmetry in Rings of Coupled Biological Oscillators of Physarum Plasmodial Slime Mold,” Phys. Rev. Lett., **87**(7), Art. no, 078102 (2001).

[26] L. Györgyi and R. J. Field, “A three-variable model of deterministic chaos in the Belousov–Zhabotinsky reaction,” Nature, **355**, 808-810 (1992).

[27] K. A. Blaha, K. Huang, F. D. Rossa, L. Pecora, M. Hossein-Zadeh, and F. Sorrentino “Cluster Synchronization in Multilayer Networks: A Fully Analog Experiment with LC Oscillators with Physically Dissimilar Coupling,” Phys. Rev. Lett., **122**(1), Art. no. 014101 (2019).

[28] M. A. Schwemmer, T. J. Lewis, “The Theory of Weakly Coupled Oscillators,” Phase Response Curves in Neuroscience, **6**, 3-31 (2012).

[29] D. Yuan, F. Lin, L. M. Wang, D. Y. Liu, J. Z. Yang, and Y. Xiao, “Multistable states in a system of coupled phase oscillators with inertia,” Sci. Rep., **7**, Art. no. 42178 (2017).

[30] B. Pietras, and A. Daffertshofer, "Network dynamics of coupled oscillators and phase reduction techniques," Phys. Rep., **819**, 1-105 (2019).

Appendix A: Relation between RF driving power and equivalent acoustic force

As mentioned in section 4.6 in chapter 4, in order to simulate the variation of lock range and relative oscillation phase as a function of the RF power fed to the PZT (P_{PZT}) using coupled differential Eqs. (4.2) and (4.3), the radial component of the equivalent acoustic force (F_{A0}) experienced by the microtoroid should be known as a function of P_{PZT}. Here we present the calculation procedure that leads to Eq. (4.4). We used Finite Element Modeling (COMSOL electrical mechanical package) for these calculations. Since modeling configuration-2 and -3 requires a relatively large model and therefore long simulation time, we have limited our calculation to mode-1 ($f_{\mathrm{OMO},1} = 2.7$ MHz) excited via configuration-1.

The cylindrical symmetry of configuration-1 allows reducing the simulated zone without significant impact on the outcome. Figure A.1(a) shows the configuration used in the simulation where the silicon and acrylic tape thicknesses are selected based on experimental values while the area of the chip below OMO is reduced to $80 \times 80\ \mu\mathrm{m}^2$. The thickness of the PZT is also reduced as the software allows adjusting the PZT parameters such that its response is similar to that of the actual PZT without the need to model the whole PZT thickness.

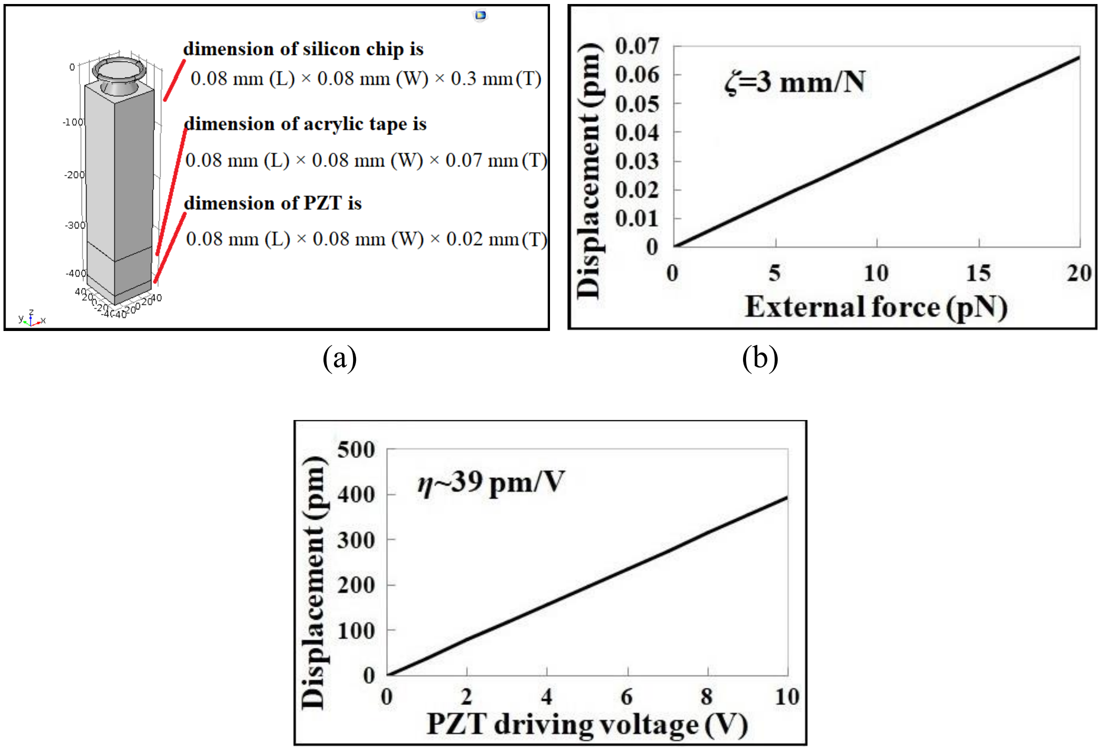

(a) (b)

(c)

Fig. A.1. (a) The model used for calculating the relation between F_{A0} and P_{PZT} using the Finite Element Modeling. (b) Calculated displacement amplitude (d_{r0}) as a function of the amplitude of the external force (F_{A0}) inserted on the toroidal section of the microresonator. (c) Calculated displacement amplitude (d_{r0}) as a function of the amplitude of the voltage ($V_{RF,0}$) applied on the PZT.

As the software did not allow direct calculation of the amplitude of the force experienced by a certain mechanical mode (F_{A0}) we used amplitude of the radial displacement of toroidal section to find the relation between F_{A0} and P_{PZT}. First, we calculated the relation between an external harmonically varying radial force ($F_A = F_{A0}\cos(\Omega_{PZT})$ where $\Omega_{PZT} = 2\pi f_{OMO,1}$) inserted on the toroidal section of the microresonator and the resulting displacement amplitude ($d_r = d_{r0}\cos(\Omega_{PZT})$. Figure. A.1(b) shows that d_{r0} varies linearly with F_{A0} with a slope of 3 mm/N. Next we calculated the d_{r0} as a function of the amplitude of the RF voltage (peak voltage) applied on the PZT ($V_{RF} = V_{RF,0}\cos(\Omega_{PZT}t-\theta)$). The PZT parameters and mechanical boundary conditions were selected such that the acoustic waves generated by the PZT for a given RF power is the same as the actual PZT. This was done by exciting the same mechanical mode (thickness mode) of the PZT that is excited in the experiment and adjusting the piezoelectric and mechanical properties of the PZT according to its actual specifications (extracted from the spec sheet). Figure 4.A.1(c) shows that d_{r0} varies linearly as a function of PZT driving voltage with a slope of 39 pm/V. As mentioned earlier the limitation of our software did not allow extracting the phase difference (θ) between V_{RF} and d_r.

As such we concluded that the amplitude of the equivalent radial force is related to the amplitude of the applied RF voltage via:

$$F_{A0} = \frac{\eta}{\zeta} \times V_{RF,0} = \frac{39\times10^{-12}}{3\times10^{-3}} \times V_{RF,0} = 13 \times 10^{-9} \times V_{RF,0}. \qquad \text{(A-1)}$$

The impedance of the RF source is 50 Ω and the estimated impedance of the PZT at 2.7 MHz (based on its value at resonance) is about 32 Ω. So $V_{RF,0}$ in the above equation can be replaced by P_{PZT}:

$$F_{A0} = \left(\frac{\eta}{\zeta}\right)\sqrt{\frac{2Z}{1000} \times 10^{(P_{PZT}/10)}} = 3.3 \times 10^{-9} \times 10^{(P_{PZT}/20)}. \qquad \text{(A-2)}$$

here the unit of P_{PZT} is dBm, F_{A0} is in Newton.